**The Dissertation Committee for Carey Wayne King certifies that
this is the approved version of the following dissertation:**

Design Synthesis of Multistable Equilibrium Systems

Committee:

_____
Joseph J. Beaman, Jr., Supervisor

_____
Matthew Campbell, Co-Supervisor

_____
S. V. Sreenivasan

_____
Raul Longoria

_____
Ofodike Ezekoye

_____
Dean Neikirk

Design Synthesis of Multistable Equilibrium Systems

by

Carey Wayne King, BSME

Dissertation

Presented to the Faculty of the Graduate School of

the University of Texas at Austin

in Partial Fulfillment

of the Requirements

for the Degree of

Doctor of Philosophy

The University of Texas at Austin

May 2004

This work is dedicated to all of those people who have ever given more to someone than they took.

"As my late grandmother Dorthy used to say 'álleh', which I always supposed was Czechoslovakian for 'that's a bunch of bull', I say it to all those who think knowledge can't prevent social, economic, and technological disaster. Or maybe it was just her own slang? Nonetheless, you get the point. We might as well give it our best shot."

Acknowledgment

Design Synthesis of Multistable Equilibrium Systems

Publication No. _____

Carey Wayne King, Ph.D.
The University of Texas at Austin, 2004

Supervisors: Joseph J. Beaman and Matthew I. Campbell

Mechanical systems are often desired to have features that can adapt to changing environments. Ideally these systems have a minimum number of parts and consume as little power as possible. Unfortunately many adaptable systems either have a large number of heavy parts and/or continuous actuation of smart materials to provide the adaptive capabilities. For systems where both adaptability and power conservation are desired characteristics, adaptability can be limited by power consumption.

Multistable equilibrium (MSE) systems aim to provide a type of adaptable system that can have multiple mechanical configurations, or states, that require no power to maintain each stable configuration. Power is only needed to move among the stable states, and a level of adaptability is maintained. The stable equilibrium configurations are defined by a system potential energy being at a minimum. The design of a MSE system is based around locally shaping a

potential energy curve about desired equilibrium configurations, both stable and unstable, such that the basic design goals of position, linearized natural frequency, and transition energy can be specified for the MSE system.

By mapping the performance space from the design space in tandem with stochastic numerical optimization methods, the designer determines if a certain system topology can be designed as a MSE system. Qualitative and quantitative mapping procedures enable the designer to decide whether or not the desired design lies near the center or periphery of a performance space. The performance space is defined by the desired design criteria (i.e. locations of the equilibria, natural frequency at the equilibria, etc.) that the designer deems important. If the desired design lies near the periphery of the performance space, a series of optimization trials is performed. This series shows the tendency of the problem to be solved as the desired MSE system characteristics are varied within the performance space from a location where the solution is known to exist to the true desired location where the solution is not guaranteed to exist. Upon analysis of the resulting optimization trends, the designer is able to determine whether or not a feasible limit in the system performance has been reached.

Table of Contents

List of Figures

xvi

List of Tables

Chapter 1: Introduction to Multistable Equilibrium Systems

1.1 INTRODUCTION AND MOTIVATION

In designing new products, engineers often look to improve on the existing product by increasing its functionality or efficiency. Oftentimes these two areas of improvement are conflicting. For example, to make a system respond faster and be more precise, more powerful parts and actuators are often needed. This can inherently increase the system complexity, size, and cost [Otto, K. and Wood, K., 2001].

In engineering design there is a natural tendency to put as much function as possible into a single system or structure. Creating a replacement system with the same or less number of parts, but with more functionality, can give more options to the user. This inherently maximizes utility of a device while at the same time minimizing parts and assembly. Fewer parts, in turn, means less costs in manufacturing and maintenance while creating a design with increased longevity [Otto, K. and Wood, K., 2001].

It is often a search for minimizing the number of moving parts in a design which leads engineers to explore the use of adaptable structures and materials to do exactly that [Barrett, 1996]. Adaptive structures typically use active, or smart, materials such as piezoelectric materials and shape memory alloys to provide a small range of performance characteristics about a single operating point, but they require continuous power input. In certain applications, the amount of power and energy requirements can make them infeasible for use. At other times, the

1

actuators simply do not have the range of operation desired by the engineer, and therefore, there are limits on how adaptable a design can be.

The concept of multistable equilibrium (MSE) systems bridges these gaps between adaptive structures and their limited range and energy inefficiency. The goal of MSE structures is to create a wide range of operating regimes for existing and novel mechanical systems, but without undue power consumption. The key aspect of the MSE systems is that they can act as passive structures for the vast majority of time, only requiring actuation to move among stable positions or about the current equilibrium point. Thus, MSE systems introduce a new design philosophy in adaptable, or reconfigurable, structures.

Many current engineering designs have a single equilibrium passive structure that may be operated upon by an active, power consuming, and complicated control method. The idea of MSE systems is that their multiple passive equilibrium configurations provide the versatility in function, while the actuators and control stay relatively simple. The design methodology of MSE devices focuses on creating reliable, power efficient, and repeatable adaptive structures by shaping a system's potential energy and minimizing dissipative effects. Since the stable configurations are dictated solely by potential energy storage, the reliability and repeatability of the designs can be high as long as the integrity of the potential energy storage devices is maintained.

The true spirit of MSE system design lies in making systems that focus on one or both of the following design areas:

(1) creating a range of operation exceeding that of a similar design that has only one stable equilibrium point while possibly using the same actuator(s) or system input(s),

(2) operating under multiple conditions where each uses vastly different physical principles.

An example of the first MSE design area is a standard automotive transmission. The engine has one specific torque and speed output, but by connecting a transmission, the effective torque vs. speed, or force vs. speed, relationship of the automobile is able to be 'tuned' by the driver according to the current needs (i.e. high torque or high speed). Another example corresponds to MSE systems that can be reconfigured in response to uncontrollable system inputs, such as wind speed for a wind-powered electric generator. The blade, rotor, or possible gear transmission of the windmill could be tuned to a natural frequency relevant to the input wind speed. Thus, at multiple predetermined wind speeds, the system as a whole could have multiple configurations that produce optimum output torque for a few predetermined wind speeds, even though the blades may need to spin at constant speed.

The second design area of potential interest for MSE systems can be exemplified by a fluid dynamics application. Imagine a robotic fish that at some times is shaped like a tuna to enable efficient long-range swimming and speed, but at other times is shaped like an eel to accentuate high mobility and agility. The tuna and eel swim by using different physical principles because their shape and

body stiffness correspond to different Reynolds numbers and tail-beat frequencies. Thus, a novel MSE system could be a fish that can reconfigure itself to optimize its performance, efficient swimming or agility, according to the current task.

The concept of the two major MSE design areas is depicted by Figure 1.1. Figure 1.1 (a) shows that the desired operating range is much larger than the actual range of operation that is available due to the limiting ability of the actuator. Compare this scenario with that of Figure 1.1 (b), where there are four stable equilibrium points and an actuator associated with control about each point. The desired range of operation is the same, but the actual range of operation is increased due to the system's multiple stable equilibrium operating points. Note that it is assumed that the same type of actuator is used in each case of Figures 1.1 (a) and 1.1 (b), and that the range of operation about each stable equilibrium is of similar size. Thus, the control complexity is not increased dramatically as each operating point could be based on a local, or linearized, model. The MSE representation of Figure 1.1 (b) has the added complexity of actuation among the equilibria and the complexity of design. It is the design framework and methodology required for this increased complexity in design that this dissertation provides.
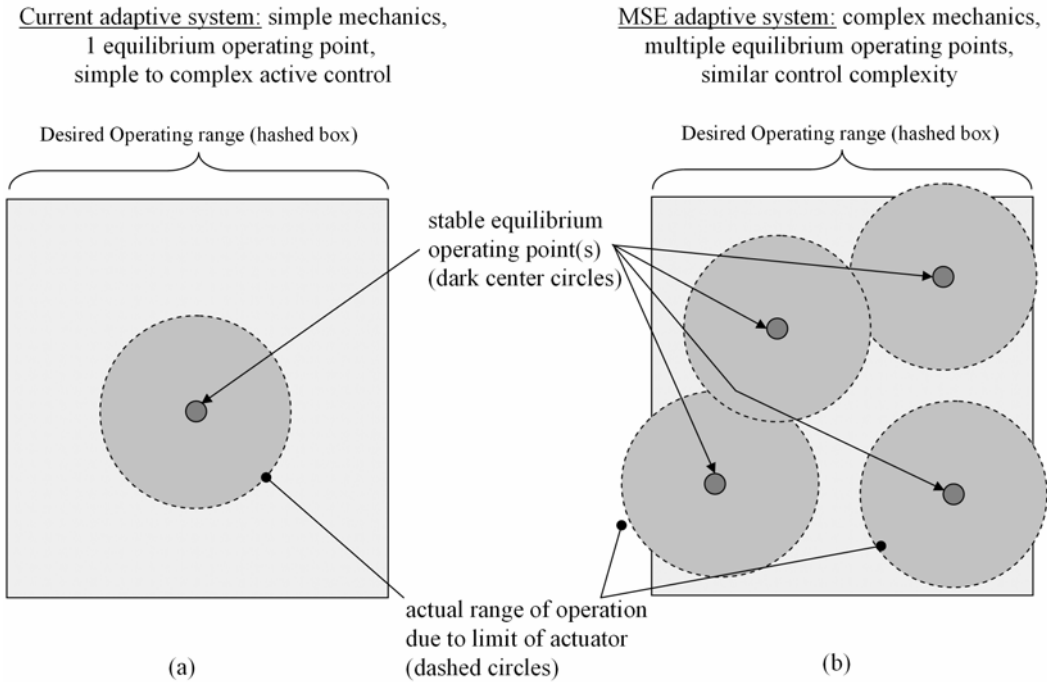
Figure 1.1. Pictorial representation of the desired operating range versus the actual operating range for the case of (a) one stable equilibrium point and one actuator, and (b) four (multiple) stable equilibrium points using the same actuators.

1.2 GENERAL CONTENT OF DISSERTATION

Before delving into the major body of the dissertation, this section dictates clearly what is and is not claimed as part of the intellectual merit of this work. This section does not outline the limitations or feasibility of the proposed design methodology since that is reserved for the body of the text and conclusions in Chapter 6.

The major claim of this work is the development and demonstration of a design methodology for the synthesis of multistable equilibrium systems. Specifically what is claimed is the following:

(1) Definition and classification of MSE systems,

(2) Development of a qualitative mapping technique to visualize solution space for MSE systems,

(3) Development of a quantitative mapping technique to characterize solution space for MSE systems,

(4) Quantitative method to synthesize desired solution, and

(5) Solution of two benchmark problems with experimental verification of one.

Although the design methodology described in the text of this dissertation relies on the use of numerical optimization techniques, there is no claim to have derived or advanced the effectiveness of any optimization algorithm. The inherent nature of MSE systems introduces highly nonlinear design spaces, and solving optimization problems upon these spaces can be more amenable using certain numerical optimization algorithms over others. Also, this dissertation does not claim to provide any new intellectual knowledge of how to choose an appropriate optimization algorithm as part of the design synthesis methodology.

Although there is data relating the design methodology predictions to experimental models, there is no experimental verification of the *benefits* of MSE systems in terms of system performance or efficiency. Only the MSE system

characteristics, evaluated in terms of desired characteristics, are compared to any computational or experimental results.

The inherent nature of MSE systems requires some form of actuation to move from one stable equilibrium to another. Though proper account for actuation is crucial in designing a MSE system, this dissertation only focuses on the design of the MSE system independent of the actuation scheme. There is discussion on how to incorporate some simple actuator properties into the synthesis of the MSE system, but it supposes that the actuators act quasi-statically and that their simple force and displacement relationship is known. Fully accounting for dynamic actuation and disturbances in MSE systems, and all nonlinear dynamic effects, is crucial but is left for future work. This dissertation provides only the foundation for MSE design synthesis.

1.3 CHAPTER DESCRIPTION

The organization of the dissertation is as follows:

- Chapter 2 presents a background and literature review of applicable work relating to MSE system design,

- Chapter 3 defines what MSE systems are and provides a general classification scheme for their design,

- Chapter 4 presents the MSE design synthesis methodology,

- Chapter 5 demonstrates the design methodology by three case studies (two of them by experiment),

- Chapter 6 ends the dissertation with conclusions and future work for MSE system design.

Chapter 2: Background and literature review of multistable and adaptable structures

This chapter provides a background on current research done in the area of adaptive structures and MSE devices or systems. Section 2.1 provides a perspective on where MSE systems fit in the general category of adaptive structures. Section 2.2 gives a literature review of previous work done that specifically relates to bistable and multistable structures. Section 2.3 then concludes Chapter 2 by discussing the role of this dissertation in terms of the opportunity for engineering design synthesis that exists in the field of adaptable systems termed, MSE systems and structures.

2.1 ADAPTIVE AND SMART STRUCTURES

Adaptive, or smart, structures are typically defined as systems that have inherent sensors, actuators, and control mechanisms to sense external stimuli, respond to the stimuli in a predetermined manner and revert back to the original state with the removal of the stimuli [Suleman, 2001]. The major purpose of these systems is to provide better performance and control over structures with fewer parts, more reliability, and perhaps more efficiency. An application in which this benefit is being realized is in helicopter rotor design [Barrett, 1996]. The idea of active materials in the helicopter blades aims to change their pitch so that the helicopter can go from hover to forward motion. This is commonly done using traditional mechanical and electromechanical components. Barrett and his

colleagues used solid-state smart materials (Lead Zirconate Titanate, or PZT, piezoelectric material) to replace some of the conventional mechanical components such as linkages, motors, and flaps. This enabled them to reduce the number of parts in the helicopter rotor from 94 to 5, reduce weight by 8%, and reduce parasitic system drag by over 25%.

The typical benefits envisioned when designing adaptive structures are exactly those of MSE systems: reduced part count, possibly higher reliability and efficiency, and more functionality by having the ability to respond to changing environmental or external disturbances. Though the goals are the same, traditional smart structures and MSE systems each occupy their own niche of applications. With that being said, smart structures could be very effectively embedded within MSE systems to create a highly adaptive overall system.

There are many ways to make systems adapt to differing disturbances or environmental inputs. Wind turbine systems need to operate in a variety of wind speeds. Sometimes the wind is too low, and the power rating of the generator cannot be achieved. At other times, the wind is very high, and the blades of the windmill are pitched by a servo motor to extract less than full power from the wind. This keeps the generator at its maximum power rating, but not above. This pitch control involves the use of motors and gears where their primary function is not to extract energy from the wind, but to actually inhibit the energy extraction. Another reason for blade pitch control is to protect the turbine in very high winds that could cause structural damage.

One of the limitations on increasing wind turbine size (i.e. power rating and height) is logistical in terms of transporting the large and heavy parts and assembling them by crane. Thus, an adaptable turbine blade design has been proposed that does not need motors for pitch control, but can have bend-twist coupling as needed when the blades spin too quickly [Eisler and Veers, 1998; Griffin, 2002]. This causes the blades to extract less power from the wind due to the bending moments pitching the blade out of the wind. The reports show that the concept is likely cost prohibitive, due to materials and manufacturing, with minimal increase in functionality. Nonetheless, this shows an attempt at creating passive adaptable systems for a single equilibrium structure by minimizing parts to reduce size and weight in an application where that is a concern. Perhaps some novel MSE system could make the blades adaptable over a larger range such that their increase in functionality overcomes the cost.

General adaptive structure and smart materials designs aim to produce lighter and more capable systems. This area of research is not to be confused with the scope of MSE system design. Current adaptive and smart systems usually morph about one stable equilibrium operating point. This is acceptable for many applications, such as the helicopter rotor design discussed earlier. MSE systems are focused on *expanding* the range of adaptability in which possible adaptive systems can operate by creating more than one stable equilibrium orientation. Thus, the MSE system concept is not a replacement strategy for smart structures or adaptive systems, but simply a new concept that may or may not be used in tandem.

2.2 MULTISTABLE EQUILIBRIUM STRUCTURES AND SYSTEMS

Most of the existing literature on MSE systems is about bistable structures [Capanu, 2000; Hafez, 2002; Howell, 1994; Jensen, 2000; Jensen, 1998; Opdahl, 1998; Saif, 2000; Schomburg, 1998]. The discussion usually centers on analysis of the equilibrium positions rather than synthesis, although Schulze performed early work in synthesizing actuation force for a simple bistable design [Schulze, 1955]. Hafez et al. describe using many bistable devices in tandem to create an overall system with multiple configurations [Hafez, 2002]. The term 'bistable' is often used quite liberally as many of the design examples of bistable structures quoted in the literature are often not truly bistable at all in the sense of potential energy being at a minimum. Some are bistable in the sense of not requiring power input to maintain position, but they rely on interference fits, clamps, and friction to provide the two stable positions [Chironis, 1991; Hoffman, 1999]. Thus, these stable positions could be better characterized by hard kinematic constraints rather than minima in potential energy. These hard kinematic constraints often hamper the ability to create more stable equilibrium positions and allow for dynamic movement at each equilibrium configuration.

Much bistable literature mentions designing structures on the microelectromechanical systems (MEMS) level. Because of the dominance of surface friction forces inherent at the micro scale, many MEMS devices cannot use hinges to allow many cycles of motion. Thus, they often rely on compliance to allow motion. The bistable structure is designed such that its elastic strain

energy provides for the stability [Jensen 1998; Jensen, 2000; Saif, 2000]. One design by Capanu et al. uses simple electromagnetic actuation to move a valve from open to closed, and vice versa, while a permanent magnet keeps the valve open and elastic energy keeps it closed [Capanu, 2000]. Research coordinated under Dubowsky has produced the design of a reconfigurable robotic arm based on similar physical principles [Hafez, 2002; Wingert, 2002]. Many designs incorporating bistability use the concept of buckling [Schomburg, 1998; Vangbo, 1998]. Saif presents an extensive analysis of a buckled beam used as a bistable device while discussing the ability to tune the threshold force that moves the beam from one buckled state to the other [Saif, 2000].

Jensen and Howell establish a theory to guarantee bistable behavior in a certain class of compliant structures, but the theory treats each energy storage 'spring' independently [Jensen, 2000]. Jensen uses mechanism theory to describe when compliant mechanisms that closely resemble four-bar linkages can exhibit bistability. He limits his energy storage to strain energy and he only considers compliant mechanisms with one major tensional spring. Therefore, his results shed very little insight into the complexity of the problem when there is much coupling of kinematics and forces present in devices that have more range of motion or more than one energy storage element. Nevertheless, Jensen and Howell provide a good example for a beginning foray into synthesis for non-buckling multistable systems.

The most relevant work to MSE system design synthesis derives one-dimensional potential functions that mimic desired dynamics for a mass moving

along a curved 'roller coaster' track in a uniform gravitational field [Gottlieb, 1997]. Gottlieb solves both versions of the problem: 1) deriving a potential function for a given track shape, and 2) deriving a track shape for a desired potential function. He presents an example of deriving track shapes for a quadratic potential function, in an attempt to mimic a linear oscillator. Virgin describes the experimentation of this same problem of a cart on a track with a double potential well [Virgin, 2000]. The analysis by Virgin on the 'roller coaster' problem uses a constant track shape to discuss the dynamics that occur in a bistable system. He considers the effect of cyclic inputs on the system dynamics and covers the basic methods to describe nonlinear systems.

2.3 GAPS IN MULTISTABLE SYSTEM DESIGN

As discussed in Section 2.2, there is some literature on the design of bistable structures and mechanisms, but it appears to lack any discussion of generalizing the idea to multiple (> 2) equilibrium positions, particularly in systems that span multiple energy domains. Further, for a given application very little to no discussion is given into the restrictions and solution possibilities of the location of additional stable positions once the first one is specified. Other than the work by Gottlieb and Virgin, there is little discussion in terms of creating bistable or MSE systems with distinct natural frequencies or stiffnesses at each equilibrium position. This dissertation attempts to specifically address some of these opportunities for advances in design.

This dissertation presents a design synthesis methodology that will be a foundation for creating designs based on MSE systems that have multiple passive, but tailored, dynamic responses. Specific areas that are addressed include the exploration of the solution space, in terms of equilibrium positions and their characteristics, given the constraints of the problem. As referenced by Gottlieb, the basic idea of a local quadratic potential approximation is used to characterize MSE system equilibrium positions, both stable and unstable. Also, Gottlieb analyzes a specific problem (i.e. sliding mass on a track) and solves for solutions both explicitly and numerically depending on the problem mathematics. This dissertation presents a methodology to apply MSE design synthesis to a broad range of problems that span multiple degrees of freedom and energy domains. Thus, a numerical optimization approach, based on a system potential energy, is used to solve for unknown design variables that characterize the necessary geometry, materials, and orientation of the system energy storage elements. The goal is to make the approach general and intuitive enough to be applicable to a wide variety of problems.

There exists extensive literature on the subject of nonlinear dynamics and of systems with multiple stable (stationary and static) equilibria. This dissertation does not attempt to broaden that knowledge of dynamic stability theory. The goal of this work is to enable someone with expertise in nonlinear dynamic systems theory to begin to synthesize a nonlinear system to act as desired over a range of many equilibrium points.

Chapter 3: Classification and Definition of Multistable Equilibrium Systems

3.1 QUALITATIVE DEFINITION MULTISTABLE EQUILIBRIUM SYSTEMS

3.1.1 General definition

In this paper, a qualitative definition of multistable equilibrium systems is as follows:

> **Multistable equilibrium system** – *a mechanical system, possibly composed of subsystems described by other energy domains (i.e. electrical, magnetic, chemical, hydraulic, pneumatic, etc.), that has more than one statically stable equilibrium state where each stable equilibrium is defined as a state in which the system has a minimum in its potential energy. An unstable equilibrium is defined as a state in which the system has a maximum in its potential energy.*

Note that inherent in the definition of a MSE system, dissipative forces can be present, but they can not be the cause of the equilibria. Also, potential energy is simply defined as energy that is a function of generalized displacements, such as mechanical translation, charge, and magnetic flux. This means that buckling systems are not considered in the context of this work since they change configuration due to an application of a generalized force, which implies a source.

This is more fully discussed in Section 3.1.2. Also, only smooth, or C$_1$ continuous, potential energy surfaces are considered.

This definition can be described by a common analogy of a ball rolling on a hilly surface (See Figure 3.1). In Figure 3.1, the MSE system is the ball, the hill, and a uniform gravitational field. The potential energy is solely described by the gravitational energy of the ball as $E(x) = mgy(x)$, where m = mass of the ball, g = gravitational acceleration, and $y(x)$ = the height of the ball as a function of the independent coordinate x. Since the gravitational force on the ball is always in the negative y-direction, and assuming no other forces exist besides rolling friction, the ball will tend to rest in either position S1 or S2. Note that system is not independently the ball or the hill, since by themselves neither have the capability to store potential energy. Only the combination of the two parts, along with gravity, has the potential to be multistable.
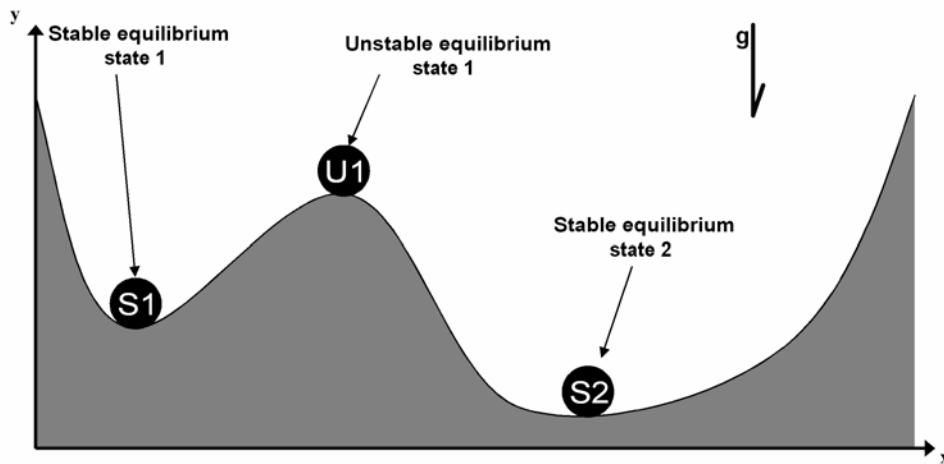
Figure 3.1:   Ball on hill analogy.

17

In terms of the definition above and depending upon the designer's needs, the MSE system equilibrium states can be described by the ball position at both the stable (S1, S2) and unstable (U1) equilibria, the hill shape, the force-displacement relationship of the ball at and between each equilibria, and approximate natural frequency at the stable equilibrium positions, S1 and S2.

Note how many of the characteristics of an MSE system are coupled, but it is up to the designer to decide which ones are most important. For example, the *shape* of the hill directly dictates the equilibrium *positions* of the ball. Thus, it is hard to conceive of having interest in designing for one and not the other. On the other hand, there can be instances in which the terms shape and position are not of mutual concern.

Again referring to the example problem in Figure 3.1, one can be interested in the *force-displacement* relationship of the ball on the hill. This can be interpreted in many ways with which the designer may or may not be concerned. One way to interpret the force-displacement relationship in the MSE system is by how much force is required to push the ball as small amount, δx, away from a stable equilibrium position. There is a small region, $\pm \delta x$, determined by the shape of the hill at the stable equilibrium, where this force can be assumed linear. With this linear force we can then extract an approximate *natural frequency* of the ball at the equilibrium position. This natural frequency can then be used to get a feel for the *speed of response* of the system as higher frequencies typically result in faster response times.

Another interpretation of describing the force-displacement relationship of the MSE system is in terms of how to move the ball from position S1 to position S2 by going through position U1, and vice versa. The value of force in the x-direction to move the ball is $F_x(x) = \partial E(x)/\partial x = mg[dy(x)/dx]$. This value is in general not constant along the curve between S1 and S2. If there is an actuator pushing the system form S1 to S2, then one must make sure that it has a force-displacement output sufficient to roll the ball over the hill.

The designer can also characterize the force-displacement relationship as the change in energy, or energy input, required to move from S1 to S2, or S2 to S1. Note that one only needs to input energy to get to the top of the hill, point U1, since the energy of the system decreases beyond that point. For instance, in moving from S1 to S2, the required energy input needed is $E_{S1-S2} = mg[y(U1)-y(S1)]$, but to move from S2 to S1, the required energy input is $E_{S2-S1} = mg[y(U1)-y(S2)]$. Note that $E_{S1-S2} < E_{S2-S1}$ since $y(S2)$ is smaller than $y(S1)$. This information can not only help design for desired actuation between the stable positions, but it can also prevent undesired movement between the stable positions. Imagine an earthquake acting on the hill and treat it as a disturbance of some amplitude and frequency. Depending on the characteristics of the earthquake, it may induce the ball to move between the stable positions. Since more energy is required to go from S2 to S1 than from S1 to S2, this could lead to general design understanding that disturbances will be more prone to dislodge the ball from S1 than from S2. Being able to dictate these kinds of energy relationships is what MSE system design is for. Of course, nonlinear dynamic

effects and possible resonance with the disturbance can also be major factors, but considering simple energy differences can be a start in design [Virgin, 2000].

3.1.2 Consideration of Actuators, or Energy Inputs, in MSE systems

If a device is in a stable configuration, does it have to stay that way if its power source is shut off? If not, then is it really in a stable configuration? For the purposes of this dissertation, the answers to these two questions are yes and no, respectively. The following example demonstrates how this is interpreted.

Consider a lever pivoting on one end and attach a linear spring to the other end as shown in Figure 3.2. The potential energy in the system is $E(\theta) = k(l(\theta) - l_o)^2/2$ where $l(\theta)$ is the length of the spring, k = linear spring stiffness, and l_o = free length of spring. If in the configuration shown in Figure 3.2 the spring is at its free length, i.e. $l(\theta) = l_o$, then the system is at a minimum of zero potential energy. Note, due to symmetry about the y-axis there is also a corresponding position of zero potential energy when the lever is at position $-\Theta$. Therefore, the two stable positions are Θ and $-\Theta$. Since there is no power supply, there is obviously no power flow necessary to keep the lever in either stable position.
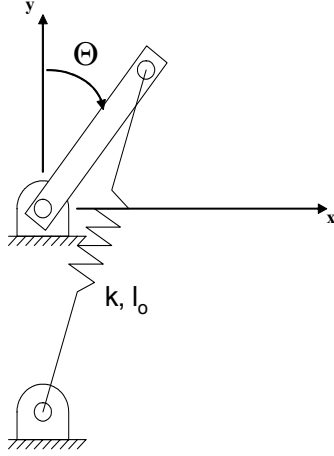
Figure 3.2: Bistable lever mechanism.

Now consider a slight variation in Figure 3.2 where a capacitor plate is added to the lever and another plate is on the ground (see Figure 3.3). The potential energy in the system can now have an electrostatic component due to the electric field between the plates. Assuming the plates are parallel and close together, this energy is approximated by $E(\theta) = [d(\theta)/(2\varepsilon_oA)]q^2$ where ε_o = free space permitivitty, A = cross-sectional area of the plates, q = charge stored on capacitor, and $d(\theta)$ = gap between the plates. If a high enough charge accumulates on each of the capacitor plates, the force will increase and the plates will approach each other due to electrostatic forces and eventually collapse on each other until they are in contact at the angle $\Theta + \delta\theta$.

Is this new position, $\Theta + \delta\theta$, a stable equilibrium? The lever is definitely stuck in a new position, but is system potential energy at a minimum? The spring

energy is definitely higher, but is there any electrostatic energy between the plates? The answer to all three questions seems to be no since there is no gap any longer, and the electrostatic energy is now zero (see Figure 3.4).
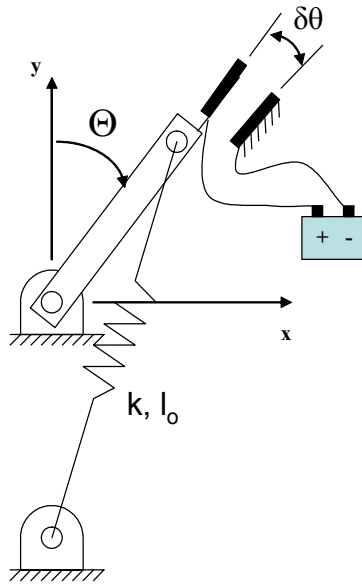
Figure 3.3: Bistable lever mechanism with capacitor plate.

So what is the total energy in the system now? Answering this question depends on how the system is defined. If the system is only the link, spring, and electric field between the plates, then the system energy at $\Theta + \delta\theta$ is not a minimum, since there is only spring energy as shown by Figure 3.4. Theoretically, the electrical energy goes back to zero as the gap between the plates goes to zero. Assume that a charge differential can instantaneously be maintained across the plates (i.e. for surfaces in contact no charge differential occurs). If the gap is increased to greater than zero by any small perturbation, the existing electric field in the gap will impose a force tending to snap the plates back together.

22
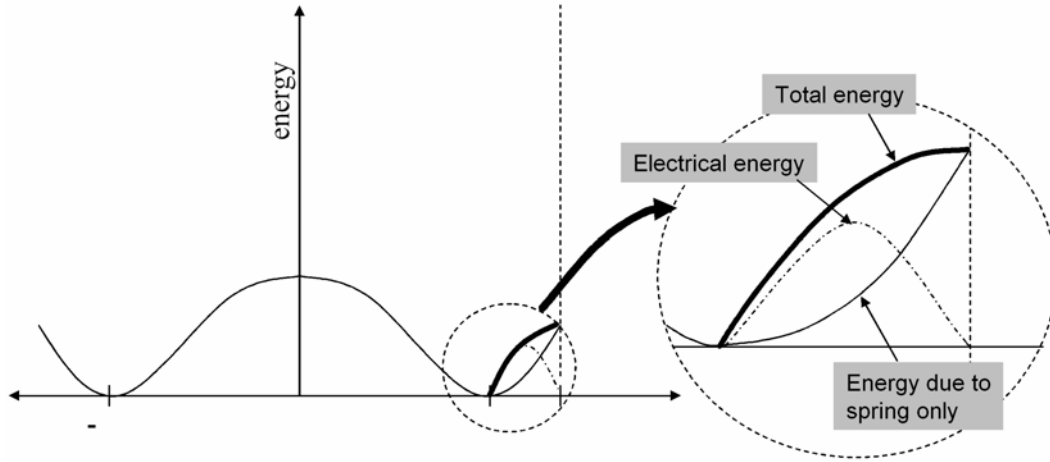
Figure 3.4: Plot of potential energy vs. angle for example in Figure 3.3.

The lever can be held in the position $\Theta + \delta\theta$ since there is an electrical force applied. While applying a voltage or imposing a charge on the capacitor, moving the plate by any small amount from the position $\Theta + \delta\theta$ results in an increase in energy and a restorative force. This is because electrical energy increases as the plates are separated. The only way the electrical energy does not increase upon separating the plates is if no electric field exists between them, i.e. there is not voltage or charge.

The point of this discussion is to distinguish what one means when classifying an orientation or position as being a stable equilibrium point or not. One must decide whether or not to account for energy sources, and characterizing position $\Theta + \delta\theta$ as a stable position or not is as much a matter of semantics as anything. In this dissertation, the situation shown in Figure 3.3 represents the

23

process of actuating or tuning the system about one of the many stable equilibria of an MSE system. At an appropriate voltage, the position $\Theta + \delta\theta$ is maintained, but *only because of an actuator and control scheme*. If the power supply were shut off, the system would revert back to the stable equilibrium position Θ. On the other hand, the lever could accumulate enough charge to hold the position $\Theta + \delta\theta$ even when the voltage source is removed *only if the electrical circuit is opened and there is no charge leakage*. In this case, the device that opens and closes the circuit (possibly a electromechanical switch) is the MSE device that enables the position $\Theta + \delta\theta$ to be stable, not the input voltage source.

Figure 3.3 does represent one of the potential benefits and driving forces for using MSE system design. Imagine if one were limited to electrostatic actuation, where the force is proportional as $F \propto V^2 d^{-2}$, and V is the applied voltage and d is the distance between capacitor plates. When limited to low voltage ranges the capacitor plates must be quite close, i.e. small d, to obtain appreciable forces. For example, let the available actuator have capability to move the beam $\pm\theta_{act}$. If there is only one stable equilibrium position, say at $\theta_{eq} = 0$, then the operating range of the beam is just $\pm\theta_{act}$. Now if the beam is designed as part of a MSE system with two stable equilibria which lie at $\theta_{eq} = \pm\Theta$, then the total range of operation could be expanded to $\pm2\theta_{act}$. Since no power is required to stay at each equilibrium position, only one actuator at a time, perhaps the same actuator, is required to move about the stable positions. In an ideal scenario, one actuator could simply 'pass on' the task of actuation to the next actuator, thus

effectively increasing the range of operation without increasing power consumption.

3.2 CLASSIFICATION OF MSE SYSTEMS

In this section MSE systems are classified according to the primary use of the design at the stable equilibrium configurations. Note that these classifications are mostly used to visualize different uses of MSE systems even though the design methodology will later show that the same engineering design considerations hold for each class. Since MSE systems can inherently incorporate multiple energy domains, terms such as 'configuration' and 'impedance' can have different meanings. For the purposes of this categorization, the categories are based on the *mechanical* properties of the design, although there may be other energy domains.

An initial classification breakdown is shown in Figure 3.5, and there are three basic categories:

(1) MSE for configuration or position,

(2) MSE for impedance, and

(3) MSE for both configuration and impedance.
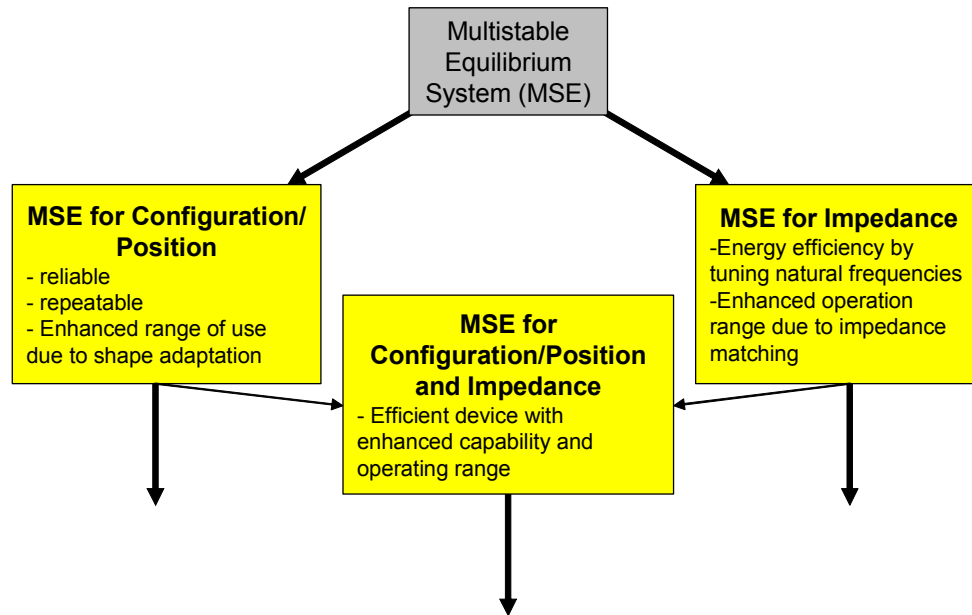
Figure 3.5:   Initial classification of MSE systems.

3.2.1 MSE design for configuration or position

Designing a MSE system for configuration or position means that transient responses about the equilibrium point are not important. The idea of creating a system that can undergo transformations from one configuration to another is useful when one can prescribe different shapes or positions that are desirable.

Applications are those that require a specific point, say on a four-bar linkage as part of a manufacturing step, to go among several locations on its coupler curve and stay at each one while a machining or assembly task is performed. Also, a MSE antenna could be shaped or sized differently to receive different frequencies or transmit different shaped electromagnetic lobes. Here the

mechanical configuration dictates an electrical impedance. This concept has already been explored by researchers at the University of Colorado by using switches to change the conducting pattern of a microelectromechanical systems (MEMS) antenna [Gupta *et al.*, 2000]. In addition, a MSE system designed for configuration could have an adaptable aerodynamic shape to minimize/maximize drag for when it experiences flow conditions at varying mach numbers.

One previously researched application for a MSE device whose purpose is multiple configurations is a MEMS optical switch; although very few of the designs are multistable by the definition used in this dissertation. Nonetheless, their goal of a device that switches and needs no power to maintain the position is the same. An optical switch is used to position a mirror or optical fiber in one of a multiple number of positions that correspond to different outputs for an optical signal. Many designs exist for mechanical optical switching [Giles, 1999; Aksyuk, 2001; Hoffman, 1999]. A MSE system could create a stable equilibrium for each optical position [Michalicek, 2000]. There are several aspects of a MSE optical switch that can affect the reliability of the device: (1) because the stable positions make feedback control unnecessary for alignment of the optical output beams, the system can have both less electronics and less cost, (2) if there is ever a power failure in the optical switch, then a viable communications path will remain, and (3) because the MSE design approach concentrates on energy storage, the design can minimize dissipative effects such as stiction and friction to create structures that are especially amenable to the MEMS area where these surface forces dominate and any particle generation due to friction can be catastrophic.
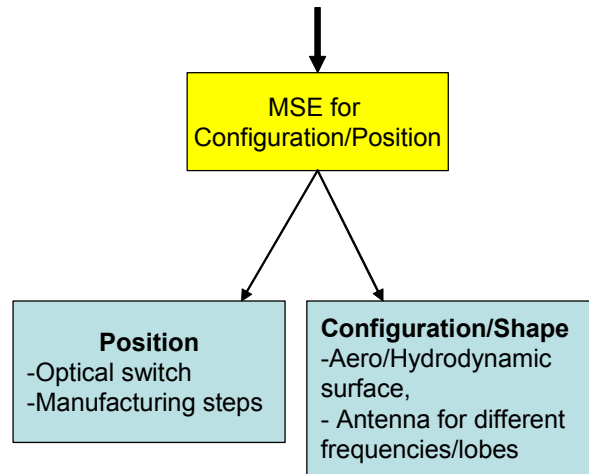
Figure 3.6: Classification and examples of MSE systems designed for configuration, shape, or position.

3.2.2 MSE design for impedance

Multistable equilibrium systems can be used for tuning the impedance of a device (see Figure 3.7). Here, impedance is defined as the response of the MSE system, about a stable equilibrium point, to a control input or external disturbance. The input or disturbance need not be periodic or transient in nature. The term impedance is used here in an attempt to characterize the concept of frequency and transient responses by using the same term.

The hope is that MSE systems can have different stable natural frequencies corresponding to each stable equilibrium configuration, and that the overall device is made more energy efficient or capable because of this concept. The damped natural frequency of a system is that frequency of a linear system at which the maximum output amplitude occurs for the free response [Greenwood, 1988]. For sinusoidal inputs, maximum output occurs at the resonant frequency, which is often very close to the damped natural frequency. Thus, if a system is actuated near its resonant frequency, it takes much less input to create a large output. Therefore, one key aspect of MSE systems is to design devices such that we can create many natural frequencies. Each natural frequency can correspond to a desired mode of operation for the device. Battery operated devices are especially prone to the problem of limiting performance due to energy inefficiency because of their reliance on a fixed energy supply. Thus, if we could make these devices have stable equilibria and frequencies about positions that correspond to each possible operating task, we could make the entire system significantly more efficient.

29
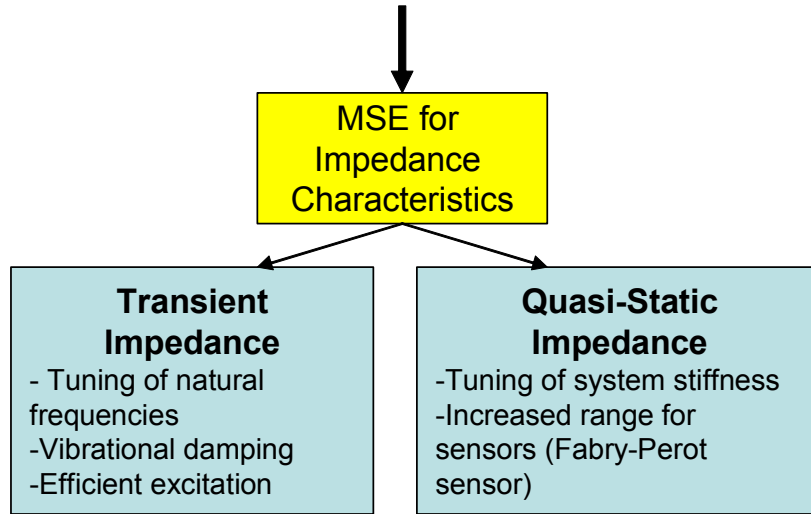
Figure 3.7:   Classification and examples of MSE systems designed for impedance characteristics.

An example of designing MSE systems for impedance, and in particular mechanical stiffness, is a Fabry-Perot sensor [Kim, 1998]. The sensed phenomenon is measured by the intensity of reflected light from a mirror that displaces as pressure changes. Here the stiffness of the mirror is tailored for a specific pressure range. Due to interference effects, the intensity of the reflected light is highly nonlinear as the mirror deflects. Thus, the range of sensing is usually limited to a small range where a given output can be caused by only one input, say below X_{limit} (high stiffness) in Figure 3.8. The high stiffness of the membrane creates a high resolution sensor, but it limits the range to below, say X_{limit} (high stiffness) for the given measurement. Otherwise one would not know if the input was X_1, X_2, or X_3. If we want a higher range of sensor inputs, we can

reduce the stiffness of the membrane to create a new sensor characteristic where the input can go as high as X_{limit} (low stiffness). Now the inputs X_1, X_2, and X_3 all have unique outputs, albeit at a lower resolution. Thus, by accurately changing to one of multiple stiffnesses for the reflecting surface, an MSE system could allow multiple ranges and resolutions for a sensor.
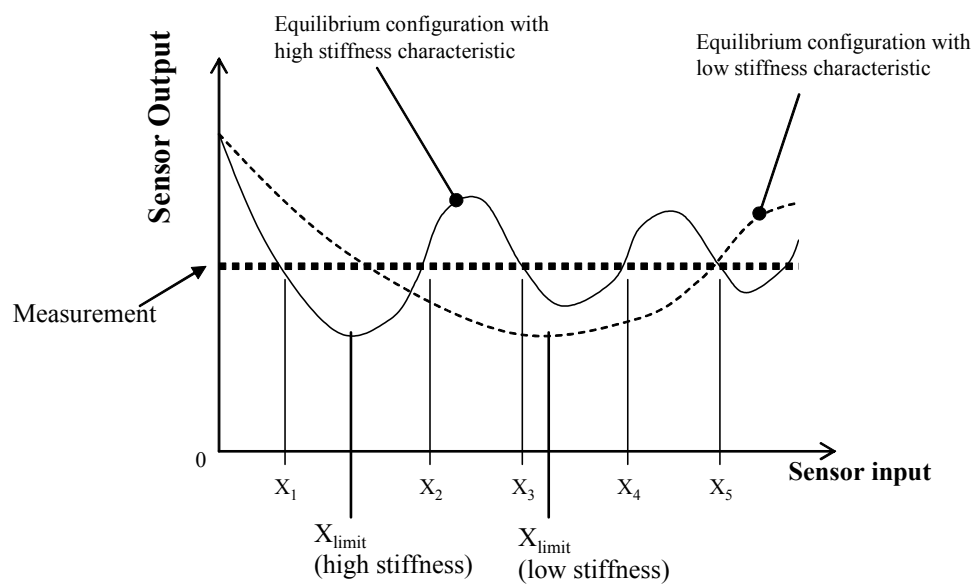
Figure 3.8: Nonlinear output of a Fabry-Perot sensor.

3.2.3 MSE design for configuration/position and impedance

Some applications combine the aspects of changing between different configurations *and* having a particular impedance that is suited for each configuration (see Figure 3.9). Robotics is an area that can make use of this combined MSE concept. Recent demands in this field are driven by a desire for smaller, faster and more versatile robots. The versatility and speed of a robot is often extremely limited by the actuators available to the engineer. Also the size and mass of the system can be hampered by the bulkiness of common actuators such as DC motors and solenoids. Smaller actuators, such as piezoelectrics and shape memory alloys, often lack one or more critical design needs such as appropriate displacement, force, or bandwidth. To combat this dilemma, one could use the MSE concept to add versatility and function to the mechanical structure itself instead of the actuation [Wingert, et al., 2002; Hafez et al., 2002].

One common example of a MSE system, although one may not have thought of it in this manner, is a manual car transmission. The driver provides the input to change stable among the stable configurations, in this case gears. When in gear, the transmission stays in place with no additional power input. The reason the transmission is part of the drive train is specifically so that the input (combustion engine) to output (wheel torque and speed) relationship can be altered depending on the desired performance and environment (i.e. need for speed, need for torque going uphill, etc.).

```
                    ↓
        ┌───────────────────────┐
        │  MSE for Configuration │
        │     And Impedance      │
        │     Characteristics    │
        └───────────────────────┘
           ↙                 ↘
┌─────────────────────┐   ┌─────────────────────┐
│     Transient       │   │    Quasi-Static     │
│     Impedance       │   │     Impedance       │
│ -Create different   │   │ -Create different   │
│ input/output        │   │ input/output        │
│ relationships for   │   │ relationships for   │
│ sensors/actuators   │   │ sensors/actuators   │
│     - car transmission│  │     - Impedance control│
│     - robotics, i.e. adaptable│ │  - haptic interface │
│     fish            │   │                     │
│ -Tune shape with impedance│ │                 │
└─────────────────────┘   └─────────────────────┘
```
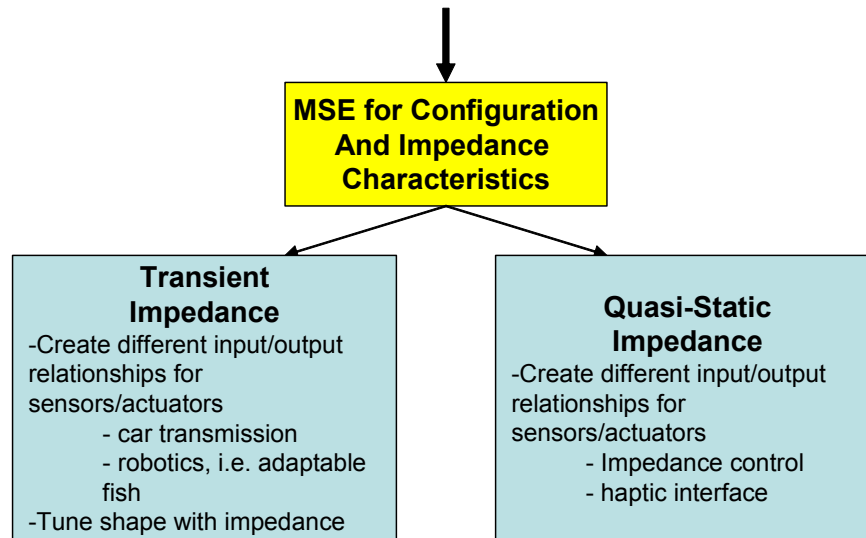
Figure 3.9:   Classification and MSE examples of designing for both configuration and impedance.

Another example is a robotic submersible vehicle used in either underwater reconnaissance or exploration where it is dangerous for humans or other trained animals to go. Possible applications are mine clearance, exploration of wreckages or contaminated water, and oceanic research [Jalbert, 1995]. A novel approach using MSE systems is to create fish-like aquatic propulsion that can have vastly different characteristics depending on the desired function at the time. Creating a MSE structure with multiple shapes and corresponding impedances could yield versatile and efficient adaptable robots or propulsive devices. This concept stems from the fact that different types of fish use vastly different propulsion techniques that are efficient but only suited to a specific niche [McHenry, 1995; Long, 1994; Weihs, 1989; Pabst, 1995; Taubes, 2000; Wardle, 1995].   Thus, one could design a single MSE fish-like propulsion system that has

equilibrium states corresponding to different niches. For enhanced agility the MSE system could take on the properties of an eel, and for enhanced long-range swimming efficiency the system could act much like a tuna. Also, if the robot is made somewhat flexible, changing its volume could therefore change its force of buoyancy for depth control. Making several stable volumes could decrease the power necessary for depth control.

Chapter 4: MSE Design Synthesis Methodology

4.1 GENERAL CONTENT OF MSE DESIGN PROCESS

The MSE design synthesis methodology presents the user with a way to interpret engineering factors into a mathematical form that can be used for MSE system design. The mathematical basis of the proposed design methodology focuses on how to properly shape the potential energy curve of the MSE system to create the desired system performance. Information from the kinetic coenergy is also used to approximate system dynamics. The shapes of the system energy curves are dictated by the design variables in the constitutive relations governing the potential energy storage elements in the MSE system. It is also be possible to shape the inertia, or effective mass, of the system to design approximate dynamic responses.

The overall MSE design synthesis methodology is set up to allow a designer to determine if a solution to the proposed problem can be solved in an acceptable amount of time. Due to nonlinear constitutive laws and constraints in the problem, the existence of a solution for a MSE system may not be apparent. Given a calculable probability for a desired solution to exist, numerical optimization techniques are used to solve for appropriate design variables that govern the energy storage in the MSE system.

An example problem formulation suitable for using the proposed design methodology would be to say that one wants to create a flexible robotic fish that

in one configuration is characterized by a tuna-like shape, with lunate tail, of high tail-beat frequency (2-3 Hz) for efficient long range swimming, and another equilibrium is characterized by a long, slender, eel-shaped body with lower stiffness and tail-beat frequency (0.1-0.5 Hz) for high mobility and agility. Also, a tuna normally swims with less than one wavelength along its body where an eel swims with greater than one wavelength. Thus, system natural frequency and shape can be coupled together in thinking of modal characteristics of the system. Note that although in each configuration the function of the fish robot is always to swim, the different stable configurations are required to take advantage of the entirely different physical principles involved for each mode of swimming.

At this point, to apply the MSE design synthesis technique, one only needs a way to model the robot's shape (for hydrodynamic considerations), mass, and stiffness (for frequency response and possible mode shape consideration) in terms of the unknown design variables. As this example shows, the criteria for deciding on the important properties of an MSE system are problem dependent and entirely up to the system designer to choose and model them correctly.

The flow chart of Figure 4.1 shows a methodology process to create a thorough understanding of the MSE design problem. The numbers in parentheses in each box correspond to the three major design steps that are described in detail in Section 4.3. For now a rough description of the design process will hopefully introduce the reader to the overall philosophy of the design synthesis process.

To start the design process, one models the system potential energy and kinetic coenergy. A Monte Carlo mapping is performed on the model to describe

the solution space both qualitatively and quantitatively. One can then choose a desired MSE solution and attempt to solve it using numerical optimization. If the problem is not readily solved, then further analysis is performed to determine the feasibility of the desired solution.

From the Monte Carlo mapping data, a probability is calculated. Probabilities greater than zero ($P > 0$) mean the solution is possible, and probabilities equal to zero ($P = 0$ case) mean more work needs to be done to determine solution existence. For the $P = 0$ cases, the desired solution is perturbed until $P > 0$, such that we can then gain a baseline understanding of how well the chosen optimization algorithm can solve a similar problem that is known to have an existing solution. A run-length distribution (RLD) is created for this baseline perturbed case. The RLD is used as a measure of how well the chosen optimization algorithm can solve the MSE design problem. As the solution is perturbed back to the original desired solution (i.e. with $P = 0$), the trend established by each successive RLD for each newly perturbed case tells the designer what likelihood there is of solving for the original desired solution.
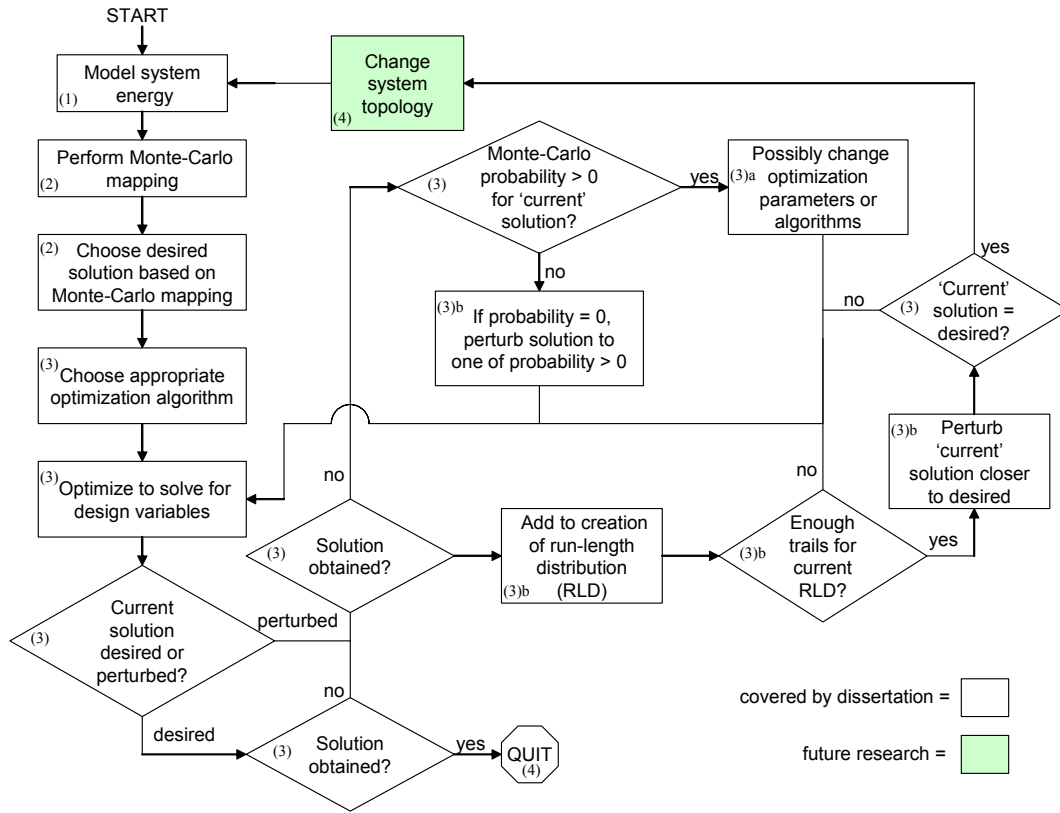
Figure 4.1. Flow chart of the MSE design synthesis methodology.

4.1.1 Aspects not included in the design methodology

From Chapter 2 it is evident that there is substantial interest in the design of MSE systems, and particularly at the moment, bistable systems and mechanisms. It is not the purpose of this design methodology to explain why one would want to create a MSE system, but only how one can design a MSE system. The philosophical issues of why to design an MSE system must be resolved

beforehand. Nonetheless, knowing why a particular MSE system is being considered will lead the designer to pinpoint the important characteristics of the MSE system (i.e. position, configuration, shape, stiffness, frequency, etc.).

The design synthesis methodology presented here does not include any new descriptions or modifications of dynamical stability theory. The methodology only uses existing descriptors of stability theory and interprets them for use in MSE system design. Also, should a problem be deemed with the assumed topology, one could add energetic components to the system to make the desired solution possible. When and how to add these components, and thus change the system topology, is beyond the scope of this work (shaded box, (4), in Figure 4.1). This is seen as a very necessary and fruitful area of research for future study.

The MSE design methodology inherently assumes that all nonlinearities in the system are smooth and continuous even though one might not have a continuous description of them. These nonlinearities include those in the potential energy storage elements, kinematic energy storage elements, and dissipative elements. Thus, even though nonlinearities, such as backlash and stiction, exist in real systems, they are not included as effects that can affect stability positions or system dynamics.

4.2 MATHEMATICAL FOUNDATION OF DESIGN SYNTHESIS METHODOLOGY

To correctly design a MSE system, one needs a way to interpret qualitative and quantitative engineering characteristics into a meaningful mathematical form that can be problem independent. This chapter shows that

given the ability to model a system's energy, one can create a framework about which a MSE system can be designed. The design methodology focuses on using a potential energy of the system so that multiple energy domains (i.e. mechanical, electrical, magnetic, etc) in any given system can all be taken into account.

4.2.1 Definition of Equilibrium Position

Consider each stable equilibrium state of an MSE system as one in which a combination of kinematic constraints and potential energy storage elements are such that, within a finite range about the local equilibrium, any incremental generalized displacement of the system produces a larger amount of potential energy in the system. Therefore, if the system is slightly disturbed from an equilibrium, it will tend to restore itself to the equilibrium position. As a consequence, a stable configuration can be maintained with no power input.

To set up the synthesis optimization problem, we derive a performance index that involves descriptions of the equilibrium positions. To understand the derivation of the performance index, the conditions for equilibrium are first developed. The conditions for the ith local equilibrium can be stated using the following equations:

$$\delta E_i = \left.\frac{\partial E(q,p)}{\partial q}\right|_{eq} = 0 \qquad i = 1, 2, \ldots n \qquad (4.1)$$

$$K = \left(\left.\frac{\partial^2 E(q,p)}{\partial q^2}\right)\right|_{eq} \qquad (4.2)$$

41

where q is a general displacement (for now a scalar), **p** is a vector of system design variables, E(q,**p**) is a system potential energy, and K is a general system energy 'stiffness' at each equilibrium [Greenwood, 1998]. Note that for stable equilibria K>0, and for unstable equilibria K<0.

4.2.2 Relation of Equilibrium definition to Engineering Principles

The dynamic equations and potential energy of MSE systems are inherently nonlinear. But to create a MSE system design approach, Equations (4.1) and (4.2) are related to each local equilibrium by assuming that in a small region, $\pm\delta q$, the potential energy is quadratic with respect to the generalized displacement. A quadratic is the minimum order of a polynomial that can represent an energy curve about an equilibrium position. Assuming a second order curve also guarantees that no more than one extremal gets characterized in the region of interest. Note that the region $\pm\delta q$ can always be chosen small enough such that no more than one extremal occurs in the local region of the potential energy curve. Also, the quadratic energy approximation inherently represents all forces as linear about the equilibrium point. In other words, all force terms of order $(\delta q)^2$ and higher are neglected. The quadratic energy approximation is used primarily as a tool for system design, and is not necessarily meant to fully characterize the system static or dynamic properties about the equilibrium point. Nonetheless, the desired properties of the ith local equilibrium, both stable and unstable, can be approximated as:

$$E_{des,i}(q) \cong c_{des,i}(q - a_{des,i})^2 + b_{des,i} \qquad (4.3)$$

where $a_{des,i}$, $b_{des,i}$, and $c_{des,i}$ are constants which represent the ith equilibria's desired position, energy value, and energy curvature, respectively (see Figure 4.2a). Note that $c_{des,i}>0$ and $c_{des,i}<0$ for a stable and unstable equilibrium, respectively.
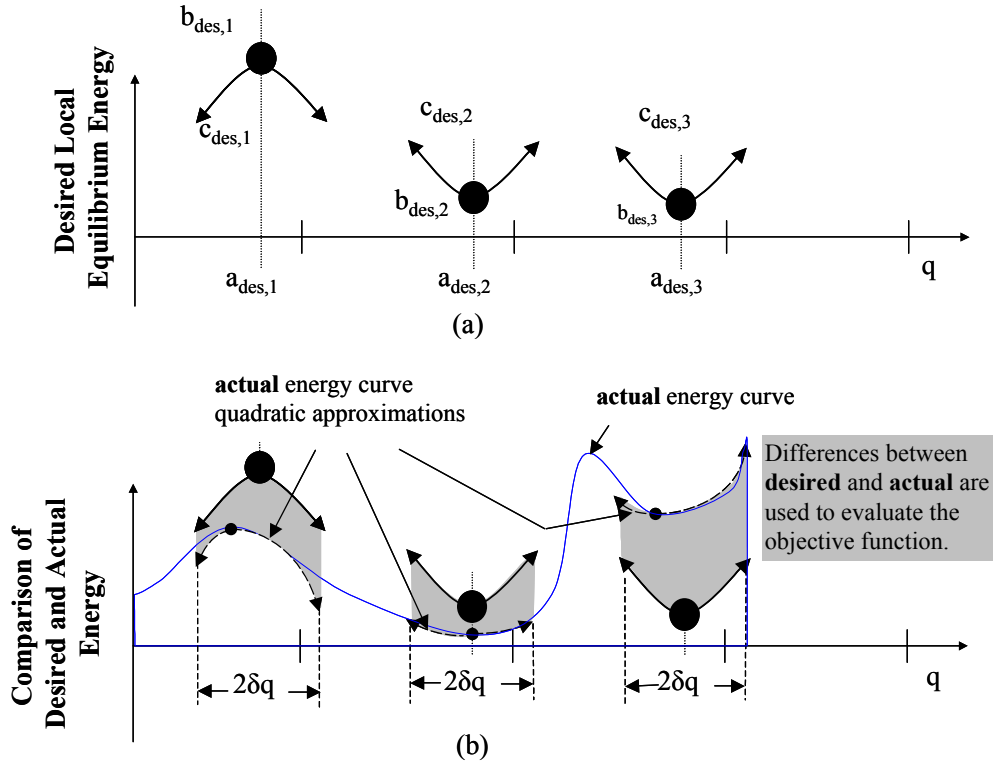
Figure 4.2. (a) The desired local equilibrium curve fit parameters. (b) Desired (solid) and candidate (dashed) quadratic curve fit approximations at the equilibrium points.

Since the forces are assumed linear in the region of interest, $\pm\delta q$, one can define a natural frequency at each stable equilibrium. Approximating the MSE system at the ith equilibrium as a generalized mass-spring system, the governing linear ordinary differential equation for the undamped free response is:

$$m_{eff,i}\,d^2q/dt^2 + K_{eff,i}(q - q_{eq,i}) = 0 \quad (4.4)$$

where $m_{eff,i}$, and $K_{eff,i}$ are the effective inertia, and stiffness, respectively, and $q_{eq,i}$ is the local equilibrium position for the ith equilibrium. Thus, the approximate natural frequency, f, of the system at equilibrium i in coordinate direction q is given by Equation (4.5).

$$f_i = (K_{eff,i}/m_{eff,i})^{1/2} \quad (4.5)$$

The derivation of $K_{eff,i}$ and $m_{eff,i}$ now follows. $K_{eff,i}$ must now be described in terms of the quadratic energy approximation shown in Equation (4.3). From Equation (4.4), the local linear generalized restoring force is $F = K_{eff,i}(q - q_{eq,i})$ so that the potential energy of the localized mass-spring system is approximated as:

$$
\begin{aligned}
E_i(q,p) &= \int F(q)dq \\
&= \int K_{eff,i}(q - q_{eq,i})dq \quad\quad\quad (4.6) \\
&= \tfrac{1}{2} K_{eff,i}(q - q_{eq,i})^2 + E(q_{eq,i}) + E_{nom}
\end{aligned}
$$

where $E(q_{eq,i}) + E_{nom}$ is the value of energy at the equilibrium point. $K_{eff,i}$ is the generalized spring stiffness that accounts for all mechanical forces acting on the system with respect to coordinate q. Equation (4.2) shows that by taking the second derivative of the potential energy Equations (4.3) and (4.6), one obtains $2c_{des,i}$ and $K_{eff,i}$, respectively. Thus, equate $K_{eff,i} = 2c_{des,i}$, and the effective stiffness is related to the desired potential energy curvature.

In order to describe a natural frequency, one must also derive the effective mass, $m_{eff,i}$, of Equation (4.5). To do this, one can follow the method of Lagrange's equations. This requires an expression for the Lagrangian composed of the system kinetic coenergy ($T(q,\dot{q})$) and potential energy ($V(q)$): $L = T - V = T(q,\dot{q}) - V(q)$. The form of the Lagrangian is as assumed in Equation (4.7), and the equation of motion for an undamped and unforced single degree of freedom system is as in Equation (4.8).

$$L(q,\dot{q}) = T(q,\dot{q}) + V(q) = \tfrac{1}{2} m_{eff}(q)\dot{q}^2 + V(q) \qquad (4.7)$$

$$
\begin{aligned}
0 &= \frac{d}{dt}\left(\frac{\partial L(q,\dot{q})}{\partial \dot{q}} \right) - \frac{\partial L(q,\dot{q})}{\partial q} \\
&= \frac{d}{dt}\left(m_{eff}(q)\dot{q} \right) - \left(\tfrac{1}{2}\frac{\partial m_{eff}(q)}{\partial q}\dot{q}^2 - \frac{\partial V(q)}{\partial q} \right) \\
&= m_{eff}(q)\ddot{q} + \frac{dm_{eff}(q)}{dq}\dot{q}^2 - \tfrac{1}{2}\frac{\partial m_{eff}(q)}{\partial q}\dot{q}^2 + \frac{\partial V(q)}{\partial q} \\
&= m_{eff}(q)\ddot{q} + \tfrac{1}{2}\frac{dm_{eff}(q)}{dq}\dot{q}^2 + \frac{\partial V(q)}{\partial q}
\end{aligned}
\qquad (4.8)
$$

In Equations (4.7) and (4.8), $\dot{q}$ is the time derivative of the general displacement, q, and $m_{eff,i}(q)$ is the generalized effective mass as function of position. Note that for a full nonlinear system, one must account for the inertial effects of the second effective mass term which is the middle term in Equation (4.8). But, since a quadratic form of localized potential energy is assumed, and therefore a linearized model, all terms of order two and higher are neglected. The same linearizing assumption is made for kinetic coenergy. Thus, the "$\dot{q}^2$" term in Equation (4.8) is inherently deemed negligible. Also, one can see that for a system with constant mass, the middle term of Equation (4.8) goes away. So for slowly varying and localized systems, a linearized model without the "$\dot{q}^2$" is a reasonable approximation.

Similarly to assuming a constant stiffness, $K_{eff,i}$, due to small variations about the equilibrium of the potential energy, to estimate a natural frequency we assume a constant effective mass. This is a necessity for evaluating frequency as a desired design criterion, even though $m_{eff}(q)$ in Equation (4.8) is generally not constant since $q = q(t)$. This mass, at the ith equilibrium, is evaluated from Equation (4.7) or (4.8) as $m_{eff,i} = m_{eff,i}(q_{eq,i})$. Note that the assumption of constant mass and neglecting the second term in Equation (4.8) is not a more limiting simplification, since the concept of natural frequency is only defined for linear systems. Thus, inserting $2c_{des,i}$ for $K_{eff,i}$ in Equation (4.5) produces:

$$f_{des,i} = (2c_{des,i}/m_{eff,i}(q_{eq,i}))^{1/2} \qquad (4.9)$$

Derivation of how to equate the quadratic factor, $c_{des,i}$, of Equation (4.3) to $K_{eff,i}$ in Equations (4.4-4.6) has already been shown. Further equating coefficients of Equations (4.3) and (4.6) shows that $a_{des,i} = q_{eq,i}$ and $b_{des,i} = E(q_{eq,i}) + E_{nom}$. Note from Equation (4.6) that E_{nom} is essentially an arbitrary constant since the value of potential energy is a relative quantity, and not absolute. Therefore, only the difference of two potential energies bears meaning if both have the same arbitrary constant (i.e. E_{nom}), and that is negated when they are subtracted. However, this does not mean that the factor $b_{des,i}$ of Equation (4.3) has no use.

The significance of $b_{des,i}$ in Equation (4.3) lies in determining how much disturbance or actuation energy is required to move from one stable equilibrium to the next by going through an unstable equilibrium. For example, consider a system to have equilibria at $q_{eq,1} = 1.0$, $q_{eq,2} = 3.0$, and $q_{eq,3} = 5.0$, where $q_{eq,1}$ and $q_{eq,3}$ are stable and $q_{eq,2}$ is unstable. To actuate from position $q_{eq,1}$ to $q_{eq,3}$, one needs to use an actuator with enough actuation energy to overcome the increase in potential energy from $q_{eq,1}$ to $q_{eq,2}$, equal to $\Delta E_{12} = b_{des,2} - b_{des,1}$. As a consequence, sufficient system disturbances could also cause the system to transition among equilibrium positions. Thus, designing ΔE_{12} of a sufficiently high value could help prevent this undesirable change of equilibrium but at the expense of a more capable actuator.

4.2.3 Creating the Performance Index

Criteria have now been established to form a performance index. The values a, b, and c in Equation (4.3) have engineering significance in being the position, energy value, and curvature (which relates to system stiffness and frequency) of each equilibrium position, respectively. Thus, during each iteration of the optimization scheme, perform a second order least squares curve fit approximation in a region $\pm\delta q$ about each desired equilibrium point to obtain the candidate equation of Equation (4.3) as:

$$E_{cand,i}(q_{cand,i},p) \cong c_{cand,i}(q - a_{cand,i})^2 + b_{cand,i} \quad (4.10)$$

In essentially taking the difference between Equations (4.3) and (4.10), one creates a basic performance index, F, which compares the desired and candidate potential energy curve fitting parameters about each equilibrium:

$$F = \sum_{i=1}^{n} w_{a,i}(a_{des,i} - a_{cand,i})^2 + w_{b,i}(b_{des,i} - b_{cand,i})^2 + w_{c,i}(c_{des,i} - c_{cand,i})^2 \quad (4.11)$$

where n is the number of equilibrium positions and $w_{a,i}$, $w_{b,i}$ and $w_{c,i}$ are the weights for the curving fitting parameters a, b, and c from Equations (4.3) and (4.10). Depending on what the designer is interested in, he could leave out certain terms of Equation (4.11), weight each term to give priority to the most important design consideration (i.e. equilibrium location, stiffness, or energy increase for equilibrium transition), and include both stable and unstable equilibria.

4.2.3.1 Different approaches to optimizing frequency in performance index

In Equation (4.11), the third term in the performance index uses desired and candidate curvature values instead of frequency, which is the true desired design criterion for stable equilibria. The reason is that Equation (4.11) can assume that the curve fit is being performed *about the desired equilibrium position, $a_{des,i}$,* and not the candidate equilibrium position, $a_{cand,i}$. This position, $a_{des,i}$, is fixed throughout the optimization routine, and there is a possibility that there will be a negative curvature calculated where a positive curvature is desired. If this occurs, $f_{cand,i}$ will be imaginary as shown by Equation (4.9) since the square root of $c_{cand,i}$ is needed. Then, when inputting this $f_{cand,i}$ into the performance index, a negative quantity is created due to act of squaring the terms. Therefore, if curve fitting occurs *at fixed $a_{des,i}$,* the factor c must be used in the performance index instead of the frequency, f.

A simple modification of Equation (4.9) produces c in terms of f, as shown in Equation (4.12). Therefore, in the performance index, use the $c_{des,i}$ from Equation (4.12), and whatever $c_{cand,i}$ is derived from the candidate energy equation.

$$c_{des,i} = (f_{des,i})^2 \, m_{eff,i}/2 \qquad (4.12)$$

An alternate approach is to curve fit *only* at locations of equilibria, stable or unstable. This requires a search before curve fitting to find where the equilibria

49

occur, and one can simultaneously categorize them as stable or unstable. When one is curve fitting an unstable point, simply use the c factor since frequency is undefined. When curve fitting stable position, use Equation (4.9) with the candidate curvature, $c_{cand,i}$, to calculate the candidate frequency $f_{cand,i}$. Therefore, a term such as '$(f_{des,i} - f_{cand,i})^2$' can be used in the performance index since it is guaranteed to only be positive. This method allows the possibility that fewer equilibrium positions in the candidate energy curve can actually occur that desired. A factor can be added to the performance index to penalize for this, as discussed in the next section.

4.2.3.2 Alternate Performance Index factors

Equation (4.11) is a 'basic' performance index since the problem formulation allows the user to create a performance index which makes sense for the particular problem being solved. Thus, the formation of the performance index, equality constraints, and inequality constraints is problem dependent. The factors included and the weights given to each factor are essentially open-ended, and the types of factors that can be included in a performance index, or as constraints, are numerous. Some more examples of factors are listed below:

(1) $(a_{cand,2} - a_{cand,1} - \Delta q_{12,des})^2$: where $a_{cand,2} > a_{cand,1}$ and $\Delta q_{12,des}$ is the desired distance between two equilibria $a_{cand,2}$ and $a_{cand,1}$. This type of factor specifies that the only concern for the equilibrium positions is that they are separated by some amount $\Delta q_{12,des.}$ (i.e the relative

50

position of the equilibria is important, not absolute position). Each of the two equilibria can be stable or unstable.

(2) **-($a_{cand,2}$ − $a_{cand,1}$):** where $a_{cand,2} > a_{cand,1}$. This factor maximizes the relative distances between equilibria (stable or unstable).

(3) **($b_{cand,2}$ − $b_{cand,1}$ - $\Delta E_{12,des}$)^2:** where $b_{cand,2} > b_{cand,1}$ and $\Delta E_{12,des}$ is the desired amount of actuation energy to move from the stable equilibrium position 1 to the unstable equilibrium position 2.

(4) **-($b_{cand,2}$ − $b_{cand,1}$):** where $b_{cand,2} > b_{cand,1}$. This factor maximizes the actuation energy needed to go from stable equilibrium, with energy $b_{cand,1}$, to the next stable position by going through the unstable equilibrium, with energy $b_{cand,2}$.

(5) **-($c_{cand,stable}$) and ($c_{cand,unstable}$) :** The first factor maximizes the potential energy curvature (and therefore approximate natural frequency) of a stable equilibrium point. The second factor minimizes the potential energy curvature (or maximizes its magnitude) of unstable equilibrium points to create large 'snap-through' forces when traversing from one stable equilibrium to the next.

(6) **-abs($c_{cand,stable1}$ − $c_{cand,stable2}$):** This factor dictates that for two stable equilibrium positions, the difference in value of potential energy curvature (or natural frequency) is desired to be maximized. The usefulness of this type of factor can be in creating structures with natural frequencies varying over certain magnitudes, perhaps for damping or vibration applications.

(7) *($x_{cand,i}$ − $x_{des,i}$) if ($x_{cand,i}$ − $x_{des,i}$)>δx_i, 0 otherwise, and ($x_{des,i}$ − $x_{cand,i}$) if* *($x_{des,i}$ − $x_{cand,i}$)>δx_i, 0 otherwise:* Here, x is any design criteria of interest, such as equilibrium position or natural frequency. This factor enables the concept of a threshold range, a distance $\pm\delta x_i$ away from the desired, which it is imperative that the candidate solution be within. When in this range, there is no added penalty to the performance index, and when out of this range, there is a penalty added.

(8) ($numstable_{cand}$ - $numstable_{des}$) if ($numstable_{cand}$ - $numstable_{des}$) < 0: This factor penalizes the candidate energy solution if there are not enough stable positions (i.e. energy minima) in the energy curve. If there are at least as many stable equilibria as desired, then there is no penalty added to the performance index.

4.2.4 Issues in creating the Performance Index

One point regarding the formation of the performance index that warrants some discussion is the use of curve fitting to get local energy approximations as in Equation (4.10). Every time a candidate energy curve is calculated during the optimization routine, one needs a 2nd order curve fit about the desired (or actual) equilibrium point locations. The methodology uses least squares curve fitting. In doing so, one must choose: 1) the number of points with which to curve fit, and 2) the range, $\pm\delta q$, to use in curve fitting (see Figure 1b). Both decisions affect how the optimization results compare to a real world problem.

In a quadratic approximation, one needs at least three data points to fit, and for exactly three data points, the quadratic curve fit is exact to the points. Of course, due to likely modeling errors and distance between energy points, this does not mean that the curvature, or natural frequency, approximation is exact. More data points are not necessarily good if the points are equally spaced, since the curve fit will weight each one the same. The linearization is best for locations near the equilibrium, thus one would prefer the points near the equilibrium remain dominant.

For instance, it could make sense, that if we desire or expect the system to oscillate in a very narrow range, we can make δq quite small. If we desire or expect the system to oscillate in a wide range, we can make δq larger. The δq is a very system dependent parameter, possibly depending on things such as the magnitude of the system inertia and system disturbances. For nonlinear systems, the natural frequency at an equilibrium point is a linearized approximation. The approximation becomes more valid as displacement, potential energy curvature, and effective mass get smaller [Virgin, 2000]. Also, as the mass in the system becomes more concentrated (i.e. point-like) the natural frequency approximation becomes better. In general, nonlinear system 'frequencies' and free responses depend upon motion amplitude, and Virgin shows how to calculate this for a canonical nonlinear oscillating system. Others also show how the coordinate system, or independent coordinate, one chooses can affect the shape of the potential that acts on the system mass [Shaw and Haddow, 1992, Gottlieb, 1997].

As a rough rule of thumb, an upper limit on δq is the point at which the energy has an inflection point or begins to have nearly constant slope. This gives some reasonable location at which to have an upper bound on δq since negative energy curvatures (for stable equilibria) definitely violate the quadratic energy curve assumption as they represent a softening spring effect.

Note that MSE systems are necessarily nonlinear, and the quadratic energy approximation may be quite invalid. Nonetheless, the notions of the parameters a, b, and c in Equation (4.10) can still help in design. To quantify the accuracy of the curve fit, one can incorporate the concept of statistical correlation, or correlation coefficients. Essentially, finding the correlation coefficient between two sets of data can indicate how similar the two sets are, i.e. how correlated they are. For identical sets of data, the correlation coefficient is one and for unrelated data the correlation coefficient is zero. To use this concept in the design methodology, one set of data is the true energy values from closed form, Equation (4.6), and the other data set is energy values generated by Equation (4.10) that uses the curve-fitted energy parameters, a_{cand}, b_{cand}, and c_{cand}. Thus, one compares data points from the true energy curve, Equation (4.6), with the data derived from curve fitting the true energy curve, Equation (4.10). By calculating the correlation coefficient for these two data sets, one can measure the accuracy of the 2nd order approximation and have a direct way to quantify how well the local linearized energy approximation compares to the true nonlinear model. If the accuracy is not high enough, then one can simply discard that solution, add a penalty factor to the

performance index, or decrease the range, δq, of the curve fit until the correlation is high enough.

4.2.5 Expansion of the design criteria to multiple degree of freedom systems

When considering systems with more than one kinematic degree of freedom, the basic design criteria of a_{des}, b_{des}, and c_{des} don't relate to system dynamics straightforwardly as in the one degree of freedom case. Equations (4.1) and (4.2) hold for a multiple degree of freedom system where q is now a vector, and the stiffness, K, is a matrix that must be positive definite for local stability. Consider a two degree of freedom system in a small region about an equilibrium point. Following the single degree of freedom quadratic assumption, a general second order curve fit has the following form:

$$E \cong e_1 x^2 + e_2 y^2 + e_3 xy + e_4 x + e_5 y + e_6 \qquad (4.13)$$

where x and y are the kinematic degrees of freedom. Using two independent energy expressions one can write a two degree of freedom version of Equation (4.10) for the ith equilibrium as:

$$E_i(x,y,p) \cong E_{x,i}(x,y_{eq},p) + E_{y,i}(x_{eq},y,p)$$
$$E_i(x,y,p) \cong c_{x,i}(x-a_{x,i})^2 + c_{y,i}(y-a_{y,i})^2 + \frac{(b_{x,i}+b_{y,i})}{2} \qquad (4.14)$$

where $(a_{x,i}, a_{y,i})$ is the equilibrium position, $b_{x,i}$ and $b_{y,i}$ are both the energy value at the equilibrium, and $c_{x,i}$ and $c_{y,i}$ are the curvatures at the equilibrium position in the x and y directions respectively. The problem with Equation (4.14) approximating Equation (4.13), is that there is no 'xy' term in Equation (4.14). Nonetheless, one can solve for the coefficients in Equation (4.14) in terms of Equation (4.13) as:

$$c_{x,i} = e_1$$
$$c_{y,i} = e_2$$
$$a_{x,i} = \frac{-e_4}{2c_{x,i}} \qquad\qquad (4.15a\text{-}4.15e)$$
$$a_{y,i} = \frac{-e_5}{2c_{y,i}}$$
$$\frac{b_{x,i} + b_{y,i}}{2} \cong b_{total} = e_6 - a_{x,i}^2 c_{x,i} - a_{y,i}^2 c_{y,i}$$

To ensure that the curve fitting is done about a point that is truly an equilibrium, a simple line search in each coordinate direction can be performed. A stable equilibrium point will thus be at a point in the line search where every adjacent coordinate has a larger energy value. Unstable equilibria have some adjacent coordinate points with smaller energy values. This should ensure that the stiffness matrix is positive and negative definite for stable and unstable points, respectively. In this two-dimensional case, K is given in Equation (4.16) by using the second partial derivatives of the potential energy, Equation (4.13).

$$K \cong \begin{bmatrix} \dfrac{\partial^2 E(x,y)}{\partial x^2} & \dfrac{\partial^2 E(x,y)}{\partial x \partial y} \\ \dfrac{\partial^2 E(x,y)}{\partial y \partial x} & \dfrac{\partial^2 E(x,y)}{\partial y^2} \end{bmatrix}_{eq} = \begin{bmatrix} e_1 & e_3 \\ e_3 & e_2 \end{bmatrix} = \begin{bmatrix} c_{x,i} & e_3 \\ e_3 & c_{y,i} \end{bmatrix} \qquad (4.16)$$

Thus, to ensure a point is stable during any calculations, ensure that the matrix $K > 0$. The same procedure can be done to curve fit unstable points by requiring that $K < 0$.

Looking again at Equations (4.13 – 4.15), it is clear to see that they are not equal. Equation (4.14) is equal to Equation (4.13) only if the coefficient e3 = 0. To calculate a_{cand}, b_{cand}, and c_{cand} for use in the performance index, the coefficients from Equation (4.13) can be used as shown in Equation (4.15). One can also use individual energies that are a function of only one coordinate, with the other being fixed. This becomes the case when the potential energy in the x-direction is independent of the potential energy in the y-direction, and $E_i(x, y) = E_{x,i}(x, y_{eq}) + E_{y,i}(x_{eq}, y)$. If one assumes this is the case, then individual quadratic energy approximations can be made for each coordinate direction just as in the single degree of freedom case. Forming an equation of the form of Equation (4.3) for x-direction ($E_{x,i}$) produces the coefficients $a_{x,i}$, $b_{x,i}$, and $c_{x,i}$ and likewise for the y-direction ($E_{y,i}$) $a_{y,i}$, $b_{y,i}$, and $c_{y,i}$. Because there is only one value of energy at a given equilibrium point, $b_{x,i} = b_{y,i}$ at the equilibrium as shown by the last term in Equation (4.14) where the two b coefficients are averaged. As the candidate two degree of freedom energy curve becomes closer to the desired two degree of freedom energy curve, the two 'b' values approach each other. Therefore, the

57

individual energy approximations, $E_{x,i}$ and $E_{y,i}$, along with their respective curve fitting parameters, can be used in the performance index for the optimization routine, just as in the single degree of freedom case. Again, this approach neglects the use of the 'xy' term in Equation (4.13), but this is considered a minimal loss in utility considering that putting an 'xy' term in the performance index means the user must know a desired coupling between the energies in the two directions.

Expanding the same procedure to an $N > 2$ degree of freedom system involves similar approximations given in Equations (4.13 − 4.15). Stable and unstable points can be found by a line search, and thus the sign of the stiffness matrix can be correct. Therefore Equation (4.13) must still be calculated to so that the stiffness matrix can be calculated to quantify the stability of the equilibrium point even if all individual 'c' terms are positive. The equilibrium point is then characterized by the 'a' terms in Equation (4.14) and the stiffness matrix from a full N dimensional quadratic curve fit of Equation (4.13).

4.3 STEP-BY-STEP SYNTHESIS PROCESS

The point at which the MSE design synthesis methodology begins, assumes that one can calculate the system potential energy of the system in any desired configuration.   One also must be able to model the effective inertia of the system if the dynamic response of the MSE system is important.   This modeling can be in closed form equations or results from other analyses, such as finite element analysis. Once the energy and effective inertia can be calculated for the system as a function of the kinematic degrees of freedom, one can use the

proposed design methodology to solve for the allowable MSE system characteristics, as well as the unknown values for the design variables that are needed to produce the desired MSE system.

The design method is more than simply optimization. Proper attention must be given to problem formulation such that the MSE system is synthesized correctly. As the designer, one must know what engineering factors are important and how to use them to phrase a problem for optimization. Because MSE systems must have nonlinear characteristics to create the multiple equilibria, solution possibilities may escape the intuition of the engineer. The emphases of the design steps are in problem formulation and getting insight into the solution space prior to and during optimization. Hopefully, the acquired problem insight will aid the last two steps in choosing a correct optimization algorithm, knowing how difficult the solution might be to obtain, and interpreting the solution results. Note that numbers in the boxes of Figure 4.1 refer to what step of the solution process they represent.

<u>Step</u> <u>Description</u>

(1) MSE problem definition: decide on desired location of equilibria and the important engineering characteristics (i.e. stiffness, frequency, energy value) of the MSE system at each equilibrium. Also, an acceptable range about the desired solution must be proposed.

(2) Perform Monte Carlo mapping and decide on the feasibility, by a probability calculation (P_{total}), of the desired solution. If $P_{total} > 0$, the solution is possible and proceed with optimization with the expectation of finding the solution 'easily'. If $P_{total} = 0$, then a more elaborate approach is needed to determine if the desired solution is possible (Step (3)).

(3) Interpretation of resulting probability, P_{total}, and taking appropriate steps to solve for design variables.

(a) If $P_{total} > 0$ from Step (2), create performance index and weight the different factors according to importance in design. Choose appropriate optimization algorithm (i.e. simulated annealing, genetic algorithm, etc.) and optimize for the unknown design variables such as length, spring constant, magnet coercivity, etc. to at least the range of accuracy from Step (1) used when calculating the probability in Step (2).

(b) If $P_{total} = 0$ from Step (2), create a 'perturbed' solution from the desired solution so that $P_{total} > 0$ for the perturbed solution. Form an appropriate performance index that enables one to dictate optimization 'success' when all design criteria are inside their respective ranges specified in Step (1), and needed for the probability calculation. Then create run-length distributions as the 'perturbed' case is moved toward the desired case to track the feasibility of the desired solution. This enables the designer to

determine where the boundary between possible and impossible solutions may lie.

(4)   If at any point the desired solution is found, then quit. If $P_{total} > 0$ for the desired solution and the optimization problem is not readily solved, then one needs to consider changing either the optimization algorithm or the parameters that govern the chosen algorithm. If $P_{total} = 0$ for the desired solution, and the RLD disappears as the perturbed solution of Step (3)b moves back to the original desired, then one needs to consider that the solution is not possible with the current system topology. At this point, one must either quit as the solution is not possible to achieve, or one must change the system topology with respect to how it stores energy.

In order to more easily facilitate the understanding of the steps involved, the results from an example problem are used throughout Section 4.3. Refer to Section 5.2 for an explanation of the example four-bar linkage problem.

4.3.1 Step 1: Decide on important Engineering Characteristics of each Equilibrium

This first step involves nothing more than correctly defining the problem to be solved. The user must ask what characteristics of the equilibrium positions are important. For instance, are potential energy curvatures of unstable equilibria of concern as well as stable equilibria? Is the natural frequency important?

Decide on a range for each desired design criterion. For example, if one desires a natural frequency of 1.0 Hz, is it acceptable to be at 0.8 Hz or 1.2 Hz? Putting a range about each design criterion is necessary to calculate probability in Step 2, discussed in the next section. However, the solution can be further refined after the all of the design criteria are found within their respective ranges.

4.3.2 Step 2: Monte Carlo mapping and probability calculation

The Monte Carlo mapping is both a qualitative and quantitative tool to give the designer insight into the solution space of the problem before an optimized solution is attempted. The reason this is important is that, at the beginning of the MSE synthesis process, the goals of the problem are already defined, yet the solution space can be completely unintuitive. For example, one may desire two stable equilibria within two meters of each other where the first equilibrium produces a system natural frequency below 1 Hz and the other produces a natural frequency above 10 Hz. In addition, because of certain disturbances to the system, specify that at least 10 J of energy must be overcome to move between the stable equilibria so that the system is not unexpectedly excited into the wrong equilibrium configuration.

After problem definition, the first question in MSE synthesis is: Does a design exist that meets all constraints of the design problem? The coupling of the nonlinear constraints in the problem can make answering this question very difficult. The Monte Carlo mapping is specifically designed to help answer the question of whether or not a solution is feasible so that little time is spent attempting to attain a solution that is unlikely. By mapping where certain combinations of equilibria, stiffnesses, frequencies, and potential energy values can occur *together*, the designer can gain insight before the optimization begins.

In creating the Monte Carlo mapping perform the following six basic steps:

(i)   Set allowable ranges of the problem design variables.

(ii)   Generate random value for each design variable (usually with uniform distribution).

(iii)   Calculate system potential energy and effective inertia.

(iv)   Perform a line search along each coordinate direction to find all equilibrium positions in the potential energy curve. By curve fitting about the equilibria, calculate the important energy parameters as decided from Step 1 of design process (Section 4.3.1) and as described in Section 4.2.

(v)   Plot energy curve parameters of Step iv) to visualize the patterns (qualitatively) of possible solutions, and analyze patterns to quantify solution space by use of a probability number.

(vi)   Repeat Steps ii)-v) for as many iterations as desired, or until a defined pattern emerges in the mapping to enable a decision on whether or not the desires solution is possible.

A simple example of a meaningful mapping is one that plots the natural frequencies versus the relative stable equilibrium positions where they occur. From this one can see what frequencies are likely at certain equilibrium positions. Note, since the random design variables used in the Monte Carlo method can create energy curves with different numbers of equilibria, there needs to be a separate mapping for the separate cases of unistable, bistable, tristable, etc. designs.

4.3.2.1 Mapping Equilibrium positions (qualitative)

The most basic information used for design of MSE systems is the locations of the stable, and unstable, equilibrium positions themselves. These can be plotted in a couple of manners to provide a qualitative feel for the possible stable position sets for a given problem. Figure 4.3 shows a qualitative phase plot, or plot of stable equilibrium position one and stable equilibrium two for the case of two equilibrium positions occurring, or a bistable design. Note that the data in Figure 4.3 (and all data in subsections of Section 4.3.2) comes from a problem involving a single degree of freedom rotating linkage in which the maximum position (along x-axis) is 360 degrees, or 2π radians. Therefore, all example data in this chapter used to describe the mapping method will have equilibrium positions only in the range $[0, 2\pi]$ radians. See Section 5.2 for a complete description of the problem.

Note in Figure 4.3, that the first stable equilibrium position is plotted in the form of a cumulative distribution function. Use of this concept will be described in Section 4.3.2.4 to quantify the feasibility of any desired solution for the MSE design problem. For now, one can think of the cumulative probability as the probability that the variable of interest (in Figure 4.3 this is equilibrium position one) has some value, x, or less. For instance, using Figure 4.3, equilibrium one has a 0.5, or 50%, probability of having a value of $\theta_{eq,1} = 1.75$ rad or less. In this case the minimum possible value is $\theta_{eq,1} = 0$.
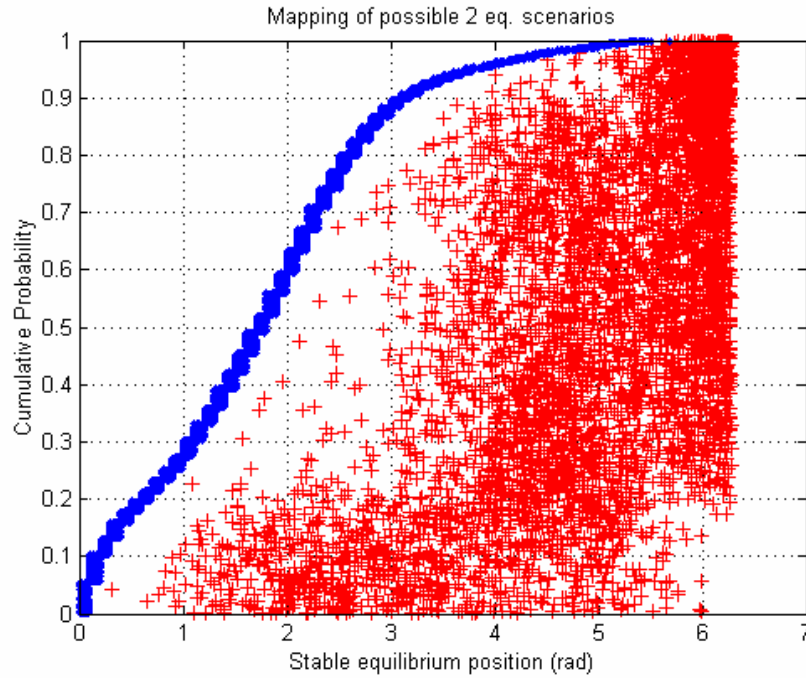
Figure 4.3. Qualitative mapping for two equilibrium positions. The first position is represented by blue '·'s, and the second by red '+'s.

The plot in Figure 4.3 arranges the data such that the equilibrium with the lowest value is always the 'first' equilibrium, or equilibrium one. Thus, the second stable equilibrium position, represented by the red '+', can only be greater than the first equilibrium. Also, one can notice where the second equilibrium positions tend to be located relative to the first equilibrium position. By viewing where the red '+' marks tend to reside for any chosen 'first' equilibrium point, one can gain an appreciation for where the second equilibrium position, *dependent upon the first*, can likely occur.

Similar mappings can be made for systems that are tristable, quadrastable, etc. Figure 4.4 shows the mapping for a system with three stable equilibrium

positions, or a tristable system. Note how there seems to be certain bands where the stable equilibria can occur. Patterns such as this one will be unique for each system, and for simple and low degree of freedom systems graphical mappings can qualitatively represent the solution space quite well.
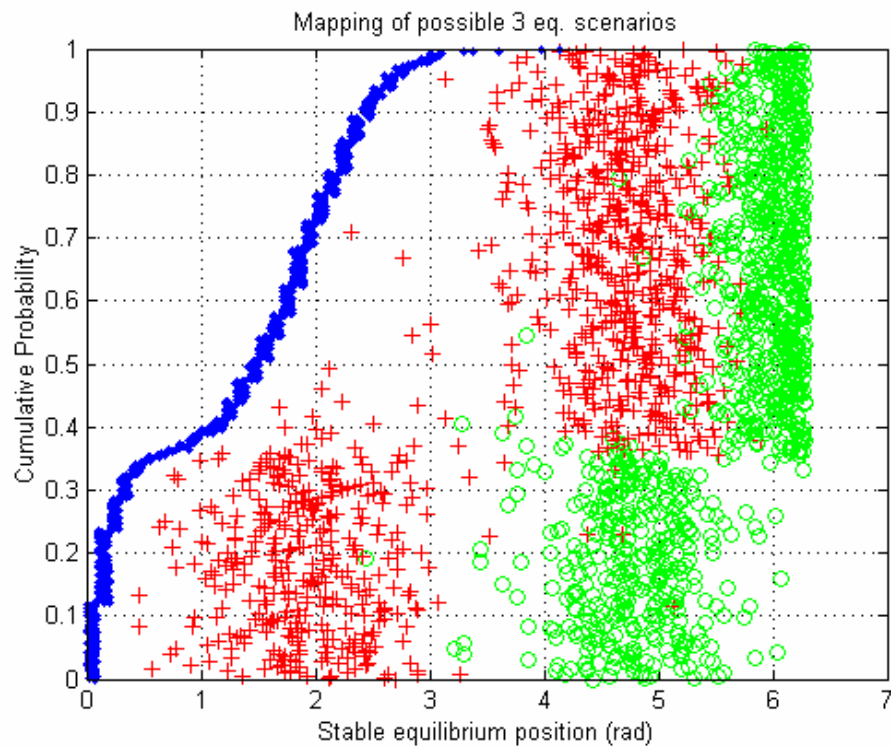
Figure 4.4. Qualitative mapping for a system with three equilibrium positions. The first position is represented by blue '·'s, the second by red '+'s, and the third by green 'o's.

4.3.2.2 Mapping natural frequencies and/or curvatures (qualitative)

Just as done in Section 4.3.2.1, one can visualize other important design information, such as the natural frequency, of the desired MSE design solution.

By plotting the natural frequency of each stable equilibrium position versus the equilibrium position itself, one can begin to envision the possible frequencies attainable in the design. Figure 4.5 is an example plot of natural frequency and position for the case of two stable equilibria occurring during the Monte Carlo trials. Note how one can begin to visualize the range zof natural frequencies possible at each equilibrium position. The highest values for the first stable equilibrium position tend to be near zero radians and seem to get smaller as the first stable position gets larger. The possible natural frequencies of the second stable equilibrium seem to be highest near 6.2 radians with another high grouping around 4.2 radians. Figure 4.6 shows the natural frequency mapping for the tristable case.
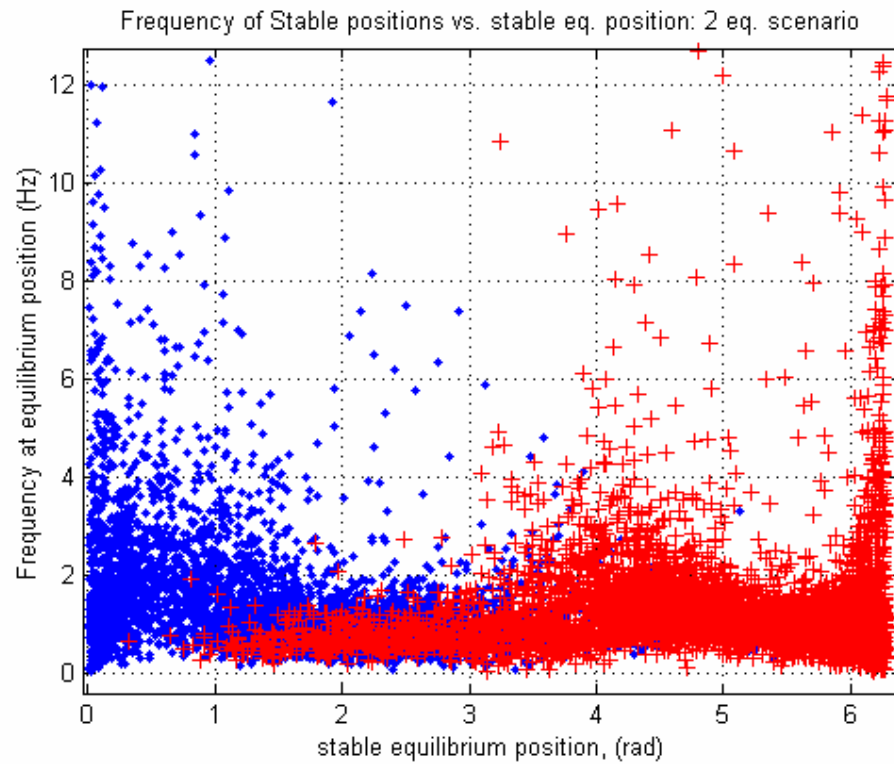
Figure 4.5.   Mapping showing the range of natural frequencies versus the stable equilibrium positions at which they occur. This shows the corresponding data for the bistable MSE system represented in Figure 4.3. Blue '·', and red '+' represent the first and second equilibrium positions respectively.
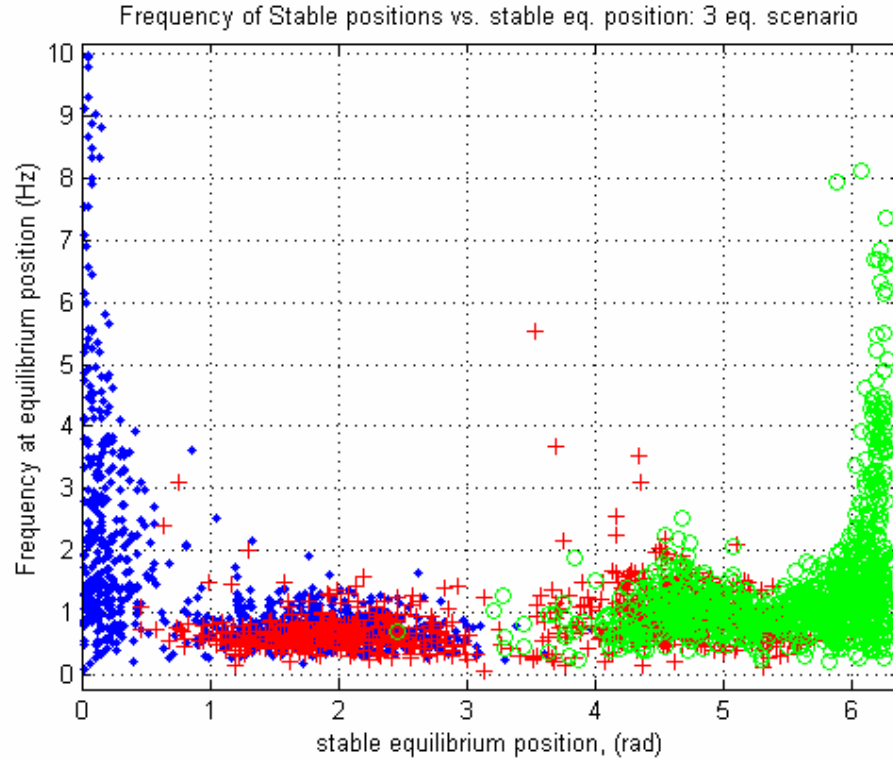
Figure 4.6.   Mapping showing the range of natural frequencies versus the equilibrium positions at which they occur, for the case of a tristable MSE system. Blue '·', red '+', and green 'o' represent the first, second, and third equilibrium positions respectively.

Remember that each data point in Figures 4.5 and 4.6 represents a solution that occurs with a probability of one, since the Monte Carlo random trials indeed found this solution. Thus, one can imagine, that as the number of iterations in the Monte Carlo mapping increase to infinity, a complete representation of the solution space will unfold. As one attempts to solve for natural frequency and equilibrium position combinations that lie outside the ranges shown in Figures 4.5

and 4.6, one can expect increasing difficulty and time in finding the unknown design variables. Again, this issue is more formally addressed in Section 4.3.2.4.

4.3.2.3 Mapping energy values (qualitative)

The third basic design information for a MSE system is the system energy increase required to move from one stable position to another stable position. This is essentially the energy difference between adjacent stable and unstable equilibrium positions, and it represents a threshold energy to overcome when changing stable equilibrium states. For the case of a bistable MSE system, this energy difference is plotted against the location of the stable equilibrium positions in Figure 4.7 (again for the same data as in Figures 4.3 and 4.5).
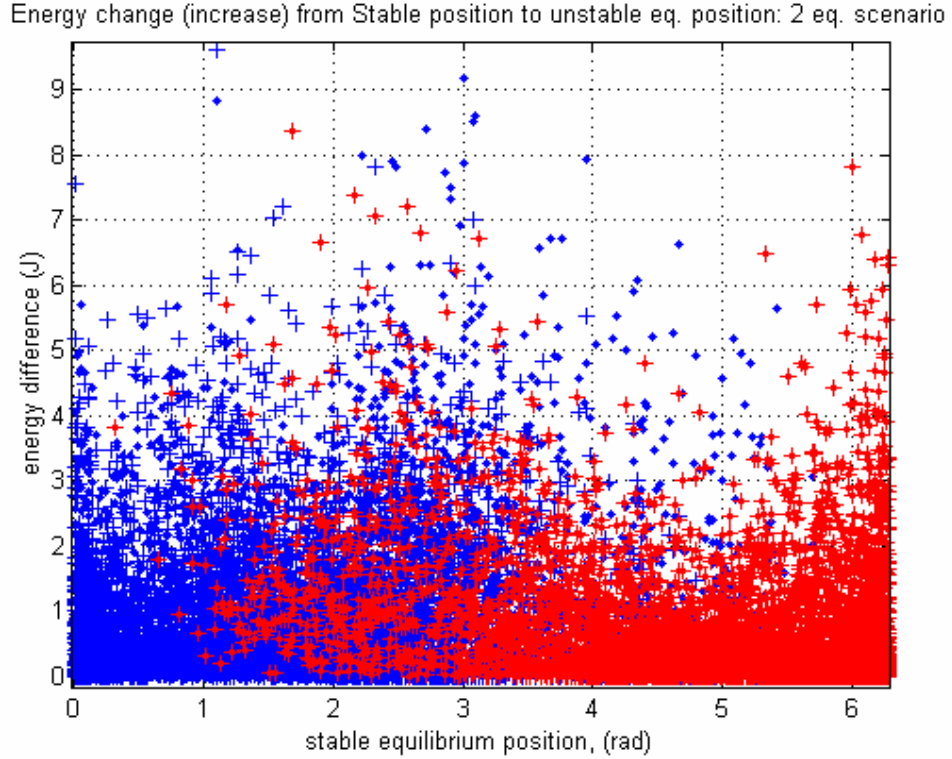
Figure 4.7.   Mapping showing the range of energy thresholds versus the stable equilibrium positions from which they occur for the case of a bistable MSE system. Blue '·' and '+' represent the energy increase required to get to the second equilibrium by going to the left and right respectively. The red '·' and '+' represent the same information for the second equilibrium position.

As seen in Figure 4.7, the energy threshold values seem to mostly lie in the range of zero to four joules, but energy differences up to 9 joules and over are clearly possible. There is a region near 4.5 radians for the second stable equilibrium where most of the energy differences are below 2 joules. This gives an indication that a second stable equilibrium position located near 4.5 radians may not be the most stable position since less energy, or disturbance, may be

required to perturb the MSE system from that position. Thus, if a design criterion is to make the MSE stable positions very immune to system disturbances, then one may think about avoiding the position of 4.5 radians for the second stable position.
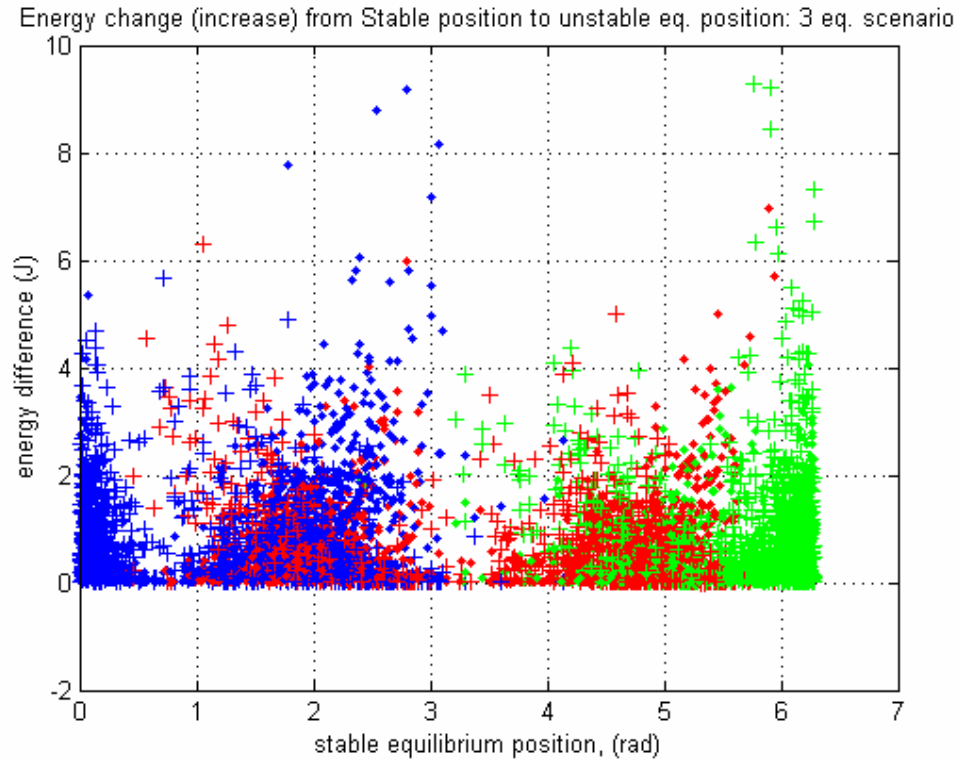
Figure 4.8. Mapping showing the range of energy thresholds versus the stable equilibrium positions from which they occur for the case of a tristable MSE system. Blue '·' and '+' represent the energy increase required to get to the second equilibrium by going to the left and right respectively. The red and green '·' and '+' represent the same information for the second and third equilibrium positions respectively.

Figure 4.8 shows the same energy threshold information for the tristable system represented in Figures 4.4 and 4.6. Note now how the breadth of possibilities has decreased as the energy thresholds are on average less than those

for the bistable case. This is to be expected since there are more extremals in the energy curve in the same amount of space (i.e. in range of [0, 2π] radians). Thus, there is less distance to travel between equilibrium positions in which to greatly increase or decrease the energy.

4.3.2.4 Mapping interpreted as a Probability (quantitative)

The information presented in Sections 4.3.2.1 – 4.3.2.3 shows the three main design criteria for MSE systems: stable equilibrium position (Section 4.3.2.1), natural frequency of a stable position (Section 4.3.2.2), and energy difference necessary to overcome when escaping from an equilibrium position (Section 4.3.2.3). While the design engineer can gain valuable insight from the information represented in the figures of those sections, the same insight becomes more difficult to gain for systems with more stable positions and kinematic degrees of freedom. Also, the mappings of figures (Figures 4.3 - 4.8) are only general guides to design, since when one wants to design for multiple criteria simultaneously (i.e. stable position, frequency, and energy threshold) the coupling of the data becomes very unintuitive for the designer.

This section aims to build on the following three sections by quantifying the Monte Carlo mapping method in a way that is not limited by the complexity of the problem in terms of number of stable equilibria or kinematic degrees of freedom. Section 4.3.2.1 hinted at the method when noting the use of a cumulative distribution function (CDF). To use a CDF, consider each design criteria as a random variable. By creating conditional CDFs for each design

criterion, one can take their derivatives to create conditional probability density functions (PDF). With a conditional PDF for each design criterion, one can integrate in a range about the desired values to quantify a probability, or likelihood, of a solution being possible. This probability is a number that can be related to the ease of a numerical optimization routine to solve for the unknown design variables.

Keep in mind that engineering judgment is required to interpret this probability of finding a desired MSE system solution. Although this section describes quantifying the solution space for a given MSE system, the stochastic nature of the Monte Carlo mapping method does not allow one to describe the solution space with absolute certainty. Nonetheless, it helps achieve the goal of exploring the solution space while attempting to solve for the unknown design variables. The issue of how to interpret the results from the conditional PDF analysis is left for Section 4.3.3.

4.3.2.4.1 Creating Cumulative Distribution Function (CDF)

To describe the calculation of a probability, define the continuous CDF, *CDF$_X$(b)*, of a random variable X as follows:

$$CDF_X(b) = P\{E_b^X\} = P\{\omega \mid X(\omega) \leq b\} = P\{X \leq b\} = \int_{-\infty}^{b} PDF_X(z)dz \qquad (4.17)$$

for all real values b in the range $-\infty \leq b \leq \infty$ [Bowker and Lieberman, 1972]. In Equation (4.17), E_b^X is the event, or set of outcomes in the solution space, such

that the function $X(\omega)$ is less than or equal to the real number b, and $PDF_X(z)$ is the probability density function. Here ω is an element of the solution space, Ω, that represents a possible design criteria (i.e. stable equilibrium position, natural frequency, etc.) that has been generated during the Monte Carlo iterations. The notation $P = \{E_b{}^X\} = P\{ \omega \mid X(\omega) \le b\}$ is interpreted as the probability that the event $E_b{}^X$ will occur. Thus, as $b \to -\infty$, $CDF_X(b) \to 0$, and as $b \to \infty$, $CDF_X(b) \to 1$.

The practical approach to creating a $CDF_X(b)$ from the Monte Carlo data is to arrange the data by ordering a desired design criterion in a monotonically increasing fashion. Also, due to the problem kinematics, there may be some minimum and maximum values that the random variables, or design criteria, can attain, and the real number b in Equation (4.17) will have those same limits.

Assume there is a total of N data sets generated during the Monte Carlo iterations. Some number of the N data sets, N_1, have just one stable equilibrium position (event E_{1eq}), some number, N_2, have two stable equilibria (event E_{2eq}), and so on. In designing a bistable MSE system, then consider only event E_{2eq} with N_2 sets of bistable data. To create the $CDF_X(b)$ for the first equilibrium position, pick an increment, for example 0.05 radians, which will define the resolution of the $CDF_X(b)$. Now cycle through each incremental range [0.0, 0.05], (0.05, 0.1], (0.1, 0.15], … and cumulatively count the number of sets from E_{2eq} that have the first equilibrium in each range. By doing this, one can create a $CDF_X(b)$ for the first equilibrium position as shown in Figure 4.9.
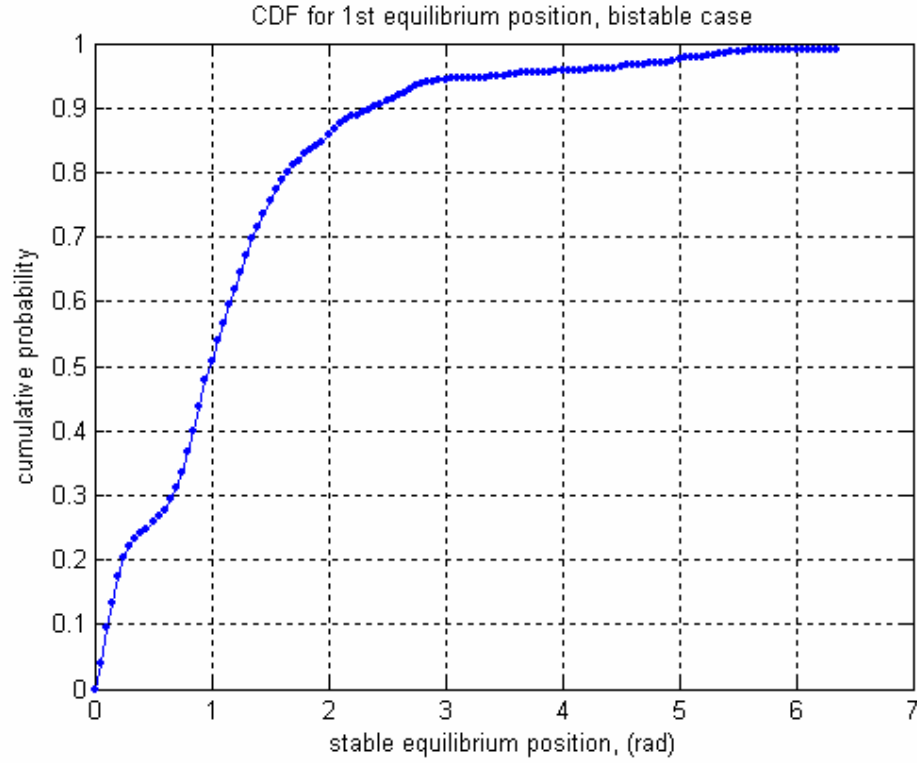
Figure 4.9. Cumulative distribution function for stable equilibrium position one of a bistable MSE system.

4.3.2.4.2 Creating Probability Density Function (PDF)

Once one obtains the *CDF$_X$(b)* for a design criteria of interest, creating the PDF for that random variable is straightforward. The *PDF$_X$(z)* for the continuous random variable, X, is the derivative of the *CDF$_X$(b)* of Equation (4.17) (see Equation 4.18).

$$PDF_X(z) = \frac{dCDF_X(z)}{dz} \qquad (4.18)$$

Note that the notation *PDF$_X$(b)* refers to the probability density of the random variable X to obtain the value z = b. To obtain a probability, one must integrate over some range of z values. The expression $P\{x_2 \leq X < x_3\}$ is the probability of the occurrence of the event, E_2, containing ω in the Monte Carlo sample space such that $X(\omega)$ is greater than or equal to x_2 and less than x_3. In this instance, to obtain the probability of X being between x_2 and x_3, use those values as the integration limits of Equation (4.17) (see Equation 4.19).

$$P_X(E_2) = CDF_X(x_3) - CDF_X(x_2)$$
$$= P(x_3) - P(x_2) \qquad (4.19)$$
$$= \int_{x_2}^{x_3} PDF_X(z)dz$$

Note that there are only two requirements for the *PDF$_X$(z)* to satisfy:

(i) *PDF$_X$(z)* ≥ 0 for all z, and

(ii) $\int_{-\infty}^{\infty} PDF_X(z)dz = 1$

In performing the calculations shown in Equation (4.18) on the *CDF$_X$(b)* shown in Figure 4.9, one obtains the *PDF$_X$(z)* for the first equilibrium position shown in Figure 4.10. Note in Figure 4.10 that there are two peaks of high probability density for the first equilibrium position to occur: one near 0.2 radians and the other near 0.9 radians. This shows how arbitrary the *PDF$_X$(z)* can be for any given design criterion, or random variable. By performing the mapping

78

completely numerically, this method avoids the problem of fitting the data to any predetermined $PDF_X(z)$ (such as normal or exponential distributions).
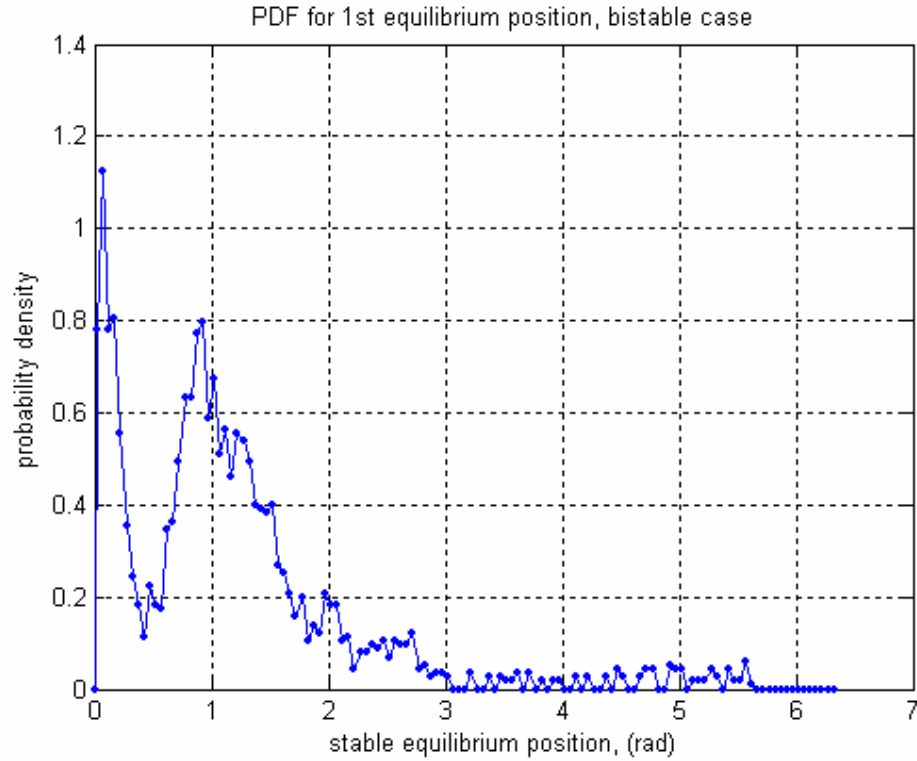
Figure 4.10.   Probability density function for stable equilibrium position one of a bistable MSE system.

The usefulness of the PDF (for simplicity in notation simply say PDF = $PDF_X(z)$) lies in its ability to provide a quantitative measure of the likelihood of being able to design the MSE system with a desired set of design criteria. In Figure 4.10, this desired design criterion is the location of the first equilibrium

position. In using a PDF, such as the one in Figure 4.10 and described in Equation (4.19), it is important to remember that to obtain a probability one must integrate the corresponding PDF over some range of desired design criterion.

4.3.2.4.3 Conditional probability density functions to describe local solution space

Sections 4.3.2.4.1 and 4.3.2.4.2 establish the method for creating probability density functions to describe the probability, or likelihood, of a design criterion to reside near the desired value. When one wants to describe the likelihood of more than one design criterion for the MSE system to occur simultaneously, the use of PDFs can again be used. This time each additional PDF is a conditional PDF. The computation of conditional probability is equivalent to calculating probabilities of events defined in a 'reduced' sample space. In other words, a conditional probability is defined as the occurrence of the event E_2 relative the reduced sample space defined by event E_1. This is exactly the interpretation that will be used in this quantitative mapping method. Formally, the conditional probability can be represented as in Equation (4.20):

$$P\{E_2 \mid E_1\} = \frac{P\{E_2 \cap E_1\}}{P\{E_1\}} \qquad (4.20)$$

where $P\{E_1\}>0$ must be true [Bowkers and Lieberman, 1972]. Equation (4.20) is read as 'the probability of event E_2 such that E_1 is true.'

In a similar manner, the conditional probability density function itself is defined. Suppose (X_1, X_2) represents a bivariate continuous random variable. In the MSE design situation, this is interpreted as if there are two design criteria of interest, for example (equilibrium position one, natural frequency at position one) = (E_{eq1}, f_1). These two variables have a joint PDF as $PDF_{X1,X2}(u,v)$ and marginal PDFs of $PDF_{X1}(u)$ and $PDF_{X2}(v)$. Then the conditional PDF of X_2, given that $X_1 = x_1$ (i.e. that X_1 is fixed), is:

$$PDF_{X_2|X_1=x_1}(v) = \frac{PDF_{X_1X_2}(x_1,v)}{PDF_{X_1}(x_1)} \qquad (4.21)$$

if $PDF_{X1}(x_1) > 0$, and the conditional PDF of X_1, given that $X_2 = x_2$, is:

$$PDF_{X_1|X_2=x_2}(u) = \frac{PDF_{X_1X_2}(u,x_2)}{PDF_{X_2}(x_2)} \qquad (4.22)$$

if $PDF_{X2}(x_2) > 0$. Note that Equation (4.21) can be interpreted as the "probability density function of variable X_2 given that the event $X_1 = x_1$ has occurred."

In using the Monte Carlo mapping method, explicit functional forms of the joint $PDF_{X1,X2}(u,v)$ and the marginal PDFs, $PDF_{X1}(u)$ and $PDF_{X2}(v)$, are unknown. Since the probabilities are calculated numerically, the accounting for the concept of joint PDFs is done by neglecting all Monte Carlo mapping data that does not satisfy the constraint of the previous random variable having already occurred. For example, assume there are 1000 sets of Monte Carlo data (i.e. 1000

equilibrium position one (Eq_1) data points and the respective 1000 data points for the natural frequency at equilibrium one (f_1)). If $Eq_1 = 1.0$ is desired, and a range of ± 0.2 about Eq_1 is considered viable for design, then say 300 data points satisfy the inequality $0.8 \leq Eq_1 \leq 1.2$. To formulate the conditional PDF = $PDF_{f1|Eq1=1.0}(1.0,v)$, simply follow the methodology of Sections 4.3.2.4.1 - 4.3.2.4.2 except using only the 300 data sets corresponding to the condition Eq_1.

The benefit of the use of conditional PDFs described in this section is that the idea can be applied over and over again for each additional design criteria. For example, imagine an MSE system has two kinematic degrees of freedom (X, Y) and the goal is to have two equilibrium positions, (Xeq_1, Yeq_1) and (Xeq_2, Yeq_2), with a minimum energy increase to go between stable positions of ΔE_{12}. This means that there are the following five design criteria [Xeq_1, Yeq_1, Xeq_2, Yeq_2, ΔE_{12}] to consider. Thus, one needs to have 5 - 1 = 4 conditional probability distributions to describe the system. This is not a problem since the design methodology leaves no inherent limit on the number of PDFs that can be used. Calculating conditional probabilities is valid as long as each one has P > 0. Should one eventually calculate a conditional probability of zero, there will be no data left for any subsequent calculations. The question of how to interpret this scenario is discussed fully in Section 4.3.3.2.

4.3.2.5 Example use of mapping method with conditional PDFs

This section describes the use of the conditional *PDFs* to explore the solution space generated by the Monte Carlo iterations. The same data is used as

is shown in Figures 4.3, 4.5, and 4.7. This example use of the method demonstrates the probability calculations, and the following section, Section 4.3.3, discusses some of the drawbacks and limitations of the probability mapping method.

The problem to explore is to find the probability:

(i)   of acquiring two stable equilibrium positions at $x_1 = 0.5$ and $x_2 = 5.0$ radians, and

(ii)   for the stable equilibiria to have natural frequencies of $x_3 = 1.5$ rad/s and $x_4 = 2$ rad/s for the first and second position respectively.

In finding the *CDFs* for each design criteria, the increment to characterize the resolution of each *CDF* is 0.05 radians or rad/s. Also, the range about each desired design criteria for integrating each *PDF* is ±0.2 radians or rad/s. The minimum and maximum values for each equilibrium position are 0.0 radians and 2π radians respectively (as determined by the problem geometry). Also, from Figure 4.5, both the first and second equilibrium natural frequencies seem to have an allowable range of about 0 - 13 rad/s. Thus, all of the necessary parameters are set to evaluate the solution space by use of the conditional *PDF* approach.

The first probabilistic event, E_1, to occur in the data is that there are two stable equilibrium positions. The probability for this is estimated as in Equation (4.23).

$$P\{E_1\} \approx N_{\text{trials with 2 equilibria}} \Big/ N_{\text{Monte Carlo trials}} = 5413 \Big/ 49541 = 0.109 \qquad (4.23)$$

The second event, E_2, is the occurrence of the first equilibrium position in the desired range. The first *PDF*, generated for the first equilibrium position, is shown in Figure 4.11. Note that the desired equilibrium position, $Eq_1 = 0.5$ radians, is near a low spot in the probability density, yet clearly nonzero. A location of low probability density means there were relatively few data points generated by the Monte Carlo simulation at that location. Thus, when we perform the next conditional *PDF* calculation, there will be a relatively small amount of data left to analyze. This issue can result in running out of data points to use as more and more design criteria are analyzed, and Section 4.3.3.2 discusses this topic.
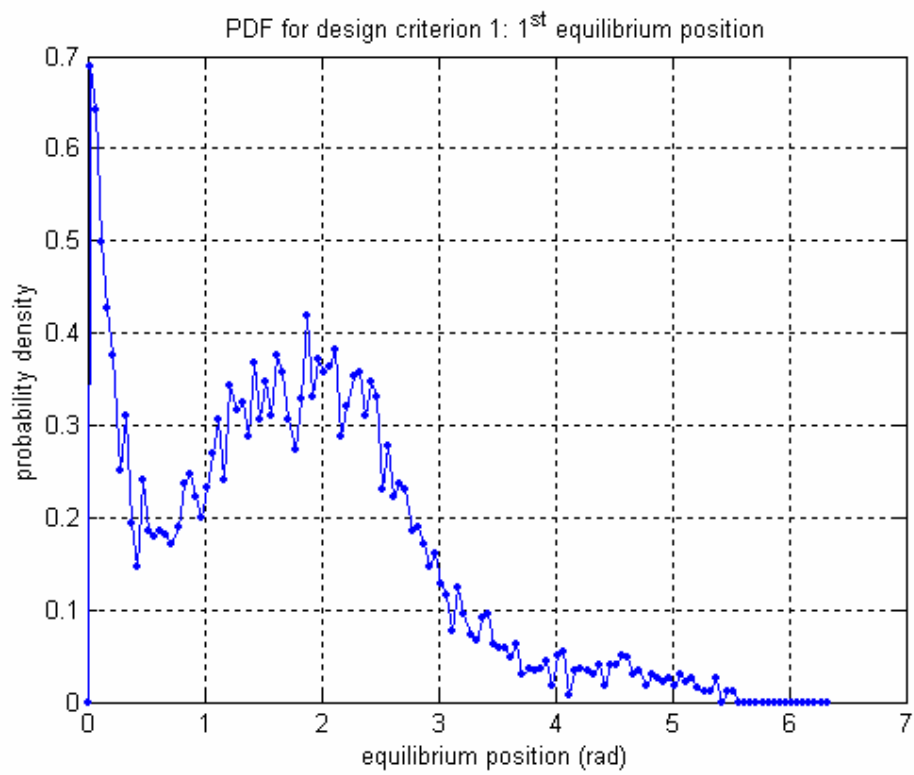
Figure 4.11.   Probability density function for the first stable equilibrium position
the example bistable MSE system.

Subsequent calculation of the three additional conditional PDFs results in the profiles shown in Figure 4.12. Following the notation of the bivariate distribution shown in Equations (4.21) and (4.22), the PDF in Figure 4.11 can be expressed as $PDF_{Eq1 \mid 2eq}(2eq, x_1)$ and interpreted as 'the probability density function of Eq_1 given that there are two equilibria present.' Similarly, the probability density of Eq_2 conditioned on $Eq_1 = 0.5$ radians is written as $PDF_{(Eq2 \mid Eq1 = 0.5, 2eq)}(2eq, 0.5, x_2)$ and is shown in Figure 4.12(a). For the remaining design criteria, the $PDF_{(f1 \mid Eq2=5.0, Eq1=0.5, 2eq)}(2eq, 0.5, 5.0, x_3)$ is shown by Figure 4.12(b), and $PDF_{(f2 \mid f1=1.5, Eq2=5.0, Eq1=0.5, 2eq)}(2eq, 0.5, 5.0, 1.5, x_4)$ is shown by Figure 4.12(c).
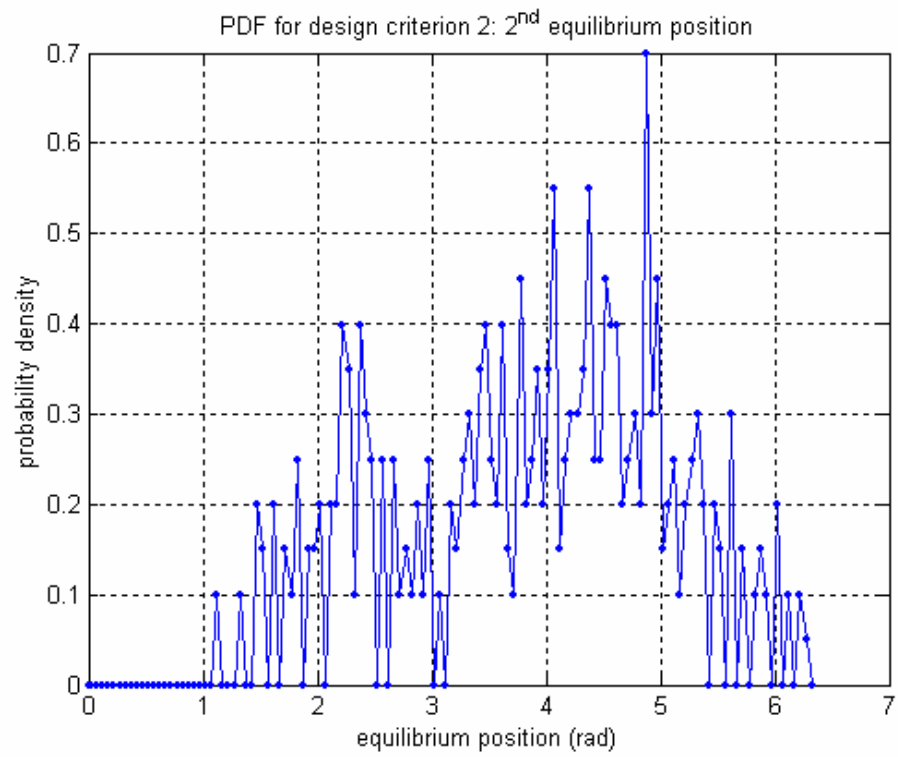
Figure 4.12 (a) Conditional probability density function for the second equilibrium position.
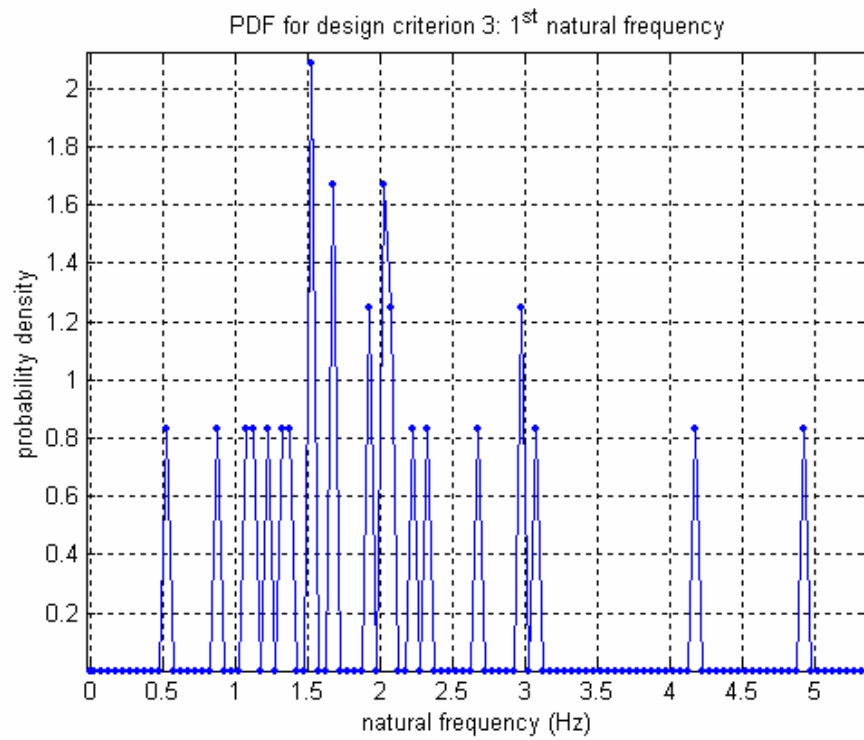
Figure 4.12 (b) Conditional probability density function for the natural frequency of the first equilibrium.
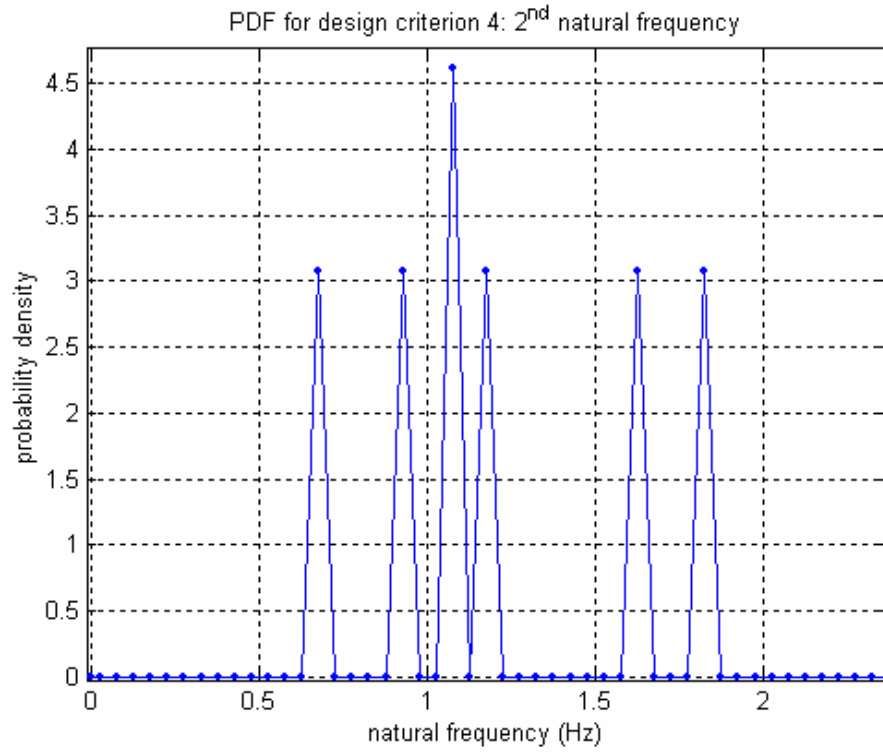
Figure 4.12 (c) Conditional probability density function for the natural frequency of the second equilibrium.

Note how each conditional PDF can be viewed as only a bivariate PDF, with the 'first' event, E_1, being all of the previously occurring variables (or design criteria), and the 'second' event, E_2, being the next random variable (design criterion) to be considered. In the current example, for the first PDF, shown in Figure 4.11, the first event is that the data contains two stable equilibrium values, $E_1 = \{\omega \mid 2eq\}$, and the second event is that the first equilibrium is at $x_1 = x_{1,des} = 0.5$, $E_2 = \{\omega \mid x_1 = Eq_1 = x_{1,des}, 2eq\} = \{\omega \mid x_1 = Eq_1 = x_{1,des}, E_1\}$. Also, for the

second PDF, shown in Figure 4.12(a), the first event is the second event of the previous bivariate distribution. Thus, in calculating Figure 4.12(a), the 'first' event is $E_2 = \{\omega \mid x_1 = Eq_1 = x_{1,des}, E_1\}$, and the 'second' event is $E_3 = \{\omega \mid x_2 = Eq_2 = x_{2,des}, x_1 = x_{1,des}, 2eq\} = \{\omega \mid x_2 = Eq_2 = x_{2,des}, E_2, E_1\}$. Following the same pattern in no0tation, for the third PDF shown in Figure 4.12(b), the first event is E_3, and the second event is $E_4 = \{\omega \mid x_3 = f_1 = x_{3,des}, E_3, E_2, E_1\}$. Again for the fourth PDF in Figure 4.12(c), the first event is E_4, and the second event is $E_5 = \{\omega \mid x_4 = f_2 = x_{4,des}, E_4, E_3, E_2, E_1\}$.

To find the probability for each event, E_i, integrate the respective *PDF* about the desired value for the design criterion. For example, event one, E_2, is defined as the first equilibrium point being in the range $[0.3 \leq x_1 < 0.7)$. This corresponds to $P(E_2) = P_{Eq1}(0.7) - P_{Eq1}(0.3)$. Equation (4.23) shows this calculation.

$$P\{E_2\} = \int_{0.3}^{0.7} PDF_{Eq_1}(z)dz = 0.086 \qquad (4.23)$$

Similar calculations for the other conditional probabilities results in $P\{E_3 \mid E_2, E_1\} = 0.171$, $P\{E_4 \mid E_3, E_2, E_1\} = 0.153$, and $P\{E_5 \mid E_4, E_3, E_2, E_1\} = 0.0$. Thus, the total probability is the multiple of all probabilities from the mapping method, given in Equation (4.24).

$$P_{total} = \prod_{i=1}^{5} P\{E_i\}$$

$$= P\{E_1\} \cdot P\{E_2 \mid E_1\} \cdot P\{E_3 \mid E_2, E_1\} \cdot P\{E_4 \mid E_3, E_2, E_1\} \cdot P\{E_5 \mid E_4, E_3, E_2, E_1\}$$

$$= (0.109)(0.086)(0.171)(0.153)(0.0)$$

$$= 0.0$$

(4.24)

Equation (4.24) shows a probability of zero. The reason is that a desired solution was chosen where none exists *in the Monte Carlo data*. This does not mean that the solution cannot occur, only that it is unlikely to be derived by randomly choosing design variables. Performing the same probability analysis, but slightly perturbing the desired set of design criteria could produce a probability greater than zero. In this way one can 'probe' the solution space to understand the possible solutions that can exist. This idea is more fully discussed in Section 4.3.3.2.

The next section (Section 4.3.3) discusses more fully how to interpret the probability and *PDF* results from the quantitative Monte Carlo mapping method. Generalizations are made to predict how long one must run an optimization routine to obtain a desired solution, and how the designer can have confidence that he has put enough effort into solving the problem.

4.3.3 Step 3: Interpretation of conditional PDF results

The process of creating conditional probabilities is continued until all design criteria have been explored, or until one runs out of data. In reality, given the constraints of the problem, a solution either exists (probability of one) or it

91

does not (probability of zero). The problem is that there may not be enough information to make this decision. Performing slightly more statistical analysis on the Monte Carlo data can help make this decision, although in many cases, the determination of solution existence cannot be known with absolute certainty.

There are the following possible outcomes from the mapping method that warrant discussion:

Case 1: $P_{total} > 0$, and

Case 2: $P_{total} = 0$.

The following subsections 4.3.3.1 and 4.3.3.2 discuss how to make a decision on solution existence for each case of $P_{total} > 0$ and $P_{total} = 0$. Note the optimization results for all subsections of Section 4.3.3 result from using a genetic algorithm [Houck et al.]. In all cases, the parameters governing the operation of the genetic algorithm are kept the same in order to accurately compare the results. The focus here is on obtaining information gained from the mapping procedure and not on enhancing performance by tuning any particular optimization algorithm. Of course, different heuristic techniques and optimization algorithms may be better or worse at solving any particular problem, but performing the procedures outlined here are possible with the use of any algorithm with significant stochastic properties.

The reason that stochastic optimization or search algorithms are needed for solving MSE system problems is for two main reasons: 1) the solution space is

inherently nonlinear making deterministic and gradient based solvers get easily trapped in local minima, and 2) the Monte Carlo mapping procedure is based on complete randomness and the more randomness in an algorithm, the more one can expect it to follow the Monte Carlo patterns.

In choosing an optimization algorithm, or a heuristic search method, to solve an optimization problem, one can envision a continuum of optimization searching algorithms [Cagan et al., 2002]. Figure 4.13 shows this continuum representation used by Cagan in relation to packing problems, where some commonly used algorithms are placed in accordance to their amount of

HR   MC
GM   EPS   HB   SA   GA   RS

deterministic ⟷ random
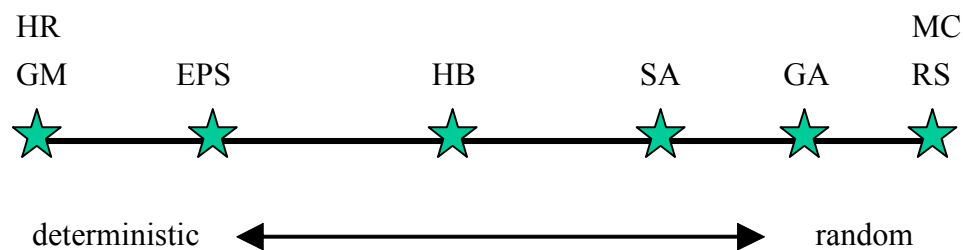
Figure 4.13. A continuum of search algorithms for solving optimization problems.

randomness. To the far left of the continuum are completely deterministic methods (GM = gradient method, HR = heuristic rule) with no randomness. To the far right are completely random methods (RS = random search, MC = Monte Carlo) with no guiding principle or intelligence. In the middle of the continuum are (going left to right in increasing randomness) extended pattern search (EPS) algorithms that have some stochastic elements into an otherwise deterministic search method. Hybrid methods (HB) are those that use stochastic methods early

in solution to navigate the solution space and then use heuristic rules or gradient methods to reduce and refine the solution space. Simulated annealing (SA) methods and genetic algorithms (GA) incorporate a large amount of randomness and thus are often less efficient than methods further to the left on the continuum. They are also less likely to get stuck in local minimal solutions.

Therefore, a rule of thumb in interpreting the results of the Monte Carlo mapping in terms of optimization algorithm performance is that the more randomness in the algorithm, the more one can expect the results to mimic those of the Monte Carlo data. This does not preclude the use of deterministic methods to solve MSE problems since they can be used in tandem with stochastic algorithms as hybrid methods. Although the choice of an appropriate optimization algorithm is a necessary step in the synthesis of MSE systems, this dissertation proposes no general method to choose a correct method. The body of literature on choosing correct numerical optimization algorithms for certain classes of problems is extensive, and any generalization on how to choose an appropriate algorithm for MSE systems is beyond the scope of this dissertation.

To make the connection between the Monte Carlo data and optimization results, use is made of the concept of a run-length distribution (RLD) [Stützle and Hoos, 1999]. Here, the word 'length' is represented by the number of iterations required to solve the problem. The 'speed' at which a problem reaches solution is measured in how many iterations are needed (i.e. the fewer iterations required the easier and faster the problem is to solve). Either time or iterations can be used to

quantify how long it takes for an optimization algorithm to solve a problem, but iterations is used to make the discussion independent from computer capability.

The RLD is a cumulative distribution function of the iterations required to solve the desired problem to within some threshold of the performance index. This threshold value is directly correlated with the Monte Carlo probability calculation. Recall that to obtain a probability it is necessary to specify a range about a desired design criterion. For example, if one desires an equilibrium position, $x_{1,eq}$, we specify an acceptable range, dictated by $\pm \delta x_1$, for the actual equilibrium position. There is an associated range with each desired design criteria. For the purpose of creating RLDs, when each design criterion is inside its respective range, the solution is said to be found, and the algorithm stops iterating over the design variables.

By altering the performance index of Equation (4.11), one can create a performance index incorporating the concept of the threshold value. To do this, have a term for each desired design criterion that is positive when the design criterion is outside of the acceptable range and is zero when it is inside the range. Equation (4.25) demonstrates this concept:

$$PI = \sum_{i=1}^{n} \begin{pmatrix} w_i \left(d_{cand,i} - d_{des,i} \right) \text{if } d_{cand,i} > d_{des,i} \text{ and } d_{cand,i} > \left(d_{des,i} + \delta d_i \right), 0 \text{ otherwise} \\ w_i \left(d_{des,i} - d_{cand,i} \right) \text{if } d_{cand,i} < d_{des,i} \text{ and } d_{cand,i} < \left(d_{des,i} - \delta d_i \right), 0 \text{ otherwise} \end{pmatrix}$$

$$(4.25)$$

where n is the number of design criteria in the performance index, d is a generic design criterion, w_i is the weighting of the ith design criterion, and $d_{max,i}$, $d_{min,i}$, and

95

$d_{des,i}$, are the maximum allowed, mininum allowed, and desired values for design criterion i. Thus, the threshold value for the performance index in Equation (4.25) is the minimum of all terms in Equation (4.25). If Equation (4.25) equals the threshold value, then it goes to zero and one is assured that all of the desired design criteria are within the allowed range as dictated in the probability calculation. Note the threshold value for the performance index in Equation (4.25) increases with larger ranges, $\pm\delta d_i$, making it easier to effectively solve the problem and reach zero performance index. In practice one can also incorporate the basic structure of Equation (4.11) to further refine the answer as much as possible.

4.3.3.1 Step3a: $P_{total} > 0$

In this scenario, because the total probability of the mapping method is nonzero, there is at least one Monte Carlo data point inside the desired range for the design criteria. This actually means that there is a *probability of one* for obtaining the desired solution within the specified tolerance. Therefore, any nonzero probability means a solution does exist for the desired solution. At this point, one can proceed to using an optimization algorithm to solve for the unknown design variables.

In calculating the probability one has already interpreted the desired engineering characteristics in terms of the parameters that describe the system potential energy about each local equilibrium. In other words, as described in Section 4.2, translate terms such as equilibrium position and natural frequency

into $a_{des,i}$, $b_{des,i}$, and $c_{des,i}$ of Equation (4.3). These factors can go into a performance index form similar to that of Equation (4.11) that may incorporate other factors including, but not limited to, those shown in Section 4.2.3 and its subsections.

This section provides no examples of solving this case of $P_{total} > 0$ since they are inherently considered in the next section where $P_{total} = 0$. Refer to Section 4.3.3.2 for the trends of solution run-length as P_{total} decreases from a positive number to zero. These trends present a understanding of how to interpret the Monte Carlo probability calculation.

4.3.3.2 Step 3b: $P_{total} = 0$

Unlike the case where $P_{total} > 0$ guarantees that a solution exists, the calculation of $P_{total} = 0$ does not guarantee that a solution does not exist. But, by using an additional statistical analysis, one can gain a level of confidence in the existence of the desired MSE solution, and make a decision on how hard the problem might be to solve.

Recall that each conditional *PDF* is composed of fewer data points than the one before, and thus it is quite feasible that one will run out of data points before calculating all conditional probabilities. First of all, the problem of determining if there is enough data is only relevant for the case when $P_{total} = 0$. This result stems from Section 4.3.3.1 which states if $P_{total} > 0$, the solution does exist within the specified bounds, and one needs no further probability analysis to define solution existence. Having $P_{total} = 0$ essentially means that for some event,

E_i, the conditional probability is zero, $P_i = 0$, for $i < n$ where n is the total number of design criteria, and all $P_j > 0$, for $j < i$. There is only one way in which $P_i = 0$ occurs: the ith desired design criterion range does not include the space where any existing data points lie. In other words, looking at Figure 4.15 for the 3rd design criterion, this is as if one desires a value of 10 ± 0.2 rad/s. Since the probability density function is zero about 10 rad/s, this conditional probability is zero. All further j^{th} probabilities, for $i < j \leq n$, are also zero by definition of the conditional probability.

Note that the earlier $P_i = 0$ occurs (i.e. smaller 'i'), the less information that exists and the less knowledge one has of the full desired solution occurring. A problem in using the Monte Carlo data is knowing if one has produced enough data points. If the probability calculation results in $P_{total} = 0$, one can gain a feel for how probable the solution is in reality, by searching the solution space with the mapping method until one achieves a solution with $P_{total} > 0$.

It is relatively easy to 'search' the solution space for probable solutions by perturbing the desired design criteria and viewing each *PDF* independently as one calculates the probability. Suppose one wants the following bistable desired design criteria: $x_{1,des} = 0.3 \pm 0.2$ and $x_{2,des} = 4.0 \pm 0.2$ radians, and $x_{3,des} = 3.0 \pm 0.2$ and $x_{4,des} = 2.1 \pm 0.2$ rad/s. The respective *PDF*s are shown in Figure 4.14, and the calculated probability of the desired solution is zero. To ensure a solution with probability greater than zero, the designer can do one or both of two things: increase the allowable range of some desired criteria or change one or more desired design criteria values to those where the respective probability is not zero.

Figure 4.15 shows a case in which the allowed range for the desired frequencies is increased to vary by ± 0.3 rad/s, and now the expanded range encompasses a mapping data point such that $P_{total} > 0$. Also, Figure 4.16 represents the case where the allowed range about each data point is kept the same, but the desired value, $x_{4,des}$, is changed to $x_{4,des} = 2.0 \pm 0.2$ rad/s. Again, the probability is now greater than zero, showing that this desired solution exists for these 'perturbed' cases. Both of the results from Figures 4.15 and 4.16 give one reason to believe that the original desired solution, with the PDFs in Figure 4.14, is actually quite close to known existing solutions from the Monte Carlo mapping data.
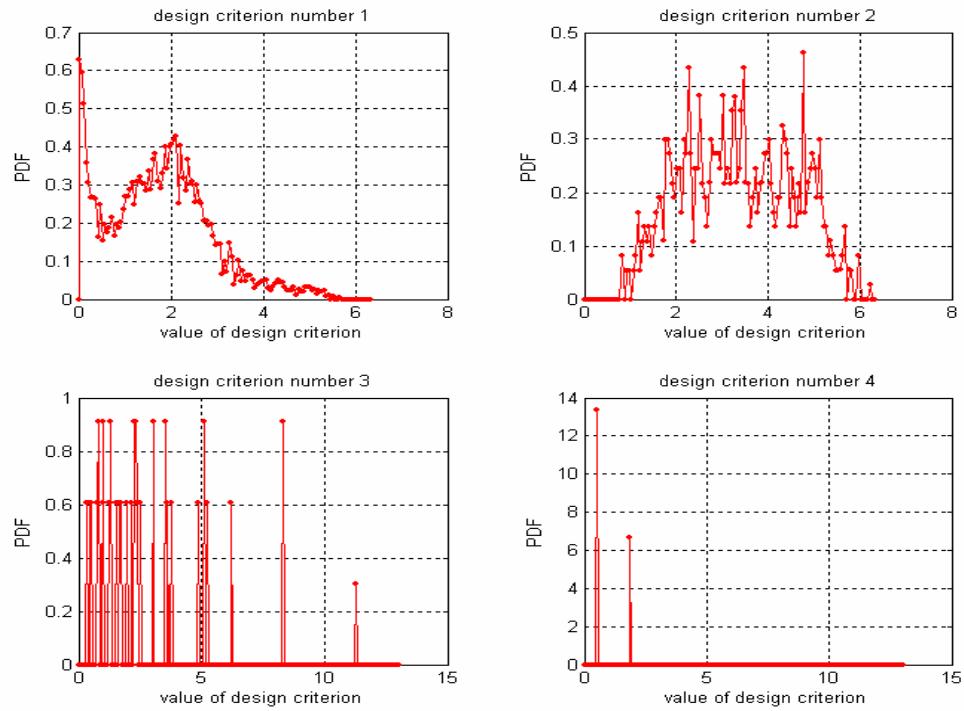
Figure 4.14.   Individual conditional PDFs. The total probability is zero since the desired value of the 4th design criterion is 2.0 rad/s is out of the range of data.
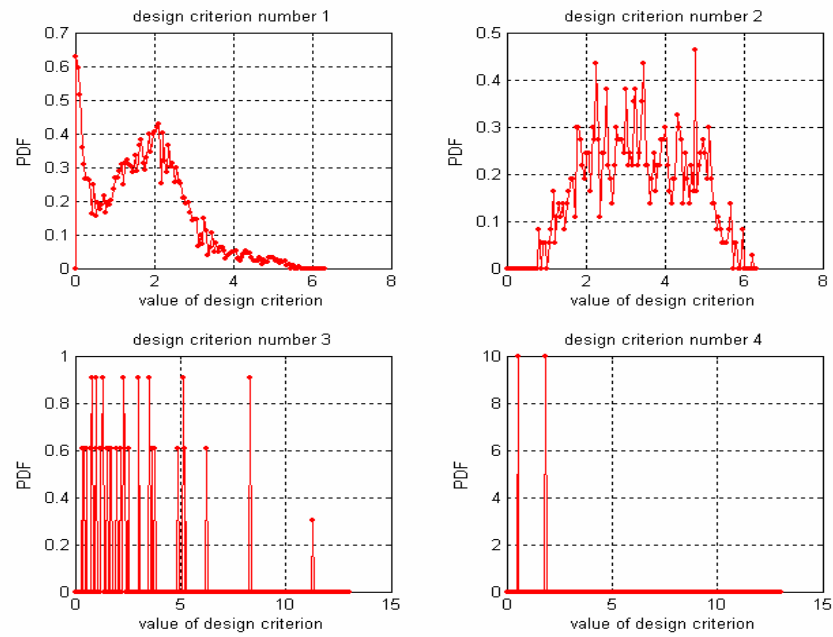
Figure 4.15.   Individual conditional PDFs. The total probability is now greater than zero since the allowed range for the 3rd and 4th design criteria are increased.
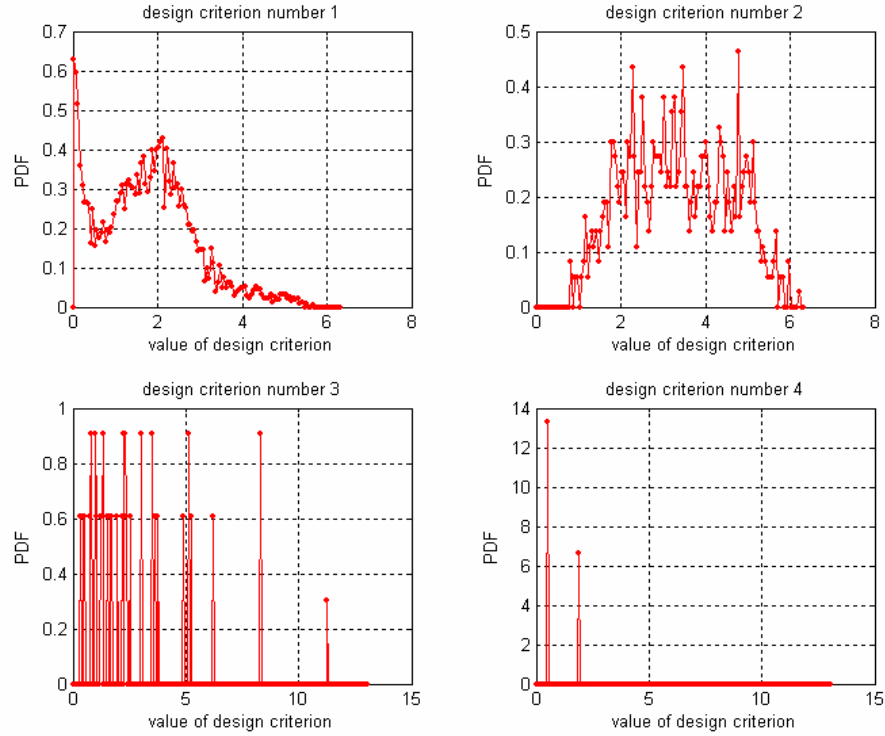
Figure 4.16.   Individual conditional PDFs. The total probability is now greater than zero since the desired value for the 4th design criterion is decreased slightly to include at least one data point.

To obtain a feel for the influence of the probability number on the ease of solving a problem, a series of solutions are analyzed where there is a decreasing probability as one of the design criteria is moved from its feasible range, as defined by the mapping procedure.

Consider the example linkage problem of Chapter 5 in Section 5.2 where the link lengths are of a fixed length, and the springs attached to the ground are

also in a fixed position. There are six desired design criteria: the three equilibrium positions and their respective frequencies. A set of Monte Carlo mapping data is generated with 33892 points and 1009 of them have three equilibria. The desired design criteria are $[\theta_{1,eq}, \theta_{2,eq}, \theta_{3,eq}, f_1, f_2, f_3] = [0.2 \pm 0.2, \theta_{2,eq} \pm 0.2, 4.5 \pm 0.2, 1.80 \pm 0.2, 0.65 \pm 0.2, 1.10 \pm 0.2]$, where $\theta_{2,eq}$ varies with the following desired values $\theta_{2,eq} = [2.5, 2.6, 2.7, 2.8, 2.9, 3.0, 3.1]$. The total probability associated with each of the seven trials is shown in Figure 4.17 as probability versus $\theta_{2,eq}$.

The probabilities for $\theta_{2,eq} = [2.5, 2.6]$ are nonzero. Thus, one would expect their solution to be relatively easy since a randomly generated set of design variables with no intelligence produced the desired solution in almost 34,000 tries. The other five desired solutions have zero final probability. Figures 4.18 and 4.19 show each successive probability value as each design criteria was considered with its conditional probability. Figure 4.19 is a close-up view of Figure 4.18. The x-axis is the cumulative number of design criteria considered, with the first criterion being the probability of having three stable equilibria anywhere (assumed $= N_{3eq}/N_{trials}$). The other criteria considered in order from 2-7 are $\theta_{1,eq}, \theta_{2,eq}, \theta_{3,eq}, f_1, f_2,$ and f_3, respectively.
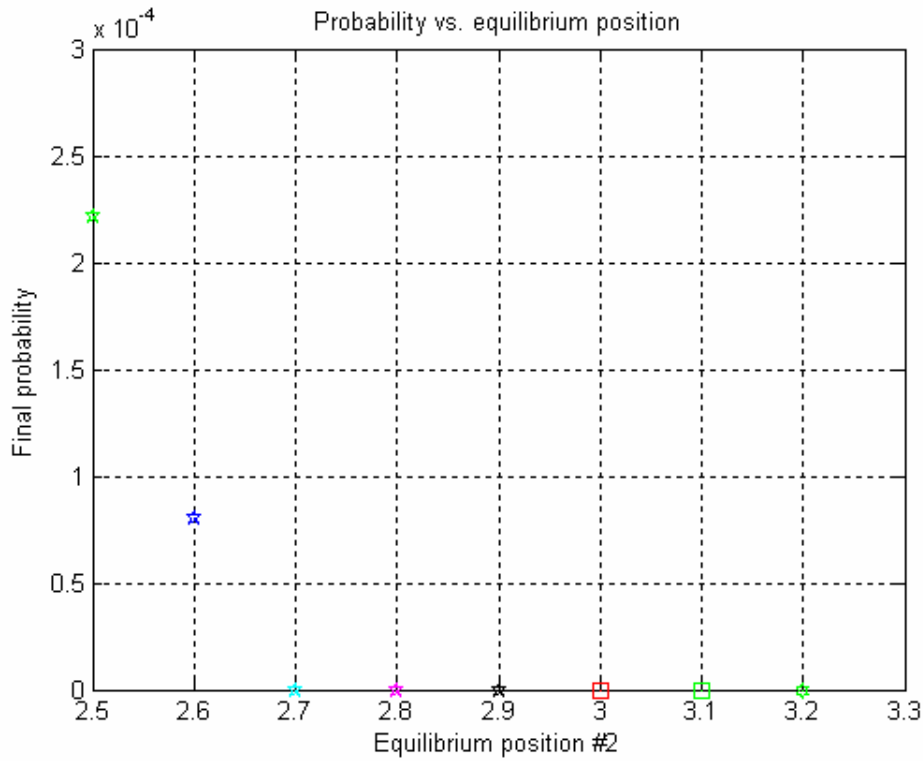
Figure 4.17.   Total probability from the Monte Carlo mapping data as the second equilibrium position is varied from 2.5 radians to 3.2 radians.

From looking at Figures 4.17 – 4.19, since the second desired criterion is varied from a location of nonzero mapping probability to a location of zero mapping probability, it makes sense that at some value the solution may no longer be possible. The desired solution will eventually leave the locally feasible range. The critical value of this varying design criterion is an unknown, and it defines a local boundary of the possible solution space. A goal of the Monte Carlo mapping method is to enable the design engineer to find this boundary with some degree of confidence.

Notice in Figures 4.18 and 4.19, that as $\theta_{2,eq}$ increases, the probability values at and after the third design criteria (i.e. $\theta_{2,eq}$) decrease. Not only do the

probability values decrease, but the number of data points left for subsequent conditional probability analysis also decreases. This is important to note because, as the accumulating probability in Figures 4.18 and 4.19 decreases at a faster rate, the less one knows about the subsequent design criteria. This follows from the basic premise of the statistical law of large numbers. The more data one has, the more confident one becomes of any emerging pattern, or statistical measures.
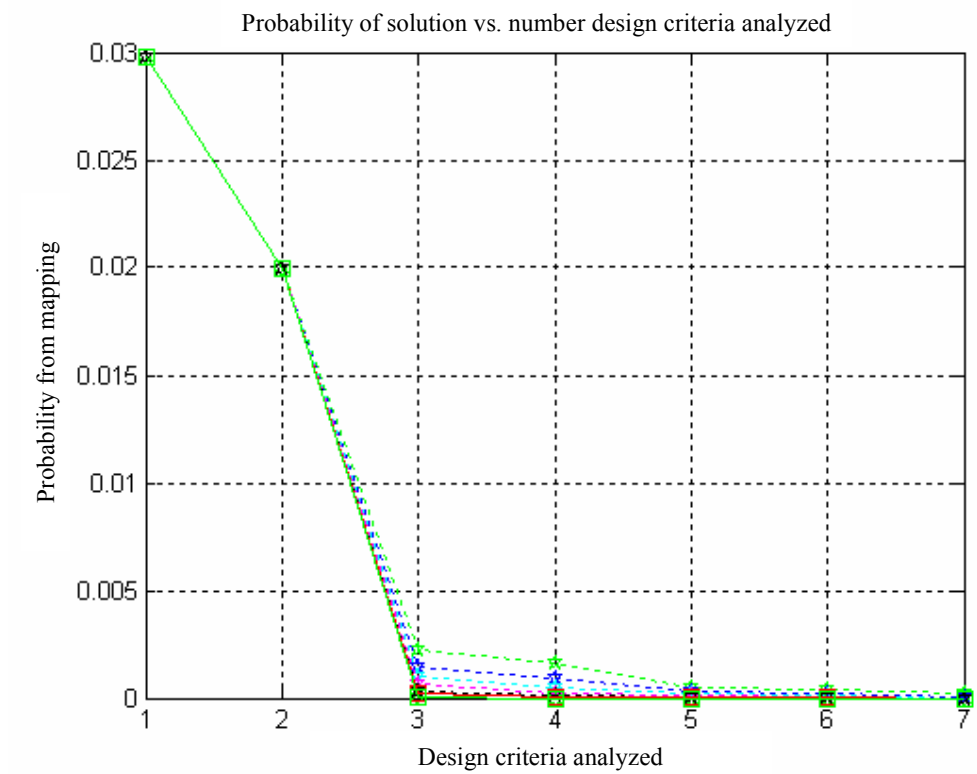
Figure 4.18.   Accumulating probability from the Monte Carlo mapping data as subsequent design criteria are analyzed.

The major result of the probability derived from the Monte Carlo mapping is that its probability correlates directly to the run-length required to find a desired solution to a problem. Figure 4.20 shows the run-length distribution (RLD) for solving the seven different sets of design criteria using a genetic algorithm. The RLD is a cumulative distribution function of the number of iterations, or run-length, required to satisfactorily solve the optimization problem. As is easy to be seen from Figure 4.20, the most probable solutions (in the Monte Carlo probability sense) are solved most quickly and most assuredly. Figure 4.20

106

represents 30 attempts to solve for each of the seven sets of design criteria with a limit of 5000 iterations each trial. The solution attempts whose RLD goes to one means that every attempt succeeded in finding the desired solution within the specified tolerances for each design criterion. These tolerances are determined by the ranges used to calculate the Monte Carlo probability (see Sections 4.3.2.4 and 4.3.2.5). For instance, if the candidate solution produces all design criteria within their acceptable ranges of $\pm$ 0.2 about the desired value, then the candidate solution is considered successful. Note in Figure 4.20, only the trial with the second desired equilibrium as $\theta_{2,eq}$ = 3.2 radians fails to solve the problem at all after 30 attempts of 5000 iterations. Also, the trial with $\theta_{2,eq}$ = 3.1 radians solves the problem satisfactorily about half of the time within 5000 iterations. Thus, one can conclude that there is a definite tendency for problems to become less probable to solve as the Monte Carlo mapping probability goes further from the boundary where $P_{total} > 0$.

In viewing Figure 4.20, it is obvious that a result of $P_{total} = 0$ from the Monte Carlo mapping does not mean a solution does not exist. What it does mean is one of two things: (i) either the desired solution is not possible, or (ii) the solution is possible but lies very near a boundary that separates possible from impossible solutions. As one attempts to obtain solutions further away from those with $P_{total} > 0$, the solution takes longer and soon will become impractical, if not impossible, in terms of the number of iterations required to solve.
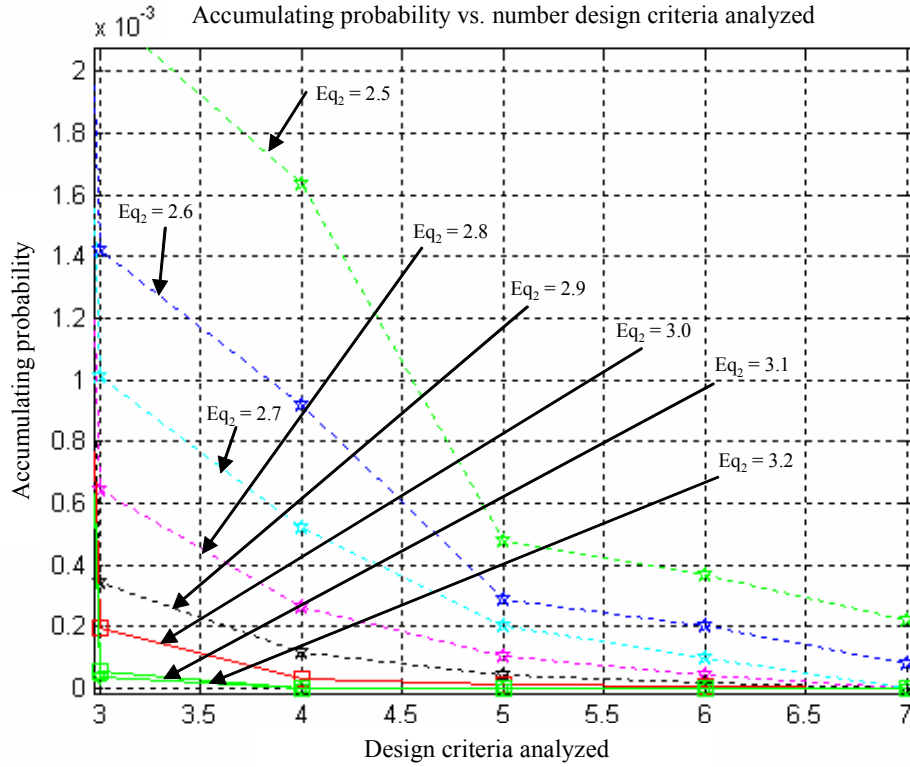
Figure 4.19.   Zoomed view of Figure 4.18.

The characteristic shape of RLDs of Figure 4.20 are fairly typical of results from solving constraint satisfaction problems (CSP) with methods called stochastic local search algorithms [Stützle and Hoos, 1999]. These are also often called Las Vegas algorithms, and their main characteristic is that if a solution exists, they are guaranteed to find it by searching the entire solution space. The CSP is a mathematical problem composed of clausal statements such as "x_1 or not-x_2 or not-x_3." Generally each variable, x_i, can be true or false. There are several variables and clauses, and the task is to find the assignment of truth values

to the variables such that a set of clauses is satisfied. Solving these problems is generally accomplished by branching algorithms which are essentially heuristic search techniques that can search all of the solution space given enough time.

This connection of the CSP with the MSE design problem is not direct since CSPs deal with discrete (values of true or false) instead of continuous design variables. In the CSP, the changing value, say from true to false, of one variable can make a satisfiable problem suddenly unsatisfiable. Thus, a defined boundary separating possible from impossible problems is likely not continuous, but the distinction of a solvable problem is obvious: either all constraints (clauses) are satisfied or they or not.

In the MSE design problem, the constraints are not necessarily so easily written or checked, but the concept of a distinct boundary which separates possible from impossible solutions is most certainly locally continuous. This is because MSE systems, as defined in this dissertation, are only composed of energy storage elements with smooth and continuous nonlinearities. So ignoring effects such stiction, backlash, and quantum energy levels removes any possibility for energy storage elements whose energy is not C_1 continuous.

The RLDs from solving 'easy' CSPs often follow the cumulative distribution function of the exponential distribution as their probability goes to one. Sometimes only the beginning of RLD will follow the exponential distribution where the RLD then has a plateau in which very few to no more solutions are found [Stützle and Hoos, 1999]. Other times the RLD rises faster than a best-fit exponential distribution. This has practical significance in choosing

how long to run the optimization routine, and whether or not to use a restarting procedure.

A characteristic of an exponentially distributed random variable, in this case run-length, enables one to determine effective run-lengths to use for solving problems with exponential RLDs. This property is that if a given algorithm has an exponential RLD, then the probability of finding a solution by running the algorithm n times for time t is the same as when running the algorithm once for time nt [Stützle and Hoos, 1999]. Even if the RLD is not sufficiently exponentially distributed, it still gives information on the speed, or ease, at which the problem is solved. *This information leads to coming up with a rationale for deciding how much effort to spend in solving a problem with $P_{total} = 0$.* This determination of 'effort' is the most important purpose of the Monte Carlo mapping method, and by relating it to the Monte Carlo probability, it is algorithm independent (although any RLD is algorithm dependent). By using both the Monte Carlo probability and the RLD concept, one can characterize the boundary that divides existent MSE solutions from the nonexistent.
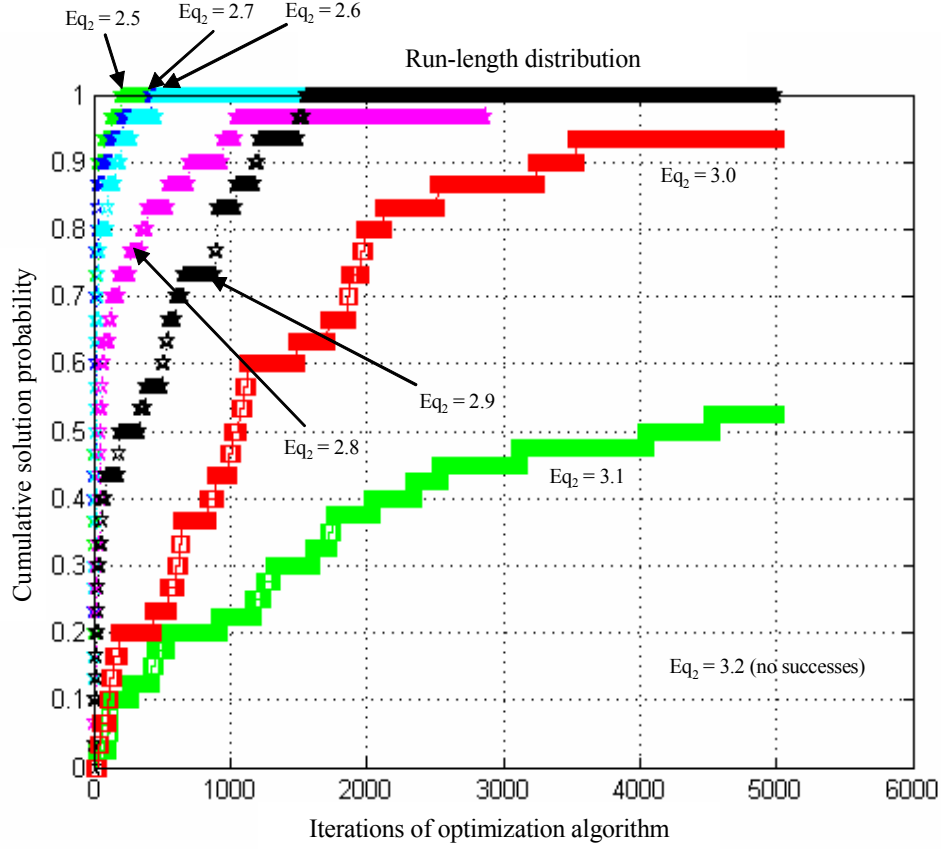
Figure 4.20.   RLD of the eight different desired solutions with probabilities shown in Figures 4.17 - 4.19.

A safe assumption on the minimum run-length for finding the desired solution where $P_{total} = 0$, can be the run length of a nearby perturbed case where $P_{total} > 0$. This is exemplified by Figure 4.20 showing that the RLD increases more slowly as one gets further from the mapping region where $P_{total} > 0$. Thus, from the probability information in the Monte Carlo mapping, one creates a sort of baseline best-case scenario for how long it will take to solve the desired problem. The designer can reasonably expect the RLD of the $P_{total} = 0$ case to be

worse than the incrementally perturbed case where $P_{total} > 0$. By monotonically changing the perturbation of the chosen desired design criteria from a solution space where $P_{total} > 0$ into the region where $P_{total} = 0$, one can obtain RLDs for each perturbed case such as in Figure 4.20.

As one creates the RLD, one of two things will end the search for the solution: (i) the perturbation from the original $P_{total} = 0$ case will be zero and the problem will be solved, or (ii) for some perturbation away from the original $P_{total} = 0$ case, the RLD will become sufficiently long as to influence the designer that too much time is required to solve the problem with the given algorithm and parameters (note the limit on this time is infinity for a problem with no solution). For instance, from Figure 4.20, one can see that a desired solution with θ_2 in the range [2.5, 3.1] radians is easily attained. If one desires a solution with θ_2 near 3.2 radians, one can note that a considerable amount of time (number of iterations or restarts) is required to solve the problem. One can also begin to expect that a solution does not exist and that the topology of the problem must change to pursue the desired solution further. But, a question may still remain as to whether the designer's optimization algorithm is ineffective, or if the desired solution is indeed outside of the possible solution space. Because of the nature of MSE system design being based on energy curves, there is a way to make this determination.

The difference in the use of the RLD for CSPs and MSE problems lies in the goal for each problem. Most of the time, the goal of analyzing CSPs is to test new algorithms and document their effectiveness relative to other algorithms or

the particular branching heuristic used. In the MSE design problem, the type of optimization algorithm used to solve the problem is not of tantamount importance, although an effective algorithm is necessary. What is important is *if* a desired solution can be achieved and how long it might take to achieve it. The investigation of this goal is done by looking at how the shape of the energy curve changes as a desired solution becomes impossible in a region of $P_{total} = 0$ from a region of $P_{total} > 0$.

Consider solving for the three equilibrium positions and frequencies as demonstrated in Figures 4.17 – 4.20. As the second equilibrium position, $\theta_{2,eq}$, is increased, the solution eventually becomes infeasible in the sense that it takes more than 5000 iterations of the genetic algorithm to obtain a solution. In terms of the energy curve shape, what is happening? A pitchfork bifurcation diagram, shown in Figure 4.21, helps explain. It is often used to describe equilibria of a single nonlinear differential equation of one state variable. Often a single parameter is varied that changes the equilibrium locations for the dynamic system. In Figure 4.21, as the parameter λ is increased, one stable equilibrium splits into three equilibria, two stable and one unstable, upon reaching a critical value. In terms of a MSE system, the pitchfork bifurcation can describe the transformation of a local equilibrium (stable or unstable) point. Figure 4.21 can also be viewed going left or right and for the situation in which the stable and unstable locations are switched.
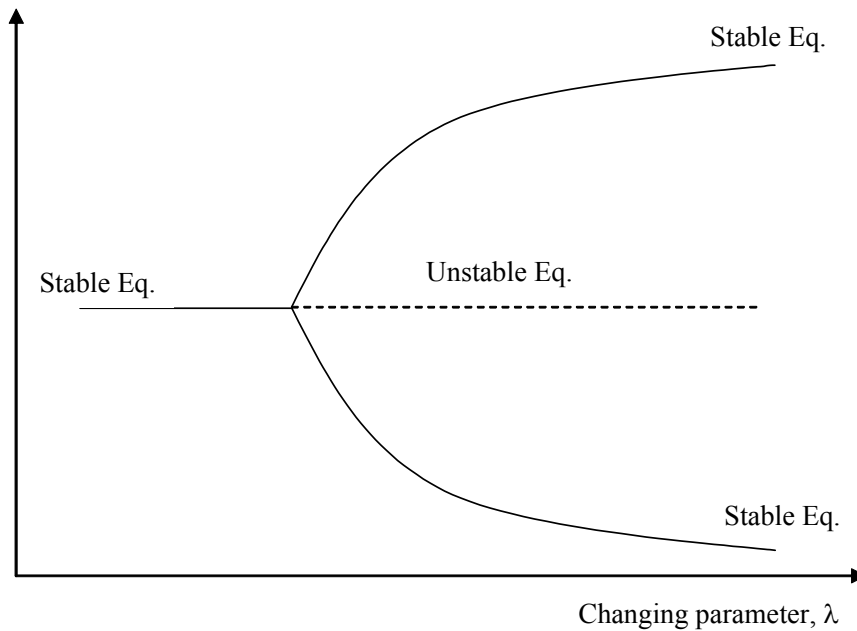
Figure 4.21.   Pitchfork bifurcation diagram showing one stable equilibrium split into two stable and one unstable equilibria as a parameter is varied.

For a dynamic system with one state variable, the equilibria presented in the pitchfork bifurcation diagram are static. For systems with more than one state, one must consider bifurcations of dynamic equilibrium positions as well. Since MSE systems only design static stable positions, only the potential energy curve need be discussed in terms of bifurcating extremal points. This is essentially a limiting case of full dynamic stability where all generalized momenta of the system are zero.

As the MSE system design methodology is described, only the energy of the system need be calculated to perform the design synthesis. Again, the reason for this is to simplify the mathematics for problems with large numbers of

parameters, or design variables. In viewing a bifurcation scenario, the MSE design methodology does not look at varying design variables, but instead at varying a design criterion. This falls in line with the methodology's focus on the desired design criteria (i.e. equilibrium position, frequency, etc.) and not design variables.

Recall again the design case represented in Figures 4.17 - 4.20 that varies the second desired equilibrium position. Upon reaching an infeasible region in the solution space, one 'far' from the region with $P_{total} > 0$, the desired solution with $\theta_{2,eq} = 3.2$ seems no longer possible. As an equilibrium point moves out of a feasible region, this means that it essentially disappears from the energy curve. For visualization purposes, one scenario has three equilibria (two stable and one unstable) converge into one stable point. This situation is as shown in Figure 4.21 for decreasing λ. Here, in the case of the MSE system, the incrementing parameter is not a single system design variable, but instead is a design criterion, $\theta_{2,eq}$. This is fundamentally different than the traditional view of bifurcation analysis. Instead of varying a parameter and solving for the equilibrium point, one can vary the equilibrium point and see if the optimization routine can solve for it while it varies *every* parameter, or design variable.

Figure 4.22 shows a schematic of what one might expect to happen when an equilibrium position becomes no longer valid as its desired value is increased out of its feasible range (from region of $P_{total} > 0$ far into a region of $P_{total} = 0$). The equilibrium, $E_{stable,1}$, has its desired value incrementally increased, and the optimized energy curve must have a slightly different shape to accommodate this change. After the desired value is increased too much, constraints in the problem cause the three equilibria to 'converge' together at the new $E_{unstable,2}$. This phenomenon can be described by using the three main variables that have been the focus of the entire design method: equilibrium position (a), equilibrium energy value (b), and equilibrium curvature (c) (see Equations 4.3 and 4.10).
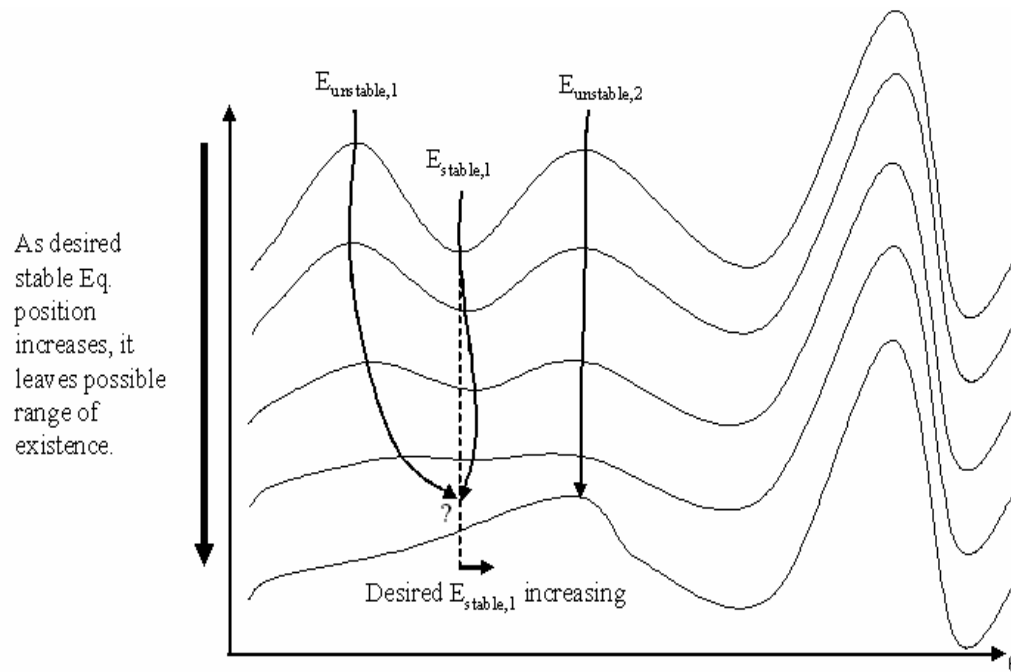
Figure 4.22. Example of equilibrium points converging (reverse bifurcation) as the desired value, $E_{stable,1}$ is increased out of its possible range.

As a design criterion is varied to a value not in the solution space, the equilibrium positions and energy values of some adjacent unstable and stable equilibria *must* become equal as they converge. If they did not become equal, then by definition they could never converge to the same point in the bifurcation diagram. Also, the curvatures of these equilibria approach the same value as the bifurcation point is approached as described in LEMMA 1.

LEMMA 1:   Consider the solution space limit where three adjacent equilibria, two stable and one unstable (two unstable and one stable) converge to one stable (unstable) equilibrium. As a pair, one stable and one unstable, of these three adjacent equilibrium points approach the bifurcation point, they also approach each other. Also, in the limit, they acquire both equal energy value and curvature.

The proof of LEMMA 1 is done by using a cubic polynomial to describe the local energy about two equilibrium points, one stable and one unstable. Just as a quadratic polynomial is the lowest order that can describe one equilibrium position, a cubic polynomial is the lowest order that can describe two adjacent equilibria. Equation (4.26) is the cubic polynomial that describes the local energy about the two equilibria. Other equations of relevance are Equations (4.27 -4.29) which are the first derivative, second derivative (curvature), and equation of the equilibrium points respectively, corresponding to Equation (4.26).

$$E(q) = e_1 q^3 + e_2 q^2 + e_3 q + e_4 \qquad (4.26)$$

$$\frac{dE(q)}{dq} = 3e_1 q^2 + 2e_2 q + e_3 \qquad (4.27)$$

118

$$\frac{d^2 E(q)}{dq^2} = 6e_1 q + 2e_2 \qquad (4.28)$$

$$q_{eq} = \frac{-2e_2 \pm \sqrt{4e_2^2 - 12e_1 e_3}}{6e_1} \qquad (4.29)$$

Equation (4.29) is the solution in setting Equation (4.27) to zero, and solving for the displacement, q. The solution to Equation (4.29) can be two real numbers or a complex conjugate imaginary pair, depending on the coefficients, e_i. This dependence is dictated by the descriminant, terms under the square root, of Equation (4.29). If the descriminant is negative, the solutions are imaginary, and if it is positive, the solutions are real. Imaginary solutions mean the equilibria do not exist in the energy curve, and real solutions mean that they do exist. Repeated roots represent a critical point where the equilibria have converged together. When three equilibria converge into one, as depicted in Figure 4.22, this essentially means that two solutions have 'vanished'. In reality, they have not vanished, but their solution has become imaginary, as dictated by the descriminant of Equation (4.29) going from positive to negative.

During the optimization procedure of the design methodology, one tries to make a candidate energy shape approach the desired energy shape. If the candidate energy curve can approximate the desired energy closely enough, a candidate version of Equation (4.29) produces two real solutions where one is a stable equilibrium and the other an unstable equilibrium. If not, the candidate

energy in the region of interest can only produce imaginary solutions, thus signifying that the solution is not being achieved. This transition from real possible solutions in a region of $P_{total} > 0$ to imaginary solutions in a region of $P_{total} = 0$ must occur as the two desired equilibria of Equations (4.27) and (4.29) approach each other. As they approach each other, by definition their location becomes the same, at which case Equation (4.29) has repeated roots. Since the two equilibria cannot have the same sign in curvature when real, when they become repeated roots they have equal curvature. Also, obviously the repeated roots have the same energy value.

LEMMA 1 is represented in Figure 4.22 by the fact that the energy curve tends to a straight line in the region where the bifurcation is taking place. The reason that $\theta_{stable,2}$ and $\theta_{unstable,2}$ seem to 'disappear', is that their position becomes imaginary. The trend described in LEMMA 1 is exemplified in Figure 4.23 for the optimization solutions represented in Figures 4.17 – 4.22. Pay attention to the solutions that are less probable and have longer RLDs. For these cases the distance between the second stable and second unstable, $(\theta_{unstable,2} - \theta_{stable,2})$, becomes smaller. Also, the energy curve becomes more flat as the energy values of $\theta_{stable,2}$ and $\theta_{unstable,2}$ approach the same value near 0.025 J.
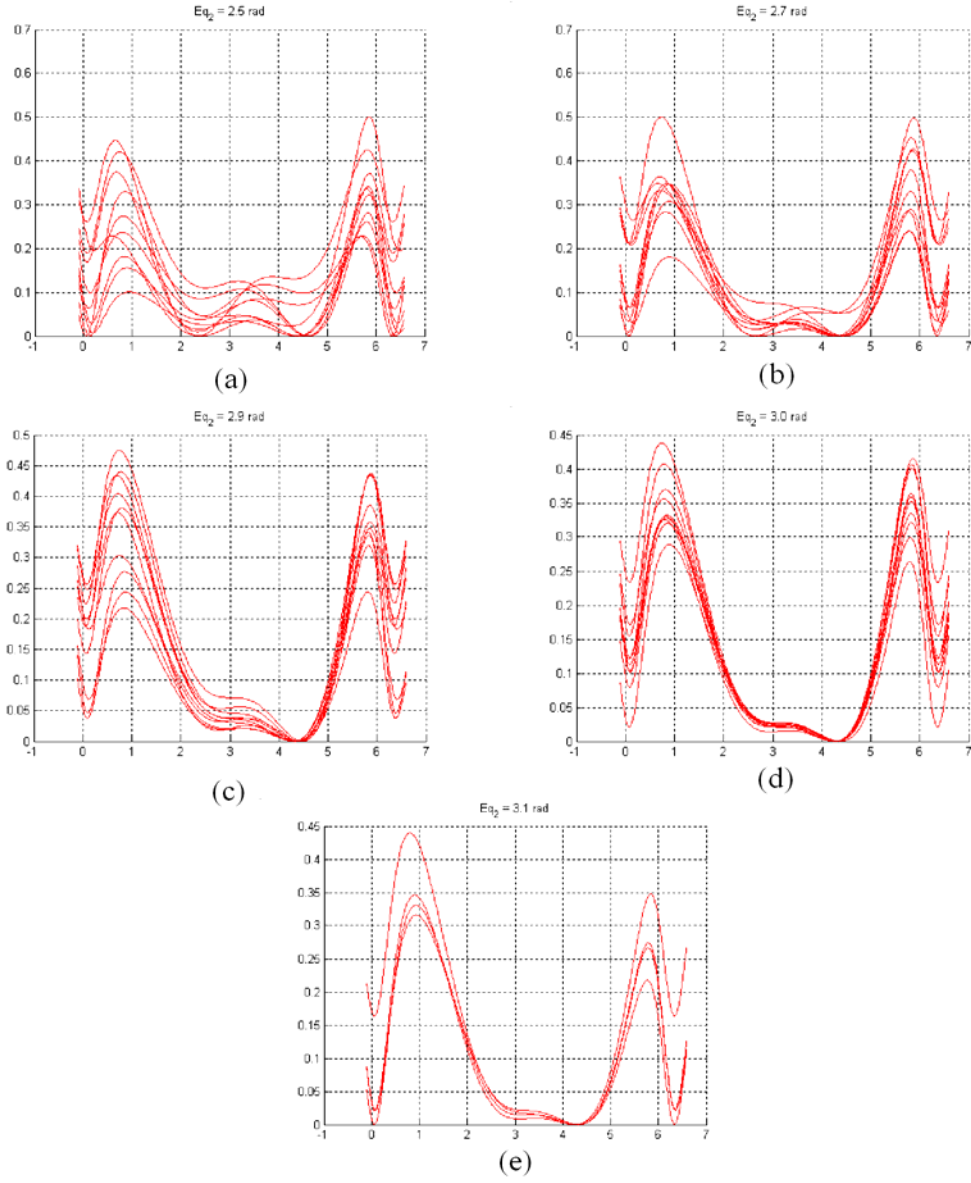
Figure 4.23. Representative energy (in joules) curves that corresponding the RLDs of Figure 4.20 for (a) $\theta_{2,eq} = 2.5$, (b) $\theta_{2,eq} = 2.7$, (c) $\theta_{2,eq} = 2.9$, (d) $\theta_{2,eq} = 3.0$, and (e) $\theta_{2,eq} = 3.1$ radians.

121

The solution trend of a cubic polynomial approximating the local energy of two equilibria leads to a guiding principles to decide if one is indeed trying to solve for a solution which is possible. As discussed previously, the equilibrium positions of the cubic become imaginary when there are no longer two 'humps' in the energy curve, signifying that the equilibria are non-existent in the energy curve. As the cubic goes from real to imaginary solutions, both the equilibrium positions and their energy values approach each other at the transition. Thus, one can use these trends to see the *rate* at which one is approaching an impossible solution space. If one plots the difference in position and energy value for all adjacent equilibria (i.e. stable and unstable pairs), one set will approach zero as the solution leaves the possible solution space. The rate at which these approach zero as one increments the desired solution from a position in the space with P_{total} > 0 to somewhere far into P_{total} = 0 can indicate the boundary between possible solutions and impossible solutions. Figure 4.24 shows this trend corresponding to the plots in Figure 4.23.

In Figure 4.24 (a), the trends of the difference in energy values of adjacent equilibria, $(E_{unstable} - E_{stable}) = (b_{unstable} - b_{stable})$, are plotted for each stable equilibrium position as the desired solution becomes less probable moving to the right. Note there are two values for each stable point, represented by a dot and a plus, since there is an unstable point both to the left and right. Figure 4.24 (b) shows the trend in $(\theta_{unstable} - \theta_{stable}) = (a_{unstable} - a_{stable})$ for each stable equilibrium. As the arrows in Figure 4.24 (a) show, there is a revealing rate of decrease for the

values involving the second and third stable equilibrium. From this Figure and in terms of the bifurcation diagram of Figure 4.21, the three equilibria that are 'converging' to one are $\theta_{stable,2}$, $\theta_{unstable,2}$, and $\theta_{stable,3}$, where the unstable point is between the two stable points. As per the bifurcation diagram, these converge to leave one stable equilibrium in the local region. This is shown in Figure 4.23 as the final equilibrium positions go from $[\theta_{stable,2},\ \theta_{unstable,2},\ \theta_{stable,3}] \rightarrow \theta_{stable,3} = 4.5$ radians.
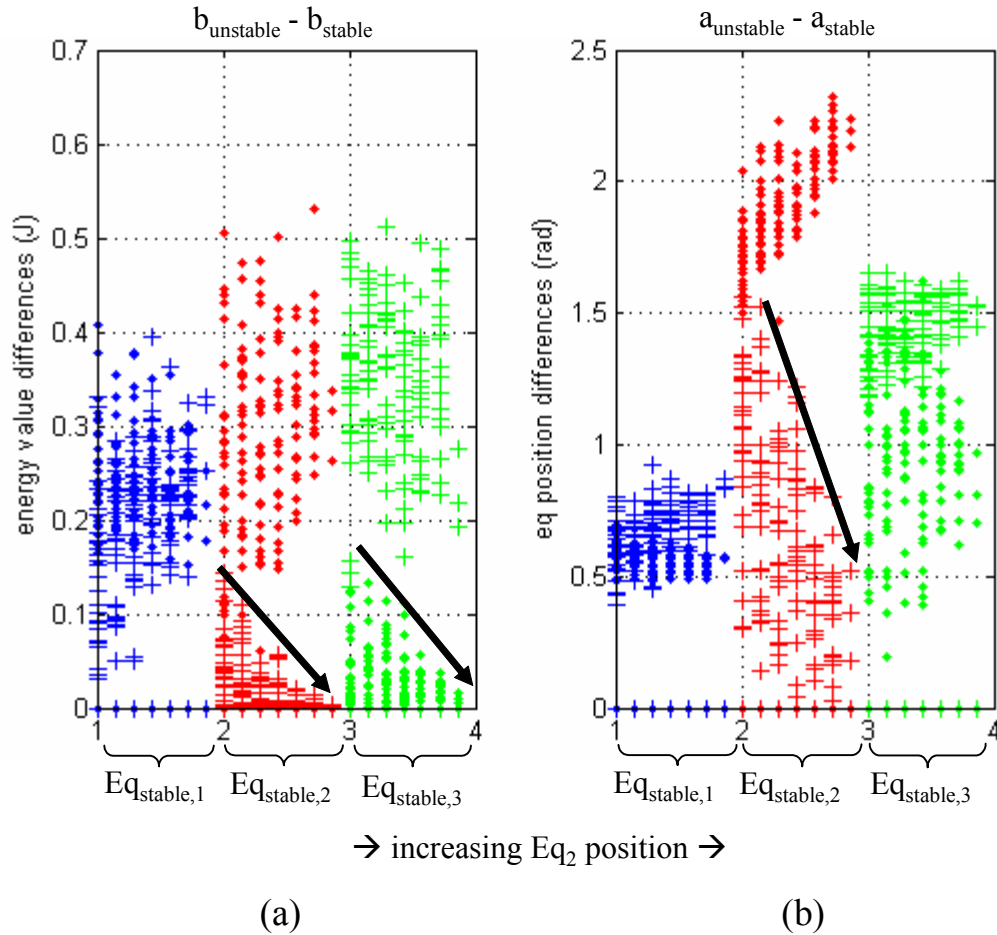
Figure 4.24. As $Eq_{stable,2}$ is increased, and thus the Monte Carlo probability decreases, the difference between stable and unstable energy values (a) goes to zero, as shown by the arrows. Also, (b) shows the tendency of the difference equilibrium position between adjacent equilibria goes to zero.

Figure 4.25 shows the same results, except by plotting the actual energy and equilibrium position values. Figure 4.25(b) clearly shows the perturbed variable, $Eq_{stable,2}$, being increased. Note how $Eq_{unstable,2}$ decreases to converge to the same location as $Eq_{stable,2}$. This is precisely the data that is indicated in Figure

4.24 as the difference between the 2nd stable and unstable points, both in position and energy value, goes to zero.
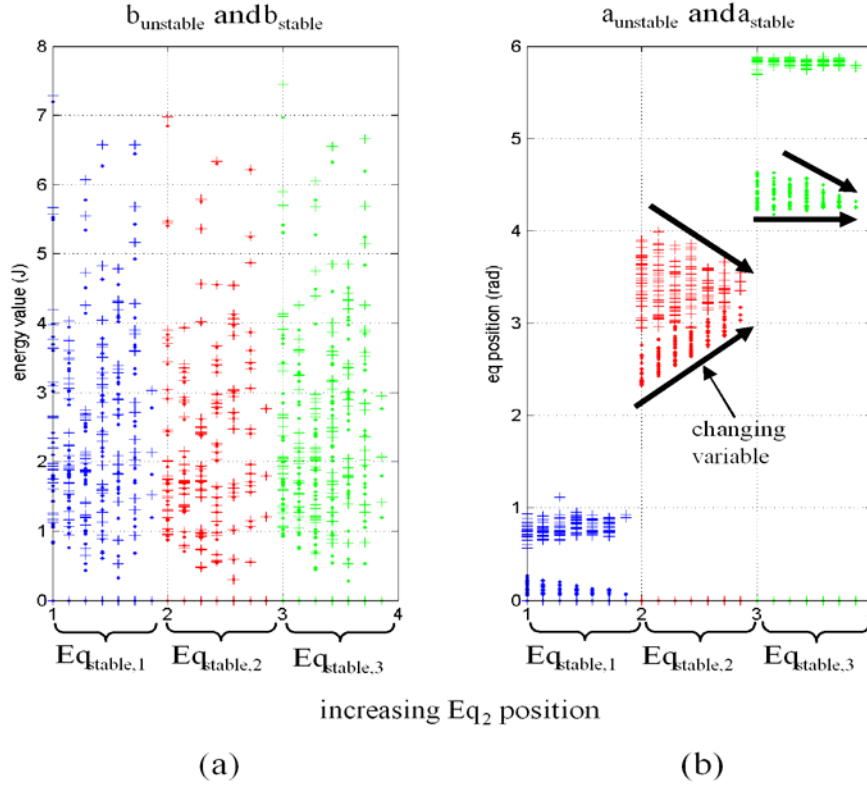
Figure 4.25. Tracking the trends in (a) equilibrium energy value and (b) equilibrium position, as $Eq_{stable,2}$ is increased. Stable and unstable positions are represented by '·' and '+', respectively.

4.3.4 Mapping in multiple degree of freedom systems

Expanding the mapping procedure to systems with more than one kinematic degree of freedom is straightforward by following the previously

described approach. There is more computational effort required due to the need to search for equilibrium points in multidimensional spaces. Remember, the equilibrium points in the energy 'surface' must be found first before curve fitting and logging the second order coefficients as parameters characterizing the equilibrium points. Thus, more time and data storage are required as the degrees of freedom increase. The determination of equilibrium points is done following the procedure outlined earlier in Section 4.2.5.

Now the quantitative mapping method using the conditional *PDFs* becomes even more useful. An additional degree of freedom provides no difficulty in analyzing the data. It simply becomes another variable in the analysis that can be represented by a *PDF*.

4.4 SUMMARY OF DESIGN SYNTHESIS METHODOLOGY

This chapter discusses all implications of synthesizing MSE systems. It begins with a discussion of the philosophy behind the design process. Then the mathematical foundation, based on mechanical stability theory, is derived and put into a form which is useful for numerical optimization. A Monte Carlo mapping method provides a way to 'visualize' the possible solution space. This mapping is discussed in both a qualitative and quantitative way, such that MSE problems of any size (number of design variables or degrees of freedom) can be designed given that the energy of all energy storage elements can be calculated. The chapter concluded with a discussion pertaining to determining the existence or nonexistence of solutions.

CHAPTER 5: CASE STUDIES AND EXPERIMENTAL RESULTS

5.1 DESCRIPTION OF CHAPTER CONTENTS

This chapter describes results of using the design methodology of Chapter 4, and some experimental results of example MSE systems. Section 5.2 describes a purely computational case study of a four-bar linkage problem. The problem is a great problem for study because of its high nonlinearity yet well-understood kinematics and energy storage. Section 5.3 discusses some experimental results on a problem that involves a pendulum, springs, and permanent magnets to create multiple stable equilibrium points. This problem is mostly concerned with validating the design methodology in terms of its approximations of stable frequency and position. The benefit of analyzing the problem in Section 5.3 is that it is intuitive and gives confidence for the use of the methodology. Finally, Section 5.4 discusses a problem that has two kinematic degrees of freedom. The problem is inspired by the concept of making a fish change its length and have a different natural frequency at each length. Thus, the two degrees of freedom are length and rotational angle. This problem is composed of an "x-shaped" linkage structure that changes length, and the stable lengths are determined by the energy change between permanent magnets located on the system.

5.2 FOUR-BAR LINKAGE CASE STUDY

The sample synthesis problem is that of a four bar linkage with linear springs attached to the links of the mechanism (see Figure 5.1). The linkage is assumed a Grashof mechanism, or Class I linkage, throughout the entire discussion [Erdman, et al., 2001]. Thus the linkage is sized such that the input crank (link I) can fully rotate 360°. The linear translational springs are the only energy storage elements. Although the springs are linear, the linkage provides the nonlinear motion that enables multiple stable equilibria. Kinematically this is a one degree of freedom system described by the input crank angle, θ.

The goal of the synthesis problem is to determine a combination of the following design variables: the spring constants (k_i), and free lengths (lo_i) of the eight springs, the locations of anchors for the springs fixed to the ground (x_1, x_2, y_1, and y_2), and link lengths such that the MSE system has desired equilibrium properties for each equilibrium position, θ, stable or unstable. The problem is solved in two solution scenarios: Problem 1 of Section 5.2.1 assumes the link lengths and spring anchors (x_1, x_2, y_1, and y_2) are fixed, and Problem 2 of Section 5.2.2 allows those characteristics to become design variables during optimization.

128
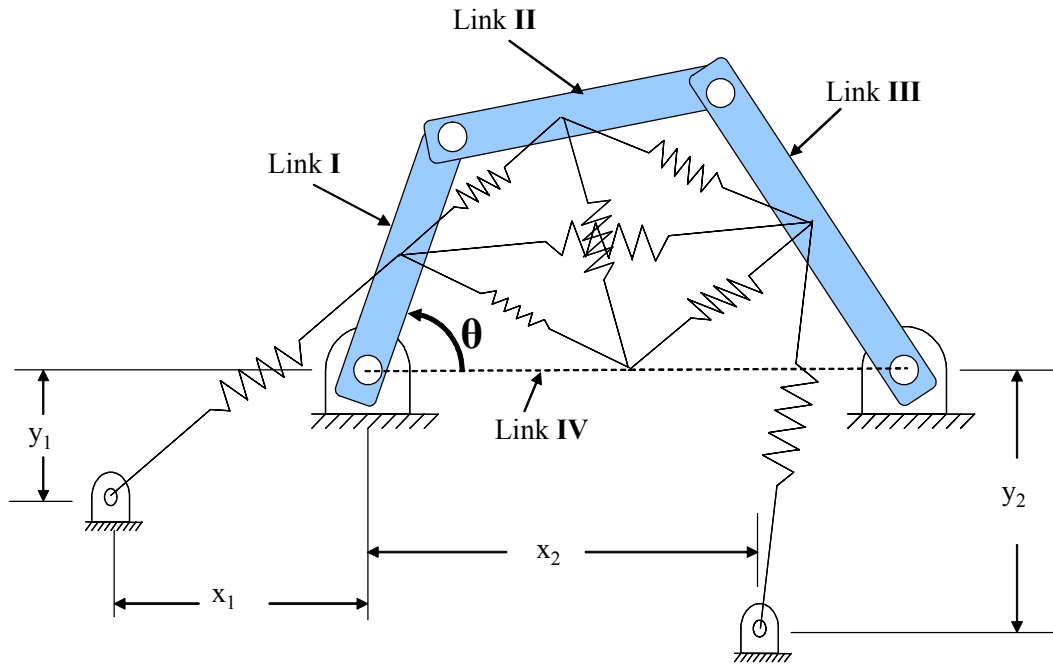
Figure 5.1. The case study consists of a four-bar linkage with eight linear springs connected as shown in the figure.

More formally, a description of the synthesis problem is to design the MSE linkage system to meet any combination of the following objectives:

1) stable equilibrium at θ_n, $n = 1, 2, \ldots$
2) natural frequency $\omega_{n,n} = f_n$ at stable equilibrium θ_n, $n = 1, 2, \ldots$
3) unstable equilibrium at θ_m, $m = 1, 2, \ldots$
4) curvature at unstable equilibrium θ_m, $m = 1, 2, \ldots$
5) certain difference in energy between equilibria,
    $\Delta E = E_{stable,n} - E_{unstable,m}$ $n, m = 1, 2, \ldots$

The potential energy of the system is the summation of the eight spring energies:

$$E(\theta) = \sum_{i=1}^{8} \frac{1}{2} k_i \left(l_i(\theta) - lo_i \right)^2 \qquad (5.1)$$

where k_i and lo_i are the spring constant and free length for spring 'i' respectively, and $l_i(\theta)$ is the length of spring 'i' as a function of θ. Writing out the full expression for the energy in the system as an explicit function of θ involves many trigonometric functions needed to determine the link positions of a four bar linkage. Theoretically, one could take the full energy expression, $E(\theta)$ of Equation (5.1), and solve for design variables that satisfy the set of Equations (4.1) and (4.2). But in practice, the mathematics is unwieldy and forces one to consider the many imaginary as well as real solutions without the guarantee of a real solution existing. Because of this, we use the design synthesis methodology of Chapter 4 that involves numerical optimization and mapping information from the system potential energy.

5.2.1 Problem 1: Linkage link lengths are fixed

The first example problem is now described. The subsections of this section correspond to the basic design steps of Section 4.3 in Chapter 4.

5.2.1.1 Step 1: Decide on important Engineering Characteristics of each Equilibrium

Solving the linkage problem with fixed link lengths corresponds to a scenario in which the linkage has previously been designed to go through certain coupler positions or to have a desired coupler curve. Thus, changing the lengths of the links is not a design option, since differing link lengths would cause new kinematics that differ from the already desired kinematics. Since the kinematics are predetermined, solving for equilibrium positions (θ) is a feasible design goal given that one may have certain linkage orientations that need be stable. One can also meaningfully synthesize the frequency, curvature and energy value at each equilibrium. In this problem it is also assumed that the links have a fixed linear density (and thus mass and rotational inertia), and that the springs attached at positions (x_1, y_1) and (x_2, y_2) are fixed.

Thus, the purpose of this MSE synthesis problem is defined as creating a desired number of stable equilibrium positions with prescribed locations and natural frequencies. Formally, we can describe the optimization problem as follows:

$$\min F(k_i,\, lo_i) \qquad i = 1, 2, \ldots, 8$$

s.t.
1) $k_i,\, lo_i \geq 0$, - spring constants and free lengths positive
2) $k_i < k_{max}$, - spring constants below some maximum
3) $lo_i < lo_{max}$, - free lengths below some maximum

The performance index, $F(k_i, lo_i)$, used for this problem is arranged as described in Chapter 4, Section 4.3.2.5. There is a desired set of solution criteria along with an acceptable range about each desired criteria. For Problem 1, the desired solution criteria are the (1) stable equilibrium positions, $\theta_{des,stable}$, (2) respective natural frequencies, $f_{n,des}$, and (3) unstable equilibrium curvatures for three stable equilibria, or a tristable design. The performance index is specified in Equation (5.2) for the three desired stable and unstable equilibrium positions in this example.

For the equilibrium positions, a:

$$F_a = \sum_{i=1}^{3} \left(\begin{array}{l} w_{a,i}\left(a_{cand,i} - a_{des,i}\right) \text{if } a_{cand,i} > a_{des,i} \text{ and } a_{cand,i} > \left(a_{des,i} + \delta a_i\right), 0 \text{ otherwise} \\ w_{a,i}\left(a_{des,i} - a_{cand,i}\right) \text{if } a_{cand,i} < a_{des,i} \text{ and } a_{cand,i} < \left(a_{des,i} - \delta a_i\right), 0 \text{ otherwise} \end{array} \right)$$

(5.2)

For the unstable curvatures and stable natural frequencies (converted to energy curvature), c:

$$F_c = \sum_{i=1}^{3} \left(\begin{array}{l} w_{c,i}\left(c_{cand,i} - c_{des,i}\right) \text{if } c_{cand,i} > c_{des,i} \text{ and } c_{cand,i} > \left(c_{des,i} + \delta c_i\right), 0 \text{ otherwise} \\ w_{c,i}\left(c_{des,i} - c_{cand,i}\right) \text{if } c_{cand,i} < c_{des,i} \text{ and } c_{cand,i} < \left(c_{des,i} - \delta c_i\right), 0 \text{ otherwise} \end{array} \right)$$

$$F = F_a + F_c$$

From Equation (5.2), if $F = 0$, then the performance index has reached the minimum, and the desired solution criteria have been attained. Notice that the Equation (5.2) uses the energy curvature, c, and not the natural frequency. The reasoning for this is to keep the correct sign of the performance measure as discussed in Section 4.2.3.1 of Chapter 4. The conversion of desired natural frequency to desired curvature is shown in Equation (4.12) of that Section 4.2.3.1.

The performance index weightings for this problem were set equal at $w_{a,i} = w_{c,i} =$ 10.

5.2.1.2 Step 2: Monte Carlo mapping and probability calculation

For the solution demonstration, the following fixed design parameters were chosen: $l_I = 0.7$, $l_{II} = 0.9$, $l_{III} = 1.6$, and $l_{IV} = 1.7$ for the link lengths and $x_1 = 1.9$, $y_1 = -0.7$, $x_2 = 0.2$, and $y_2 = -0.7$, all in meters. The maximum values for the design variables are $k_{max} = 3.0$ N/m and $lo_{max} = 2.0$ m, and the minimum values are $k_{min} = lo_{min} = 0.0$ m. The linear density of the links is 1 kg/m, to produce the following link masses and mass inertias about the center of mass: $m_I = 0.7$ kg, $m_{II} = 0.9$ kg, $m_{III} = 1.6$ kg, $I_I = 0.0286$ kg*m^2, $I_{II} = 0.0607$ kg*m^2, and $I_{II} = 0.3413$ kg*m^2.

A Monte Carlo simulation was performed using 20,000 random iterations of the design variables. For all energy curve-fitting involved in this problem, the number of data points used is five, and the data points are equally spaced with respect to θ every 0.01 radians. The mapping representing the 823 tristable designs is shown in Figure 5.2. There were no generated energy curves that had more than three stable equilibria. Notice from Figure 5.2 what combinations of solutions are probable. For instance, in the mappings of Figure 5.2 one can notice the pattern of where the stable equilibria are likely to be. In Figure 5.2 the three equilibria are represented by a '•', '+', and 'o'. As shown in Figure 5.2c, the stable equilibria tend to be in three basic regions of crank angle: (-0.3, .7), (0.9,

3.1), and (3.7, 5.6) radians. Notice that the θ position -0.3 rad = 5.98 rad due to the ability of the input crank to fully rotate 2π radians.
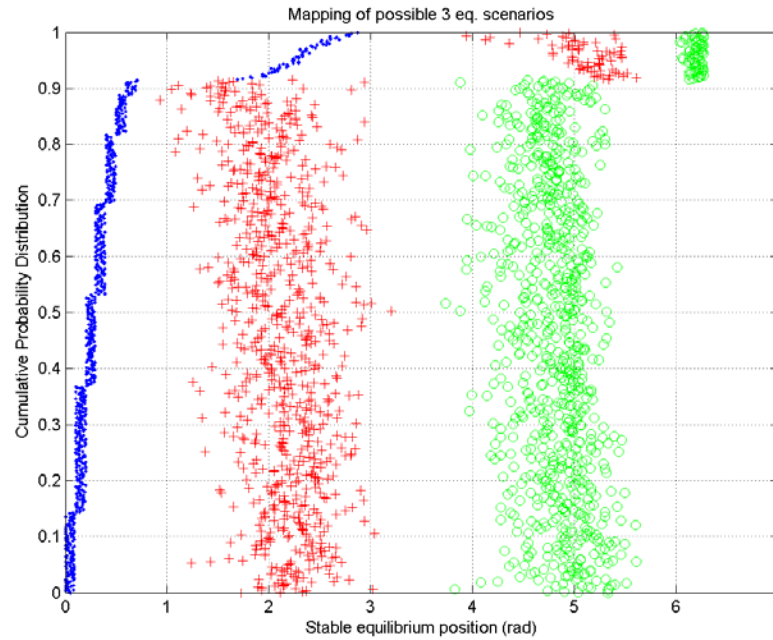
Figure 5.2. Mappings represented by cumulative distribution functions showing the possible locations of stable equilibrium positions in terms of the input crank angle (x-axis).

Note that in producing Figure 5.2 the results were sorted to produce a pattern in which the lowest equilibrium value (represented by '●') is monotonically increasing along the x-axis. The y-axis represents the relative frequency of occurrence, or the cumulative probability that the lowest equilibrium

value will occur. The data for the second and third stable equilibria are not arranged in any further order. This arrangement of the first stable equilibrium position is in the form of a cumulative distribution function to better visualize the results.

Figure 5.3 is a mapping of the natural frequencies at each stable equilibrium position and energy curvatures at each unstable equilibrium for the same Monte Carlo data represented in Figure 5.2. Note for every data point in Figure 5.2, there is a corresponding positive point in Figure 5.3 that shows what natural frequency occurs at that equilibrium point. The first, second, and third stable equilibrium positions are again represented by '•', '+', and 'o' respectively. The unstable points are all represented by dots and distinguished by being negative.
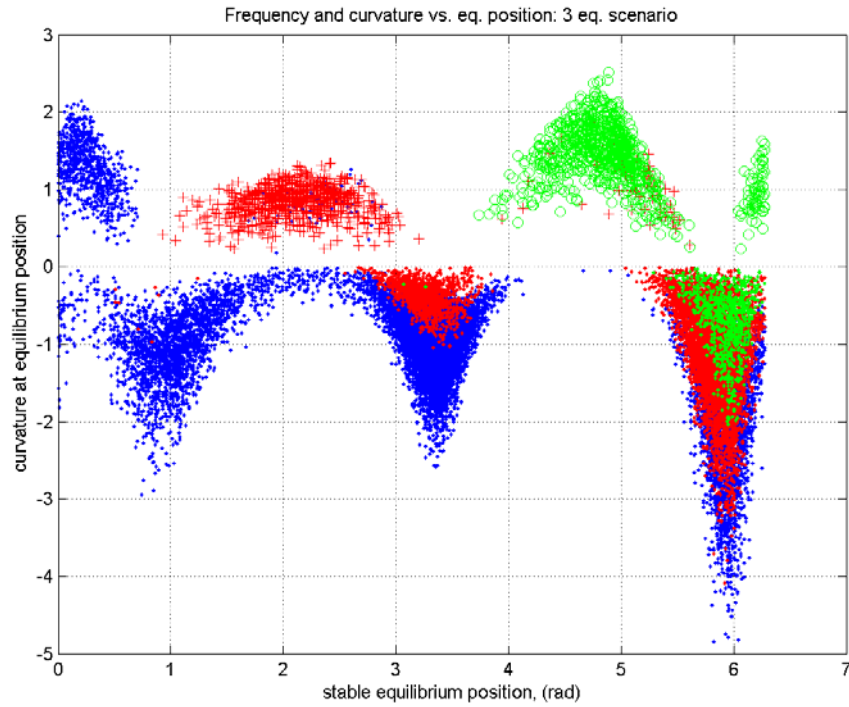
Figure 5.3. Natural frequency (stable) and curvature (unstable) versus equilibrium position for the tristable Monte Carlo results. Note how each equilibrium region has a limited range of frequencies.

From looking at the mappings of Figures 5.2 and 5.3, the desired design criteria were chosen. The goal is to choose three stable equilibria with similar natural frequencies, while maximizing the magnitude of the energy curvature at the unstable equilibria. Because the spring torque on the linkage is the first derivative of the energy, maximizing unstable curvature magnitude creates a system with maximum force necessary to move from one stable position to the next. The desired design criteria are specified as follows:

(1) stable equilibria at $\theta_{des,stable}$= [0.4, 2.3, 4.8]   radians,

(2) natural frequencies f_n = [1.6, 1.0, 1.5] rad/s, and

(3) maximum curvature magnitude at unstable equilibria, J/rad^2.

The first set of desired design criteria (i.e. unstable curvature values with constant stable equilibrium properties) were chosen such that the calculated Monte Carlo probability was greater than zero. Then the unstable energy curvatures are increased until the solution is no longer possible. The goal of the problem is then to determine the maximum unstable curvature magnitudes where they are all the same value.

In choosing the desired unstable curvature values, they were altered and lowered until the Monte Carlo probability was greater than zero signifying a solution guaranteed to exist. The curvature values were then subsequently perturbed in the negative direction, but increasing magnitude, and the problem was optimized to track the results.

The desired solution criteria sets optimized for are shown in Table 5.1. The last column shows the calculated Monte Carlo probability values. Thus, one expects to easily solve trials 1-3 since they are guaranteed to exist. As the solution is perturbed further from the solution of Trial 1, the limiting pattern from the optimization results will show the maximum unstable curvature magnitudes that are possible.

Trial set	θ_{stable} (rad)	$f_{n,stable}$ (rad/s)	$c_{unstable}$	P_{tot}
1	[0.4, 2.3, 4.8]	[1.6, 1.0, 1.5]	[-0.4, -0.4, -0.8]	4.2e-4
2	[0.4, 2.3, 4.8]	[1.6, 1.0, 1.5]	[-0.5, -0.5, -0.8]	5.0e-4
3	[0.4, 2.3, 4.8]	[1.6, 1.0, 1.5]	[-0.6, -0.6, -0.8]	4.4e-4
4	[0.4, 2.3, 4.8]	[1.6, 1.0, 1.5]	[-0.7, -0.7, -0.8]	0
5	[0.4, 2.3, 4.8]	[1.6, 1.0, 1.5]	[-0.8, -0.8, -0.8]	0
6	[0.4, 2.3, 4.8]	[1.6, 1.0, 1.5]	[-0.9, -0.9, -0.9]	0
7	[0.4, 2.3, 4.8]	[1.6, 1.0, 1.5]	[-1.0, -1.0, -1.0]	0
8	[0.4, 2.3, 4.8]	[1.6, 1.0, 1.5]	[-1.1, -1.1, -1.1]	0

Table 5.1. Trial sets of desired design criteria with corresponding Monte Carlo probability.

5.2.1.3 Step 3: Optimization and interpretation of results

This section first describes why the solution space is multi-modal and why a stochastic optimization approach is needed for this problem. Figure 5.4 shows the inherent nature of the optimization problem by plotting the length of a typical spring as a function of input crank angle, θ. The y-axis also can represent the free length of the spring, lo, increasing from zero to one. If this is the only spring in the system, the equilibria reside where lo is closest in length to the actual spring length. In other words, the energy in the system is $E(\theta)=(1/2)k(l(\theta)-lo)^2$, and this energy is minimized/maximized when $dE/d\theta= k(l(\theta)-lo)(dl(\theta)/d\theta)=0$. Thus, if at any θ $lo=l(\theta)$, then that θ represents a stable position. If the condition $lo=l(\theta)$ is not met, then the equilibria lie at the θ where $dl(\theta)/d\theta=0$ which is where the spring reaches a minimal or maximal length.
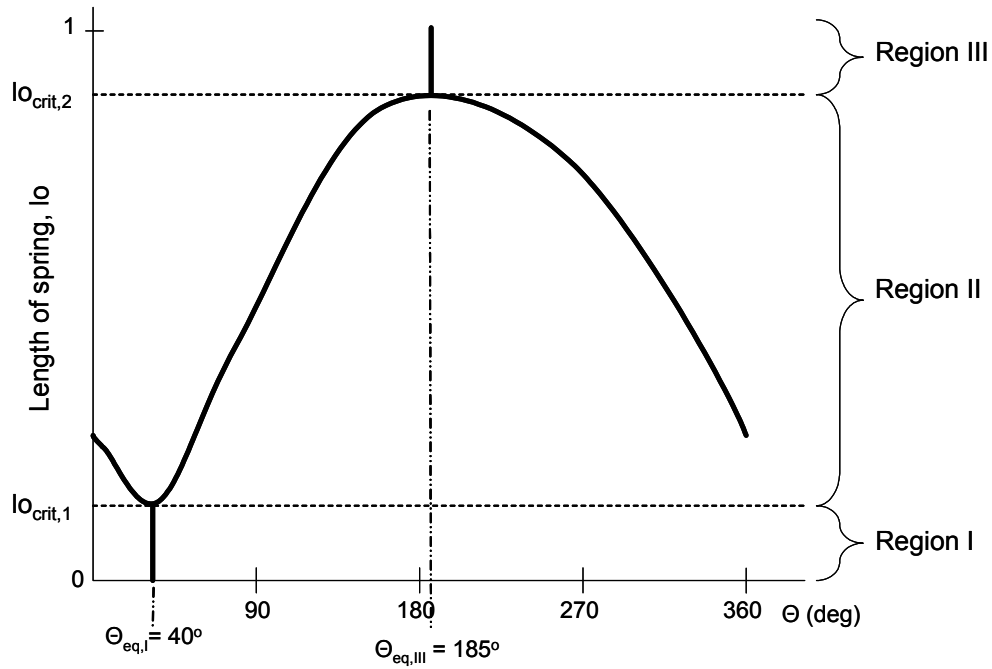
Figure 5.4. For only one spring, a plot of the spring length versus θ shows how the choices of the spring free length can determine where the stable equilibria lie.

In Figure 5.4, one can see that as lo increases from 0 to 1, the stable equilibria bifurcate from one region to the next. In Region I, $lo \neq l(\theta)$, $dl(\theta)/d\theta=0$, and the stable equilibrium is $\theta_{eq,I} = 40^o$. Then, in Region II, since $lo_{crit,I} < lo < lo_{crit,2}$, and the condition $lo=l(\theta)$ is met. Also, the one stable equilibrium becomes two and the former stable equilibrium at $\theta_{eq,I} = 40^o$, becomes unstable. Finally, when $lo>lo_{crit,2}$ in Region III, the two stable equilibria merge back into only one stable equilibrium at $\theta_{eq,III} = 185^o$ and again $dl(\theta)/d\theta=0$.

This bifurcating nature of the linkage problem is typical of MSE systems and poses inherent difficulties for gradient-based optimization methods. For example, in Region I, $lo<lo_{crit,I}$ and the derivative of the equilibrium position with

139

respect to the design variable *lo* (i.e. d*F*/d*lo* = d/d*lo*{(a_{des}- a_{cand})^2} = 0) will be zero, and the optimization algorithm will have no viable information for choosing a search direction.

Because of reasons mentioned regarding the bifurcation of equilibrium solutions and the lack of meaningful gradient information, the problem necessitates a stochastic optimization approach. In this section, results from both a genetic algorithm [Houck, et al.] and adaptive simulating annealing [Ingber, 1989] are compared with respect to themselves and the desired solution. The parameters used in each optimization code are kept constant for every trial in Table 5.1. The values of the optimization tuning parameters are not extremely important for demonstrating the MSE synthesis design method. One simply needs a set of parameters that effectively solves an MSE problem for a solution that exists with probability of one. Then keeping the parameters constant as the solution is perturbed to those with lower probabilities gives one a baseline to compare the solution performance for harder solutions.

Figures 5.5 and 5.6 show the run-length distributions (RLD) for solving each trial of Table 5.1 ten times using the genetic algorithm and adaptive simulated annealing (ASA), respectively. The maximum number of generations used in the genetic algorithm is 2500, and the maximum number of iterations in ASA is 15,000. Each of these maximum limits is two orders of magnitude more than the number of generations/iterations needed to solve Trial 1.
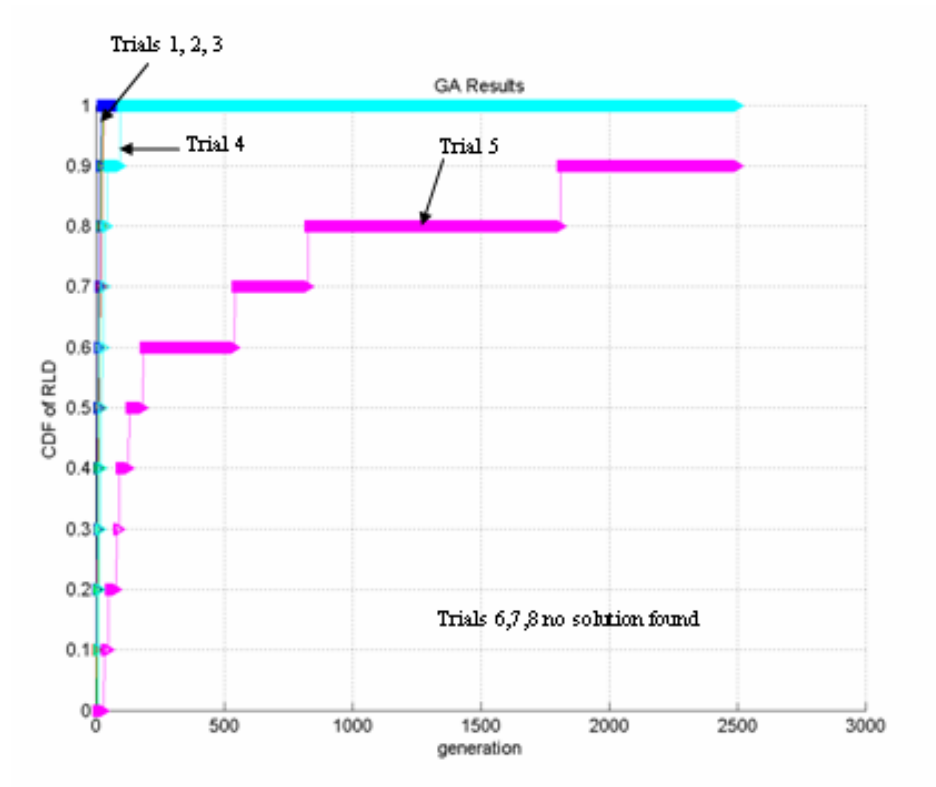
Figure 5.5. RLD for solving Problem 1 using a genetic algorithm. Trials 6-8 did not find a solution.
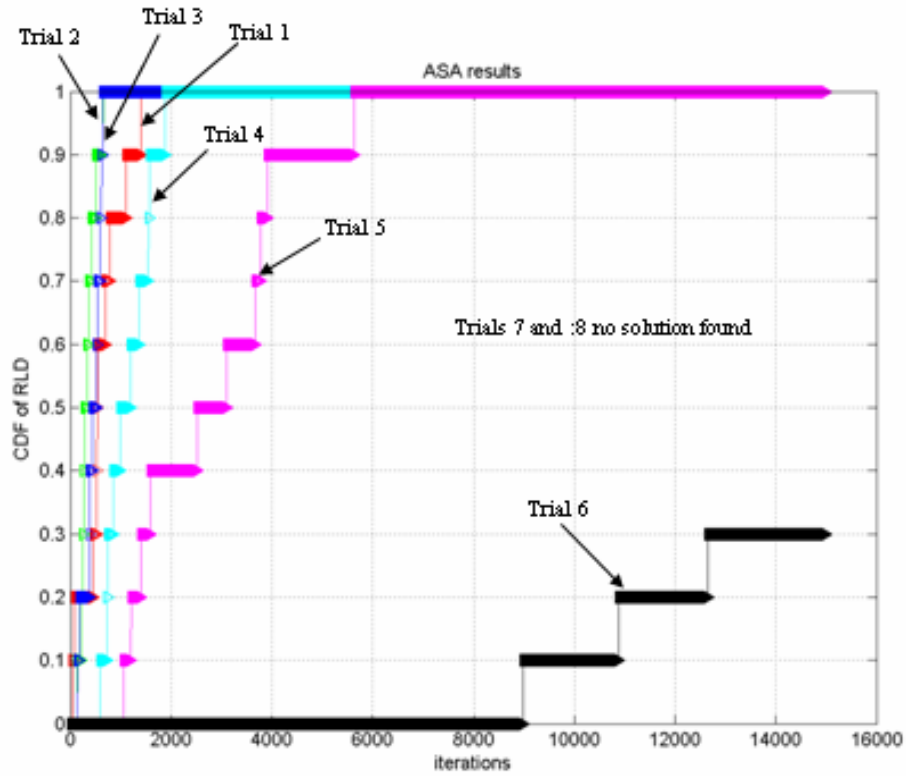
Figure 5.6 RLD for solving Problem 1 using adaptive simulated annealing. Trials 6-8 did not find a solution.

In viewing Figures 5.5 and 5.6, one can see some similarity in form between the two sets of RLDs even though they are generated using completely different algorithms. Thus, the strength of the design synthesis methodology in being somewhat algorithm independent (for algorithms with some stochastic nature) is evident here. Both Figures 5.5 and 5.6 show Trials 1-3 having very similar relatively short solution run-lengths. Also, both show a distinguishable run-length increase from Trial 3 to Trial 4, and from Trial 4 to Trial 5. Neither

142

algorithm was able to solve Trials 7-8. The only major difference is that ASA could successfully solve for Trial 6 whereas the genetic algorithm could not. In general, the RLDs lead one to believe that for the desired stable equilibrium locations and frequencies in Table 1, the maximum unstable curvature attainable for all unstable points is somewhere between −0.9 and −1.0, with the acceptable difference of ±0.2 J/rad^2 specified in the problem statement.

Recall from Section 4.3.3.2 of Chapter 4 that one can further investigate if the limiting boundary between possible and impossible solutions has indeed been found by tracking the trends in the equilibrium properties. In that section the highlighted trends were the distances between equilibrium points and the differences in energy value between stable and unstable points (see Figure 4.23). This information in Figure 4.23 was also corroborated in Figure 4.24 by plotting the trends of the actual equilibrium energy and position values.

In this Problem 1, the perturbed desired quantity is the unstable equilibrium curvature, as its value is decreased for all unstable points in general. Figure 5.7 shows the equilibrium property trends as these desired properties are perturbed. Figure 5.7(c) shows most clearly how a boundary of feasible solutions has been reached. The dotted lines represent the acceptable range for the desired design criteria, which is ± 0.2 rad/s for the frequency and ± 0.2 J/rad^2 for the unstable curvature. The frequencies are held constant, and thus their range has no slope whereas the unstable curvature range is decreased for each trial, and thus has a negative slope. The solid arrows in Figure 5.7 highlight the properties of the energy curve that reach limiting values. In Figure 5.7(b), the second stable

143

equilibrium position reaches its lower limiting value near 2.1 radians. In Figure 5.7(c), both the frequencies for second and third stable positions, but most clearly the third position, converge to the maximum possible limit. For the third frequency, this value is 1.7 rad/s. Thus, if one desires the equilibrium curvatures to be further reduced, a likely constraint that needs to be relaxed is the upper bound on the frequency for the third stable position.

Figure 5.7 confirms what the RLD of Figure 5.5 shows: that a local boundary in the feasible solution space has indeed been reached. Figure 5.8 shows the same equilibrium trends as Figure 5.7, except using the results from the ASA algorithm. The plots of Figure 5.7 and 5.8 look practically identical giving high confidence that the local boundary to the solution space has indeed been found.
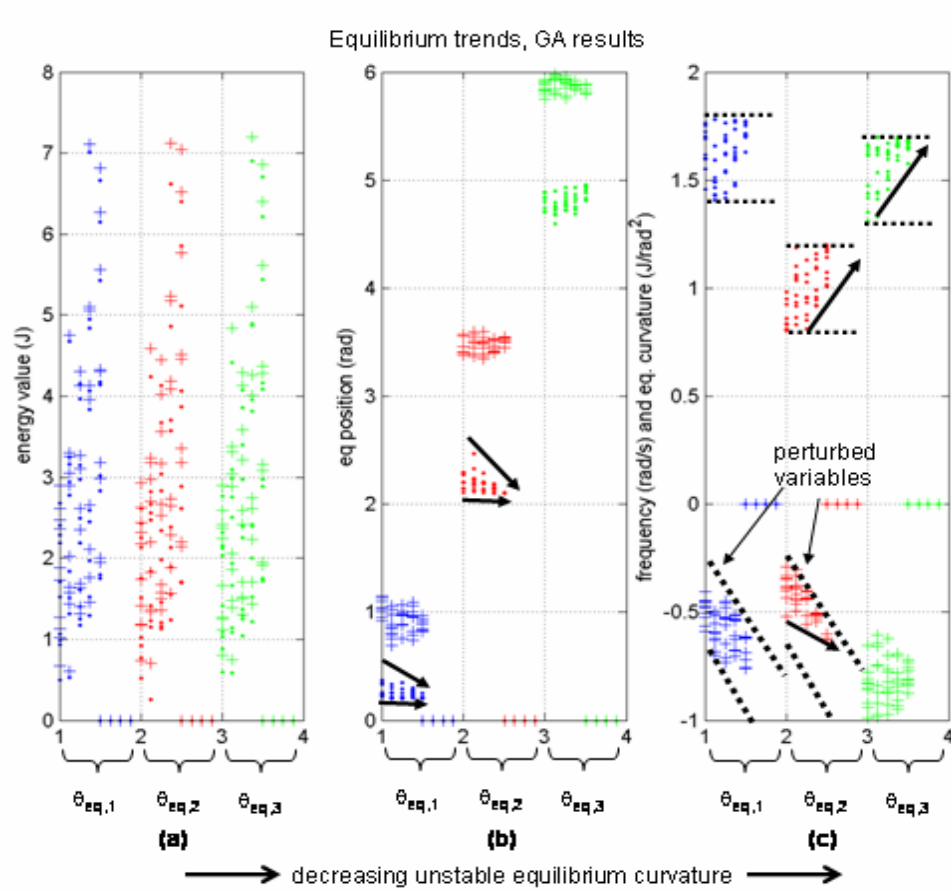
Figure 5.7. Equilibrium trends from solving Problem 1 using the genetic algorithm: (a) energy values, (b) equilibrium position, and (c) stable equilibrium frequency and unstable equilibrium curvature. In all graphs, stable and unstable points are represented by '·' and '+', respectively.
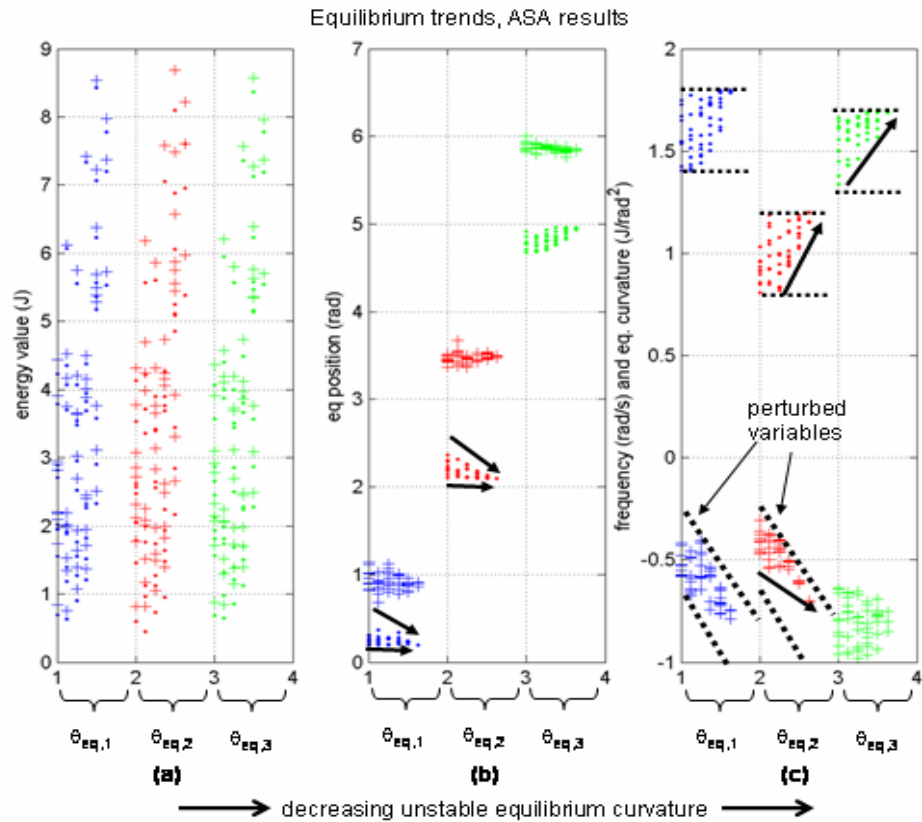
Figure 5.8. Equilibrium trends from solving Problem 1 using the genetic algorithm: (a) energy values, (b) equilibrium position, and (c) stable equilibrium frequency and unstable equilibrium curvature. In all graphs, stable and unstable points are represented by '·' and '+', respectively.

5.2.1.4 Simulation of Linkage system to compare with optimized results

In this section, the dynamics of the four-bar linkage system is simulated to compare to the predicted results solved for in the synthesis methodology [Erdman

et al., 2001]. Figure 5.9 shows a typical response from simulating one of the solutions of Trial 5. In each simulation, the linkage started at a perturbation of 0.02 radians from the equilibrium position. This perturbation is the same distance used in curve fitting the potential energy during the optimization. Figures 5.9 (a-c) are the velocity versus position phase plots of local responses about stable equilibria one through three, respectively. Figures 5.9 (d-f) show the time response of the input crank angle about each stable equilibrium.
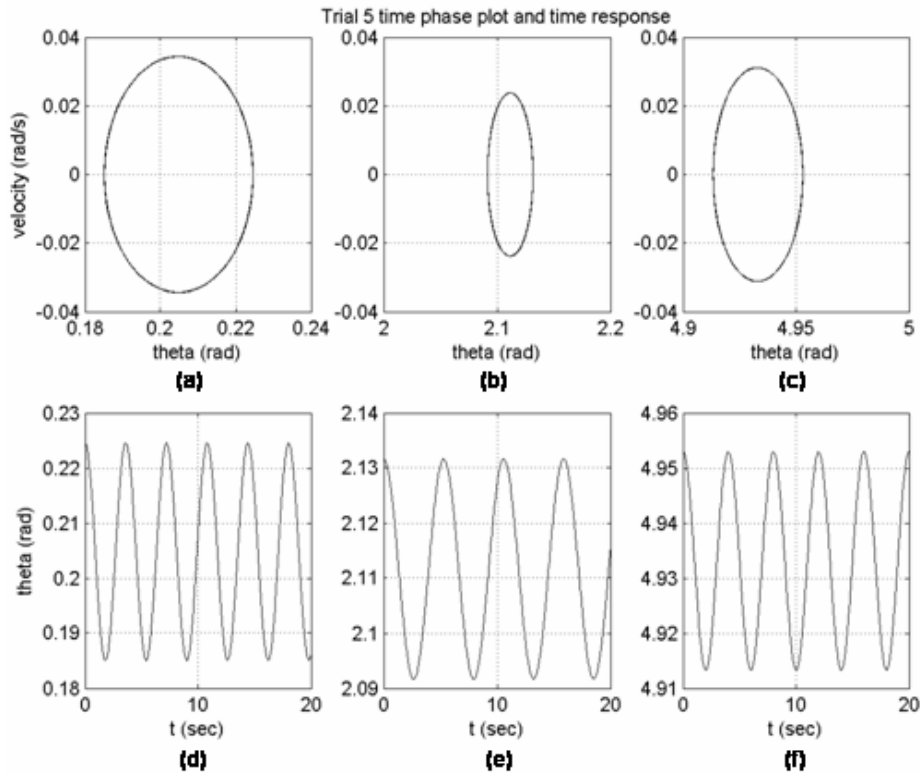
Figure 5.9. Typical local dynamic responses of the MSE linkage system of Problem 1: (a) & (d) show response about $\theta_{eq,1}$, (b) & (e) show response about $\theta_{eq,2}$, and (c) & (f) show response about $\theta_{eq,3}$.

The potential energy and effective inertia curves for the system simulated in Figure 5.9 are shown in Figure 5.10. Figure 5.10 (a) is the potential energy, and Figure 5.10 (b) is the effective linkage inertia. Note how both are quite nonlinear, and very unintuitive to visualize from the geometry of the linkage. For Problem 1, the effective inertia curve is constant. In the next section Problem 2 solves the linkage problem with a varying inertia curve. Recall the desired and candidate stable equilibrium positions are θ_{des} = [0.40, 2.30, 4.80] and θ_{cand} = [0.20, 2.11, 4.93] radians respectively. The potential energy minima in Figure 5.10 (a) demonstrate these values.
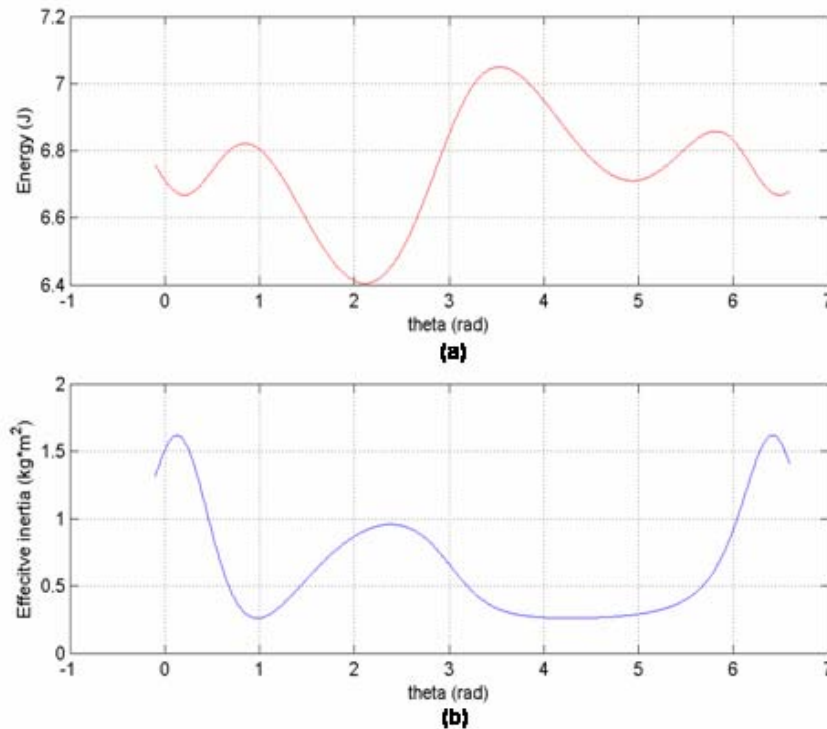
Figure 5.10. (a) The potential energy curve and (b) effective inertia curve versus the input crank angle.

5.2.2 Problem 2: Linkage link lengths are not fixed

5.2.2.1 Step 1: Decide on important Engineering Characteristics of each Equilibrium

The problem of not having fixed link lengths corresponds to a scenario in which one can be interested in the frequency, curvature and energy value at each equilibrium, but not absolute position. Because the links can be various lengths during optimization, the coupler curve of the linkage is completely unknown, and thus must be unimportant to the design. Nonetheless, one may want to attach this type of MSE system to another system simply to alter its performance or make it have multiple stable positions with certain natural frequencies.

Because absolute position of the linkage in Problem 2 is not fixed, a solution approach to the optimization of Problem 2 is specified by the relative positions of the equilibrium points, or Δa_{des}. For example, if one wants two stable equilibria to be two radians apart, then this idea can be incorporated into the performance index. The same concept can apply to actuation energy (or b_{des} values) also. The performance index can typically look like:

For the distance between equilibrium positions, Δa :

$$F_a = \sum_{i=1}^{n-1} \begin{pmatrix} w_{a,i}\left(\Delta a_{cand,i} - \Delta a_{des,i}\right) \text{if } \Delta a_{cand,i} > \Delta a_{des,i} \text{ and } \Delta a_{cand,i} > \left(\Delta a_{des,i} + \delta\Delta a_i\right), 0 \text{ otherwise} \\ w_{a,i}\left(\Delta a_{des,i} - \Delta a_{cand,i}\right) \text{if } \Delta a_{cand,i} < \Delta a_{des,i} \text{ and } \Delta a_{cand,i} < \left(\Delta a_{des,i} - \delta\Delta a_i\right), 0 \text{ otherwise} \end{pmatrix}$$

For the energy differences between stable and unstable points, Δb :

$$F_b = \sum_{i=1}^{2n} \begin{pmatrix} w_{b,i}\left(\Delta b_{cand,i} - \Delta b_{des,i}\right) \text{if } \Delta b_{cand,i} > \Delta b_{des,i} \text{ and } \Delta b_{cand,i} > \left(\Delta b_{des,i} + \delta\Delta b_i\right), 0 \text{ otherwise} \\ w_{b,i}\left(\Delta b_{des,i} - \Delta b_{cand,i}\right) \text{if } \Delta b_{cand,i} < \Delta b_{des,i} \text{ and } \Delta b_{cand,i} < \left(\Delta b_{des,i} - \delta\Delta b_i\right), 0 \text{ otherwise} \end{pmatrix}$$

For the unstable curvatures and stable natural frequencies (converted to energy curvature), c :

$$F_c = \sum_{i=1}^{n} \begin{pmatrix} w_{c,i}\left(c_{cand,i} - c_{des,i}\right) \text{if } c_{cand,i} > c_{des,i} \text{ and } c_{cand,i} > \left(c_{des,i} + \delta c_i\right), 0 \text{ otherwise} \\ w_{c,i}\left(c_{des,i} - c_{cand,i}\right) \text{if } c_{cand,i} < c_{des,i} \text{ and } c_{cand,i} < \left(c_{des,i} - \delta c_i\right), 0 \text{ otherwise} \end{pmatrix}$$

For the cases in which the candidate number of equilibria are less than the desired number :

$$F_{numstable} = 1e3(numstable_{des} - numstable_{cand}) \text{ if } (numstable_{des} - numstable_{cand}) > 0, 0 \text{ otherwise}$$

$$F = F_a + F_b + F_c + F_{numstable} \tag{5.3}$$

where *n* is the number of equilibria (stable and unstable) and *Δa* and *Δb* are the differences between the curve fitting parameters for any two equilibria of interest. To use this design approach, one has to line search through the energy values calculated for the given design variables, find where the extremals occur, and perform the curve fit about these points. The difference between this method and that described in Section 4.2 is that the point about which to curve fit is unknown *a priori*. Thus, the equilibrium points must be found each iteration. There is also no guarantee that the correct number of equilibria will be present for any given iteration. A penalty factor can be incorporated into the performance index if this occurs. The remainder of this subsection presents an example of using this approach.

Problem 2 uses the same design variables as for Problem 1, but with eight additional variables. Four of the design variables are for the four link lengths with lower limits of length 0.1 m and upper limits of length 2.0 m. The last four design variables are for the (x, y) coordinates of the anchor points for the springs attached to the ground. The limits of these anchor points are set to create an allowable space around the fixed base of links *I* and *III*, where $dx_{max} = 0.75$ m and $dy_{max} = 0.75$ m (see Figure 5.2 and Section 4.1). The addition of these design variables makes the solution space much more extensive due to the effective inertia, and thus the kinetic coenergy, now being configurable as well as the potential energy. This introduces the fundamental concept in MSE systems of now shaping both the kinetic coenergy and potential energy curves.

We assume the links have a fixed mass per unit length and an inertia that is only a function of link length (i.e. idealized one-dimensional links just as in Problem 1). The problem statement is stated as follows:

min $F(k_i, lo_i, x_1, x_2, y_1, y_2, a, b, c, d)$ i = 1, 2, …, 8   (equation 5.3)

s.t. 1) k_i , $lo_i \geq 0$,   - spring constants and free lengths positive
   2) $k_i < k_{max}$,   - spring constants below some maximum
   3) $lo_i < lo_{max}$,   - free lengths below some maximum
   4) $x_1 < dx_{max}$,   - point x_1 less than some maximum
   5) $x_2 < d + dx_{max}$,   - point x_2 less than some maximum
   6) $x_1 > -dx_{max}$,   - point x_1 greater than some minimum
   7) $x_2 > d - dx_{max}$,   - point x_2 less than some minimum
   8) $y_i > -dy_{max}$,   - points y_i greater than some minimum, i = 1,2
   9) $y_i < dy_{max}$,   - points y_i less than some maximum, i = 1,2
   10) $I, II, III, IV < l_{max}$,   - link lengths less than some maximum
   11) $I, II, III, IV > l_{min}$,   - link lengths greater than some minimum
   12) $I<II, I<III, I<IV$,   - input crank must be smallest
   13) $s + l < p + q$ - Grashof Criterion (*s*-shortest link, *l*-longest link, *p* and *q* are other two link lengths)

With the problem now fully defined, the specific goal for example Problem 2 is to obtain two stable equilibria having the same natural frequency while specifying the energy differences between stable and unstable equilibria. The positions of the stable equilibria should be separated by a maximum distance possible (between 3.1 and 3.2 radians for a rotational system), and the frequencies are the same and meant to be easily achievable. The goal will be to maximize the energy differences, Δb, for one of the stable equilibria, and keep the Δb's for the other equilibria constant at a relatively small value. This will test the design methodology for concurrently optimizing very small and large energy thresholds. The Monte Carlo mapping in the next section dictates the specific values chosen for design, given the already discussed qualitative description.

5.2.2.2 Step 2: Monte Carlo mapping and probability calculation

The qualitative results from the Monte Carlo mapping technique, characterizing the situation of two stable equilibrium positions, are shown in Figure 5.11. There were 35,000 Monte Carlo iterations used to generate the data. In Figures 5.11, the stable equilibrium angle with the lowest value is represented by a '•', and the second stable equilibrium is represented by a '+'. Figure 5.11 (a) shows what combinations stable equilibria can occur together. From this mapping it appears that for almost any initial stable position, the second one can lie almost anywhere as long as it is placed far enough away from the first one, about 1.0 – 1.5 radians on average. Figure 5.11 (b) shows that, because of the low density of

data points, obtaining natural frequencies above about 15-20 rad/s may be quite difficult. On the other hand, there are frequencies mapped up to over 25 rad/s. Figures 5.11 (c) displays the energy difference, both to the 'left' and 'right' of stable equilibrium one, using a '•' and '+', respectively. Figure 5.11 (d) shows the same information for the second stable equilibrium.
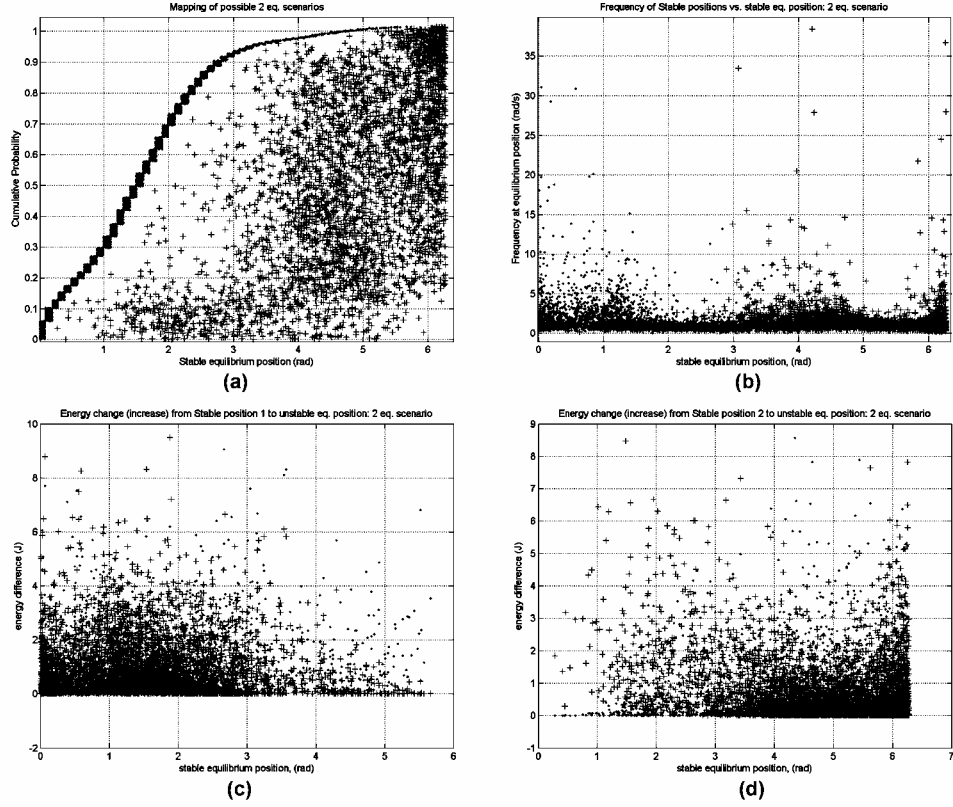
Figure 5.11. The Monte Carlo mappings show the (a) cumulative distribution function for combinations of stable equilibria that occur for 2 stable equilibria, (b) natural frequencies at the stable equilibria, (c) energy differences about stable equilibrium one, and (d) energy differences about stable equilibrium two.

From looking at Figures 5.11 (a), it seems quite feasible to design for the stable equilibria to be 3.2 radians apart. Because the input link rotates a full 2π radians, this is approximately the largest possible distance between two stable equilibria. Therefore, $\Delta a_{des,1}=(a_{stable,1} - a_{stable,2})_{des,1} = 3.2$ rad. The desired frequencies are chosen as $f_{des,stable} = [1.0, 1.0]$ rad/s to not be a relatively large problem in the design (due to a high density of points in Figure 5.11 (b) being

154

near 1 rad/s). The final design criterion is to maximize the energy difference for one of the equilibria (say the first one, $\Delta b_{des,1}$), and keep the energy difference for the other stable equilibrium small, $\Delta b_{des,2}$.

The quantitative method of the Monte Carlo mapping procedure is performed to begin to specify the remaining desired design criteria. The expected result is to define the maximum energy difference for the first equilibrium, given all of the other desired design criteria have been met. After initial probability calculations, a nonzero probability of $P_{tot} = $ 3.67e-5 was found for the scenario in which the desired characteristics are [$\Delta a_{des,1}$, $f_{des,1}$, $f_{des,2}$, $\Delta b_{des,1,left}$, $\Delta b_{des,1,right}$, $\Delta b_{des,2,left}$, $\Delta b_{des,2,right}$] = [3.2 ± 0.2 rad, 1.0 ± 0.2 rad/s, 1.0 ± 0.2 rad/s, 1.0 ± 0.2 J, 1.0 ± 0.2 J, 0.25 ± .1 J, 0.25 ± 0.1 J]. The last two desired design criteria have a smaller range of allowed values due to the fact that their desired values are so close to zero. Thus, a lower limiting energy hump of $\Delta b = $ 0.25 − 0.1 J = 0.15 J is used to maintain a basic minimum distance from the value zero which signifies that an equilibrium likely does not exist (recall Section 4.3.3.2 and Equations (4.26 − 4.29)).

The perturbed quantities from the $P_{tot} > 0$ to find the maximum limit are $\Delta b_{des,1,left}$, and $\Delta b_{des,1,right}$. These were increased until there was high confidence that their limiting values had been reached. Table 5.2 shows the trials optimized, each ten times, in finding the solution boundary limit for the desired MSE design. During optimization it was found that the solution could be perturbed quite far from the $P_{tot} > 0$ starting case derived from the Monte Carlo probability calculation. The results of the optimization runs are discussed in the next section.

Trial	$\Delta a_{des,1}$	f_{des}	$[\Delta b_{des,1,left},\ \Delta b_{des,1,right},\ \Delta b_{des,2,left},\ \Delta b_{des,2,right}]$	P_{tot}
1	3.2	[1.0, 1.0]	[1.0, 1.0, 0.25, 0.25]	3.67e-5
2	3.2	[1.0, 1.0]	[2.0, 2.0, 0.25, 0.25]	0
3	3.2	[1.0, 1.0]	[3.0, 3.0, 0.25, 0.25]	0
4	3.2	[1.0, 1.0]	[4.0, 4.0, 0.25, 0.25]	0
5	3.2	[1.0, 1.0]	[5.0, 5.0, 0.25, 0.25]	0
6	3.2	[1.0, 1.0]	[6.0, 6.0, 0.25, 0.25]	0
7	3.2	[1.0, 1.0]	[7.0, 7.0, 0.25, 0.25]	0
8	3.2	[1.0, 1.0]	[8.0, 8.0, 0.25, 0.25]	0
9	3.2	[1.0, 1.0]	[9.0, 9.0, 0.25, 0.25]	0
10	3.2	[1.0, 1.0]	[10.0, 10.0, 0.25, 0.25]	0
11	3.2	[1.0, 1.0]	[11.0, 11.0, 0.25, 0.25]	0
12	3.2	[1.0, 1.0]	[12.0, 12.0, 0.25, 0.25]	0
13	3.2	[1.0, 1.0]	[13.0, 13.0, 0.25, 0.25]	0
14	3.2	[1.0, 1.0]	[14.0, 14.0, 0.25, 0.25]	0
15	3.2	[1.0, 1.0]	[15.0, 15.0, 0.25, 0.25]	0
16	3.2	[1.0, 1.0]	[16.0, 16.0, 0.25, 0.25]	0
17	3.2	[1.0, 1.0]	[17.0, 17.0, 0.25, 0.25]	0
18	3.2	[1.0, 1.0]	[18.0, 18.0, 0.25, 0.25]	0
19	3.2	[1.0, 1.0]	[19.0, 19.0, 0.25, 0.25]	0
20	3.2	[1.0, 1.0]	[20.0, 20.0, 0.25, 0.25]	0
21	3.2	[1.0, 1.0]	[21.0, 21.0, 0.25, 0.25]	0
22	3.2	[1.0, 1.0]	[22.0, 22.0, 0.25, 0.25]	0
23	3.2	[1.0, 1.0]	[23.0, 23.0, 0.25, 0.25]	0

Table 5.2. Trial sets of desired design criteria with corresponding Monte Carlo probability for Problem 2.

5.2.2.3 Step 3: Optimization and interpretation of results

For reasons described in Section 5.2.1.3, a stochastic algorithm is chosen was chosen for the optimization algorithm. In particular, the genetic algorithm, developed by Houck et al., is again used because of its relatively fast performance over the adaptive simulated annealing algorithm of Problem 1. As noted in

solving Problem 1, the resulting solution trends are quite similar between the two algorithms even though the ASA algorithm seems slightly more robust in finding the global minima for the linkage Problem 1 (for the parameters used in each algorithm).

The RLD from solving Trials 1-23 of Problem 2 is shown in Figure 5.12. There seems to be four distinct regions of distributions in solving the trial problems of Table 5.2. Trials 1-4 get solved relatively quickly, showing that the baseline $P_{tot} > 0$ case is solved easily by the chosen genetic algorithm parameters. Trials 5-9 and 12 are solved a bit more slowly followed by Trials 10, 11, and 13-18, although the distinction between these two groups is not entirely distinct. Finally, a fourth group of trials does not appear on the graph at all, Trials 19-23, as none of them were successfully solved by the optimization algorithm. This follows an expected trend of having more difficulty, or needed more iterations/time, in solving the optimization problem while moving further from the base $P_{tot} > 0$ condition of Trial 1. Note that for none of the trials did the optimization solve for the design variables all ten attempts.

The unsolved problems occur after the desired energy difference about stable equilibrium one has reached 19.0 ± 0.2 J. Thus, one can believe this is near the limiting value possible considering the current desired design criteria. In the same manner as in Problem 1, looking at the trends of the desired design criteria can confirm that a solution space boundary is indeed being met during the optimization perturbation process.
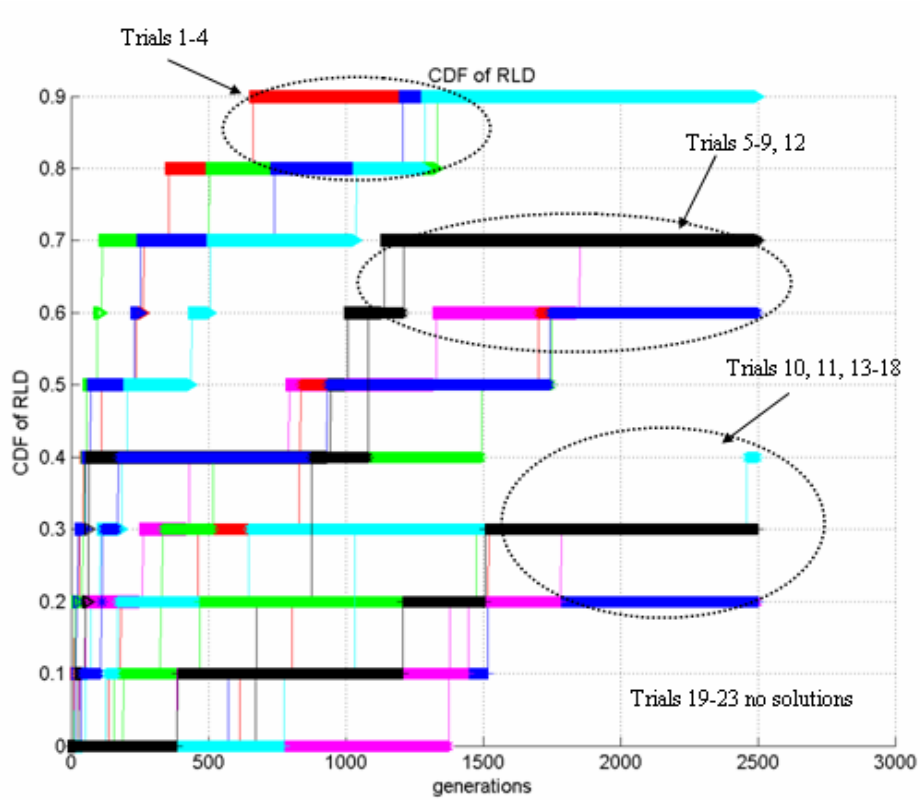
Figure 5.12. RLD for using genetic algorithm to solve for design variables of Problem 2.

Figure 5.13 plots some equilibrium trends that show a limit being reached during the design synthesis process. The Trial number of Table 5.2 increases along the horizontal axis of each graph. Data is only shown for successfully achieved solutions to the trials of Table 5.2. Figure 5.13 (a) plots the energy differences between the unstable and adjacent stable equilibria. The '•' represents $\Delta b_{cand,,left}$, and the '+' represents $\Delta b_{cand,right}$. For $\theta_{eq,2}$ the values are barely discernable since they are in the range 0.25 ± 0.1 J. Figure 5.13 (b) plots the stable equilibrium positions, '•', and the unstable equilibrium positions, '+'. Figure 5.13

158

(c) plots the frequencies and unstable curvatures at the stable and unstable equilibria, respectively.
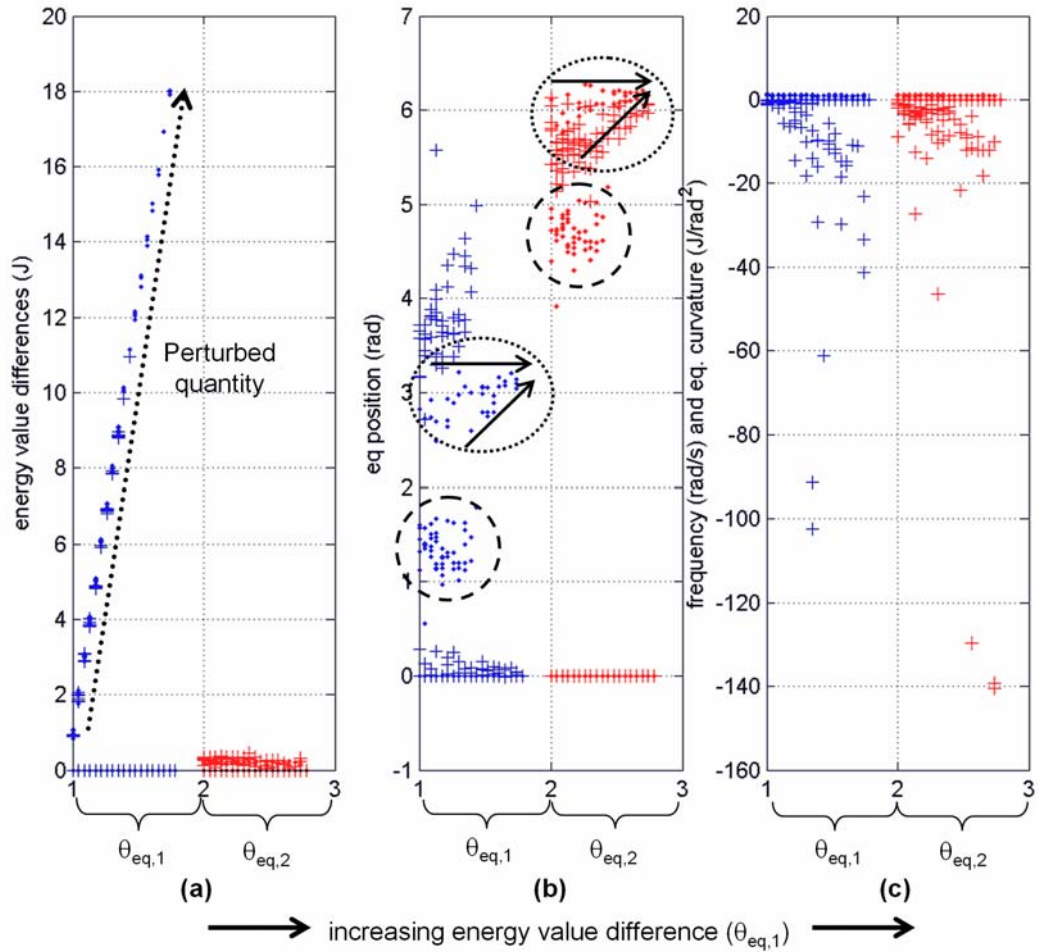
Figure 5.13. Equilibrium trends for solving Trials for Problem 2 in Table 5.2: (a) energy difference between adjacent unstable and stable equilibria, (b) equilibrium position, and (c) stable equilibrium frequency and unstable equilibrium curvature. Trial number increases as one moves right along the horizontal axis.

Figure 5.13 (b) is the most telling in terms of information corroborating that a solution space boundary is indeed being reached after Trial 18. Notice that

for 'small' $\Delta b_{des,1}$, Trials 1-11, there are two groups of stable equilibrium positions. These two groups are represented by the dotted and dashed ellipses in Figure 5.13 (b). Recall that the design criteria for the equilibrium positions is not absolute position, but a relative position where there is 3.2 radians between the two stable equilibria. After Trial 11, the group of solutions in the dashed ellipse no longer exists as a viable solution. One of two possible solution space regions has effectively been eliminated due to the increasing constraint, $\Delta b_{des,1}$. After Trial 10, all solutions are now encompassed in the dotted ellipse. As the trial number is increased, the solutions for $\theta_{eq,1}$ converge to a value near 3.2 radians, and the solutions for $\theta_{eq,2}$ converge to a value near 6.2 radians. There is a difference of 3.0 radians between these two values. This is the lower limit allowed under the constraint of the desired design criteria, $\Delta a_1 = 3.2 \pm 0.2$ radians.

Figure 5.14 plots these two groups of solutions, or energy curves, for Trials 1 and 10. Note for each trial there are two distinct groups of curves corresponding to the groups in Figure 5.13. These are correspondingly labeled as the 'dashed' and 'dotted' groups. As predicted from Figure 5.13, these two groups of curves do have distinct shapes between the two groups, but similar shapes within the group. Therefore, each group is its own localized solution space. For Trials 12-18, the 'dashed' solution space no longer exists. For Trials 19-23, neither solution space exists. Figure 5.15 plots all successful energy curves for Trials 12-18 confirming that only one basic shape of potential energy curve exists in the 'dotted' solution region. This characterizes the local solution space found by the optimization algorithm.

160
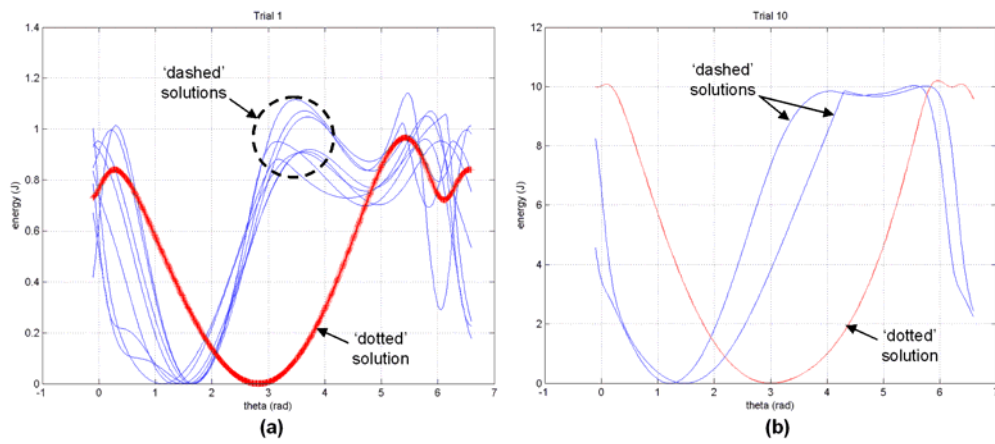
Figure 5.14. Potential energy curves for (a) Trial 1, and (b) Trial 10.
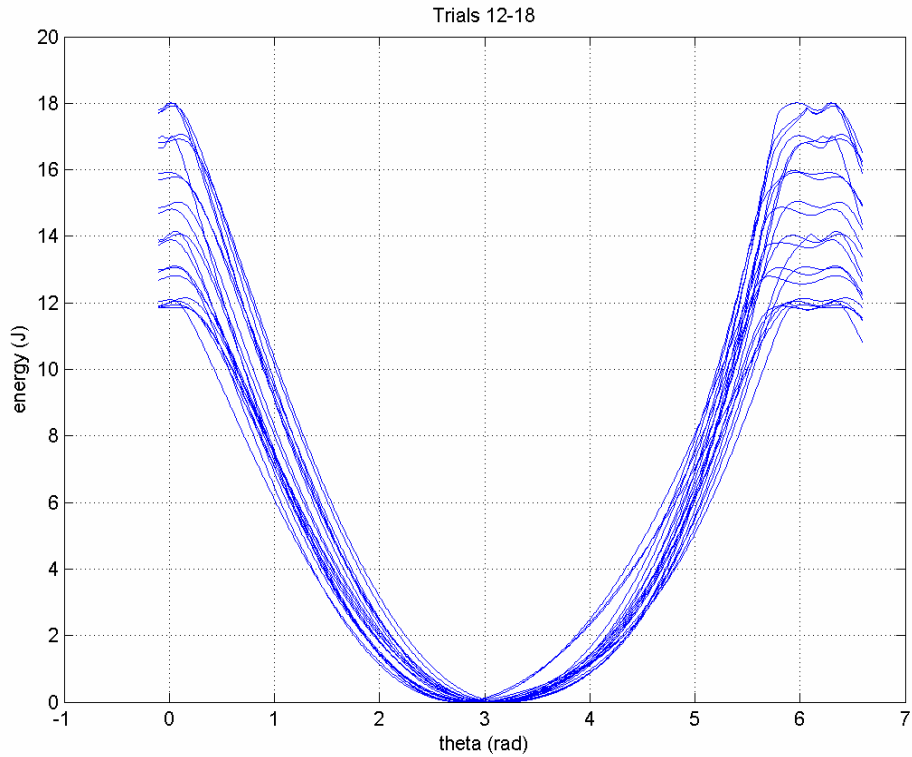
Figure 5.15. Successfully solved potential energy curves for Trials 12 – 18. These are all solutions in the 'dotted' group of Figure 5.13.

5.2.2.4 Simulation of Linkage system to compare with optimized results

In this section, the dynamics of the four-bar linkage system of Problem 2 is simulated to compare to the predicted results solved for in the synthesis methodology. Figure 5.16 shows a typical response from simulating one of the successful solutions of Trial 12. In each simulation, the linkage started at a perturbation of 0.02 radians from the equilibrium position. This perturbation is the

same distance used in curve fitting the potential energy during the optimization. Figures 5.16 (a-b) are the velocity versus position phase plots of local responses about stable equilibria one and two, respectively. Figures 5.16 (c-d) show the time response of the input crank angle about each stable equilibrium. Figure 5.17 shows the (a) energy curve and (b) effective inertia for the simulated case shown in Figure 5.16. The stable curvatures are c_{cand} = [1.27, 3.50] J/rad^2 and effective inertias are J_{eff} = [1.71, 5.72] kg*m^2 to give the same approximate natural frequencies. The designed candidate frequencies are 1.14 and 1.08 rad/s, and the simulated frequencies are 1.21 and 1.09 rad/s for the first and second stable equilibrium, respectively.
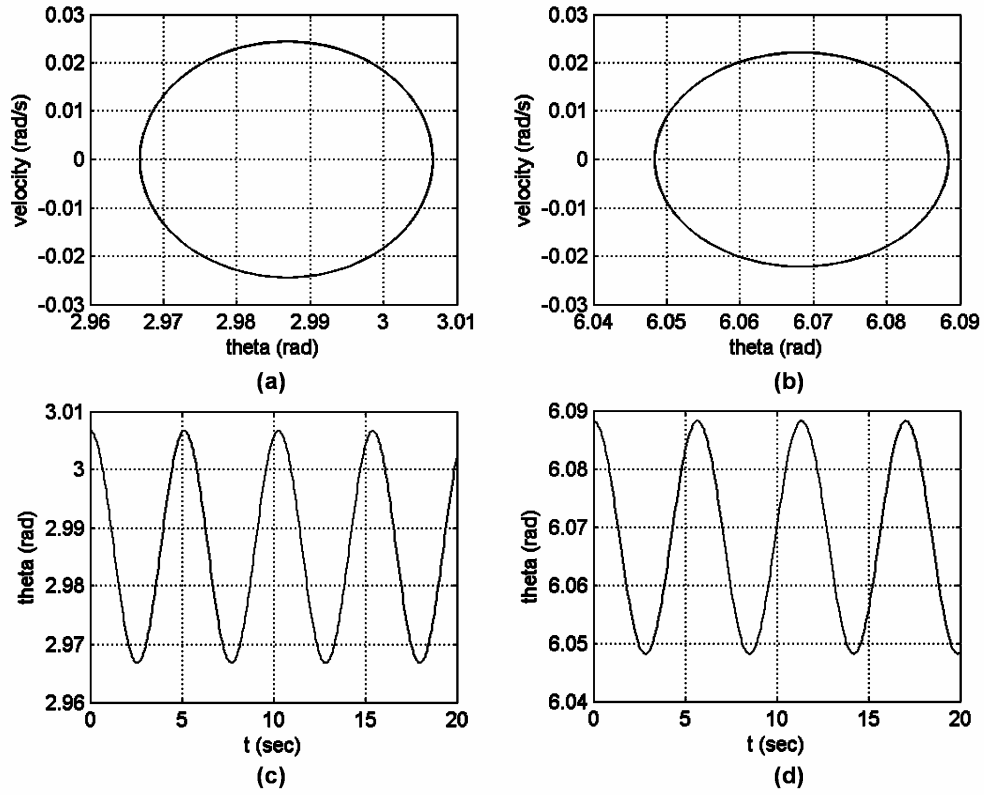
Figure 5.16. Typical local dynamic responses (Trial 12 solution) of the MSE linkage system of Problem 1: (a) & (c) show response about $\theta_{eq,1}$, and (b) & (d) show response about $\theta_{eq,2}$.
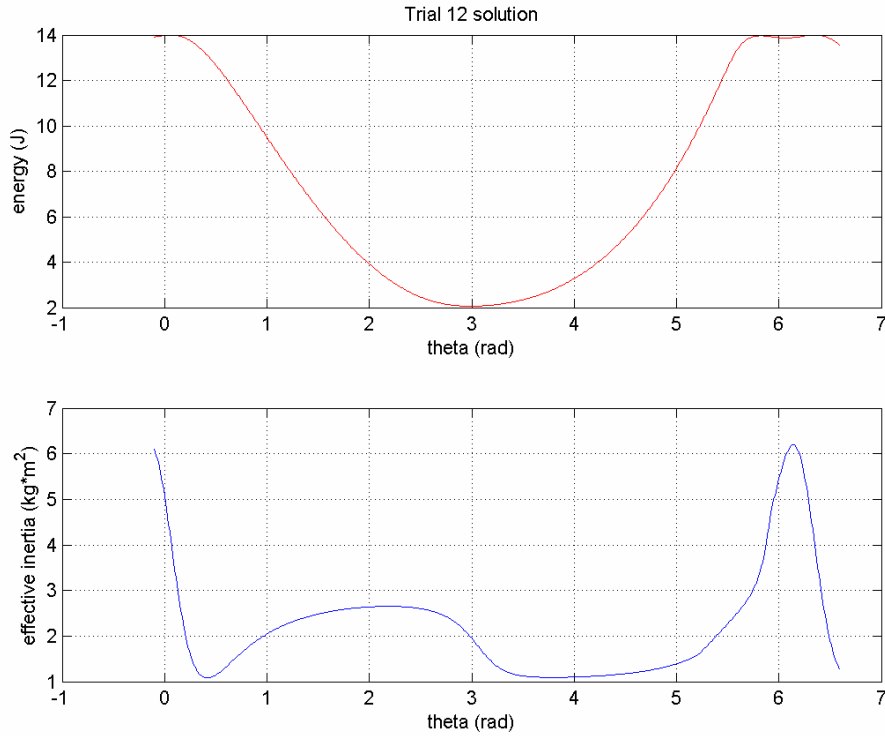
Figure 5.17. (a) The potential energy curve and (b) effective inertia curve versus the input crank angle for a Trial 12 solution.

5.2.3 Conclusions on Linkage Case Study

Generally the linkage problem is an ideal case study for the design synthesis of MSE systems. The problem contains nonlinearities in both the potential energy storage elements and the kinetic coenergy storage elements, or effective inertia. Problem 1 solved the linkage with a nonlinear, but fixed, effective inertia while Problem 2 allowed this inertia curve to vary. This makes Problem 2, with variable linkage link lengths, have a much larger solution space.

This major difference between Problem 1 and Problem 2 is the reason why Problem 2 takes longer to solve. Because the location of the desired equilibria is unknown for Problem 2, one must search for them during each iteration, and then curve fit about those points. For Problem 1, one has the option of simply curve fitting about the known desired equilibrium positions.

As seen by the qualitative mappings of both problems, Problem 1 has a much more rigidly defined solution space. This fact is made evident by more quickly finding the local boundary of the solution space in Problem 1 versus Problem 2. In Problem 2, a much larger perturbation from the initial $P_{tot} > 0$ trial was needed to find the limiting boundary for possible solutions. This is simply explained by the general observation that more design variables exist for Problem 2.

5.3 PENDULUM AND MAGNET PROBLEM

5.3.1 Problem Description

Described here is an example problem for synthesizing MSE systems. The problem consists of a pendulum that has linear springs and a permanent magnet attached to it (see Figure 5.18). There are three types of potential energy storage elements: 1) the linear translational springs which store energy only in extension, 2) the gravitational field acting on the rotating beam, and 3) the magnetic field acting between the armature and stator magnet. In Figure 5.18, m_{com}, L_{com}, and J_{eff} are the mass off the rotating pendulum system, the length to the center of mass from the pivot, and the effective inertia of the pendulum system, respectively.
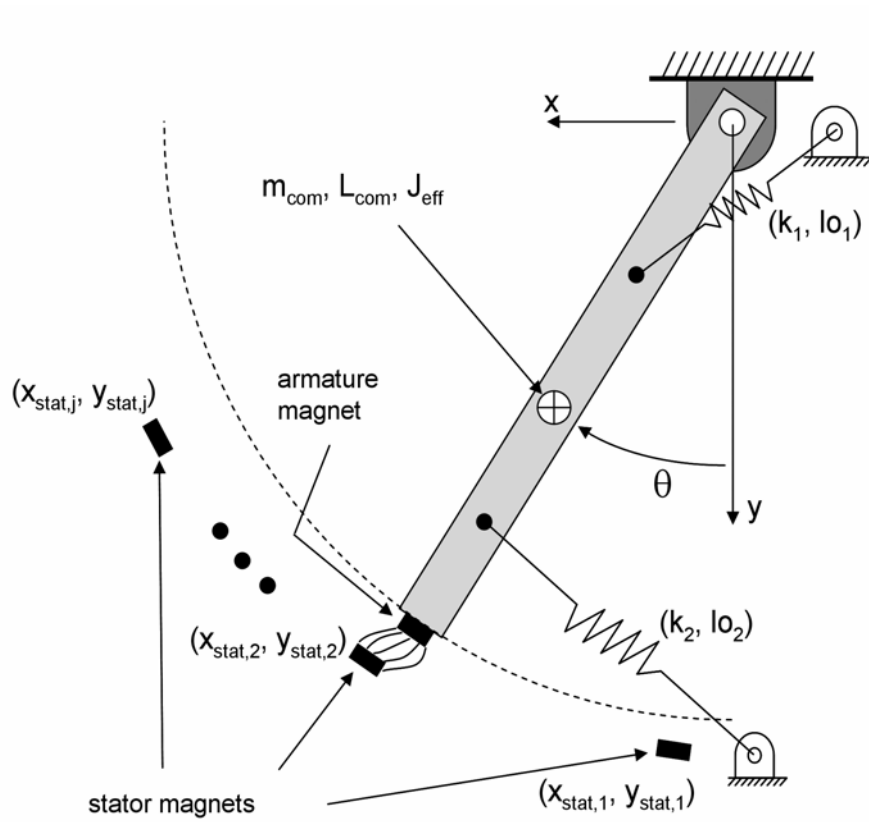
Figure 5.18. Schematic of the pendulum and magnet experiment.

Experiments were performed to obtain the change in potential energy with respect to displacing the two magnets (i.e the armature and stator) relative to each other. The magnet data obtained is valid in a range for which the magnets are polarized in the same direction (i.e. no relative angle between them) that extends one magnet length to each side, or $x_{rel} = \pm 1.0 len$, and from a 'gap' of $1.0 - 3.0$

magnet thicknesses, or relative displacements of $y_{rel} = 2.0th$ to $y_{rel} = 4.0th$ (see Figure 5.19).
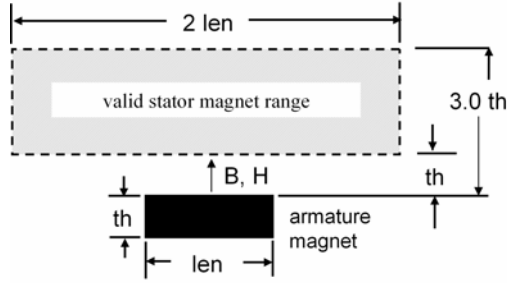
Figure 5.19. Range of stator magnet relative to armature magnet for which the magnet model is valid.

The potential energy of the system of Figure 5.18 is:

$$W(\theta) = \sum_{i=1}^{2} \frac{1}{2} k_i \left(l_i(\theta) - lo_i \right)^2 + m_{pend} g L_{com} (1 - \cos(\theta)) + W_{mag} (\theta, x_{stat,j}, y_{stat,j})$$

(5.4)

where k_i and lo_i are the spring constant and free length for spring 'i' respectively, and $l_i(\theta)$ is the length of spring 'i' at the current θ. Two types of springs are used in the experiment: $k_1 = 1$ lb/in, $lo_1 = 2$ in., and $k_2 = 0.5$ lb/in, $lo_2 = 2$ in. If an increase in free length was desired, two of the same type were used in series. The second term in Equation (5.4) is the potential energy due to gravity, and the third

169

term is the magnetic potential energy from the stator and armature magnets where $x_{stat,j}$ and $y_{stat,j}$ are the planar coordinates of the jth stator magnet.

The magnetic potential energy between the armature and any stator magnet is only available for a certain two-dimensional space for which experimental data was taken. The particular magnets used are NdFeB magnets of size 0.5" square and 0.210" thick (part # 5848K32 Grade 37 from McMaster Carr). The method for deriving the magnetic energy is explained in Section 5.3.2. Note the magnetic energy is derived from interpolated data. Thus, an expression for the magnetic energy in the system as an explicit function of θ was not derived. This does not matter in terms of the synthesis design problem. The solution methodology involves only information from the system potential energy in performing the numerical optimization.

In the case of the magnetism model in this problem, a closed-form solution for one or more of the energy storage elements may not exist. Also, due to the limited magnetic model, a restriction is imposed that the stator magnets are far enough apart such that they don't influence each other appreciably. Nonetheless, because of the lack of closed form solution, it is still difficult to gain insight into writing a performance index and constraints in terms of problem design variables, such as spring constants and masses. The MSE design synthesis methodology focuses on visualizing, or quantifying, desired properties of a MSE system (equilibrium points, natural frequencies, and energy values) to provide a systematic way to approach any MSE problem no matter what energy domains or constraints are involved. Thus, the Monte Carlo mapping qualitative method

proves useful in this problem even though the design only considers one stable equilibrium at a time during the solution process.

For the given mechanical system shown in Figure 5.18, the goal of the MSE synthesis problem is to place the stator magnets in 'j' positions $(x_{stat,j}, y_{stat,j})$, such that the rotating beam has the predetermined stable positions, $\theta_{eq,j}$, and/or natural frequencies, $f_{eq,j}$. Formally, the problem can be stated as follows:

$$min \ F(x_{stat,j}, y_{stat,j})$$

s.t. $(x_{stat,j}, y_{stat,j})$ and (x_{arm}, y_{arm}) are within data range for W_{mag},

where the performance index, $F(x_{stat,j}, y_{stat,j})$ is as defined in Equation (4.11).

5.3.2 Permanent Magnet Modeling

The data for the potential energy of the permanent magnets was obtained from an experiment in which the tangential force, F_t, and normal force, F_n, were recorded for certain relative positions, (x_{rel}, y_{rel}) of two magnets (see Figure 5.20). Thus, this data does not take into account the field from a third magnet, assumes that the influence of all other magnetic fields is negligible, and requires the magnets be polarized in the same direction with no rotational offset. After undergoing initial design attempts with a certain density of magnet data points, force data was needed for more points than were able to be accurately obtained by using the physical experiment (physical limitation of the experiment did not allow more accurate discretization of the data points). The Ansys® finite element

analysis (FEA) program was then used to perform simulations of the magnets using tuned magnet parameters of coercivity equal to 920 kA/m and relative permeability of 1.062. These two parameters provided good agreement between the finite element result and the physical experiment. Due to inefficiencies of the finite element program for simulations involving materials with small relative permeabilities, the magnetic energy calculations directly available from the finite element routine were deemed insufficiently accurate for use by themselves. Thus, force data derived from the finite element program was used to calculate the magnetic potential energy.
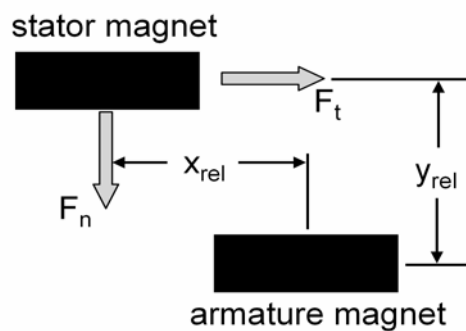
Figure 5.20. Tangential force, F_t, and normal force, F_n, were measured at various relative x and y locations.

Using force data, the potential energy can be calculated as for any conservative linear system whether or not it involves magnetism. The NdFeB magnets used in for this experiment fit this description since they have very close

172

to linear B-H curves [Fitzgerald et al., 1990]. For a conservative magnetic system, the force due to a change in magnetic energy is given by Equation (5.5).

$$F_t = F_x^{mag} = -\frac{\partial W_{mag}}{\partial x}, \quad F_n = F_y^{mag} = -\frac{\partial W_{mag}}{\partial y} \tag{5.5}$$

Conversely the magnetic energy from the experimentally measured magnetic forces is:

$$W_{mag}(x_{rel}, y_{rel}) = -\int \frac{\partial W_{mag}}{\partial y_{rel}} \, dy_{rel} + \varphi(x_{rel}) \tag{5.6}$$

with condition that:

$$\frac{\partial W_{mag}}{\partial x_{rel}} = \frac{\partial}{\partial x_{rel}}\left[-\int \frac{\partial W_{mag}}{\partial y_{rel}} \, dy_{rel} \right] + \frac{\partial \varphi(x_{rel})}{\partial x_{rel}} = F_t \tag{5.7}$$

Thus, one can solve for the arbitrary function of x_{rel}, $\varphi(x_{rel})$, as:

$$\varphi(x_{rel}) = \int \left[F_t + \frac{\partial}{\partial x_{rel}}\left[\int \frac{\partial W_{mag}}{\partial y_{rel}} \, dy_{rel} \right] \right] dx_{rel} \tag{5.8}$$

One can now use the result of Equation (5.8) in Equation (5.6) to have the total magnetic energy to within an arbitrary constant.

The magnetic forces obtained from the finite element modeling have normalized errors in the range of 10% - 15%. The energy curves resulting from using Equations (5.5-5.8) are shown in Figure 5.21. To obtain a feel for the error

of the magnetic energy curves, use Equations (5.5-5.8) and the concept of Maxwell reciprocity for conservative linear energetic systems. Maxwell reciprocity can be stated as shown in Equation (5.9).

$$\frac{\partial^2 W_{mag}(x, y)}{\partial x \partial y} = \frac{\partial^2 W_{mag}(x, y)}{\partial y \partial x} \qquad (5.9)$$

Equation (5.9) can alternatively be stated as:

$$\frac{\partial F_x(x, y)}{\partial y} = \frac{\partial F_y(x, y)}{\partial x} \qquad (5.10)$$

174
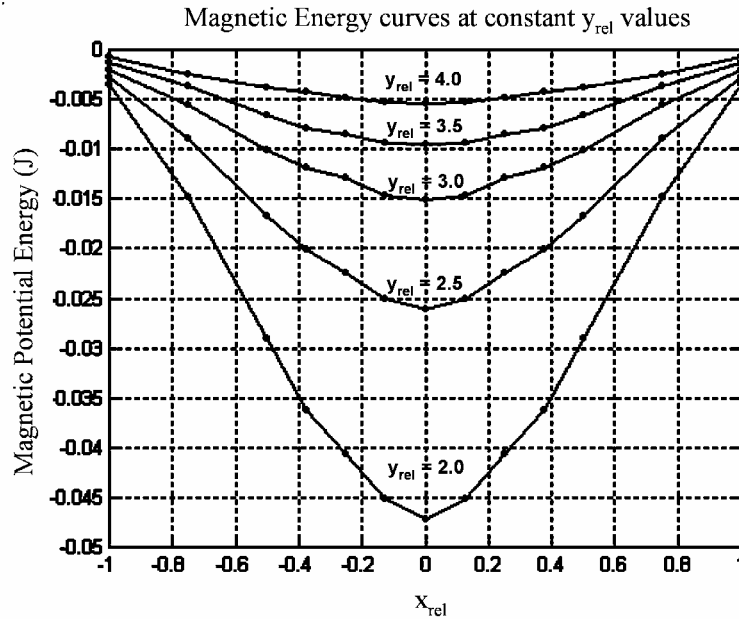
Figure 5.21. Magnetic potential energy curves, plotted at constant y_{rel} values, obtained from FEM data.

If there were no error in the finite element modeling, Equations (5.9) and (5.10) would be true. Therefore, using the finite element magnetic force data and Equation (5.10), the accuracy of the data can be checked. Figure 5.22 shows the comparison of the right hand (dots) and left hand (circles) sides of Equation (5.10). A comparison of the data is performed by calculating the correlation coefficient of the two data sets for each constant y_{rel} value. These correlation coefficients are shown in Table 5.3. Note from Table 5.3 that the finite element results become less accurate as the magnets move apart. More highly refined meshes can obtain better results, but the concentration of this FEA work is simply to use sufficiently accurate data for MSE design synthesis. From the correlation

175

coefficients, the correlation of the forces at $y_{rel} = 2.0$ is the best at approximately

93 % and the worst at $y_{rel} = 4.0$ at 42 %. Even with data that has these

inaccuracies, Section 5.3.4 shows that the magnetic energy model is sufficient for

the design synthesis.

Data Set 1	Data Set 2	y_{rel}=2.0	y_{rel}=2.5	y_{rel}=3.0	y_{rel}=3.5	y_{rel}=4.0
$\partial F_x/\partial y$	$\partial F_y/\partial x$	0.966	0.934	0.871	0.834	0.651

Table 5.3. Correlation coefficients comparing left and right sides of Equation (5.10). These correlation coefficients relate how accurate the FEM data is to itself.
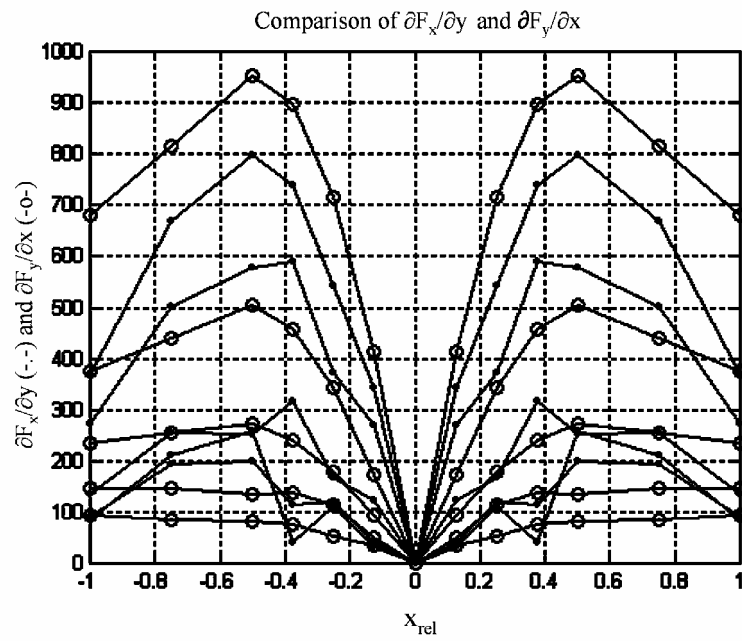
Figure 5.22. Tangential force, F_t, and normal force, F_n, were measured at various relative x and y locations.

177

5.3.3 Solution Results

Two designs were optimized using the rigid pendulum setup shown in Figure 5.18.   The parameters for each test are as follows:

Case 1:

- 200 g mass added to pendulum 1.5 inches from pivot point.
- No springs added to pendulum.

Case 2:

- 200 g mass added to pendulum 1.5 inches from pivot point.
- spring 1 - k_1 = 1 lb/in., lo_1 = 4 in., (x_{base}, y_{base}) = (-0.78 in., -0.05 in.), and attached to pendulum 5.69 in. from pivot point.
- spring 2 - k_2 = 0.5 lb/in., lo_2 = 2 in., (x_{base}, y_{base}) = (4.06 in., 2.46 in.), and attached to pendulum 4.38 in. from pivot point.

5.3.3.1 Case 1 Solution (Rigid Pendulum)

Figure 5.23 is a Monte-Carlo mapping formed by using 2000 iterations of random numbers for the design variables of the problem. Note that not all of the iterations result in a plotted point since each iteration does not produce a minimum in energy. In Figure 5.23, one can notice the trend of the possible solution space for the problem. The possible natural frequencies attainable seem to lie the range from 8 – 22 Hz for any desired equilibrium position. Thus, there seems to be little change in solution space as the equilibrium point is changed.

178

Using Figure 5.23 as a guide, the desired equilibrium positions and natural frequencies were chosen as θ_{des} = [0.3, 0.5, 0.8, 1.1] radians and $f_{n,des}$ = [21, 8, 16, 10] Hz. Table 5.4 shows the results of the optimization. In testing the system, the y_{rel} values were constrained to be equal to that of the predicted values. Then the resulting x_{rel} values f_n were measured to see how they corresponded to the desired synthesized values. Taking the minimal damping of the system into account, the experimental natural frequencies are within 10.0% relative error and 1.4 Hz absolute error of the desired values. The predicted and experimental x_{rel} values correspond very well leading one to believe that both the solution method and the model of the magnet energy have good accuracy.
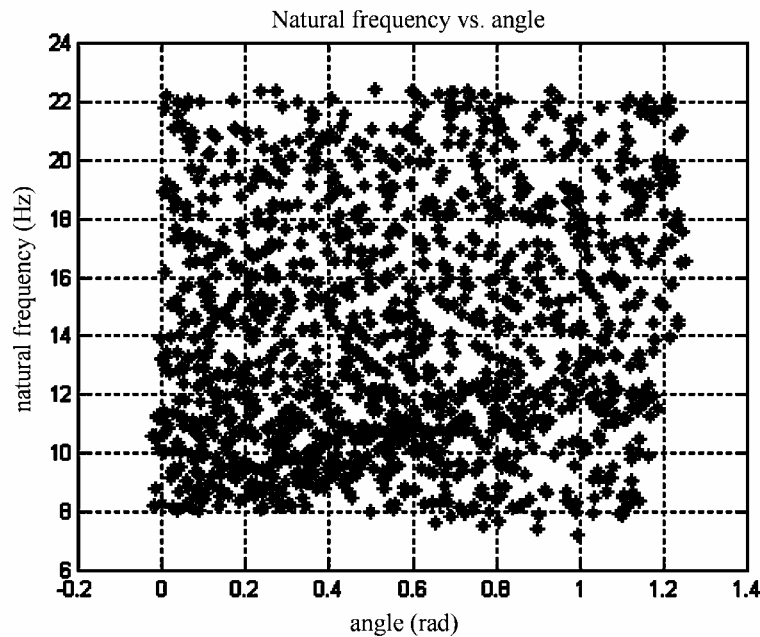
Figure 5.23. Monte Carlo mapping of natural frequency versus angle for case 1.

5.3.3.2 Case 2 Solution (Rigid Pendulum)

The Monte-Carlo mapping for case 2 used 2000 iterations and is shown in Figure 5.24. Surprisingly the springs seem to have little effect as the mapping looks quite similar to that for case 1. The feasible design range for the frequency lies between 8 and 24 Hz. From Figure 5.24 the following design criteria are chosen: four equilibrium positions at θ_{des} = [0.2, 0.4, 0.6, 0.9] radians and $f_{n,des}$ = [21, 16, 13 18] Hz. The last optimizing point at θ = 0.9 is chosen because there seems to be a hole in the mapping at that point near 18 Hz on the vertical axis. Thus, one can examine if that is simply some sort of numerical anomaly since all energy storage elements have smooth and continuous energy curves. The results from the optimization are shown in Table 5.5. The results again show good agreement in predicting the natural frequency of the pendulum as the worst error is 6.2%, or 1.3 Hz in absolute error. The optimization for 18 Hz at θ = 0.9 radians was obtained accurately, signaling that one must use some judgment in interpreting the Monte-Carlo mappings correctly in that the data points most closely represent probabilities of a solution (i.e. where points are most densely populated there is a high probability of solution, and vice versa).

$\theta_{desired}$ (rad)	$y_{rel,predict} =$ $y_{rel,experimental}$	$x_{rel,predict}$	$x_{rel,experimental}$ ($\pm$ 0.05)	$f_{n,desired}$ (Hz)	$f_{n,experimental}$ (Hz)	f_n, (% error)
0.3	2.11	0.04	0.05	21.0	20.8	1.0
0.5	3.76	0.35	0.35	8.0	7.2	10.0
0.8	2.44	0.12	0.10	16.0	17.4	8.7
1.1	3.12	0.34	0.30	10.0	9.5	5.0

Table 5.4. Results of Case 1 SQP optimization synthesis of MSE system.
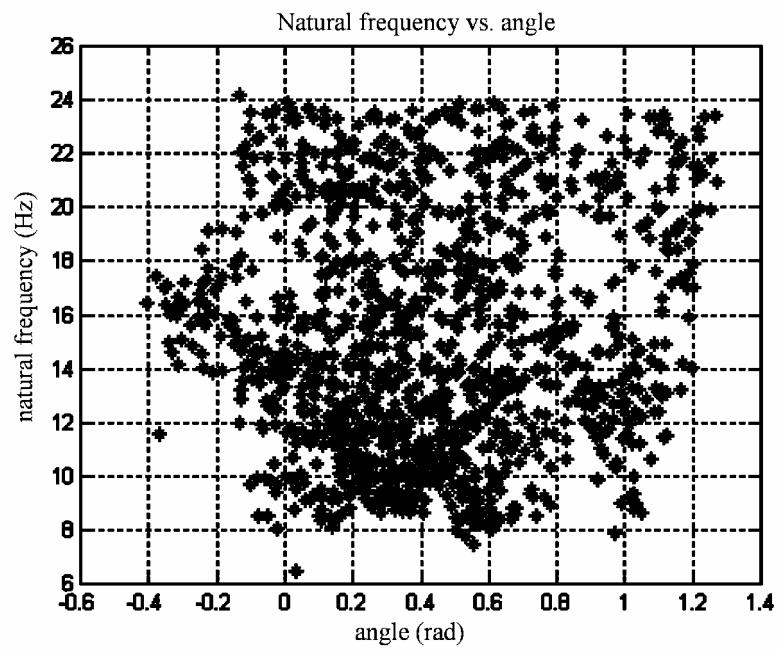
Figure 5.24. Monte Carlo mapping of natural frequency versus angle for case 2.

$\theta_{desired}$ (rad)	$y_{rel,predict} =$ $y_{rel,experimental}$	$x_{rel,predict}$	$x_{rel,experimental}$ (± 0.05)	$f_{n,desired}$ (Hz)	$f_{n,experimental}$ (Hz)	f_n, (% error)
0.2	2.11	-0.37	-0.25	21	20.0	4.8
0.4	2.54	-0.06	-0.05	16	15.1	5.6
0.6	2.68	0.05	0.00	13	13.0	0.0
0.9	2.22	0.17	0.10	18	16.9	6.1

Table 5.5. Results of Case 2 SQP optimization synthesis of MSE system.

5.3.3.3 Compliant Beam Example

The synthesis of a compliant beam was also performed to explore the use of the MSE design methodology for compliant structures. The beam is made of Duraform[TM] made in a Sinterstation 2000 selective laser sintering machine (see Figure 5.25). The pseudo-rigid-body (PRB) method was used to approximate the kinematics of the beam [Howell et al., 1994]. The stiffness of the beam used in the PRB model was approximated a constant and calculated by studying the free response of the beam during vibration. The same design approach used in the pendulum example was employed for the compliant beam. The corresponding Monte-Carlo mapping in shown in Figure 5.26 and the results of the synthesis are in Table 5.6.

The predicted position of the beam was quite good using the PRB method. All values were within one millimeter for the beam of length 175 mm. Notice in Set 1 in Table 5.6 how the predictions of the natural frequency are good for the lower angles but are quite poor for the higher angles. Also, the prediction for the x_{rel} position of the magnets is off significantly. To test the hypothesis that the error in the synthesis prediction increases with angle, the beam is synthesized to attain the same natural frequency, 25 Hz, for increasing PRB angle values. The

results are shown in Set 2 of Table 5.6. The hypothesis is proved correct as the error in prediction of frequency and position increases with angle. The results indicate that the beam stiffness, or strain energy in the beam, is over predicted. Note the x_{rel} positions are better than in Set 1, but still not accurate for large angles.
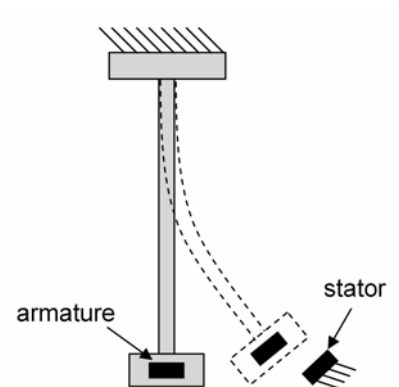
Figure 5.25. Schematic of the compliant beam used in synthesizing equilibrium positions.
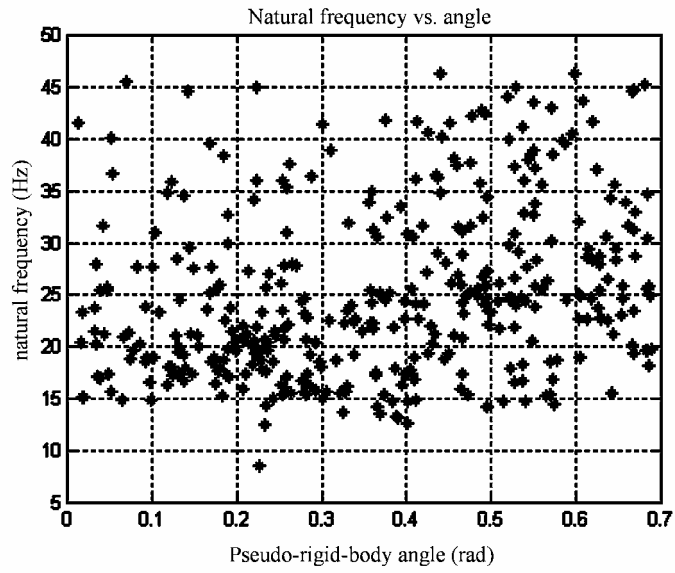
Figure 5.26. Monte Carlo mapping of natural frequency versus equilibrium position for the compliant beam.

Further experimentation of the beam stiffness error was performed by synthesizing the compliant beam position and frequency while assuming no strain energy in the beam. Using the same y_{rel} and experimental x_{rel} values from Set 2 of Table 5.6, the natural frequencies were then predicted in the computer model. As one can see in Table 5.7, the error in predicting natural frequency is now much better for the large angles, but slightly worse for the small angles. The conclusion is that the spring constant model from the PRB is insufficient to account for the strain energy stored in the Duraform[TM] beam. This is likely due to one or both of the following factors: 1) the beam material has creep occurring to relieve strain energy at large angles, and 2) the magnetic force on the beam pulls in the normal direction much harder than in the tangential direction, thus stretching the limits of applicability for the PRB model. Future work in the area

$\theta_{desired}$ (rad)	$y_{rel,predict} = y_{rel,experimental}$	$x_{rel,predict}$	$x_{rel,experimental}$ ($\pm$ .05)	$f_{n,desired}$ (Hz)	$f_{n,experimental}$ (Hz)	f_n % error
Set 1						
0.1	2.67	0.01	0.05	35	34.4	1.7
0.2	2.15	0.05	0.05	45	48.5	7.8
0.4	2.77	0.23	0.05	23	31.7	37.8
0.5	3.17	0.44	0.1	17	23.4	37.6
Set 2						
0	3.3	0	0	25	25.8	3.2
0.1	3.25	0.06	0.05	25	27.7	10.8
0.2	2.9	0.15	0.05	25	28.3	13.2
0.3	2.84	0.17	0.05	25	31.3	25.2
0.4	2.7	0.21	0.1	25	33.3	33.2

Table 5.6. Results from the MSE synthesis of the compliant beam in Figure 5.25.

of compliant structures will need to better calculate strain energy. Nonetheless, this initial experimentation into the synthesis of MSE systems made of compliant structures shows that further refinement in accounting for strain energy has promise for producing good results.

$\theta_{desired}$ (rad)	$y_{rel,predict} =$ $y_{rel,experimental}$	$x_{rel, predict}$	$x_{rel,experimental}$ ($\pm .05$)	$f_{n,experimental}$ (Hz)	$f_{n,predict}$ (Hz)	f_n % error
0	3.3	0	0	25.8	24.4	5.4
0.1	3.25	0.05	0.05	27.7	24.3	12.3
0.2	2.9	0.05	0.05	28.3	30.6	8.1
0.3	2.84	0.05	0.05	31.3	31.9	1.9
0.4	2.7	0.1	0.1	33.3	34.2	2.7

Table 5.7. Results from the numerical model prediction of natural frequency when no strain energy is assumed in the compliant beam. The x_{rel} and y_{rel} values were set to be equal to the experimentally measure values as shown in Table 5.6, Set 2.

5.3.4 Conclusions on Pendulum and Magnet Experiment

The goal of these beam experiments was to formally test the design synthesis approach for multi-stable equilibrium systems. A MSE system is a type of adaptive structure. By properly designing the kinematics and potential energy storage elements of a MSE system, one can create a structure that has multiple stable operating regimes. The synthesis approach of this paper was shown to be valid for a system involving magnetostatic, mechanical translational, and mechanical rotational energy domains. This section case study presents the ability to use lumped and field models across multiple energy domains for the synthesis

186

of MSE systems. Although the energetic magnet model has inaccuracies and also limits the design possibilities due to the fact that only two interacting magnets can be considered at a time, this does not detract from the overall design methodology using the total system energy to design the entire system. All one needs is a sufficiently accurate model of all the potential energy storage devices, and the synthesis of MSE systems is possible.

5.4 X-LINK EXPERIMENT – 2 D.O.F.

The experiment described in this section represents a two-degree of freedom situation. The problem involves the coupling of three energy storage domains: mechanical translation, mechanical rotation, and magnetic. The magnetic forces are treated as having field a function only of the configuration of the device. This means that the speed of the device in either kinematic coordinate has negligible impact on varying the magnetic field properties. As will be seen throughout this section, this assumption is not very limiting.

The concept of the experimental linkage mechanism is inspired by the concept of a MSE fish changing its shape and stiffness properties. The idea is to have a short shape with a high natural frequency (like a tuna), and a second long shape with a much lower stiffness, or higher flexibility (like an eel). Keep in mind that only the major qualitative features of the X-link system are sought since the experiment is run in air while resting on a table instead of floating in water.

Figure 5.27 shows a schematic of the experimental mechanism. The MSE system is essentially the 'X-link' shapes and the springs that connect the X-links

to the input links. The two degrees of freedom of the problem are the rotational angles θ and β. The magnets for one of the X-link pieces are shown in Figure 5.27. There are other magnets are on the opposite X-link piece, and combining the two pieces creates the characteristic 'X' shape. The two stable positions for the X-link mechanism are solely created by the magnetic torque between the two X-link pieces. The magnets have their magnetic poles aligned in the x-direction. When β changes, there is a magnetic potential energy change and a resulting torque from the relative changing magnetic configuration between the two X-link pieces. It is this magnetic torque that acts to keep the X-link system from rotating due to all other forces, or torques. See Section 5.4.1.3 for more detail on the magnetic configuration.
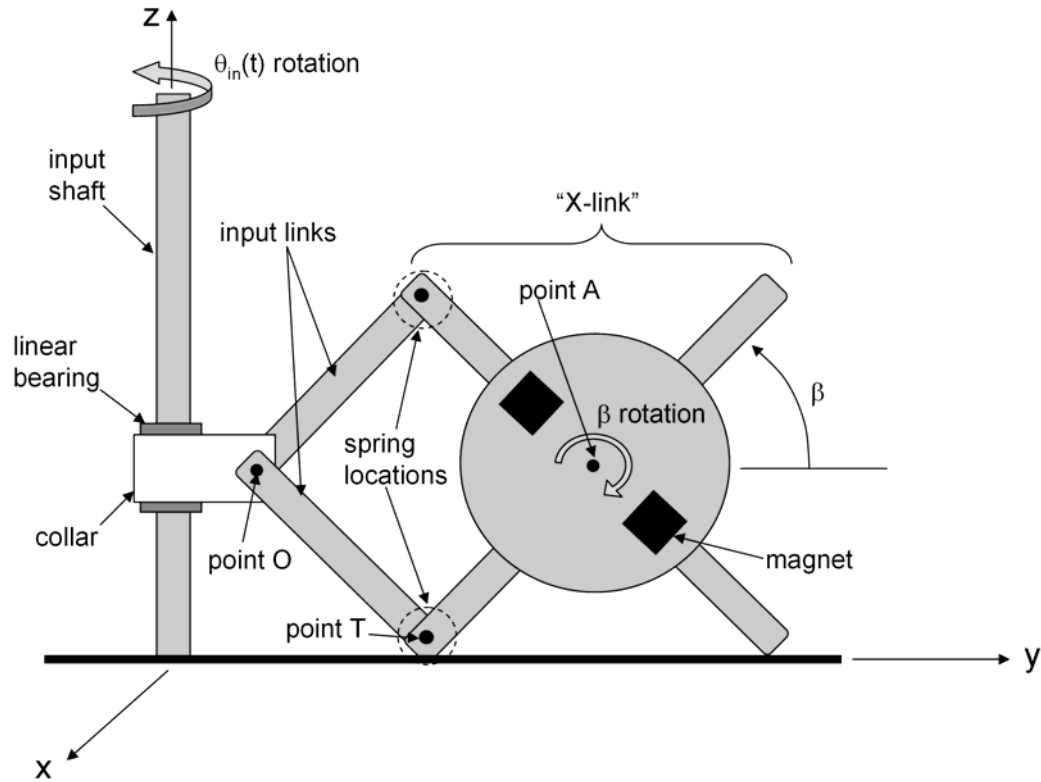
Figure 5.27. Schematic of the X-link experimental system (motor and quick-return driving system not shown).

Figure 5.28 shows a photograph of the experimental setup used to test the MSE X-link mechanism. A coupler connects the input links to a linear bearing that slides vertically along the input shaft. The shaft is a splined shaft driven by a quick-return mechanism which is then in turn actuated by a DC motor (give model name and specs of the motor). A template attached to the shaft of the motor allows the selection of different maximum input angle, $\theta_{in,max}$, magnitudes when actuating the X-link.
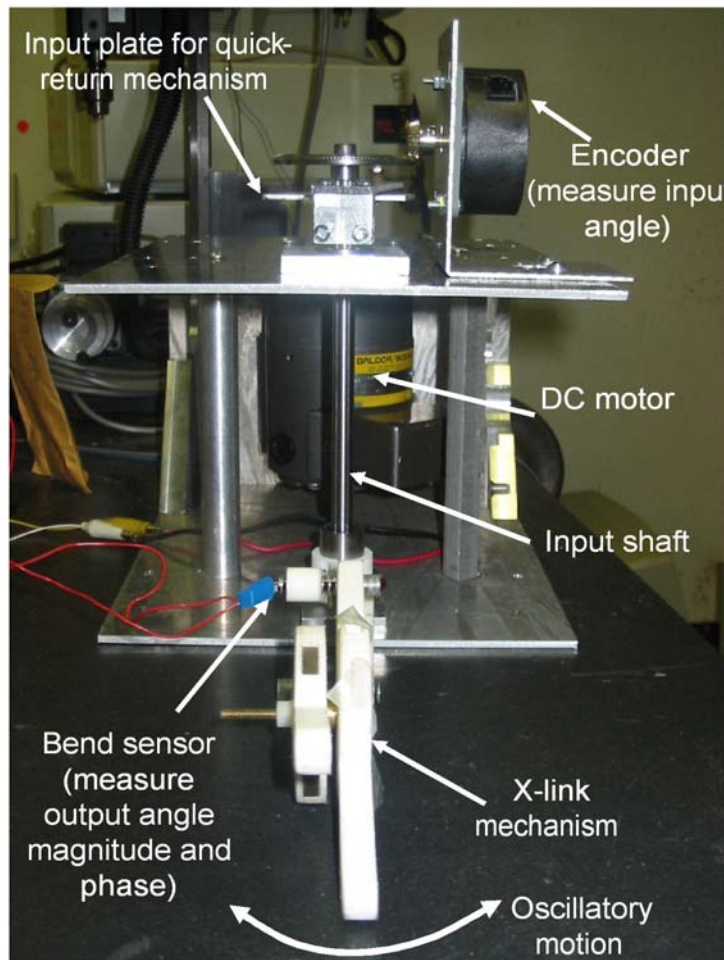
Figure 5.28. Photograph of X-link experimental setup.

The goal of designing the MSE X-link system is to design it such that both the short and the long positions have desired natural frequencies in the θ direction while maintaining each configuration, or β position, when desired. This experiment explores more of the dynamic characteristics of MSE systems, and how they can differ from the static characteristics and predictions. Gathering

system response data as input magnitude and frequency are varied produces information that can be used for deriving control strategies. By matching a computer model to the experimental results, one has a way to predict the dynamic behavior of other X-link systems that have the basic architecture but different parameters such as size, inertia, and spring stiffness. Thus, one can begin to use the model for exploration of control and design enhancements.

Section 5.4.1 derives the model used to simulate the X-link model for subsequent analysis. Section 5.4.2 verifies that the model closely approximates reality as it compares the system model response to experimental results. Section 5.4.3 ends the discussion of the X-link problem by using the model to explore the design aspects of this MSE system, and how simulation can help in design synthesis.

5.4.1 Derivation of X-link model

The dynamic model of the X-link system is derived using Lagrange's equations. Thus, one needs the kinetic coenergy and potential energy as functions of the two kinematic degrees of freedom. The kinetic coenergy and potential energy are shown in Equations (5.11) and (5.12), respectively.

$$
\begin{aligned}
T(\dot{\theta},\theta,\dot{\beta},\beta) = {}& \tfrac{1}{2}I_{zz}(\beta)\left(\dot{\theta}-\dot{\theta}_{in}\right)^2 + \tfrac{1}{2}m_X\,\dot{x}_A^2 + \tfrac{1}{2}m_X\,\dot{y}_A^2 + \dots \\
& \tfrac{1}{2}I_{xx}(\beta)\dot{\beta}^2 + \tfrac{1}{2}(m_X + m_{in\_links})\dot{z}_A^2
\end{aligned}
\tag{5.11}
$$

191

$$V(\theta, \beta) = \tfrac{1}{2} k_{sp} (\theta - \theta_{in})^2 + (m_X + m_{in\_links}) g z_A(\beta) + V_{mag}(\beta) \qquad (5.12)$$

The dot above each kinematic variable in Equations (5.11 and 5.12) denotes its time derivative. Here is a list of symbols used in Equations (5.11 and 5.12):

θ = kinematic variable designating rotational angle about z-axis (see Figure 5.27),

β = kinematic variable designating rotational angle of X-link system about x-axis (this is essentially the angle from any 'leg' of the X shape to the horizontal, or x-y, plane),

θ_{in} = rotational angle of input shaft,

$I_{zz}(\beta)$ = mass moment of inertia of X-link about z-axis,

I_{xx} = mass moment of inertia of X-link about x-axis,

$I_{in\_liinks,xx}$ = mass moment of inertia of input links about x-axis,

m_X = mass of X-link including magnets, screws, and nuts holding it together,

m_{in_links} = mass of input links including screws, coupling, and linear bearing (mass of all things that connect input shaft to X-link),

$x_A = x_A(\theta, \beta)$ = x-location of point A, the center of the X-link,

$y_A = y_A(\theta, \beta)$ = y-location of point A, the center of the X-link,

$z_A = z_A(\beta)$ = z-location of point A, the center of the X-link,

$x_T = x_T(\theta, \beta)$ = x-location of point T, the center of the X-link, and

$y_T = y_T(\theta, \beta)$ = y-location of point T, the center of the X-link,

Note that the mass moment of inertia of the X-link system is assumed independent of the angle θ. This is not entirely true since as θ varies, and the coordinate system is held fixed, the moment of inertia of the X-link with respect to the fixed rectilinear coordinate system will indeed change. This was a simplification made for modeling purposes. In later sections, the dynamic simulation and experimental results show good agreement even with this assumption.

Creating the Lagrangian from Equations (5.11) and (5.12) as L = T − V, one then performs the required derivatives to create the two second order differential equations governing the system motion. Equations (5.13-5.15) show the Lagrangian and the two differential equations that govern the X-link model. The derivation of each component follows. In Equations (5.14) and (5.15) the symbols Q_θ and Q_β represent any non-conservative forces, and there is no input in the β direction.

$$L\left(\theta,\dot{\theta},\beta,\dot{\beta}\right) = T\left(\theta,\dot{\theta},\beta,\dot{\beta}\right) - V(\theta,\beta) \qquad (5.13)$$

$$\frac{d}{dt}\left(\frac{\partial L}{\partial \dot{\theta}}\right) - \frac{\partial L}{\partial \theta} = F_{\theta,in}(t) + Q_\theta \qquad (5.14)$$

$$\frac{d}{dt}\left(\frac{\partial L}{\partial \dot{\beta}}\right) - \frac{\partial L}{\partial \beta} = Q_\beta \qquad (5.15)$$

5.4.1.1 Equation of motion in θ coordinate direction

The derivation of Equation (5.14) is now performed. First one needs the partial derivative with respect to the time derivative of θ. This is shown below in Equation (5.16).

$$\frac{\partial L}{\partial \dot{\theta}} = I_{zz}(\beta)\left(\dot{\theta} - \dot{\theta}_{in}(t)\right) + m_X \dot{x}_A \frac{\partial \dot{x}_A}{\partial \dot{\theta}} + m_X \dot{y}_A \frac{\partial \dot{y}_A}{\partial \dot{\theta}} \qquad (5.16)$$

Now taking the full time derivative of Equation (5.16), one obtains equation (5.17).

$$\frac{d}{dt}\left(\frac{\partial L}{\partial \dot{\theta}}\right) = I_{zz}(\beta)\left(\ddot{\theta} - \ddot{\theta}_{in}(t)\right) + \frac{\partial I_{zz}(\beta)}{\partial \beta}\dot{\beta}\left(\dot{\theta} - \dot{\theta}_{in}(t)\right) + m_X \ddot{x}_A \frac{\partial \dot{x}_A}{\partial \dot{\theta}} + ...$$
$$m_X \dot{x}_A \frac{d}{dt}\left(\frac{\partial \dot{x}_A}{\partial \dot{\theta}}\right) + m_X \ddot{y}_A \frac{\partial \dot{y}_A}{\partial \dot{\theta}} + m_X \dot{y}_A \frac{d}{dt}\left(\frac{\partial \dot{y}_A}{\partial \dot{\theta}}\right) \qquad (5.17)$$

The components of Equation (5.17) are now derived below in equations (5.18-5.21). Equations (5.18-5.20) show the x-position of the X-link center of mass and its velocity and acceleration. Equations (5.21-5.23) represent the same for the y-position of the X-link center of mass. Equations (5.24-5.26) and (5.27-5.29) present the position, velocity, and acceleration of the point T in the x and y directions respectively. Equations (5.30-5.32) show the position, velocity, and

acceleration of the z-direction of the point A needed to account for gravitational effects.

Equation (5.18):

$$x_A = x_T + \tfrac{l}{2}\cos\beta\sin\theta_{in}(t) + \tfrac{l}{2}\cos\beta\sin(\theta - \theta_{in}(t))$$

Equation (5.19):

$$\dot{x}_A = \dot{x}_T - \tfrac{l}{2}\sin\beta\sin\theta_{in}(t)\dot{\beta} + \tfrac{l}{2}\sin\beta\cos\theta_{in}(t)\dot{\theta}_{in} - \ldots$$

$$\tfrac{l}{2}\sin\beta\sin(\theta - \theta_{in}(t))\dot{\beta} + \tfrac{l}{2}\cos\beta\cos(\theta - \theta_{in}(t))\left(\dot{\theta} - \dot{\theta}_{in}(t)\right)$$

Equation (5.20):

$$\ddot{x}_A = \ddot{x}_T - \tfrac{l}{2}\sin\beta\sin\theta_{in}(t)\ddot{\beta} - \tfrac{l}{2}\cos\beta\sin\theta_{in}(t)\dot{\beta}^2 - \tfrac{l}{2}\sin\beta\cos\theta_{in}(t)\dot{\beta}\dot{\theta}_{in} + \ldots$$

$$\tfrac{l}{2}\cos\beta\cos\theta_{in}(t)\ddot{\theta}_{in} - \tfrac{l}{2}\sin\beta\cos\theta_{in}(t)\dot{\beta}\dot{\theta}_{in} - \tfrac{l}{2}\cos\beta\sin\theta_{in}(t)\dot{\theta}_{in}^2 - \ldots$$

$$\tfrac{l}{2}\sin\beta\sin(\theta - \theta_{in}(t))\ddot{\beta} - \tfrac{l}{2}\cos\beta\sin(\theta - \theta_{in}(t))\dot{\beta}^2$$

$$- \tfrac{l}{2}\sin\beta\cos(\theta - \theta_{in}(t))\dot{\beta}\left(\dot{\theta} - \dot{\theta}_{in}\right) + \ldots$$

$$\tfrac{l}{2}\cos\beta\cos(\theta - \theta_{in}(t))\left(\ddot{\theta} - \ddot{\theta}_{in}\right) - \tfrac{l}{2}\sin\beta\cos(\theta - \theta_{in}(t))\dot{\beta}\left(\dot{\theta} - \dot{\theta}_{in}\right) - \ldots$$

$$\tfrac{l}{2}\cos\beta\sin(\theta - \theta_{in}(t))\left(\dot{\theta} - \dot{\theta}_{in}\right)^2$$

Equation (5.21)

$$y_A = y_T + \tfrac{1}{2}\cos\beta\cos\theta_{in}(t) + \tfrac{1}{2}\cos\beta\cos(\theta - \theta_{in}(t))$$

Equation (5.22)

$$\dot{y}_A = \dot{y}_T - \tfrac{1}{2}\sin\beta\cos\theta_{in}(t)\dot{\beta} - \tfrac{1}{2}\cos\beta\sin\theta_{in}(t)\dot{\theta}_{in} - \dots$$
$$\tfrac{1}{2}\sin\beta\cos(\theta - \theta_{in}(t))\dot{\beta} - \tfrac{1}{2}\cos\beta\sin(\theta - \theta_{in}(t))\left(\dot{\theta} - \dot{\theta}_{in}(t)\right)$$

Equation (5.23)

$$\ddot{y}_A = \ddot{y}_T - \tfrac{1}{2}\sin\beta\cos\theta_{in}(t)\ddot{\beta} - \tfrac{1}{2}\cos\beta\cos\theta_{in}(t)\dot{\beta}^2 + \tfrac{1}{2}\sin\beta\sin\theta_{in}(t)\dot{\beta}\dot{\theta}_{in} - \dots$$
$$\tfrac{1}{2}\cos\beta\sin\theta_{in}(t)\ddot{\theta}_{in} + \tfrac{1}{2}\sin\beta\sin\theta_{in}(t)\dot{\beta}\dot{\theta}_{in} - \tfrac{1}{2}\cos\beta\cos\theta_{in}(t)\dot{\theta}_{in}^2 - \dots$$
$$\tfrac{1}{2}\sin\beta\cos(\theta - \theta_{in}(t))\ddot{\beta} - \tfrac{1}{2}\cos\beta\cos(\theta - \theta_{in}(t))\dot{\beta}^2 + \dots$$
$$\tfrac{1}{2}\sin\beta\sin(\theta - \theta_{in}(t))\dot{\beta}\left(\dot{\theta} - \dot{\theta}_{in}\right) - \dots$$
$$\tfrac{1}{2}\cos\beta\sin(\theta - \theta_{in}(t))\left(\ddot{\theta} - \ddot{\theta}_{in}\right) + \tfrac{1}{2}\sin\beta\sin(\theta - \theta_{in}(t))\dot{\beta}\left(\dot{\theta} - \dot{\theta}_{in}\right) - \dots$$
$$\tfrac{1}{2}\cos\beta\cos(\theta - \theta_{in}(t))\left(\dot{\theta} - \dot{\theta}_{in}\right)^2$$

The location of point T is the true input point to the X-link mechanism, and its derivation is shown below. First, the x-direction input in terms of the independent coordinates.

Equation (5.24)

$$x_T = \left(y_o + \frac{l}{2}\cos\beta\right)\sin\theta_{in}(t)$$

Equation (5.25)

$$\dot{x}_T = \left(y_o + \frac{l}{2}\cos\beta\right)\cos\theta_{in}(t)\dot{\theta}_{in} - \frac{l}{2}\sin\theta_{in}(t)\sin\beta\,\dot{\beta}$$

Equation (5.26)

$$\ddot{x}_T = \left(y_o + \frac{l}{2}\cos\beta\right)\left(\cos\theta_{in}(t)\ddot{\theta}_{in} - \sin\theta_{in}(t)\dot{\theta}_{in}^2\right) - l\sin\beta\cos\theta_{in}(t)\dot{\theta}_{in}\,\dot{\beta} - \ldots$$

$$\frac{l}{2}\cos\beta\sin\theta_{in}(t)\dot{\beta}^2 - \frac{l}{2}\sin\beta\sin\theta_{in}(t)\ddot{\beta}$$

Now the y-direction input in terms of θ and β,

Equation (5.27)

$$y_T = \left(y_o + \frac{l}{2}\cos\beta\right)\cos\theta_{in}(t)$$

Equation (5.28)

$$\dot{y}_T = -\left(y_o + \frac{l}{2}\cos\beta\right)\sin\theta_{in}(t)\dot{\theta}_{in} - \frac{l}{2}\cos\theta_{in}(t)\sin\beta\,\dot{\beta}$$

Equation (5.29)

$$\ddot{y}_T = -\left(y_o + \frac{l}{2}\cos\beta\right)\left(\sin\theta_{in}(t)\ddot{\theta}_{in} + \cos\theta_{in}(t)\dot{\theta}_{in}^2\right) + l\sin\beta\sin\theta_{in}(t)\dot{\theta}_{in}\,\dot{\beta} - \ldots$$

$$\frac{l}{2}\cos\beta\cos\theta_{in}(t)\dot{\beta}^2 - \frac{l}{2}\sin\beta\cos\theta_{in}(t)\ddot{\beta}$$

Finally, the z-position of the center of the X-link structure, needed to account for the force of gravity acting on the mechanism, is presented in equations (5.30-5.32).

$$z_A = \frac{1}{2}\sin\beta \qquad\qquad\qquad (5.30)$$

$$\dot{z}_A = \frac{1}{2}\cos\beta\,\dot{\beta} \qquad\qquad\qquad (5.31)$$

$$\ddot{z}_A = \frac{1}{2}\cos\beta\,\ddot{\beta} - \frac{1}{2}\sin\beta\,\dot{\beta}^2 \qquad\qquad (5.32)$$

Further terms needed in Equation (5.17) are the partial derivative of the mass inertia about the z-axis with respect to β. Due to β changing rather slowly in general, I assume this quantity is negligible. This assumption is shown in Equation (5.33). This does not mean that $I_{zz}(\beta)$ is not a function of β. This quantity is still allowed to vary as the X-link changes orientation, or length. The rest of the terms needed in Equation (5.17) are shown in equations (5.34-5.37).

$$\frac{\partial I_{zz}(\beta)}{\partial\beta} \cong 0 \quad (5.33)$$

$$\frac{\partial\dot{x}_A}{d\dot{\theta}} = \frac{\partial\dot{x}_T}{d\dot{\theta}} + \frac{1}{2}\cos\beta\cos(\theta-\theta_{in}(t)) = \frac{1}{2}\cos\beta\cos(\theta-\theta_{in}(t)) \qquad (5.34)$$

$$\frac{d}{dt}\left(\frac{\partial\dot{x}_A}{d\dot{\theta}}\right) = -\frac{1}{2}\sin\beta\cos(\theta-\theta_{in}(t))\dot{\beta} - \frac{1}{2}\cos\beta\sin(\theta-\theta_{in}(t))\left(\dot{\theta}-\dot{\theta}_{in}\right) \quad (5.35)$$

$$\frac{\partial\dot{y}_A}{d\dot{\theta}} = \frac{\partial\dot{y}_T}{d\dot{\theta}} - \frac{1}{2}\cos\beta\sin(\theta-\theta_{in}(t)) = -\frac{1}{2}\cos\beta\sin(\theta-\theta_{in}(t)) \quad (5.36)$$

$$\frac{d}{dt}\left(\frac{\partial\dot{y}_A}{d\dot{\theta}}\right) = \frac{1}{2}\sin\beta\sin(\theta-\theta_{in}(t))\dot{\beta} - \frac{1}{2}\cos\beta\cos(\theta-\theta_{in}(t))\left(\dot{\theta}-\dot{\theta}_{in}\right) \quad (5.37)$$

198

Now all terms of Equation (5.17) have been obtained. The partial of the Lagrangian with respect to θ is needed. Equation (5.38) shows this, where k is combined spring constant of the springs that connect the input links to the X-link.

$$\frac{\partial L}{\partial \theta} = m_A \dot{x}_A \frac{\partial \dot{x}_A}{\partial \theta} + m_A \dot{y}_A \frac{\partial \dot{y}_A}{\partial \theta} - k(\theta - \theta_{in}(t)) \qquad (5.38)$$

The underived quantities of Equation (5.38) not previously derived are shown below in equations (5.39) and (5.40).

$$\frac{\partial \dot{x}_A}{\partial \theta} = \frac{\partial \dot{x}_T}{\partial \theta} - \frac{1}{2}\sin\beta\cos(\theta - \theta_{in}(t))\dot{\beta} - \frac{1}{2}\cos\beta\sin(\theta - \theta_{in}(t))\left(\dot{\theta} - \dot{\theta}_{in}\right) \qquad (5.39)$$
$$= -\frac{1}{2}\sin\beta\cos(\theta - \theta_{in}(t))\dot{\beta} - \frac{1}{2}\cos\beta\sin(\theta - \theta_{in}(t))\left(\dot{\theta} - \dot{\theta}_{in}\right)$$

$$\frac{\partial \dot{y}_A}{\partial \theta} = \frac{\partial \dot{y}_T}{\partial \theta} + \frac{1}{2}\sin\beta\sin(\theta - \theta_{in}(t))\dot{\beta} - \frac{1}{2}\cos\beta\cos(\theta - \theta_{in}(t))\left(\dot{\theta} - \dot{\theta}_{in}\right) \qquad (5.40)$$
$$= \frac{1}{2}\sin\beta\sin(\theta - \theta_{in}(t))\dot{\beta} - \frac{1}{2}\cos\beta\cos(\theta - \theta_{in}(t))\left(\dot{\theta} - \dot{\theta}_{in}\right)$$

Now every factor needed to write Equation (5.14) is known. The next section derives the factors needed for Equation (5.15).

5.4.1.2 Equation of motion in β coordinate direction

The derivation of Equation (5.15) is now performed. First one needs the partial derivative with respect to the time derivative of β. This is shown below in

Equation (5.41). The assumption that I_{xx} and $I_{in\_links,xx}$ are not functions of β has been made.

$$\frac{\partial L}{\partial \dot{\beta}} = m_A \dot{x}_A \frac{\partial \dot{x}_A}{\partial \dot{\beta}} + m_A \dot{y}_A \frac{\partial \dot{y}_A}{\partial \dot{\beta}} + \left(I_{xx} + I_{in\_links,xx}\right)\dot{\beta} + ..$$

$$\left(m_A + m_{in\_links}\right)\dot{z}_A \frac{\partial \dot{z}_A}{\partial \dot{\beta}}$$

(5.41)

Previously underived terms of Equation (5.41) are shown below in equations (5.42-5.44).

$$\frac{\partial \dot{x}_A}{\partial \dot{\beta}} = -\left(l_{in} + \frac{l}{2}\right)\sin\theta_{in}(t)\sin\beta - \frac{l}{2}\sin\beta\sin\left(\theta - \theta_{in}(t)\right)$$

(5.42)

$$\frac{\partial \dot{y}_A}{\partial \dot{\beta}} = -\left(l_{in} + \frac{l}{2}\right)\cos\theta_{in}(t)\sin\beta - \frac{l}{2}\sin\beta\cos\left(\theta - \theta_{in}(t)\right)$$

(5.43)

$$\frac{\partial \dot{z}_A}{\partial \dot{\beta}} = \frac{l}{2}\cos\beta$$

(5.44)

Now taking the full time derivative of Equation (5.41), one obtains Equation (5.45).

$$\frac{d}{dt}\left(\frac{\partial L}{\partial \dot{\beta}}\right) = m_A \ddot{x}_A \frac{\partial \dot{x}_A}{\partial \dot{\beta}} + m_A \dot{x}_A \frac{d}{dt}\left(\frac{\partial \dot{x}_A}{\partial \dot{\beta}}\right) + m_A \ddot{y}_A \frac{\partial \dot{y}_A}{\partial \dot{\beta}} + m_A \dot{y}_A \frac{d}{dt}\left(\frac{\partial \dot{y}_A}{\partial \dot{\beta}}\right) + ...$$

$$m_A \ddot{x}_A \frac{\partial \dot{x}_A}{\partial \dot{\beta}} + m_A \dot{z}_A \frac{d}{dt}\left(\frac{\partial \dot{z}_A}{\partial \dot{\beta}}\right) + \left(I_{xx} + I_{in\_links,xx}\right)\ddot{\beta}$$

(5.45)

200

Previously underived quantities of Equation (5.45) are shown below in equations (5.46-5.48).

$$\frac{d}{dt}\left(\frac{\partial \dot{x}_A}{\partial \dot{\beta}}\right) = -\left(l_{in} + \frac{1}{2}\right)\cos\theta_{in}(t)\sin\beta\,\dot{\theta}_{in} - \left(l_{in} + \frac{1}{2}\right)\sin\theta_{in}(t)\cos\beta\,\dot{\beta} - \ldots$$

$$\frac{1}{2}\cos(\theta - \theta_{in}(t))\sin\beta\left(\dot{\theta} - \dot{\theta}_{in}\right) - \frac{1}{2}\sin(\theta - \theta_{in}(t))\cos\beta\,\dot{\beta}$$

(5.46)

$$\frac{d}{dt}\left(\frac{\partial \dot{y}_A}{\partial \dot{\beta}}\right) = \left(l_{in} + \frac{1}{2}\right)\sin\theta_{in}(t)\sin\beta\,\dot{\theta}_{in} - \left(l_{in} + \frac{1}{2}\right)\cos\theta_{in}(t)\cos\beta\,\dot{\beta} + -\ldots$$

$$\frac{1}{2}\sin(\theta - \theta_{in}(t))\sin\beta\left(\dot{\theta} - \dot{\theta}_{in}\right) - \frac{1}{2}\cos(\theta - \theta_{in}(t))\cos\beta\,\dot{\beta}$$

(5.47)

$$\frac{d}{dt}\left(\frac{\partial \dot{z}_A}{\partial \dot{\beta}}\right) = -\frac{1}{2}\sin\beta\,\dot{\beta}$$

(5.48)

Now one needs the partial of the Lagrangian with respect to β. This is shown below in Equation (5.49). The parameter g is gravitational acceleration.

$$\frac{\partial L}{\partial \beta} = \frac{1}{2}\left(\dot{\theta} - \dot{\theta}_{in}\right)^2 \frac{\partial I_{zz}(\beta)}{\partial \beta} + m_A \dot{x}_A\left(\frac{\partial \dot{x}_A}{\partial \beta}\right) + m_A \dot{y}_A\left(\frac{\partial \dot{y}_A}{\partial \beta}\right) + \ldots$$

$$\left(m_A + m_{in\_links}\right)\dot{z}_A\left(\frac{\partial \dot{z}_A}{\partial \beta}\right) - \left(m_A + m_{in\_links}\right)g\left(\frac{\partial z_A}{\partial \beta}\right) - \frac{\partial V_{mag}(\beta)}{\partial \beta}$$

(5.49)

201

Previously underived factors of Equation (5.49) are now shown in equations (5.50-5.55). Note this derivation assumes that the partial with respect to of the mass inertia in the z-direction is calculated numerically, such as by forward differencing. Thus we do not show a functional form of this term from Equation (5.49).

$$\frac{\partial \dot{x}_A}{\partial \beta} = \frac{\partial \dot{x}_T}{\partial \beta} - \left(l_{in} + \frac{1}{2}\right)\cos\beta\sin\theta_{in}(t)\dot{\beta} - \left(l_{in} + \frac{1}{2}\right)\sin\beta\cos\theta_{in}(t)\dot{\theta}_{in} - \ldots$$
$$\frac{1}{2}\cos\beta\sin(\theta - \theta_{in}(t))\dot{\beta} - \frac{1}{2}\sin\beta\cos(\theta - \theta_{in}(t))\left(\dot{\theta} - \dot{\theta}_{in}(t)\right) \tag{5.50}$$

$$\frac{\partial \dot{x}_T}{\partial \beta} = l_{in}\sin\beta\cos\theta_{in}(t)\dot{\theta}_{in} - l_{in}\cos\beta\sin\theta_{in}(t)\dot{\beta} \tag{5.51}$$

$$\frac{\partial \dot{y}_A}{\partial \beta} = \frac{\partial \dot{y}_T}{\partial \beta} - \left(l_{in} + \frac{1}{2}\right)\cos\beta\cos\theta_{in}(t)\dot{\beta} - \left(l_{in} + \frac{1}{2}\right)\sin\beta\sin\theta_{in}(t)\dot{\theta}_{in} + \ldots$$
$$\frac{1}{2}\cos\beta\cos(\theta - \theta_{in}(t))\dot{\beta} + \frac{1}{2}\sin\beta\sin(\theta - \theta_{in}(t))\left(\dot{\theta} - \dot{\theta}_{in}(t)\right) \tag{5.52}$$

$$\frac{\partial \dot{y}_T}{\partial \beta} = l_{in}\sin\beta\sin\theta_{in}(t)\dot{\theta}_{in} - l_{in}\cos\beta\cos\theta_{in}(t)\dot{\beta} \tag{5.53}$$

$$\frac{\partial \dot{z}_A}{\partial \beta} = -\frac{1}{2}\sin\beta\dot{\beta} \tag{5.54}$$

$$\frac{\partial z_A}{\partial \beta} = \frac{1}{2}\cos\beta \tag{5.55}$$

5.4.1.3 Derivation of $V_{mag}(\beta)$

This section derives a magnetic energy model, and associated magnetic torque, for the permanent magnets that create the two statically stable positions of the X-link model. As the X-link system is defined, the magnets are always at a fixed distance apart. In other words, there are magnets in each of the two pieces of Figure 5.29 that combine to form the 'X' shape, and these two pieces have magnets that are separated by some gap depicted in Figure 5.4.3. The larger this gap is, the less attraction the magnets possess, and therefore the less torque they impart in the β-direction. Figure 5.29 also shows that the magnets are attractive by specifying their magnetic North-South pole orientations.
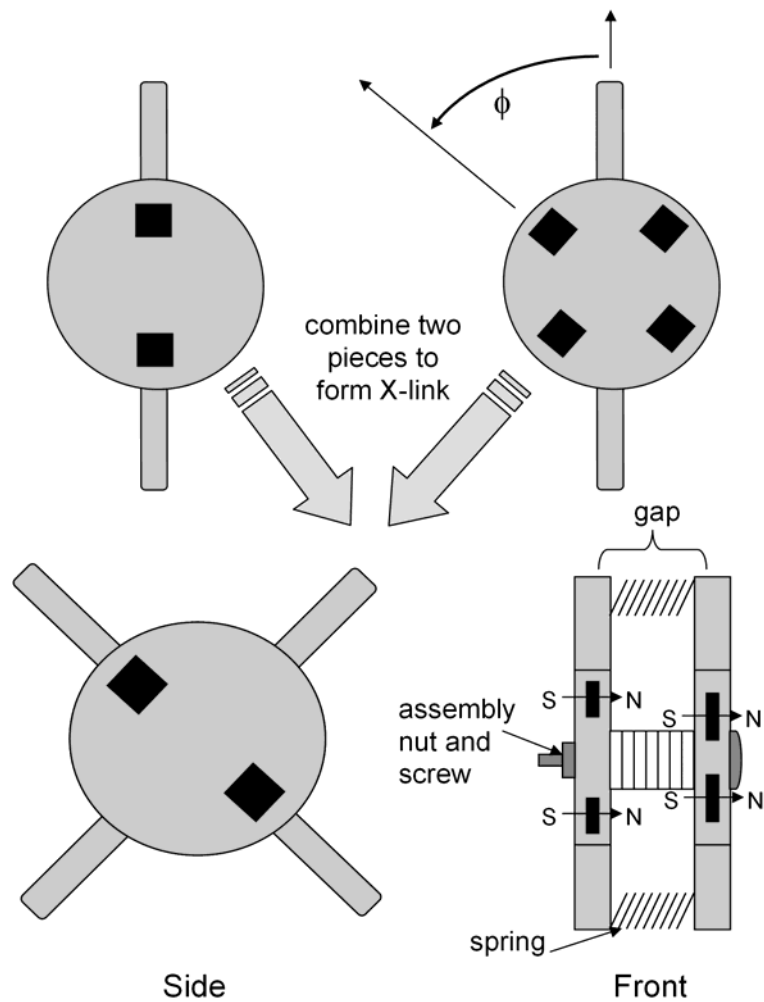
Figure 5.29. Schematic of how magnets are oriented in X-link.

The static stable positions are primarily dictated by the fixed angle ϕ shown in Figure 5.29. Neglecting gravity, or orienting the X-link such that gravity acts in the same direction as the magnetic forces, the angle ϕ solely characterizes the two stable positions. In this case, each stable position occurs when two magnets 180° apart on the four-magnet piece align with the two magnets on the

other piece of the X-link. When gravity is acting to essentially 'squash' the X-link, the stable positions are compromised. If the gap between the magnets is too great, then the magnetic torque is smaller than the torque due to gravitational forces, and the X-link system cannot maintain what would be a stable position without gravity.

In obtaining the magnet model, the X-link was assembled for different gap distances. The torque was then measured as a function of angular orientation, β, for a set X-link piece that is characterized by the angle ϕ shown in Figure 5.29. Once torque and β values are known for full motion of the X-link, then those values are integrated to obtain the magnetic energy curve. These curves were obtained for 3 different angles of ϕ, 30°, 45°, and 60°. Due to the symmetry of the magnetic orientation, the 30° case and the 60° case are sort of 'mirror images' of each other where they have the same torque values being offset by 90°.

The magnets used in the X-link model are identical NdFeB magnets from McMaster-Carr, part # 5848K32 Grade 37. They are of dimension 0.5" x 0.5" x 0.21". The force of Figure 5.30 was obtained using a Honeywell micro switch force sensor, model number FSL05N2C. Figure 5.31 shows the measured torque values, and Figure 5.32 shows the corresponding energy curves. Again recall that if gravity does not affect the X-link system, then the stable β positions are at the locations of minimum energy. In both figures, the '+', '•', and '*' marks represent $\phi = 30^o$, 45°, and 60° situations, respectively.
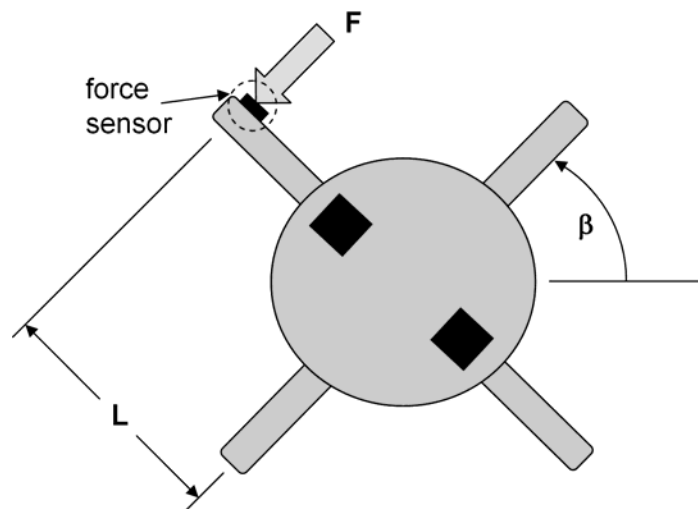
Figure 5.30. Schematic showing how magnetic torque was measured to obtain magnetic energy model.
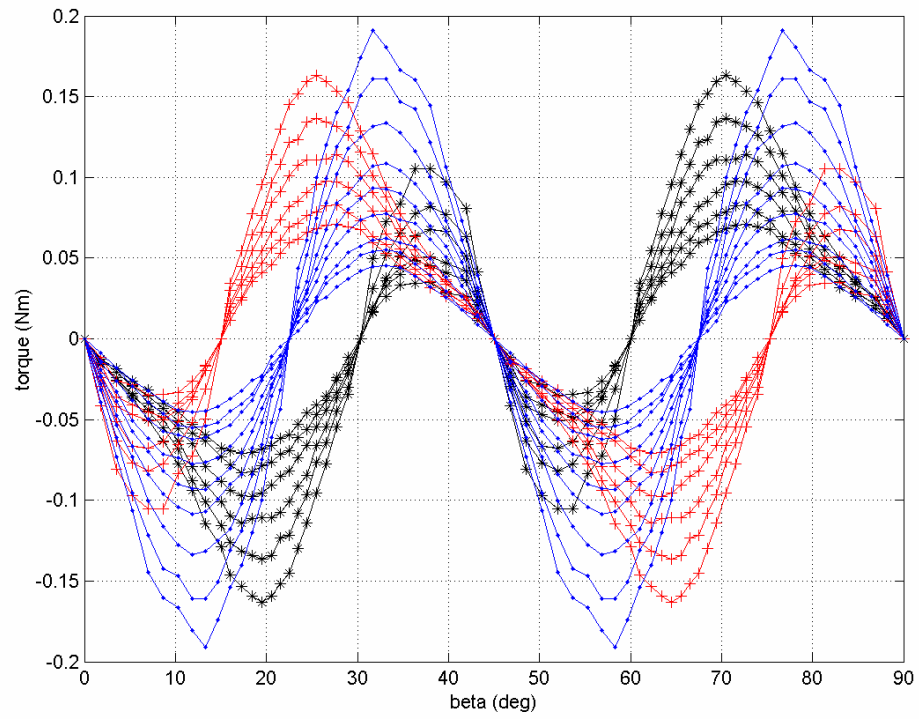
Figure 5.31. Measured magnetic torque of X-link. The '+', '•', and '∗' marks represent $\phi = 30^o$, 45°, and 60° situations, respectively.
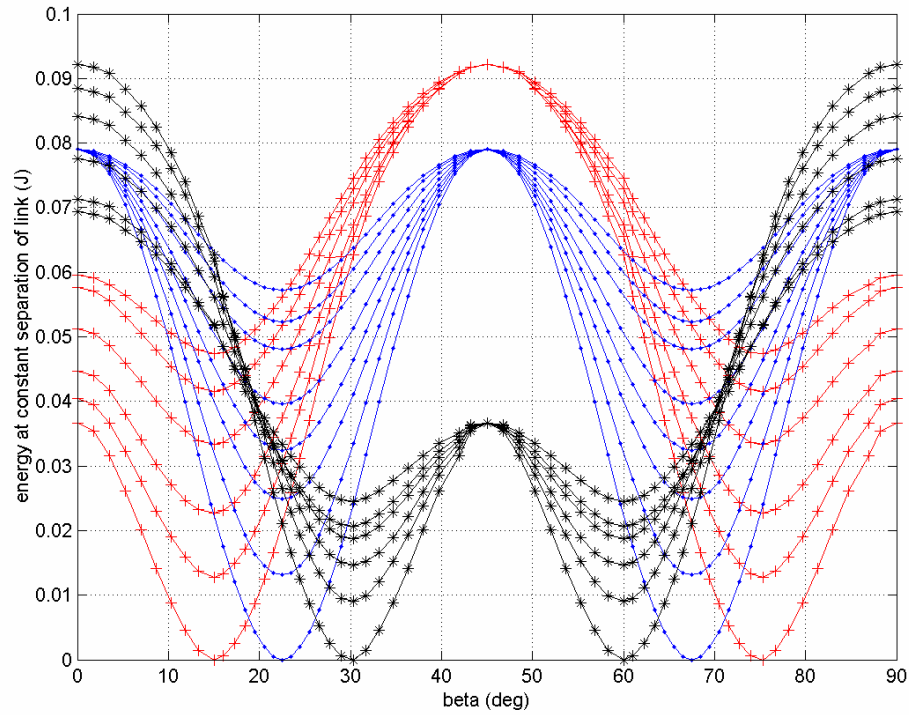
Figure 5.32. Magnetic energy for the X-link derived from torque measurements. The '+', '•', and '*' marks represent $\phi = 30^o$, 45°, and 60° situations, respectively.

Recall that the magnetic energy model used for the X-link is only a function of β, and not the gap between the magnets. Hence the energy values in Figure 5.32 at constant ϕ have the same maximum energy. This is not the true case if one were to measure the force required to increase the gap between the magnets. Since changing the gap distance of the X-link is not considered fixed once it is chosen, an energy model accounting for this variation is not needed.

208

5.4.2 Calibration of Model with Experimental Results

In the previous section 5.4.1, the entire X-link model was developed for dynamic simulation. The results of this model are now compared to some experimental results for the case of the $\phi = 45^{\circ}$ magnet configuration. The main criteria that will be used to compare the model with the experiment are mostly qualitative. The predicted magnitude at various given excitation frequency and input magnitudes are compared. The magnitude of the output is measured using a bending sensor. The sensor is made by Flexpoint. The sensor is placed in the center of the helical springs that provide the compliance between the input links and the X-link. Thus, the sensor measures the relative angle between the input angle, $\theta_{in}(t)$, and absolute angle, θ, of the X-link.

Mostly this calibration of the model to the experiment involves finding correct values for friction factors and the bending spring constant of the coil springs. In the model, there are two forms of friction added in each kinematic degree of freedom: coulombic and viscous friction. Equation (5.56) shows the basic forms of these friction models, where q is used as a generic kinematic variable. Both friction terms act in the direction opposite to the motion. Some sources of friction in the experiment are rubbing between screws and nuts used to attach the X-link together and to the input shaft. The sliding friction of the system on the table is the most dominant, mostly affecting the θ direction, but also significant for the β direction. F_N is the normal force to surface and μ is the friction coefficient for coulombic friction.

$$Q_q = Q_{coulombic} + Q_{viscous}$$

$$= \mu F_N \text{sign}\left(\dot{q}\right) + b\dot{q} \qquad (5.56)$$

The input to the experiment is a quick-return mechanism, rather than a purely sinusoidal input. This is relatively unimportant as a sinusoidal input is not necessary to analyze the general nature of the device, and for small motion the quick-return mechanism produces very close to sinusoidal motion. One can still gain an appreciative feel for the output magnitude response versus input frequency using the quick-return mechanism. It is also easier and cheaper to construct than the typical sinusoidal input mechanism, the Scotch-Yoke. Given a model that mimics the experiment using a quick-return, one can be confident of the simulated results when simulating a sinusoidal input if that is needed.

Since the input angle, velocity, and acceleration are needed in the equations of motion, they are derived here for the quick-return mechanism shown in Figure 5.33. The input to the X-link, $\theta_{in}(t)$, is given in Equation (5.57). Using the location, (x_Q, y_Q), of the input pin given in equations (5.58) and (5.59) one can derive the input angle as a function of known parameters.

$$\theta_{in}(t) = \sin^{-1}\left(\frac{x_Q}{r_B}\right) = \sin^{-1}\left(\frac{x_Q}{\sqrt{x_Q^2 + y_Q^2}}\right) \qquad (5.57)$$

$$x_Q = r\cos(\omega_{motor}t) \qquad (5.58)$$

$$y_Q = R + r\sin(\omega_{motor}t) \qquad (5.59)$$

210
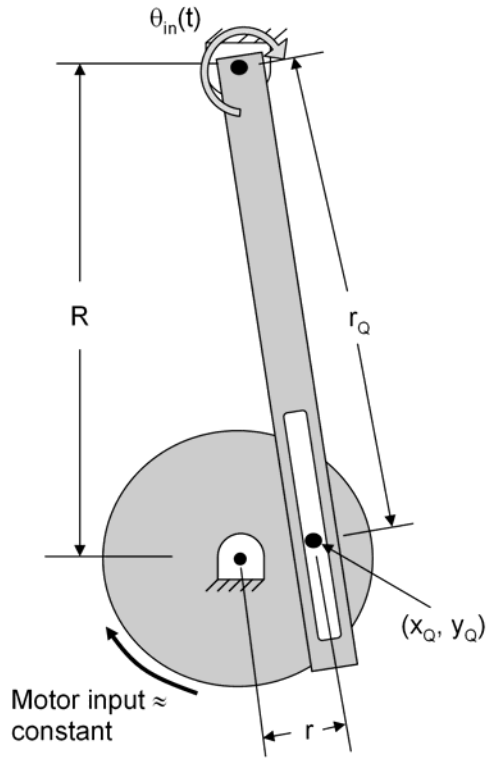
Figure 5.33. Quick-return mechanism schematic showing the location of the input to the X-link mechanism.

The first and second time derivatives of Equation (5.57) provide the other necessary input factors needed for the equations of motion. The velocity and acceleration of the input angle are depicted in equations (5.60) and (5.61), respectively. The argument of the inverse sine function in Equation (5.57) and its first and second time derivative are needed. These are given by equations (5.52 - 5.54) where the argument is represented as 'A'.

$$\dot{\theta}_{in}(t) = \left(\frac{1}{\sqrt{1 - A^2}} \right) \frac{dA}{dt} \qquad (5.60)$$

$$\ddot{\theta}_{in}(t) = \left(\frac{1}{\sqrt{1-A^2}}\right)\frac{d^2A}{dt^2} + \frac{\left(\frac{dA}{dt}\right)^2 A}{\left[1-A^2\right]^{3/2}} \qquad (5.61)$$

$$A = \frac{\cos(\omega_{motor}t)}{\sqrt{\left(R/r\right)^2 + 1 + 2\,\frac{R}{r}\sin(\omega_{motor}t)}} = \frac{\cos(\omega_{motor}t)}{den^{1/2}} \qquad (5.62)$$

$$\frac{dA}{dt} = \frac{-\omega_{motor}\sin(\omega_{motor}t)}{den^{1/2}} - \frac{\frac{R}{r}\omega_{motor}\cos^2(\omega_{motor}t)}{den^{3/2}} \qquad (5.63)$$

$$\frac{d^2A}{dt^2} = \frac{-den\,\omega_{motor}^2\cos(\omega_{motor}t) + \omega_{motor}^2\sin(\omega_{motor}t)\cos(\omega_{motor}t)\frac{R}{r}}{den^{3/2}} + ...$$

$$\frac{2\omega_{motor}^2\,den\,\frac{R}{r}\sin(\omega_{motor}t)\cos(\omega_{motor}t) + 3\omega_{motor}^2\left(\frac{R}{r}\right)^2\cos^3(\omega_{motor}t)}{den^{5/2}} \qquad (5.64)$$

5.4.2.1 Simulation with β fixed

First calibration of the model is performed with one of the kinematic degrees of freedom, β, fixed. This allows the tweaking of the friction factors for the θ-direction to be done independently of the bistable nature of the design. After several iterations of friction factors and spring constant values, the model performs well with $k = 0.1$ Nm/rad, $\mu_\theta = 0.002$ Nm, $b_\theta = 0.002$ Nm-s, $\mu_\beta = $ 1e-4 Nm, and $b_\beta = 0.1$ Nm-s.

Here are some results are shown where the X-link is held fixed in its 'short' stable position. This short position is defined by the largest stable β value dictated by the magnetic energy developed in the last section. This is called short because as β increases, the length (in y-direction) of the X-link system decreases, or gets shorter. Conversely, the 'long' X-link stable position is dictated by the smallest stable β value.

Figures 5.34-5.37 below are the magnitude versus frequency plots of the simulated versus measured response for the X-link model for various run cases when $\phi = 45^{\text{o}}$. When $\phi = 45^{\text{o}}$, the short X-link configuration is at $\beta = 67.5^{\text{o}}$. As can be seen, the qualitative nature of the problem is simulated well. The peaks for the experimental measurements are abnormally high due to the nature of the sensor used. The Flexpoint sensor measures bending mostly in one direction, and the output magnitude depends upon angle bent and radius of curvature. Thus, obtaining any specific numbers from the sensor is quite difficult. Nonetheless, its sleek design makes it appropriate for this application where the qualitative response is most important.

Figures 5.34 and 5.35 are experimental cases of the X-link being in the short position where the maximum input angle is approximately 1.8 degrees, and the magnets are separated by 1.6 cm. The frequency of actuation is stepped incrementally past the peak magnitude response, representing a resonant frequency of the device. Each time the input frequency is increased, the response is allowed to reach steady state. Figure 5.36 shows the output angle of the X-link and how it goes to steady state. Each input frequency is simulated for four

213

seconds to allow steady state response to occur. Figure 5.36 is typical of many of the responses.
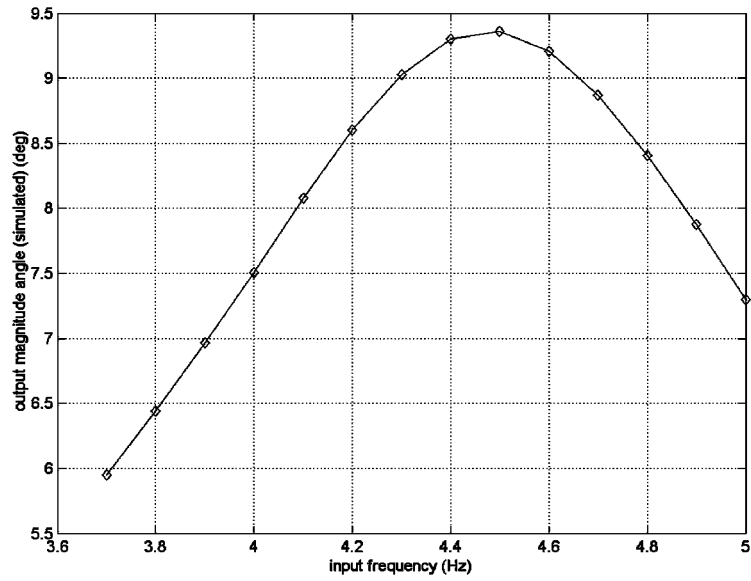
Figure 5.34. Simulated result of magnitude versus frequency for X-link with $\theta_{in,max} = 1.8^{o}$, and fixed in 'short' position.
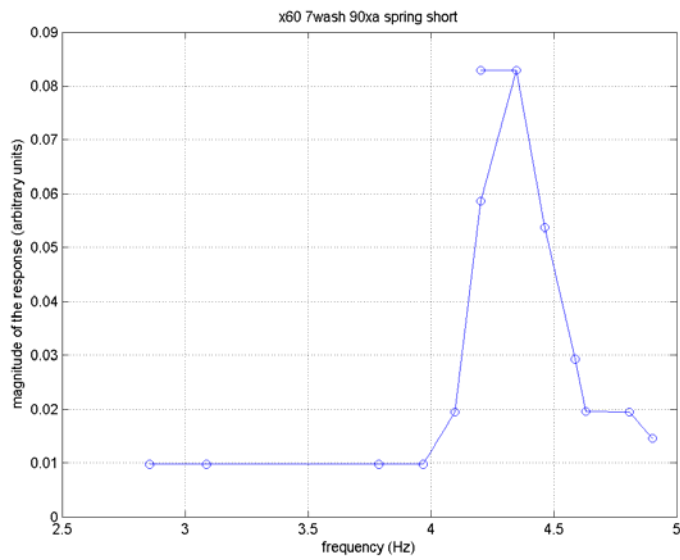
Figure 5.35. Experimental results of magnitude versus frequency for X-link with $\theta_{in,max} = 1.8^{o}$.

To see the effects of dissipation and friction in the response of the mechanism a simulation can be run with no damping. Figure 5.37 shows this case. The peak magnitude is shifted toward higher frequencies as expected from linear system theory. The ramifications for this reality are discussed later in Section 5.4.3.
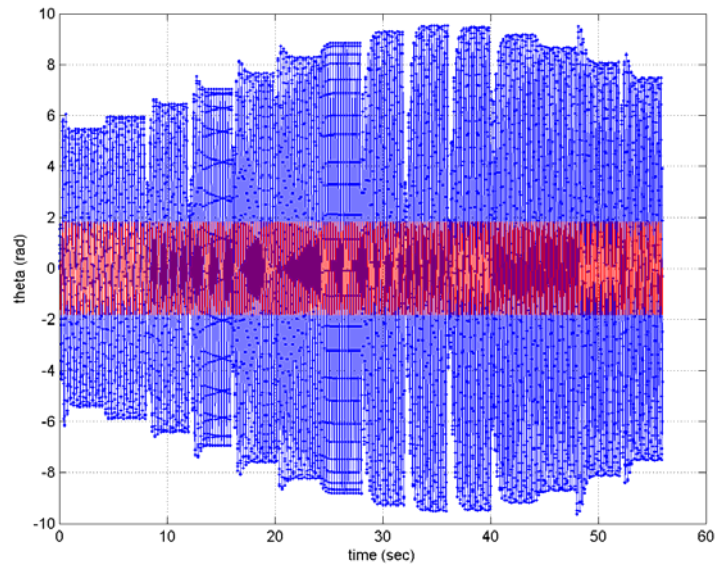
Figure 5.36. Simulated output angle versus time for the same case depicted in Figure 5.34.
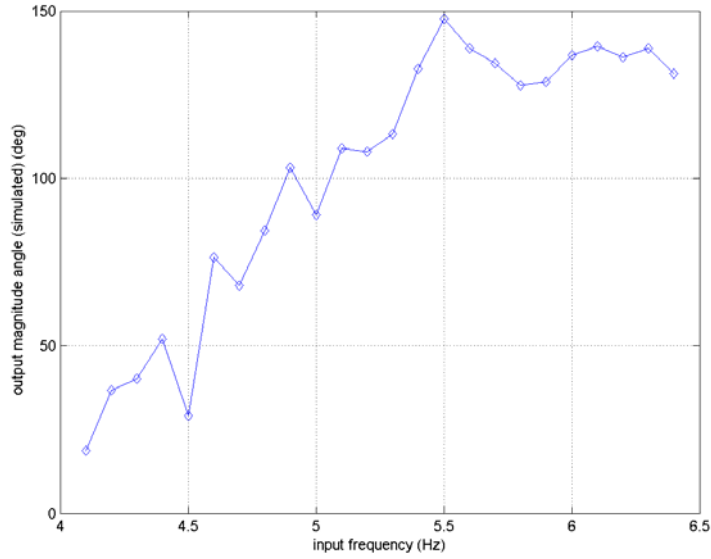
Figure 5.37. Simulated magnitude versus input frequency response for same case as in Figure 5.34.

Comparable responses for the long stable position of the X-link model are also shown in Figures 5.38 – 5.41. The long position for the case of $\phi = 45^o$ is characterized by $\beta = 22.5^o$. Figure 5.38 shows the simulated response with the proper damping, and Figure 5.39 shows the experimentally measured response for the same input parameters. These show the same qualitative correspondence with each other again verifying that the model is working well.
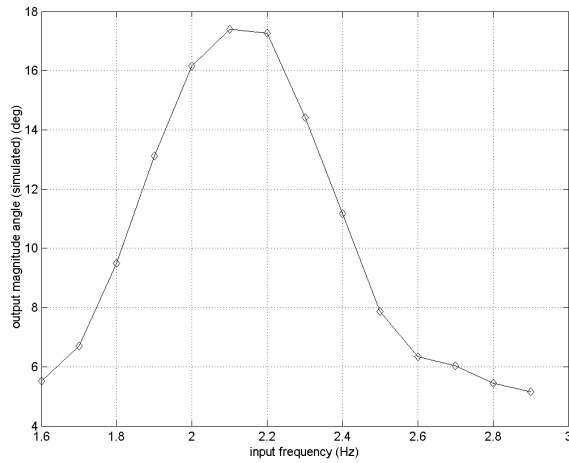
Figure 5.38. Simulated magnitude versus frequency response of X-link in the long position with $\theta_{in,max} = 1.8^{\circ}$.
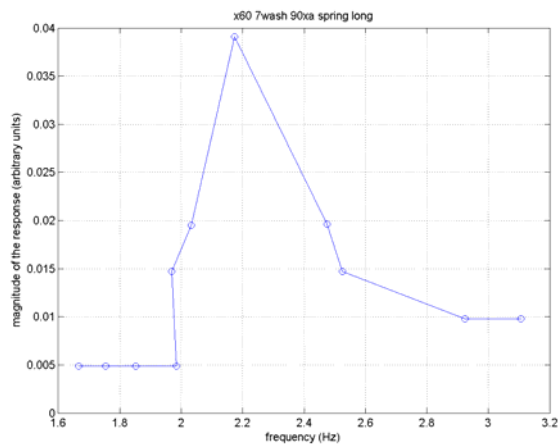
Figure 5.39. Experimental magnitude versus frequency response of the X-link under same circumstances as Figure 5.38 with $\theta_{in,max} = 1.8^{\circ}$.

5.4.2.2 Simulation with full model, β not fixed

After the simulated frictional values were tuned to obtain responses shown in the experimental configuration, the β degree of freedom is allowed to vary with the dynamics of the problem. Now a full X-link system model is simulated, and the responses are compared with the experimental results. Now not only does the oscillation in the θ-direction need to match with experimental results, but so does the β-direction motion. Intuitively, one can visualize that if enough excitation is input to the system, the X-link will move from the short position to the long position. This can mainly be attributed to the centripetal 'extending' forces from the input overcoming the magnetic 'holding' force that enables the bistability.

Figure 5.40 shows a simulated case where the X-link stays in its short position without transitioning to the long position. Figure 5.40a shows the magnitude versus frequency plot of the angle, θ. Figures 5.40b and 5.40c show the time response of β and θ, respectively. Notice how at the maximum amplitude for θ, there is the lowest β value of about 62°, meaning that is the longest configuration of the X-link. Figure 5.41 shows the corresponding experimental results. Again, the input has some fixed $\theta_{in,max}$, and the input frequency is incrementally stepped through the resonant frequency while allowing steady state to be achieved before stepping to the next frequency. For Figures 5.40 and 5.41, the magnetic gap is approximately 1.3 cm, and $\theta_{in,max} = 5.1^\circ$. Note the very good agreement on where the peak magnitude occurs, around 4.1-4.2 Hz, for both the experiment and the simulation. The data points shown in Figure 5.41 are connected as the voltage to the input motor is increased. With no load, this will

cause an increasing input frequency. However, due to the nonlinear load of the X-link imposed upon the motor, a steady increase in input frequency is not achieved. The frequency plotted against in all figures is indeed the input frequency and not the output response frequency.

(a)

(b)

(c)
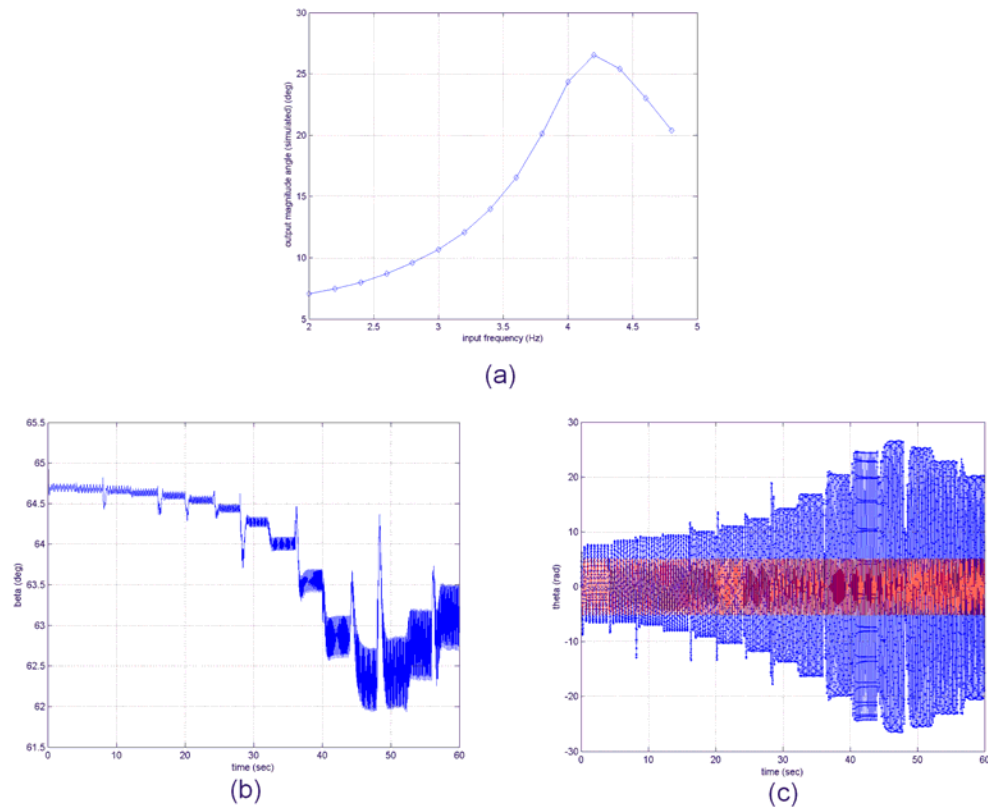
Figure 5.40. Simulated response of the full X-link model when input angle is $\theta_{in,max} = 5.1°$, and the magnets have a gap of 1.3 cm: (a) magnitude of θ versus input frequency, (b) time response of β, and (c) time response of θ.
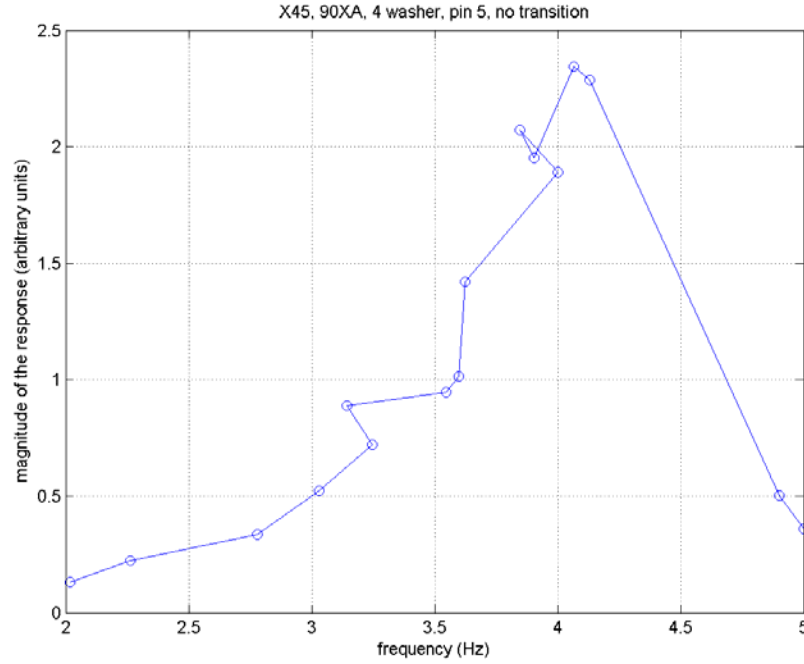
Figure 5.41. Experimental magnitude of θ versus input frequency for same case as Figure 5.40.

Now some results are shown where there is a transition from the short to long configuration of the X-link MSE system. Every parameter is kept the same as was used to produce the previous two figures, but the maximum input angle is increased to $\theta_{in,max} = 7.3^o$. The simulated and experimental results are shown in Figures 5.42 and 5.43, respectively. The transition occurs in both figures near 3.7 - 3.8 Hz. Note the motion of the angle β once the critical excitation frequency is reached making β decrease to its minimum value of 22.5^o. Note that the minimum value is not zero degrees due to the shape of the X-link system having the circular center that ends up resting on the table. Thus, the gravitational reaction force

starts acting through the center of the X-link at that point, creating no more torque to flatten the X-link.
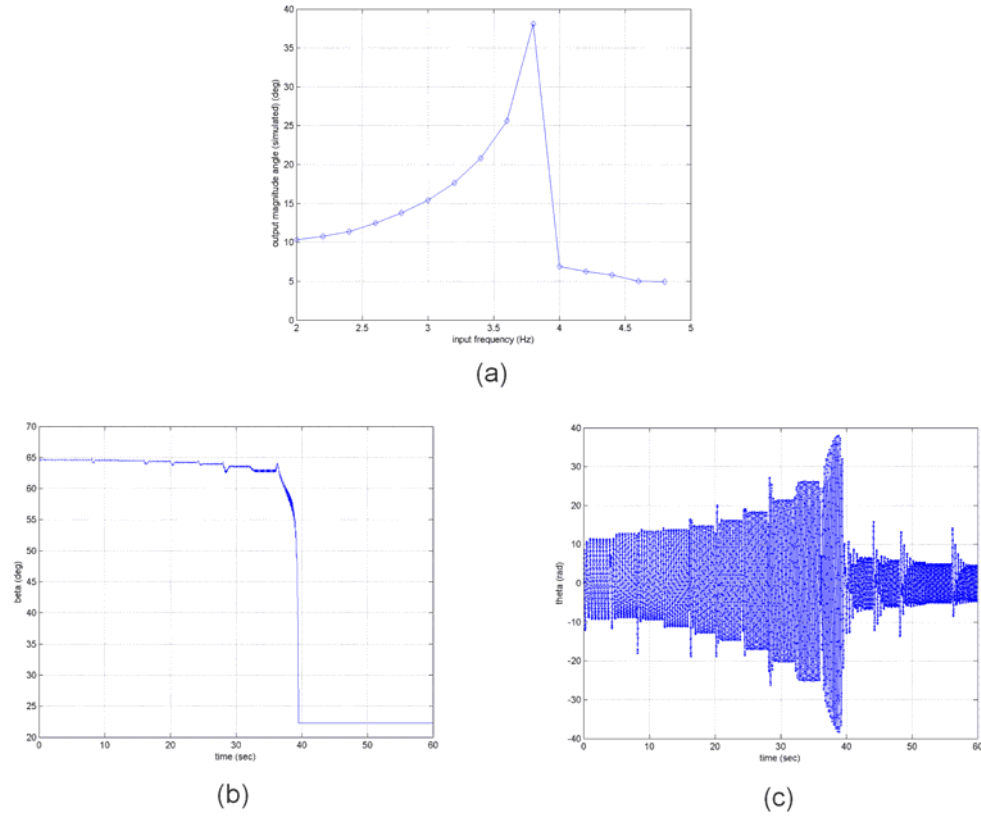
Figure 5.42. Simulated response of the full X-link model when input angle is $\theta_{in,max} = 7.3^o$, and the magnets have a gap of 1.3 cm: (a) magnitude of θ versus input frequency, (b) time response of β, and (c) time response of θ.
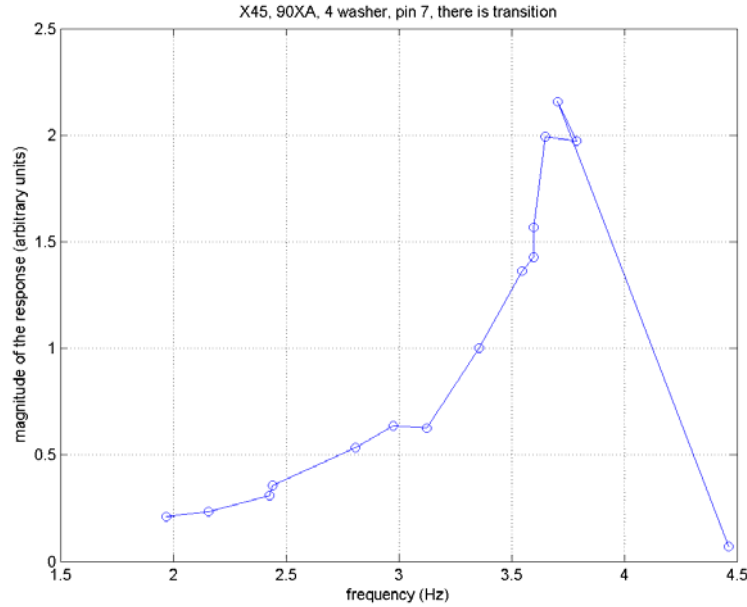
Figure 5.43. Experimental magnitude of θ versus input frequency for same case as Figure 5.42.

5.4.3 Relation of Simulation to MSE Synthesis Methodology

There is now established a valid model for predicting the dynamic response of the X-link MSE system. Given a valid X-link geometry, inertial properties, and magnetic energy model one can predict the response of the system and tailor the MSE X-link system design to desired specifications and performance. Given this valid model, the basic system response can be predicted as in Section 5.4.2, both locally about each stable position and in transition between the stable configurations. This can tie the design methodology to the realities of operating a MSE system and knowing what kinds of inputs will keep

224

the system about a particular stable equilibrium position. As mentioned in Chapter 2 of this dissertation, the scope of this work does not account for the full nonlinear dynamic nature which MSE systems can exhibit. It only considers localized dynamics that can be well approximated by linearized models. The Future Work section in Chapter 6 describes one possible way to extend the MSE synthesis methodology by incorporating nonlinear dynamic theory, in particular the Melnikov perturbation analysis.

In this section, a desired system performance is proposed, and then the MSE design synthesis methodology is used to determine if the proposed solution is achievable. During the modeling, simulation, and experimentation of the X-link model it was observed that the resonant frequency of the system in the short versus the long configuration is usually near two times as large. The reason it cannot be higher is primarily due to the limitation in the magnetic model. In order to facilitate a more extensive MSE X-link design, the magnetic potential energy model is put into the generalized form of a sixth order polynomial in β. A sixth order polynomial is chosen since it can satisfactorily characterize the experimentally determined magnetic models used for simulation in Section 5.4.2. In essence, to fully solve this X-link design problem, a separate problem is left to the designer to determine how to create the magnet model that is determined from this design process. Here it is assumed that the sixth order magnetic energy can somehow be created, perhaps by employing the MSE design methodology with finite element analysis, but that is beyond the scope of this work [Limaye, et al., 2003].

The MSE solution process is used for the rest of this Section 5.4. Section 5.4.3.1 sets up the problem, and Section 5.4.3.2 discusses the Monte Carlo mapping. Section 5.4.3.3 shows the results of using a genetic algorithm to solve for the system design variables.

5.4.3.1 Step1: Problem Description and Decide on important Engineering Characteristics of each Equilibrium

As mentioned earlier, the tested version of the X-link could not have a 'short' natural frequency that was more than around twice that of the 'long' configuration. Thus, a feasible test of the MSE design synthesis methodology is to explore what is required, in terms of the design variables, to achieve two natural frequencies that differ by a wider margin. The desired natural frequencies are to be 10 Hz and 1 Hz for the short and long configurations, respectively. This makes them an order of magnitude apart. Not much concentration will be put on at what length, or β value, the X-link will be in during each configuration, but a limit of $\beta_{max} = 85^{\circ}$ and $\beta_{min} = 4^{\circ}$ is set.

The design variables of the problem are set as follows:

1. X-link mass, m_X,

2. Input link mass, m_{input_links},

3. spring constant, k,

4. length of each X-link piece (all equal), l_X,

5. Moment of inertia of each X-link piece to form total inertia, I_{xx}, I_{yy}, I_{zz}, and

6. the seven coefficients (a_0 - a_6) of the magnetic model ($E_{mag} = a_6\beta^6 + a_5\beta^5 + a_4\beta^4 + a_3\beta^3 + a_2\beta^2 + a_1\beta + a_0$).

5.4.3.2 Step 2: Monte Carlo Mapping and Probability Calculation

The mapping procedure used is a bit different than those previously described because of the more ambiguous nature of the assumed magnetic energy model. Choosing random values for the coefficients of the sixth order model can produce a very wide variety of curves that are of no help or interest to the X-link problem. Therefore, the mapping proceeds in a slightly different manner as described next.

Due to the kinematics of the X-link, the potential energy at constant β is only a function of one design variable, k. Also, at constant θ, the potential energy is only composed of the magnetic and gravitational energies. Since the only energies that contribute to stability of the X-link in the β-direction are the gravitational and magnetic energy, the desired and magnetic energy curves can be used to solve for a reasonable magnetic curve. Therefore, in the mapping procedure, instead of generating random values for the magnetic energy coefficient design variables, random values are generated for the *desired design criteria* of the total energy in the β-direction. That is to say, at constant $\theta = 0$, the magnetic energy is the desired energy minus the gravitational energy, or $E_{mag} = E_{des} - E_{grav}$.

Using the assumed form of the magnetic energy, one can also calculate the first and second derivatives of the magnetic energy with respect to β. The models

for $E_{mag}(\beta)$ and its derivatives are shown in Equations (5.65-5.67). Giving desired design criteria for the total system energy enables one to use these values to solve for the coefficients of the magnetic energy. First, as the Monte Carlo procedure is generally used, generate random values for all design variables except for the magnetic energy coefficients. Then generate random β_{eq} positions for the stable and unstable equilibria. There is assumed to be two stable β_{eq} and one unstable β_{eq}. One also knows that at these equilibrium positions, the first derivative of the total energy is zero. This also means that the slope of the E_{mag} is equal and opposite to the slope of E_{grav}, as depicted in Equation (5.68).

$$E_{mag}(\beta) = a_6\beta^6 + a_5\beta^5 + a_4\beta^4 + a_3\beta^3 + a_2\beta^2 + a_1\beta + a_0 \quad (5.65)$$

$$\frac{dE_{mag}(\beta)}{d\beta} = 6a_6\beta^5 + 5a_5\beta^4 + 4a_4\beta^3 + 3a_3\beta^2 + 2a_2\beta + a_1 \quad (5.66)$$

$$\frac{d^2E_{mag}(\beta)}{d\beta^2} = 30a_6\beta^4 + 20a_5\beta^3 + 12a_4\beta^2 + 6a_3\beta + 2a_2 \quad (5.67)$$

$$\frac{dE_{mag}(\beta)}{d\beta} = -\frac{dE_{grav}(\beta)}{d\beta} \quad (5.68)$$

To find the seven coefficients for E_{mag}, one can specify seven design criteria within the mapping procedure to solve for the E_{mag} curve required to obtain the desired energy, E_{des}. Remember, that the desired energy curve is still randomly generated so that a good sample of the performance space is obtained.

228

Equation (5.69) shows the linear equation that is solved during the mapping procedure to obtain the E_{mag} coefficient design variables.

$$\begin{bmatrix} \beta_{eq,1}^6 & \beta_{eq,1}^5 & \beta_{eq,1}^4 & \beta_{eq,1}^3 & \beta_{eq,1}^2 & \beta_{eq,1} & 1 \\ \beta_{eq,2}^6 & \beta_{eq,2}^5 & \beta_{eq,2}^4 & \beta_{eq,2}^3 & \beta_{eq,2}^2 & \beta_{eq,2} & 1 \\ \beta_{eq,3}^6 & \beta_{eq,3}^5 & \beta_{eq,3}^4 & \beta_{eq,3}^3 & \beta_{eq,3}^2 & \beta_{eq,3} & 1 \\ 6\beta_{eq,1}^5 & 5\beta_{eq,1}^4 & 4\beta_{eq,1}^3 & 3\beta_{eq,1}^2 & 2\beta_{eq,1} & 1 & 1 \\ 6\beta_{eq,2}^5 & 5\beta_{eq,2}^4 & 4\beta_{eq,2}^3 & 3\beta_{eq,2}^2 & 2\beta_{eq,2} & 1 & 0 \\ 6\beta_{eq,3}^5 & 5\beta_{eq,3}^4 & 4\beta_{eq,3}^3 & 3\beta_{eq,3}^2 & 2\beta_{eq,3} & 1 & 0 \\ 30\beta_{eq,2}^4 & 20\beta_{eq,2}^3 & 12\beta_{eq,2}^2 & 6\beta_{eq,2} & 2 & 0 & 0 \end{bmatrix} \begin{bmatrix} a_6 \\ a_5 \\ a_4 \\ a_3 \\ a_2 \\ a_1 \\ a_0 \end{bmatrix} = \begin{bmatrix} (E_{des} - E_{grav})\big|_{eq,1} \\ (E_{des} - E_{grav})\big|_{eq,2} \\ (E_{des} - E_{grav})\big|_{eq,3} \\ -dE_{grav}\big/ d\beta \big|_{eq,1} \\ -dE_{grav}\big/ d\beta \big|_{eq,2} \\ -dE_{grav}\big/ d\beta \big|_{eq,3} \\ -d^2E_{des}\big/ d\beta^2 \big|_{eq,2} \end{bmatrix} \quad (5.69)$$

Using Equation (5.69), by providing values for the right-hand side (RHS), one can solve for the seven coefficients, a_0 - a_6. Here it is assumed that the first and third equilibria are stable, and the second equilibrium is unstable. The first three values of the RHS are generated randomly assuming arbitrarily that the energy has a value of zero at the unstable equilibrium, or $E_{des}|_{eq,2} = 0$ J. The values for $E_{des}|_{eq,1}$ and $E_{des}|_{eq,3}$ are generated randomly assuming some maximum and minimum energy that must be smaller than $E_{des}|_{eq,2}$. The $4^{th} - 6^{th}$ values on the RHS are generated numerically from the gravitation energy that is already calculated with random values. The final and 7th item if the RHS vector of Equation (5.69) must be some negative value, since it is the curvature of the desired energy at the unstable equilibrium. This curvature is randomly generated within a certain range of values.

The spring constant, k, only acts to dictate the natural frequency in the θ-direction at any constant β. Therefore, its value is not randomly generated, but rather its minimum and maximum values are used during each Monte Carlo trial to get the maximum and minimum curvatures in the θ-direction, and thus natural frequency.

The maximum and minimum ranges for the design variables, and RHS values of Equation (5.69) are now discussed. The values for these are based loosely on the values from the X-link experimental example since they are representative of reality. As the allowed range for each design variable is increased for the Monte Carlo mapping, one must consider whether or not the values are achievable in reality due to materials and manufacturing and such. Also, the combinations of design variables must be considered. For example, if an X-link has a very small rotational inertia but a large mass, one must consider that such a link may not be physically realizable with known materials. These types of issues are not considered for this exploratory research.

For the m_X the minimum is 0.01 kg, and maximum is 0.2 kg. For m_{input_links} the minimum and maximum values are 0.01 kg and 0.1 kg, respectively. The spring constant has values that surround the experimental value for the $\phi = 45^\circ$ X-link, k_{min} = 0.01 Nm/rad and k_{max} = 0.5 Nm/rad. For all inertias, the minimum value is 10^{-9} kgm^2. The maxima for I_{xx}, I_{yy}, and I_{zz} are 10^{-4}, 10^{-5}, and 10^{-4} kgm^2, respectively. The X-link link length, l_X, has maximum and minimum values of 0.5 and 0.1 m, respectively. To generate the first and third values of the RHS of Equation (5.69), the maximum and minimum energy differences from the

230

unstable energy value ($E_{des}|_{eq,2} = 0$) are 0.2 and 0.01 J respectively. These values are in the ballpark of what could be expected from the NdFeB magnets used in the X-link experiment. Finally, minimum and maximum curvature values for the 7th value of the RHS of Equation (5.69) are -10 and 0 J/rad^2. The equilibrium β values needed to evaluate the RHS of Equation (5.69) are also randomly generated in a range of β between 4° and 85°. They are generated such that $\beta_{eq,1} > \beta_{eq,2} > \beta_{eq,3}$.

In calculating the Monte Carlo probability, the desired design criteria are the frequencies in the θ-direction at the two stable positions and the location of the stable positions. Ranges for these desired design criteria which are considered acceptable are ± 1 Hz and ± 0.2 Hz for the short and long X-link configurations, respectively. The desired $\beta_{eq,1}$ (short configuration) and $\beta_{eq,3}$ (long configuration) were chosen as 82° and 25°, respectively, with a tolerance of ± 0.2 rad on each. The value desired $\beta_{eq,1}$ represents the a value near the upper limit allowed due to kinematic constraints, and the desired $\beta_{eq,3}$ value is near the lower limit from the experiment. The ± 0.2 rad tolerance on the β positions is quite liberal, as it equates to about ± 11.5°. Again, there is little emphasis on the exact equilibrium position.

The Monte Carlo mapping was run for 8000 trials. A qualitative mapping of the long natural frequency plotted against the short frequency is shown in Figure 5.44. Note a seemingly distinctive line acting as an upper limit on the graph. This line has an approximate slope of 4/5, meaning under the assumed topology, one can expect that the long natural frequency cannot be much higher

than 0.8 times the short natural frequency. There is a less distinctive lower boundary on the plot at a slope near 1/9. The desired design criteria point of 10 Hz and 1 Hz lies very near this apparent lower boundary, and thus seems to be a good test for whether or not this desired solution exists.
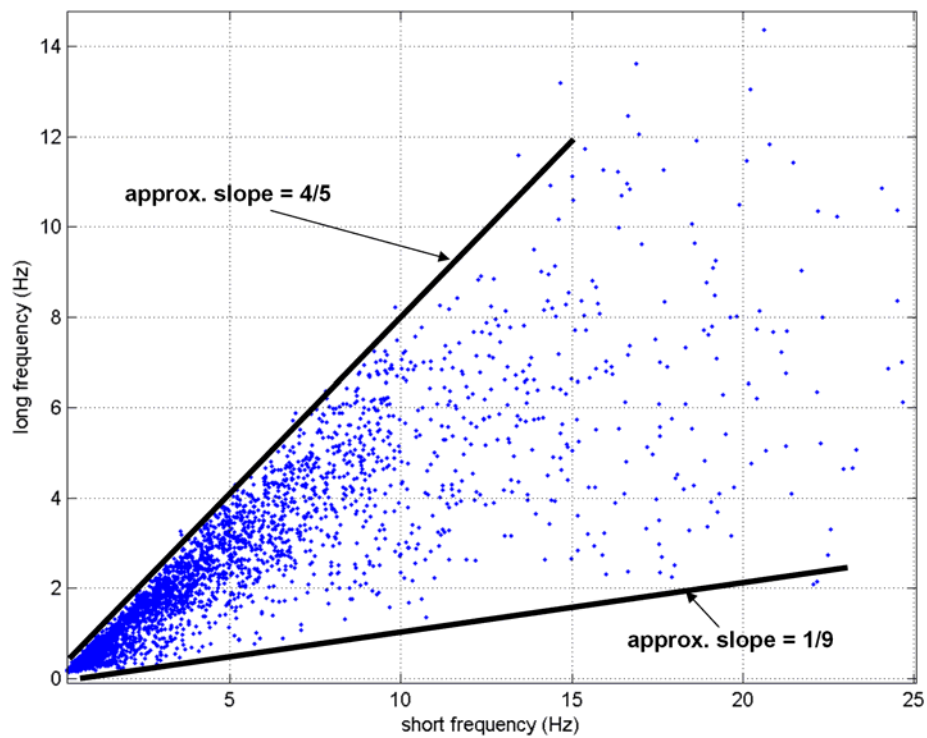
Figure 5.44. Qualitative mapping of the natural frequencies in the short and long X-link configurations.

The probability calculations for the four desired design criteria are shown in Table 5.8. Since the desired design criteria produce $P_{tot} = 0$, the high frequency criterion was perturbed to a few values that give $P_{tot} > 0$ for confirmation that the

genetic algorithm can easily solve the problems with known existence. The order in which the probability was calculated considers the frequency of the long configuration dependent upon that of the short configuration. In the trials with P_{tot} = 0, there were already no data points considering only these two criteria out of the four total.

Trial	f_{des} (Hz)	$\beta_{eq,des}$ (deg)	P_{tot}
1	[5.0 ±1.0, 1.0 ± 0.2]	[82 ± 11.5, 25 ± 11.5]	8.1e-4
2	[6.0 ±1.0, 1.0 ± 0.2]	[82 ± 11.5, 25 ± 11.5]	5.7e-4
3	[7.0 ±1.0, 1.0 ± 0.2]	[82 ± 11.5, 25 ± 11.5]	1.4e-4
4	[8.0 ±1.0, 1.0 ± 0.2]	[82 ± 11.5, 25 ± 11.5]	0
5	[8.2 ±1.0, 1.0 ± 0.2]	[82 ± 11.5, 25 ± 11.5]	0
6	[8.4 ±1.0, 1.0 ± 0.2]	[82 ± 11.5, 25 ± 11.5]	0
7	[8.6 ±1.0, 1.0 ± 0.2]	[82 ± 11.5, 25 ± 11.5]	0
8	[8.8 ±1.0, 1.0 ± 0.2]	[82 ± 11.5, 25 ± 11.5]	0
9	[9.0 ±1.0, 1.0 ± 0.2]	[82 ± 11.5, 25 ± 11.5]	0
10	[10.0 ±1.0, 1.0 ± 0.2]	[82 ± 11.5, 25 ± 11.5]	0

Table 5.8. Trial sets while calculating the Monte Carlo probability as the design criteria approach the true desired design criteria of Trial 10.

5.4.3.3 Step 3: Optimization and interpretation of results

The run-length distribution (RLD) of solving Trials 1-10 is shown below in Figure 5.45. The limit on generations for the genetic algorithm was limited to 1000. Trials 1-8 were all solved during 10 attempts for each solution, and for Trials 1-7 usually within 250 generations. This leads one to believe that the genetic algorithm is able to successfully solve the problem in a reasonable number

233

of generations. Trials 9 and 10 were not solved within the allotted number generations. Trials 9 and 10 were again attempted ten more times with a limit of 2000 generations, but they still were not solved even once. Note that the RLD in Figure 5.45 that does not reach a final value of one is for Trial 8. Also, the RLDs of Trials 7 and 8 begin to show some slower response to solution than the first six trials. This leads one to believe that the edge of the performance space is being reached near Trials 8 and 9, or near a short X-link configuration frequency of 8.8 Hz.
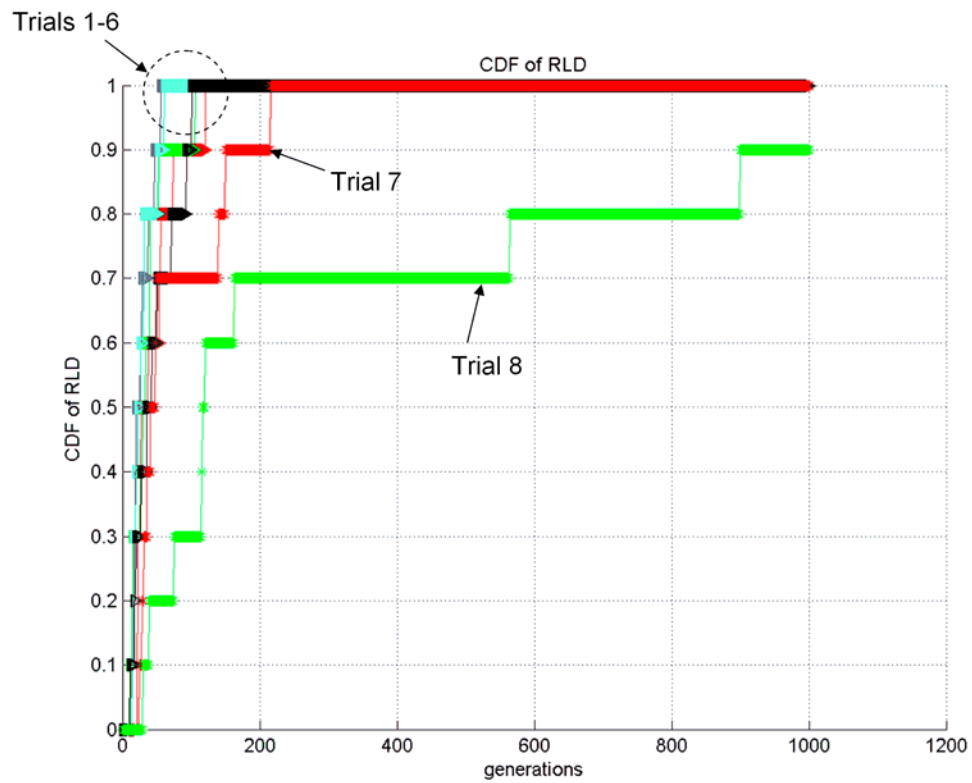
Figure 5.45. Run-length distribution for Trials 1-10 in Table 5.8. Trials 9 and 10 did not get solved.

To test further whether or not a design limit is being reached in the performance space, Trials 4-10 were run again for 30 attempts each with the second desired equilibrium position now being $\beta_{eq,2} = 15^{\circ}$. This change was made with the intuition that the further apart the equilibrium positions are in the β-direction, the more different the natural frequencies can be in the θ-direction. The RLD for the results of these trials is shown in Figure 5.46. There it is shown that the problem is more easily solved with the lower 'long' desired equilibrium position of $\beta_{eq,2} = 15^{\circ}$. There becomes much more difficulty in solving the problem when the desired short frequency is greater than 9 Hz. Thus, this critical performance space region is more fully explored.

Figure 5.46. RLD concentrating on limit in desired performance space. Only the trials for $f_{des,1} \leq 9.2$ Hz get solved successfully.

In viewing Figures 5.45 and 5.46, it seems as though the desired solution of having one stable equilibrium with a natural frequency near 10 Hz and the other with a frequency of 1 Hz is not occurring. There seems to be difficulty in convergence upon a solution when the desired short equilibrium has a frequency above 9.2 Hz.

To further check if indeed a design limit is reached, the equilibrium trends can be plotted to see if they converge to one limit or another of the desired design criteria (as in Figures 4.23-4.24). The perturbed design criterion is the natural frequency of the short X-link configuration. Upon inspection of the results used to produce Figure 5.46, there was no discernable pattern in the equilibrium trends. Therefore, several new attempts, 20 attempts, were tried for each perturbed short X-link frequency from 8 Hz to 10 Hz, but this time with very tight tolerances on the desired design criteria ($\pm$ 0.2 Hz for the frequencies and $\pm$ 0.01 rad for the equilibrium positions). Figure 5.47 shows the trends of the solutions for the desired design criteria using a very stringent fitness threshold. Figure 5.47a plots the equilibrium positions, and Figure 5.47b plots the natural frequencies in the θ-direction.

Figure 5.47. Equilibrium trends attempting to show some convergence of possible desired design criteria as the 'short' X-link frequency is perturbed toward the final desired value of 10 Hz.

238

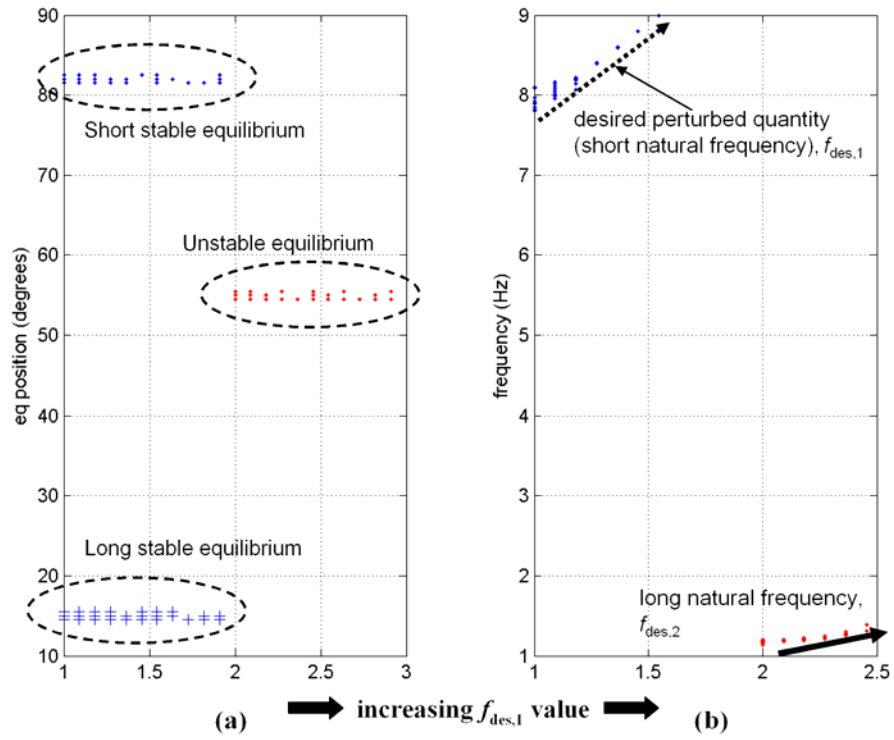In viewing Figure 5.47a, there appears to be very little limiting trends as the equilibrium positions are always in a range about the desired values of $\beta_{eq,1}$ = 82° and $\beta_{eq,2}$ = 15°. On the other hand, Figure 5.47b does show some limiting behavior. As the short frequency, $f_{des,1}$ is perturbed, the long frequency, $f_{des,2}$, proceeds in an upward trend. Recall that the desired natural frequency for the short X-link configuration is 1 Hz, but as the short frequency increases, so does the long frequency. A lower limit for the short frequency always seems to be above 1 Hz, and this lower limit increases to near 1.4 Hz where the data seizes to exist. Note that there is only data shown for when the perturbed short frequency is less than 9.2 Hz. At desired frequencies above that, no optimization runs produces results within the desired tolerance. This leads one to draw that conclusion that under the current topology and constraints set for this X-link problem, the desired MSE system is not possible. Either the topology should be changed, or a relaxation of the bounds on the design variables must occur. The latter is unlikely given that under certain samples of design variables, none lie at either their upper or lower limit.

5.4.4 Example X-link Simulation based on optimized results

Given that the fully desired MSE X-link system does not seem possible, a situation close to the desired is simulated from the trials used earlier. An example solution achieved with the tighter tolerances is one with desired frequencies of 8 and 1 Hz, and desired equilibrium positions of β = 15° and β = 82°. The tolerances used for the design criteria are ± 0.2 Hz for the frequencies and ± 5.7° for the

239

equilibrium positions. Figure 5.48 shows final potential energy curve. Figures 5.49 show the localized magnitude versus input frequency response for sinusoidal input for both the short and long X-link position. These plots depict where the resonance frequency lies, which is approximately the damped natural frequency that is sought.
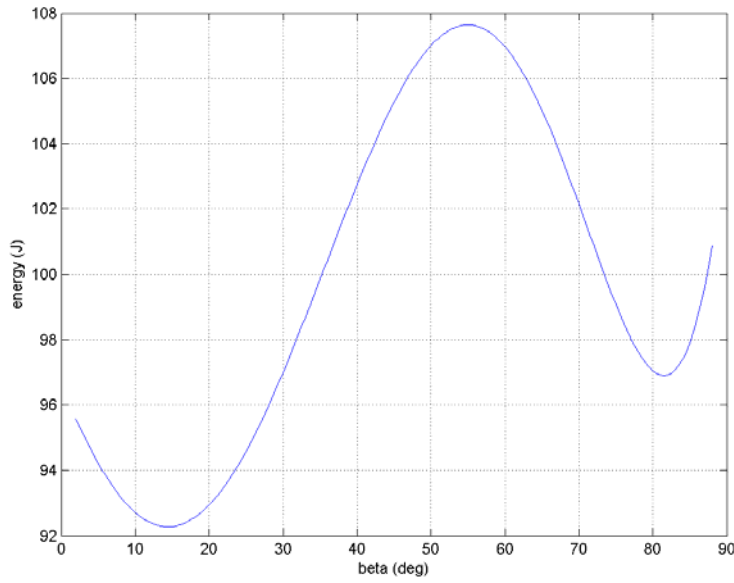
Figure 5.48. Example candidate potential energy curve for the desired design criteria of $\beta_{eq} = [15°, 82°] \pm 5.7°$ and $f_{des} = [8, 1] \pm 0.2$ Hz.

Figure 5.48 shows the stable equilibrium positions to be 81.5° for the short configuration and 14.5° for the long X-link configuration. Figures 5.49a and 5.49b show the magnitude versus input frequency for the short and long configurations, respectively. The calculated natural frequencies from the optimizations are 7.9 Hz and 1.2 Hz while the peaks in the figures occur near 7.5 Hz and 1.2 Hz.

Nonetheless, the tolerances are still within the initial desired tolerances of $\pm$ 1 Hz and $\pm$ 0.2 Hz, respectively. Figures 5.49c and 5.49d show the time response of the displacement β. Note the input magnitude for Figure 5.49 is one degree, which keeps the system in a local area near each stable equilibrium, as seen in Figures 5.49c and 5.49d.
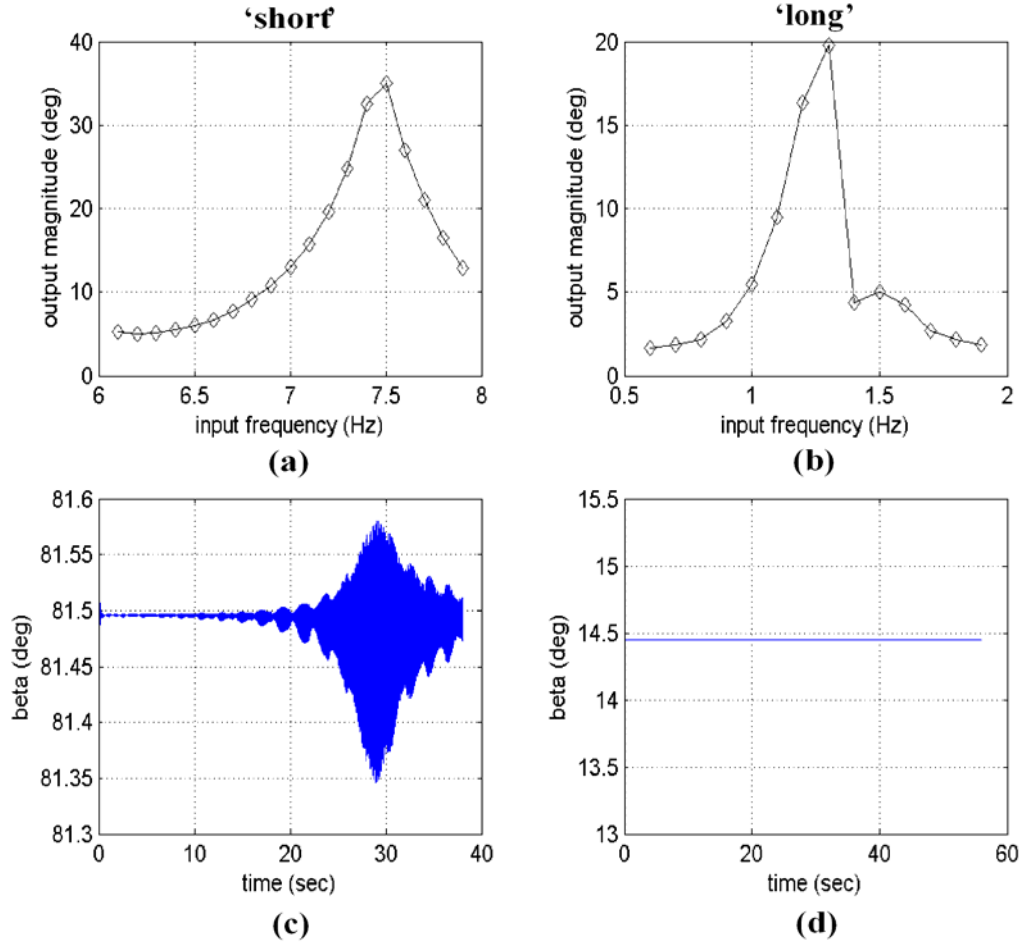
Figure 5.49. Magnitude vs. input frequency plots and transient response for example X-link solution using potential energy of Figure 5.48.

The candidate design variables optimized to produce the results of Figures 5.48 and 5.49 are $k = 0.126$ Nm, $I_{xx1} = 9.6\text{e-}5$, $I_{yy1} = 7.1\text{e-}7$, $I_{zz1} = 9.3\text{e-}5$, $I_{xx2} = 6.6\text{e-}5$, $I_{yy2} = 6.3\text{e-}6$, $I_{zz2} = 8.6\text{e-}5$ (all inertias in kg*m^2) $m_X = 0.11$ kg, and $m_{input\_links} = 0.01$ kg. Notice that each design variable is in between its maximum and minimum allowable value. Thus, no constraints are active. Figure 5.50 shows

the fitness versus generation as the genetic algorithm solves for the aforementioned design variables. This is typical for most optimization runs. When the fitness increases to zero the desired design criteria are reached to within specified tolerance. Even for trials not solved in the RLDs of Figures 5.45-5.46, the fitness goes very close to zero within 200-400 generations. Then a plateau is reached from which the fitness increases very little in ever decreasing increments.
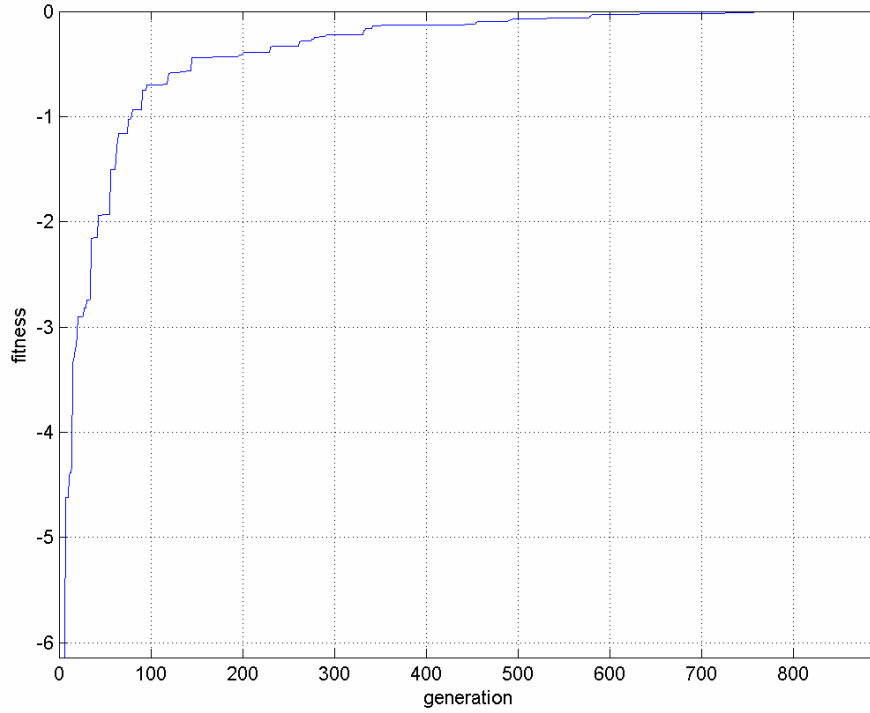
Figure 5.50. Fitness versus generation showing the progress in solving
the trial exemplified in Figures 5.48-5.49.

5.4.5 Conclusion on X-link Synthesis

The synthesis of the X-link mechanism is performed well using the synthesis methodology demonstrated in this dissertation. The attempted desired solution having f_{des} = [1 ± 0.2, 10 ± 1.0] Hz for the long and short X-link configurations, respectively, was determined not possible with the current topology. This topology assumed a 6th order magnetic energy model. There is no guarantee that the derived magnetic model can indeed be achieved in reality due to material property constraints not considered here. In all likelihood, the 6th order

244

model is very liberal, and considers energy curves that are not achievable using realistic permanent magnets. Nonetheless, even with this assumption regarding the magnetic energy model, the desired design is still not achievable. A new topology need be found to satisfy the design requirements. That is left to future work mentioned in the final chapter, Chapter 6.

Chapter 6: Conclusions and Future Work

6.1 CONCLUSIONS

The multistable equilibrium system design synthesis methodology presented in this dissertation enables a designer with an energetic model of a nonlinear system to decide what multistable designs are possible. Starting from having a model for the system potential energy and kinetic coenergy, a step-by-step design process enables one to sufficiently explore the solution space for the problem.

Past work in buckling beams and mechanisms provides mostly a very recent history into the analysis of bistable structures. Nonetheless, there is almost no work on the synthesis of bistable systems much less MSE systems. Adaptive systems using smart materials such as shape memory alloys and piezoelectric materials attempt to create structures that have variable performance parameters. Usually this adaptive behavior is about only a single equilibrium operating point. This dissertation begins a design avenue for the MSE system to become a new type of adaptive system in which there are multiple stable operating points.

Either or both of the static and dynamic local properties of the stable equilibria could be of importance to the designer. This leads to a few basic categorizations of MSE systems. MSE systems can generally be designed for static position or shape, such as for switches or aerodynamic purposes. They can also be designed for local dynamics with tuned natural frequencies for vibration

suppression or efficient excitation. Of course, sometimes the two concepts are directly coupled such as in the example of creating a robotic fish with different shapes and stiffnesses to take advantage of the different swimming niches existing in nature.

The MSE design synthesis methodology consistently focuses on the purpose of the design: to create and tailor the equilibrium positions. Thus, whenever possible, design decisions and measurements are made with regard to the equilibrium properties and not the optimized design variables. The definition of the equilibrium position is based on the minimum energy principle. Descriptors of the equilibria are derived using a second order least squares curve fit about each equilibrium. From this use curve fitting the three major characteristics of the equilibrium are derived: position, energy value, and curvature used to calculate natural frequency.

Using the three equilibrium characteristics as measurands, the solution space of a given problem is both qualitatively and quantitatively mapped to provide the designer with a comprehensive description of whether or not a chosen desired design is possible. The qualitative mapping helps in choosing initial desired design criteria, such as equilibrium positions and frequencies. To solve for the unknown design variables of the problem, numerical optimization algorithms are used. Usually stochastic algorithms are required if concurrently solving for more than one equilibrium at a time. The bifurcating nature of MSE systems creates a multimodal design space in which a stochastic optimization approach is usually necessary.

The quantitative mapping method enables the designer to determine solution existence, if necessary, through a series of solving perturbed desired designs. This solution existence determination starts with a solution of guaranteed existence, and perturbs it to the desired solution (if different). By tracking the optimization algorithm results of solving each successive perturbed solution, one is able to form an assessment of solution existence or a localized boundary to the solution space. In determining this solution space boundary, the design methodology makes use of the run-length distribution and the tracking of trends in the equilibrium solutions found during the series of optimizations.

6.1.1 Brief summary of Dissertation contributions

To sum up the contributions of this work, there was developed:

1) a statistical solution procedure for MSE systems that allows the design engineer to determine if a desired solution is feasible or not for a given system topology and energy model,

2) a definitive characterization of how to relate the engineering design characteristics of MSE systems into a problem formulation that is amenable to solution by stochastic optimization algorithms,

3) a solution procedure that is amenable to any number of equilibrium positions, generalized coordinates, or energy domains, and

4) a description of the major purposes for designing MSE systems.

6.2 FUTURE WORK

6.2.1 System Topology

There are many paths to follow for future work in the design of MSE systems. Perhaps the foremost of these, but quite complex in itself, is the determination of system topology that is referenced in the general design flow chart of Chapter 4. After completing the design synthesis process of this dissertation, it is entirely possible that the desired design is not possible. In this case one has two options: give up, or change the system topology in such a way to make the desired system now possible. Giving up is trivial and deserves no further attention, while system topology is likely quite complex.

Changing the system topology involves relaxing constraints on existing energy storage elements or adding new energy storage elements. There are a few anticipated difficulties in changing the system topology: type of energy storage element, location or connection of energy storage elements, and energetic modeling. First, when adding an energy storage element, one must decide exactly what to add to the system. There are many choices for potential energy storage elements such as springs, magnets, fluid tanks. One may also add kinetic energy storage elements to alter the transient dynamics of the system. Knowing which type, and possibly how many, new components to add could be very beneficial to the full designing of MSE systems. Knowing how to connect to, or have additional elements interact with, the existing MSE system can also influence the design. One must fully understand the consequences of each additional component to the system. For instance, a magnet moving laterally with respect to

249

another magnet can go from attractive to repulsive in a fraction of the length of the magnet depending on how it is constrained to move.

6.2.2 Modeling of Vector Potential Fields

Energetic modeling is an issue in the sense that without an effective model for an energy storage element, one cannot use it in the design methodology. For example, adding magnets to create stable positions may seem feasible, but if there can be large air gaps between magnets and any other magnetic materials, the energy storage can be difficult if not impossible to derive for arbitrary geometries. This modeling includes both analytical and experimental modeling of elements involved in the system.

The concept of arbitrary geometries for magnetic fields leads to another topic that could expand the design of MSE systems. A large potential exists for advances in MSE system design in vector potential fields. These fields could be stress, electrostatic, and magnetic to name a few. It would be useful to obtain information about the possibilities in potential fields depending on the constrained the motion of the system. For example, with one piece of iron moving around one permanent magnet, there could theoretically be any number of equilibria greater than one depending on the constrained motion of the iron piece. If the iron piece moved in a highly oscillatory circle around the magnet, there could be a stable position at every trough of the path. Yet for a straight iron path, there is likely only one stable equilibrium. Some initial exploration into this concept using finite element analysis (FEA) was performed by Limaye et al., 2003. There is

tremendous potential to make use of computational methods, such as FEA, to explore possibilities for arbitrarily shaped and coupled MSE systems. The drawback can be largely increased computational time. In these cases different levels of modeling can be used together to eliminate infeasible designs early in the design process before very costly calculations are performed. Alexandrov and Lewis (2001) use an approach called first order model management.

6.2.3 Design Synthesis of Nonlinear Dynamics of MSE Systems

Another major area for future work in MSE system design is in regard to the prediction of nonlinear dynamic nature of MSE systems. This dissertation only considers locally linearized dynamics to characterize the systems. The general area of nonlinear dynamics is extensively studied by many [Simiu, 2002; Simiu and Franaszek, 1997; Thompson, 1996]. Instead of only describing MSE systems by their potential energy and effective inertias, expansion of the MSE design methodology could describe phase portraits or shapes of the Hamiltonian adding both potential and kinetic energy. One could design MSE systems for a particular shaped separatrix to help predict both dynamic as well as static stability. Also, for substantially harmonically excited nonlinear systems, the response is a function of both input magnitude and frequency [Virgin, 2001]. Thus, mappings could be made relating to the stability range of the equilibrium points in terms of the input frequencies and magnitudes, and stochastic inputs. The goal would be able to predict the combinations of input strength and

frequency for which one could expect the system to leave or stay about the current stable equilibrium.

6.2.4 Use of Robust Optimization principles

In solving MSE problems, it is possible to have more than one design solution that can satisfy the desired design criteria. In that case, which set of design variables should the engineer use? The answer could be determined by cost. If cost is not a factor, or if many solutions have the same cost, then the best design could be the one with the least amount of sensitivity to noise in the design variables. This concept is at the heart of the field of 'robust optimization' [Gunawan and Arzam, 2003].

The robust optimization concept could also be used in the future work of topological design of MSE systems, mentioned in Section 6.2.1. If the current topology is insufficient, how does one know what kinds of new models or design variables to add to the system? By adding components and quantifying the design sensitivity when they are added may help determine the feasibility that any one added component will help achieve the desired MSE design. Also, one may even be able to determine that some components are spurious and not needed for the MSE system. The answer could lie in changing those variables with very low sensitivity relative to the potential energy curve. Maybe the robust approach could help determine that certain components are performing the same function, and therefore one can be eliminated.

Bibliography

Aksyuk, V. L.; Barber, B.; Bishop, D.; Giles, C.; and Stulz, L. (March 20, 2001) U.S. Patent No. 6205267, 'Optical Switch'.

Alexandrov, N. M. and Lewis, R. M. (2001) An Overview of First-Order Model Management for Engineering Optimization. *Optimization and Engineering*, **2**, pp. 413 - 430.

Barrett, R., Frye, P, and Schliesman, M. (1996) Design, Development and Testing of a Solid State Adaptive Rotor. *1996 Society of Photo-Optical Instrumentation Engineers Symposium on Smart Materials, Structures and MEMS*, Indian Institute of Science, Bangalore, India December 11 – 14.

Bowker, Albert H. and Lieberman, Gerald J. (1972) *Engineering Statistics*, 2nd Ed., Prentice-Hall, NJ.

Cagan J.; Shimada K.; Yin S. (2002) A survey of computational approaches to three-dimensional layout problems. *Computer-Aided Design*. **34** (8), pp. 597-611.

Capanu, M., Boyd, J. G., and Hesketh, P. J. (2000) Design, Fabrication, and Testing of a Bistable Electromagnetically Actuated Microvalve. *Journal of Microelectromechanical Systems*, **9**(2), pp. 181 – 189.

Chironis, N. P. (1991) *Mechanisms and Mechanical Devices Sourcebook*. McGraw-Hill Inc., New York.

Eisler, G. Richard; Veers, Paul S. (1998) Parameter Optimization Applied to Use of Adaptive Blades on Variable Speed Wind Turbine. Report of Sandia National Laboratory: SAND98-2668.

Erdman, Arthur G, Sandor, George N., and Kota, Sridhar, (2001) *Mechanism Design: Analysis and Synthesis, Volume 1*. 4th Ed., Prentice Hall, Upper Saddle River, NJ.

Fitzgerald, A. E., Kingsley, C. Jr., and Umans, S. (1990) *Electric Machinery*, 5th Ed., McGraw-Hill Inc., New York, Chap.1.

Giles, C.R.; Barber, B.; Aksyuk, V.; Ruel, L.; and Bishop, D. (1999) Reconfigurable 16-Channel WDM DROP Module Using Silicon MEMS Optical Switches. *IEEE Photonics Technology Letters*, **11** (1), pp. 63-65.

Gottlieb, H. P. W. (1997) Exact mimicry of nonlinear oscillatory potential motion: Nonuniqueness of isodynamical tracks. *Journal of Sound and Vibration*, **204**, pp. 519-532.

Greenwood, Donald T. (1998) *Principles of Dynamics*, 2nd Ed., Prentice Hall, NJ.

Griffin, Dayton A. (2002) Evaluation of Design Concepts for Adaptive Wind Turbine Blades. Report of Sandia National Laboratory: SAND2002-2424.

Gunawan, S., and Azarm, S. (2003) Non-gradient based Parameter Sensitivity Estimation for Robust Design Optimization. *Proceedings of the 2003 ASME Design Engineering Technical Conference*, Chicago, IL, September 2-6, paper DAC-48716.

Gupta K. C., J. Li, R. Ramadoss, C. Wang, Y. C. Lee, and V. M. Bright. (2000) Design of Frequency-Reconfigurable Rectangular Slot Ring Antennas. *Proceedings of the 2000 IEEE APS International Symposium*, Salt Lake City, UT, July 16-21.

Hafez, Moustapha, Lichter, Matthew D., and Dubowsky, Steven, (2002) Optimized Binary Modular Reconfigurable Robotic Devices. *Proceedings of the 2002 IEEE International Conference on Robotics and Automation.*

Hoffman, M., Kopka, P., and Voges, E., (1999) Bistable micromechanical fiber-optic switches on silicon with thermal actuators. *Sensors and Actuators*, **78**, pp. 28-35.

Houck, Christopher R., Joines, Jeffery A., and Kay, Michael G. *A Genetic Algorithm for Function Optimization: A Matlab Implementation*, North Carolina State University.

Howell, L. L., Rao, S. S., and Midha, A. (1994) Reliability-Based Optimal Design of a Bistable Compliant Mechanism. *The Journal of Mechanical Design*, **116**, pp. 1115 – 1121.

Ingber, A. L. (1989) Very Fast simulated re-annealing. *Journal of Mathl. Comput. Modelling*. **12**, pp. 967--973.

Jalbert, J. Kashin, S. Ayers, J., (1995) A Biologically-based Undulatory Lamprey-like AUV. *Proc. of the Autonomous Vehicles in Mine Countermeasures Symposium*, Naval Postgraduate School, pp. 39-52.

Jensen, B. D., Howell, L. L., and Salmon, L. G. (1998) Introduction of Two-Link, In-Plane, Bistable Compliant MEMS. *The Proceedings of the 1998 ASME Design Engineering Technical Conference*, Atlanta, Georgia, Paper No. DETC98/MECH-5837.

Jensen, B. D., and Howell, L. L. (2000) Identification of Compliant Pseudo-Rigid-Body Mechanism Configurations Resulting in Bistable Behavior. *The Proceedings of the 2000 ASME Design Engineering Technical Conference*, Baltimore, Maryland, Paper No. DETC2000/MECH-14147.

Karnopp, Dean C.; Margolis, Donald L.; Rosenberg, Ronald C. (1990) *System Dynamics: A Unified Approach*, John Wiley and Sons, Inc., 2nd Ed.

Kim, Y., and Neikirk, D. P. (1995) Micromachined Fabry-Perot Pressure Transducer with Optical Fiber Interconnects. *Proceedings of the SPIE conference: Micromachined Devices and Components*, R. Roop and K. Chau, eds., SPIE **2642**, Austin, Texas, pp. 242-249.

Limaye, A. A., King, C. W., and Campbell, M. I. (2003) Analysis of Multiple Equilibrium Positions in Magnetostatic Field. *Proceedings of the 2003 ASME Design Engineering Technical Conference*, Chicago, IL, September 2-6, paper DAC-48841.

Long, J. H., McHenry, M. J., and Boetticher, N. C. (1994) Undulatory Swimming: How Traveling Waves are Produced and Modulated in Sunfish (Lepomis gibbosus). *Journal of Experimental Biology,* **192**, pp. 129-145.

McHenry, M. J., Pell, C. A., and Long Jr., J. H. (1995) Mechanical Control of Swimming Speed: Stiffness and Axial Wave Form in Undulating Fish Models. *The Journal of Experimental Biology*, **198**, pp. 2293-2305.

Michalicek, M. Adrian, U.S. Patent No. 6040935, (March 21, 2000) Flexureless Multi-Stable Micromirrors for Optical Switching.

Opdahl, P.G., Jensen, B. D., and Howell, L. L. (1998) An Investigation into Compliant Bistable Mechanisms. *The Proceedings of the 1998 ASME Design Engineering Technical Conference*, Atlanta, Georgia, Paper No. DETC98/MECH-5914.

Otto, K. and Wood, K. (2001) Product Design: Techniques in Reverse Engineering and New Product Development, Prentice Hall, Upper Saddle River, NJ.

Pabst, D. A. (1995) Swimming Springs in Animals. *Proceedings of the Symposium on Aquatic Locomotion: New Approaches to Invertebrate and Vertebrate Biomechanics*, December 27-30, pp. 723-735.

Saif, M. Taher A. (2000) On a Tunable Bistable MEMS – Theory and Experiment. *Journal of Microelectricalmechancal Systems*, **9**(2), pp. 157 – 170.

Schomburg, W. K., and Goll, C. (1998) Design optimization of bistable microdiaphragm valves. *Sensors and Actuators A*, **64**, pp. 259 – 264.

Schulze, E. F. (1955) Designing Snap-Action Toggles. *Product Engineering*, **26**(1), pp. 168 – 170.

Shaw, S. W., and Haddow, A. G. (1992) On 'roller-coaster' experiments for nonlinear oscillators. *Nonlinear Dynamics*, **3**, pp 375-384.

Simiu, Emil, (2002) Chaotic Transitions in Deterministic and Stochastic Dynamical Systems: Applications of Melnikov Processes in Engineering, Physics, and Neuroscience, Princeton University Press, Princeton, NJ.

Simiu, Emil and Franaszek, Marek, (1997) 'Melnikov-Based Open-Loop Control of Escape for a Class of Nonlinear Systems, ASME Journal of Dynamical Systems, Measurement, and Control, **119**, pp. 590-594.

Stützle, Thomas and Hoos, Holger H. (1999) Analyzing the Run-time Behaviour of Iterated Local Search for the TSP. *Proceedings of the 1999 Metaheuristics International Conference*, Angra dos Reis, Brazil, July 19-22.

Suleman, A. (2001) *Smart Structures: Applications and Related Technologies*, CSIM No. 429, Springer-Verlag.

Taubes, Gary (2000) Biologists and Engineers Create a New Generation of Robots That Imitate Life. *Science*, **288**, pp. 80-83.

Thompson, J.M.T. (1996) Global Dynamics of Driven Oscillators: Fractal Basins and Intermediate Bifurcations: Chapter 1 of *Nonlinear Mathematics and its Applications*, Ed. Philip J. Aston, Cambridge University Press.

Vangbo, Mattias and Bäcklund, Ylva, (1998) A lateral symmetrically bistable buckled beam. *Journal of Micromechanics and Microenegineering*, **8**, pp. 29 – 32.

Virgin, L. N. (2000) *Introduction to Experimental Nonlinear Dynamics: A Case Study in Mechanical Vibration*, Cambridge University Press.

Wardle, C. S., Videler, J. J., and Altringham, J. D. (1995) Review – Tuning in to Fish Swimming Waves: body form, swimming mode and muscle function. *The Journal of Experimental Biology*, **198**, pp. 1626-1636.

Weihs, Daniel (1989) Design Features and Mechanics of Axial Locomotion in Fish. *American Zoologist*, **29**, pp. 151-160.

Wingert A., Lichter M., Dubowsky S. (2002) On the Kinematics of Parallel Mechanisms with Bi-Stable Polymer Actuators. *Proceedings of the 8th International Symposium on Advances in Robot Kinematics*, Spain, June.

Vita

Carey Wayne King was born in Temple, TX on November 25, 1974, the son of Ronald Joe King and Carolyn Marie King. He attended Meredith Elementary and Bonham Middle School where he was quarterback for the 8th grade B-team football team while throwing one touchdown pass for his career in a heartbreaking 36-6 loss to Travis Middle School. Later he attended Temple High School where he lettered in soccer. In the Fall of 1993 he enrolled in the College of Engineering at the University of Texas at Austin. He graduated in Fall 1997 with a BSME and highest honors, and his undergraduate success enabled him to win a National Science Foundation Graduate Fellowship to attend graduate school. Carey chose to stay in Austin and return to the University of Texas to pursue his Ph.D.

Carey's work experience includes working at the Institute for Advanced Technology during the time between undergraduate and graduate school. In the latter two years of graduate study he performed engineering consulting work for a fledgling start-up company, Uni-Pixel, that had visions of becoming the maker of the next great display technology. He also volunteered as a teaching assistant for two undergraduate upper division mechanical engineering courses.

The current publications for Carey include one:

(1) Limaye, A. A., King, C. W., and Campbell, M. I. (2003) Analysis of Multiple Equilibrium Positions in Magnetostatic Field. *Proceedings of the 2003 ASME Design Engineering Technical Conference*, Chicago, IL, September 2-6, paper DAC-48841.

Permanent Address: 12005 Fremont Cove, Austin, TX 78727

This dissertation was typed by the author.